



ÉCOLE
CENTRALE LYON

N° d'ordre NNT : 2022ECDL0023

THESE de DOCTORAT DE L'ÉCOLE CENTRALE DE LYON
membre de l'Université de Lyon

École Doctorale N° 162
Mécanique Énergétique Génie Civil Acoustique

Spécialité de doctorat : Acoustique

Soutenue publiquement le 09/12/2022, par

Martin Buszyk

**Aeroacoustics of leading edge serrations for
turbulence-cascade interaction noise reduction**

Devant le jury composé de

Bailly Christophe	Professeur des Universités	Directeur de thèse
Barrier Raphaël	Ingénieur de recherche	Membre invité
Gabard Gwénaél	Professeur des Universités	Examineur
Gervais Yves	Professeur des Universités	Rapporteur
Gloerfelt Xavier	Professeur des Universités	Rapporteur
de Laborderie Hélène	Ingénieure	Examinatrice
Le Garrec Thomas	Ingénieur de recherche	Examineur
Polacsek Cyril	Ingénieur de recherche	Examineur
Sanjosé Marlène	Professeure des Universités	Examinatrice

Résumé

Dans le domaine de l'aéroacoustique consacré aux avions de transport, le moteur est une source de bruit majeure. Avec l'augmentation du diamètre des moteurs, la contribution de la soufflante au bruit rayonné est devenue dominante. L'interaction des sillages du rotor avec les aubes du stator est le mécanisme principal du bruit tonal et à large bande des soufflantes. La conception de futurs moteurs d'avion silencieux pose deux défis majeurs : une meilleure évaluation des sources à large bande et la conception de traitements efficaces pour la réduction du bruit. Cette thèse vise à mettre en oeuvre des méthodologies dédiées à la prédiction du bruit d'interaction, en particulier pour l'évaluation de dispositifs de réduction de bruit reposant sur des ondulations du bord d'attaque des aubes du stator. Ces approches ont principalement été appliquées sur une géométrie de référence et deux concepts de réduction de bruit proposés par l'ONERA en vue d'une campagne expérimentale sur une cascade d'aubes rectiligne. Trois approches sont considérées. Premièrement, une solution analytique pour des plaques planes avec des ondulations de bord d'attaque (basse fidélité) qui est étendue à des configurations variables en envergure. Deuxièmement, une approche CFD/CAA (fidélité intermédiaire) pour laquelle une turbulence synthétique 3D par modes de Fourier est développée. Troisièmement, des calculs LBM à deux milliards de points (haute fidélité) simulant l'ensemble du banc d'essai. La comparaison de toutes ces méthodes sur une même configuration a permis de mieux comprendre comment le niveau de fidélité des approches de prédiction influence le comportement aéroacoustique. En outre, la géométrie avec bord d'attaque ondulé proposée par l'ONERA a démontré une réduction du bruit jusqu'à plusieurs décibels en configuration installée tout en limitant les pénalités aérodynamiques. Enfin, les approches de prédiction du bruit d'interaction et la méthodologie de conception des aubes avec traitement de bord d'attaque sont étendues à des configurations plus réalistes de soufflante.

Abstract

In the field of aeroacoustics devoted to transport aircrafts, the engine is a major noise source. With the increase of the engines' diameter, the turbofan contribution has become dominant. The rotor wakes interaction with the stator vanes is the main contributor to the tonal and broadband fan noise. There are two main challenges to design future quiet aeroengines: a better evaluation of the complex broadband sources and proposing effective treatments for noise reduction. This PhD, which aims at the implementation of dedicated methodologies for the interaction noise predictions, in particular for low-noise designs based on leading edge undulations of the stator vanes. These approaches have been mainly applied on baseline and two ONERA's low-noise designs in preparation for an experimental test campaign on a rectilinear cascade. These methods include: an analytical solution for flat plates with leading edge serrations (low-fidelity), which is extended to spanwise varying configurations, a CFD/CAA approach (intermediate-fidelity), for which a 3D Fourier modes synthetic turbulence is developed, and 2 billion points LBM calculations (high-fidelity) including all the test rig. Comparing all those methods on a single bench enabled a better understanding of how the fidelity level plays on aeroacoustics. In addition, the wavy leading edge solution has demonstrated up to several decibels noise reduction in an installed configuration with limited aerodynamic penalties. Finally, extension of the updated noise prediction approaches and serration design methodology to more realistic turbofan configurations has been discussed.

Remerciements

Avant toute chose, je souhaite remercier Cyril d'avoir accepté ma candidature au stage sans lequel cette thèse n'aurait pu exister.

Je tiens ensuite à remercier l'ONERA pour m'avoir accordé sa confiance pendant ces trois années au poste de doctorant, ainsi que ADEC CleanSky pour avoir financé ces travaux de thèse.

J'ai vécu trois années très enrichissantes à la fois sur le plan intellectuel, avec de nombreux moments de doute, de réflexion, d'idée et de débat, mais, également sur le plan humain avec un très chaleureux accueil des unités d'acoustique SN2A et MAXE (devenues AKOU). Ces trois années n'auraient pas été aussi agréables sans nos échanges animés en pauses café et sorties du vendredi.

Je souhaite également remercier mon encadrant d'H2T, Raphaël, pour son aide dans la conception des aubes et les calculs CFD ainsi que pour nos échanges sur les turbomachines.

Enfin, j'ai une pensée particulière pour mes deux encadrants Cyril et Thomas qui ont su à la fois me pousser à m'améliorer et aller plus loin dans le domaine de la recherche au cours de ces trois années, mais également pour tout le temps qu'ils ont consacré à me guider et me conseiller. Encore une fois, un grand merci à eux.

Je souhaite finalement remercier Christophe pour avoir accepté de diriger cette thèse ainsi que pour ces conseils pertinents lors des rédactions d'articles, du manuscrit et lors de la préparation orale. Malheureusement, à cause de la crise sanitaire nos interactions en présentiel n'ont pu être aussi nombreuses qu'escompté.

Hors du cadre professionnel, j'ai une pensée pour ma famille qui m'a apporté son soutien ainsi que mon ami de longue date Attila pour nos innombrables appels skype. Enfin je souhaiterais remercier mes compagnons du quotidien, mon excellent colocataire Martin sans qui les confinements et les soirées auraient été longues, Éloïse notre demi-colocataire pour nos débats et nos fous rires, et enfin ma copine Julia pour son soutien et sa tendresse tout au long de ces trois années.

J'aimerais conclure en évoquant le fait que j'ai l'opportunité de continuer ces travaux dans le cadre d'un contrat salarié. Passé le temps de la soutenance, je trouve intéressant d'avoir une nouvelle perspective sur les projets de recherche. Ce nouveau départ représente également une très belle occasion de mieux découvrir les membres de l'équipe qui se reconnaîtront (merci pour l'escalade et autres sorties) et à qui je souhaite dédier ces derniers mots.

Table of contents

Introduction	6
I State of the art	13
I.1 LE serrations for the RSI noise reduction	15
I.2 Dedicated analytical models	17
I.3 Dedicated numerical approaches	18
II Methods and Materials	21
II.1 Semi-analytical methods for broadband interaction noise predictions	23
II.1.1 Acoustic analogy and dedicated ONERA codes (integral methods)	23
II.1.2 Analytical models for interaction noise predictions	25
II.1.2.1 Isolated flat plate with straight leading edge: Amiet's theory	26
II.1.2.2 Isolated flat plate with a spanwise periodic leading edge pattern	28
II.1.2.3 Taking into account the cascade effect	30
II.2 Numerical tools	34
II.2.1 CAA code solving the Euler equations written in perturbation form	35
II.2.2 CFD solvers for stationary mean flow assessment	37
II.2.3 High-fidelity lattice Boltzmann code	38
II.3 Experimental set-ups	40
II.3.1 Rectilinear cascade in KCA test rig of Ecole Centrale de Lyon	41
II.3.2 Source Diagnostic Test (SDT) turbofan model at NASA Glenn	45
II.3.3 PHARE-2 ECL-B3 turbofan test facility at Ecole Centrale de Lyon	46
III Turbulence modeling	49
III.1 Characterization of turbulence fields	51
III.1.1 Geometrical notations and turbulent field definition	51
III.1.2 Representation of turbulent velocity fields in Fourier space	53
III.1.3 Modeling of main turbulent quantities and spectra	55

III.2	Overview of synthetic turbulence generation methodologies	59
III.2.1	Fourier modes decomposition	59
III.2.2	Digital filtering	62
III.2.3	Synthetic eddies methods	63
III.2.4	A few words about challenges in synthetic turbulence generation	64
III.3	Development of a 3D Fourier-mode synthetic turbulence in Cartesian coordinates	65
III.3.1	$(k_\xi, k_z = 0)$ turbulence structure	65
III.3.2	(k_ξ, k_z) turbulence structure	66
III.3.3	$(k_\xi, k_\eta, k_z = 0)$ turbulence structure	67
III.3.4	Choice of a modeling suitable for 3D turbulence (k_ξ, k_η, k_z)	69
III.3.5	Taking into account periodic and wall boundary conditions in case of 3D turbulence fields	71
III.4	Fourier-mode synthetic turbulence in cylindrical coordinates	75
III.4.1	3D turbulence field (k_ξ, k_θ, k_r) with two velocity components	75
III.4.2	3D turbulence field (k_ξ, k_θ, k_r) with three velocity components	78
III.4.3	Discussion about 3D turbulence field generation in cylindrical coordinate systems	81
III.5	A few words about code optimization	83
IV	Design of vanes with leading edge serrations: a semi-analytical methodology	85
IV.1	Implementation of an analytical tool for the prediction of the leading edge noise	87
IV.1.1	Extension of the solution accounting for finite span	87
IV.1.2	Validation of the extended WH formulation	90
IV.2	Design of a low-noise vane with leading edge serrations	93
IV.2.1	Some background on noise reduction from sinusoidal leading edge serrations .	93
IV.2.2	Choice of a pattern addressing the InnoSTAT KCA configuration	94
IV.2.3	Application of the LE pattern to a NACA7310 airfoil	96
IV.2.4	Manufacturing of the serrated vane	99
V	Aeroacoustic and aerodynamic study in a rectilinear cascade configuration: baseline and low-noise cases	101
V.1	Aerodynamic performance control through RANS simulations	103
V.1.1	RANS calculations on initial serrated designs d_0 and d_1	103
V.1.2	Proposal of an improved serrated design d_2	105

V.2	CAA predictions	108
V.2.1	Inviscid mean flow calculation	108
V.2.2	CAA simulations set-up	109
V.2.3	Preliminary simulations of a single NACA7310 airfoil with periodic boundary conditions	110
V.2.4	Parametric study of the channel spacing for a flat plate rectilinear cascade . .	113
V.2.5	Parametric study on the vane count in the CAA domain and influence of the blade to blade acoustic correlation in FWH analogy	114
V.2.6	Evaluation of the radiated sound depending on the structure of the injected turbulence	117
V.2.7	Noise reduction as a function of the injected turbulence	121
V.3	Lattice Boltzmann simulations	125
V.3.1	Set-up of lattice Boltzmann simulations	125
V.3.1.1	Overview of the iterative set-up process	125
V.3.1.2	Fine mesh refinement	132
V.3.1.3	Validation of the set-up and mean flow convergence study	135
V.3.2	LBM solution analyzes and cross-comparisons with other predictions and experimental data	137
V.3.2.1	Basic aerodynamic validation of the baseline and serrated vanes . . .	137
V.3.2.2	Characterization of the turbulent inflow	139
V.3.2.3	Far-field acoustic spectra and sound power reductions	145
V.4	Comparison of the trade-off between cost and fidelity of the different approaches	154
VI	Application to realistic turbofan configurations	157
VI.1	CAA simulations on the NASA SDT benchmark	159
VI.1.1	Set-up of the CAA simulation with a RANS mean flow	159
VI.1.2	Impact of inviscid or RANS mean flow on acoustic predictions	166
VI.1.3	Impact of the number of vanes taken into account on the far-field acoustics .	173
VI.1.4	Cross-comparisons with other numerical solutions	175
VI.2	ECL-B3 PHARE-2: preliminary serrated design and evaluation	177
VI.2.1	Backgrounds from ONERA studies on similar turbofan models	177
VI.2.2	Serrated-OGV design using turbulence inflow characteristics from RANS . .	179
VI.2.3	Analytical assessment of the noise reduction	181
VI.2.4	Future work	183
	Conclusions and perspectives	186
	Appendices	189

A	Calculation of 1D spectra from velocity Fourier transform	190
B	An algorithm to determine the direction of the velocity for 3D turbulence structures	192
C	Link between formulations based on the turbulence energy spectrum and the velocity autocorrelation spectra	193
D	Determining conditions under which a divergence-free formulation can be achieved	195
E	Flow chart representing the synthetic turbulence generation	197
F	Validation of the WH formulation on experimental data from LE parametric studies at ISVR	198
G	Application to a low-noise OGV in the framework of TurboNoiseBB	200
H	Manufacturing	204

Acronyms

ACAT1 AneCom AeroTest 1

ANCF Advanced Noise Control Fan

APP Approach

BPF Blade Passing Frequency

BPR ByPass ratio

BRM Blade Reduction Method (BRM)

CAA Computational Aero-Acoustics

CFD Computational Fluid Dynamics

CUTB CUTBack

DC Direct Coupling

FWH Ffowcs Williams and Hawkings

HIT Homogeneous Isotropic Turbulence

HRR Hybrid Recursive Regularized

InnoSTAT Innovative STATor

LBM Lattice Boltzmann Method

LE Leading Edge

LEE Linearized Euler Equations

LES Large Eddy Simulation

SDT Source Diagnostic Test

NS Navier-Stokes

OAPWL OverAll sound PoWer Level

OASPL OverAll sound Pressure Level

OGV Outlet Guide Vane

OP Operating Point

PWL sound PoWer Level

RANS Reynolds-averaged Navier–Stokes

RSI Rotor-Stator Interaction

SDL SiDeLine

SISM Shear-Improved Smagorinsky Model

SPL Sound Pressure Level

TE Trailing Edge

TI Turbulence Intensity

TLS Turbulence Length Scale L_t

TRL Technology Readiness Level

UHBR Ultra High ByPass Ratio

URANS Unsteady RANS

USF Unducted Single Fan

WH Wiener-Hopf

ZDES Zonal Detached Eddy Simulation

Nomenclature

$\langle \rangle$	=	Set average operation
$i / 1,2,3$	=	Indices/subscripts denoting a direction ($i = 1$, mean flow direction)
α	=	A random angle in $[0, 2\pi]$
α_c	=	Angle of attack
β_c	=	Inlet flow angle (with respect to x axis)
c	=	Chord of the airfoil
χ	=	Stagger angle
E	=	Energy spectrum of turbulence
f	=	Frequency
f_{min}, f_{max}	=	Respectively minimal and maximal considered frequencies
Δf	=	Frequency spacing
f_w	=	Window function
g_w	=	Correction function
h_s	=	Amplitude of the serrations
\mathbf{k}	=	Wavevector
k	=	Norm of the wavevector \mathbf{k}
\mathbf{k}^\perp	=	Wavevector component in the plane perpendicular to the z axis
(k_1, k_2, k_3)	=	Coordinates along three orthogonal directions (1, 2, 3) of the wavenumber space
(k_x, k_y, k_z)	=	Coordinates of the wavevector \mathbf{k} in the basis $(\mathbf{x}, \mathbf{y}, \mathbf{z})$
(k_x, k_θ, k_r)	=	Coordinates of the wavevector \mathbf{k} in the basis $(\mathbf{x}, \boldsymbol{\theta}, \mathbf{r})$
(k_ξ, k_η, k_z)	=	Coordinates of the wavevector \mathbf{k} in the basis $(\boldsymbol{\xi}, \boldsymbol{\eta}, \mathbf{z})$
(k_ξ, k_η, k_r)	=	Coordinates of the wavevector \mathbf{k} in the basis $(\boldsymbol{\xi}, \boldsymbol{\eta}, \mathbf{r})$
$(\mathbf{k}_a, \mathbf{k}_b, \mathbf{k}_c)$	=	A specific orthonormal basis in the wavector space
Δk	=	Wavenumber discretization step
L_l	=	Turbulence longitudinal length scale
L_t	=	Turbulence transversal length scale
L_y	=	Length in the CAA between the two sides of the periodic boundary condition
L_z	=	Span of the airfoil
L_w	=	Input parameter defining the shape of the window function f_w
λ_s	=	Serration wavelength

M	=	Mach number
n_v	=	Number of vanes in the CAA domain
ω	=	Angular frequency
ω'	=	Vorticity of fluctuating velocity
p, p_0, p'	=	Fluid static, mean, fluctuating pressure
$\varphi_{ii}^{3D}, \varphi_{ii}^{2D}, \varphi_{ii}^{1D}$	=	3D, 2D (planar), 1D autocorrelation velocity spectra along i direction
ϕ	=	Velocity potential
ψ	=	Random phase in $[0, 2\pi]$
ρ, ρ_0, ρ'	=	Fluid, mean, fluctuating density
R_{obs}	=	Distance between the (center of) the source and the observer (microphone)
R_w	=	Ratio between L_w (parameter of the window function f_w) and the span L_z
s	=	Inter-vane spacing, Stagger height
St	=	Strouhal number of the serrations ($St = f \times h_s / U$)
σ	=	Unit vector defining the direction of a given velocity fluctuation
t	=	Time
t_1	=	An arbitrary time interval
\mathbf{u}, \mathbf{u}'	=	Velocity vector, fluctuating velocity vector
\mathbf{U}	=	Mean velocity vector
$U = \ \mathbf{U}\ $	=	Norm of the mean velocity
$\mathbf{X}, \mathbf{Y}, \mathbf{l}$	=	Position vectors in the physical space
$(\mathbf{x}, \mathbf{y}, \mathbf{z})$	=	Orthonormal basis attached to the cascade (\mathbf{y} aligned with cascade and \mathbf{z} with span)
$(\mathbf{x}, \boldsymbol{\theta}, \mathbf{r})$	=	Orthonormal basis attached to the cascade ($\boldsymbol{\theta}$ aligned with cascade and \mathbf{r} with span)
$(\boldsymbol{\xi}, \boldsymbol{\eta}, \mathbf{z})$	=	Main orthonormal basis ($\boldsymbol{\xi}$ aligned with the test section and mean flow before deviation)
$(\boldsymbol{\xi}, \boldsymbol{\eta}, \mathbf{r})$	=	Main orthonormal basis ($\boldsymbol{\xi}$ aligned with the mean flow before deviation)
z_{min}, z_{max}	=	Respectively, coordinates of the bottom and top walls in the numerical set-up
r_{min}, r_{max}	=	Respectively, coordinates of the hub and shroud

Introduction

In the field of aeroacoustics applied to transport aircraft, the total radiated noise is usually divided into two principal contributions. First, the airframe noise mainly generated by the high lift-devices such as flaps and slats along with the landing gears. Second, the engine noise on which this thesis focuses. The latter is strongly connected to the engine architecture. The main configurations encountered are unducted designs such as turboprops and ducted designs like turbojets and turbofans. Each of them has its efficiency range depending on the air speed, as illustrated in Fig. 1a.

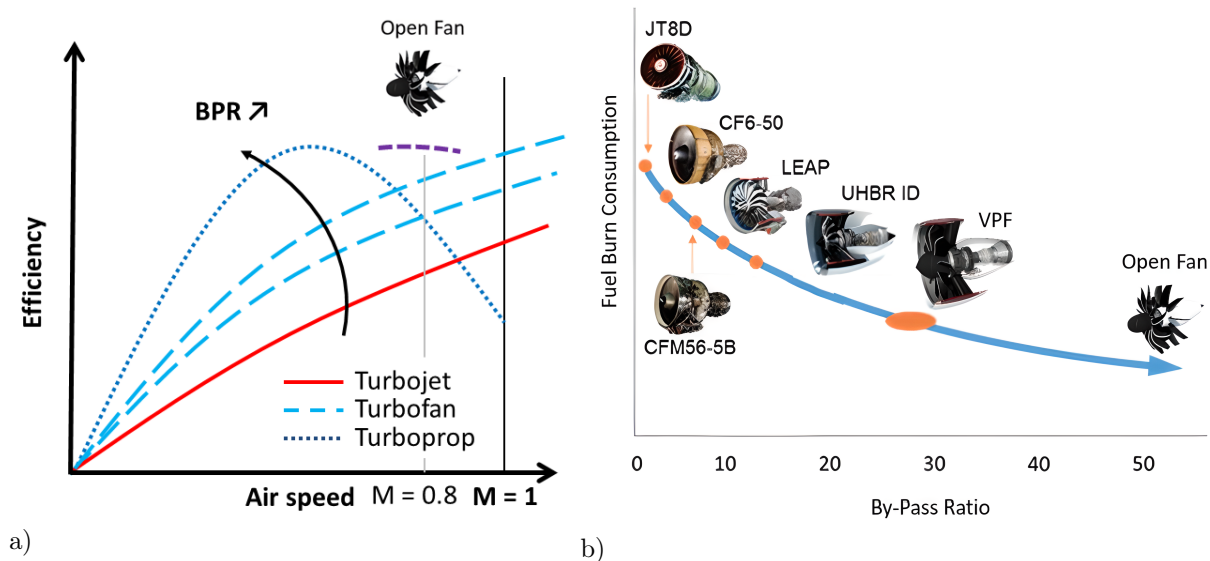


Figure 1: (a) Propulsive efficiency comparison for various gas turbine engine configurations, adapted from [5]. (b) Fuel burn consumption varying with the bypass ratio (BPR), extracted from [60].

In order to attain high-subsonic speeds, ducted geometries have been favored over propellers. One of the key parameters characterizing an engine is the bypass ratio (BPR), that is the ratio between the mass flow rate of the cold air "bypassing" the core and the mass flow rate of the hot air having passed by the engine core (turbine and combustion chamber). When there is no bypassing flow on an engine it is often referred to as a turbojet, otherwise, it is called a turbofan. From thermodynamics point of view, the higher the BPR, the higher the efficiency as illustrated in Fig. 1a. This is the reason why the BPR, and thus the fan diameter, have been increasing over the last decades to reduce the engine's consumption as depicted in Fig. 1b. To reduce even further the consumption, there is a renewed interest in open fan architectures for future aircraft lines. The new engine generation aims at achieving the same speed as current single aisle aircraft (up to Mach 0.8) with an additional 20% reduce fuel consumption. The trend towards higher BPR has been strongly influencing the distribution of the noise sources at the intake and exhaust, as illustrated in Fig. 2: compressor, fan, jet, turbine, and combustor.

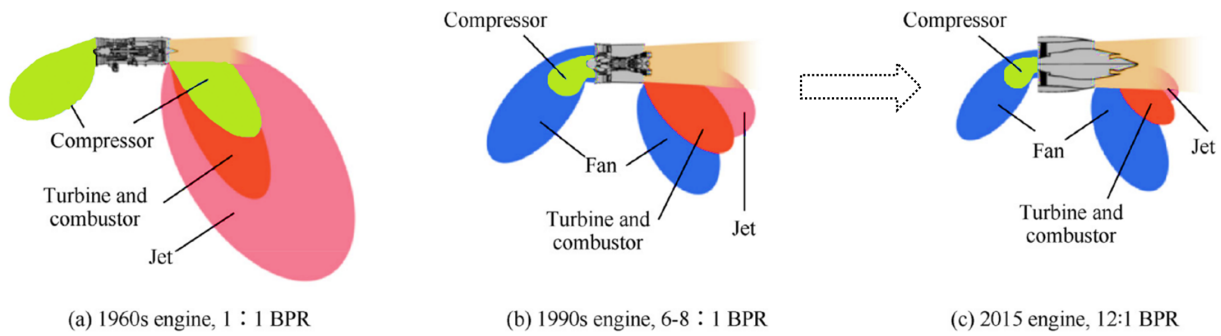


Figure 2: Amplitude and directivity of the main noise sources for a turbojet and a turbofan depending on the BPR. Extracted and adapted from [103].

With no bypassing air, the jet noise has been overwhelmingly dominant on turbojets. It has however significantly decreased with the introduction of turbofan with increasingly larger BPR. In parallel to this aerodynamic improvement, aeroacoustic mitigation of the jet noise has been extensively studied. Two noise reduction concepts can be noted: chevron shaped nacelles and nozzles with corrugated or lobe-type noise suppressors, both speeding up and short shortening the mixing between the different layers of air and thus reducing the jet noise. Consequently, the contributions of other noise sources have become prevalent, in particular the (turbo)fan, as depicted in Fig. 2.

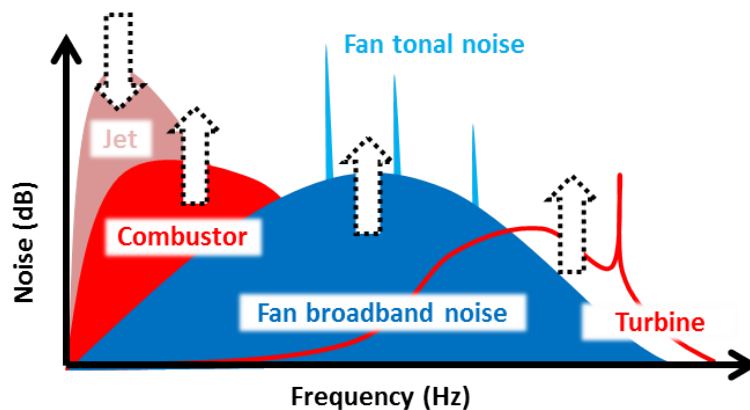


Figure 3: Noise spectra of jet engine components and future trends with the BPR increase. Adapted from [130].

A representative distribution of engine sources over the frequency range is shown in Fig. 3, pointing out the major contribution of the fan noise. The fan noise will largely contribute to the overall engine noise of novel ultra-high bypass ratio (UHBR) [130]. It is important to note that noise sources contributions vary depending on the engine Operating Point (OP). Typically, 3 OPs are of prime interest for acoustic certification. Two OPs are defined at take-off (sideline and cutback) and one at approach. The noise sources levels, depending on the engine regime, are plotted in Fig. 4.

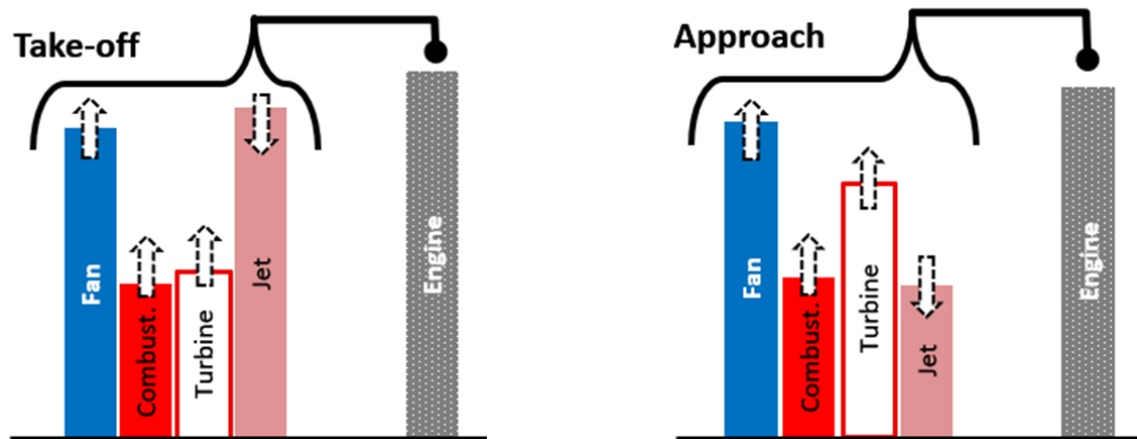


Figure 4: Typical engine noise sources distribution at take-off and approach. Adapted from [9].

The fan noise is again found to be a major contributor, in particular at the approach OP. Several physical mechanisms are at stake with respect to the fan noise. These mechanisms are listed in Fig. 5.

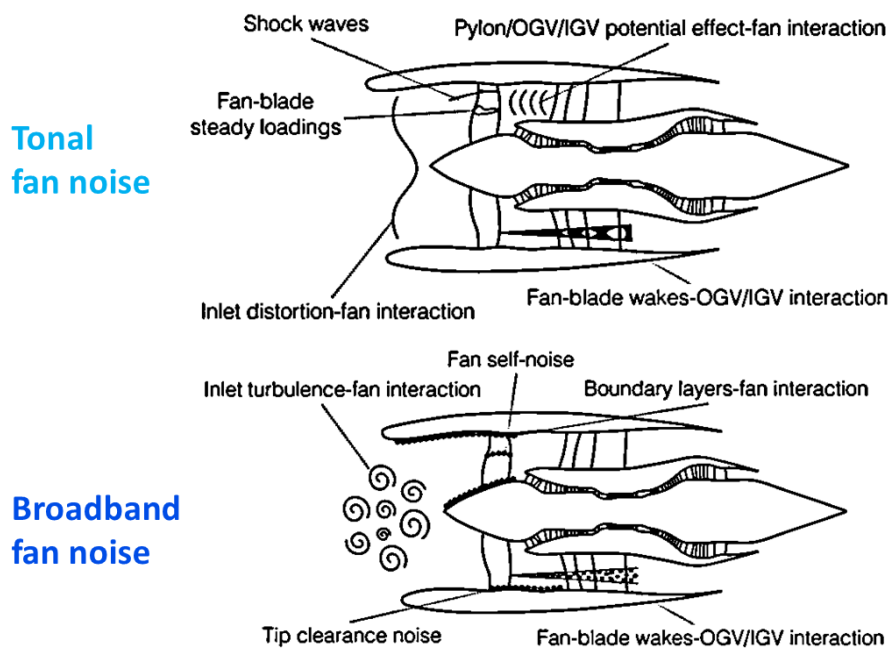


Figure 5: Mechanisms generating fan tonal and broadband noises. Adapted from [66, 117].

In nearly all cases, the fan-blade wakes-Outlet Guide Vane (OGV) interaction, also called the Rotor-Stator Interaction (RSI) is the main contributor to the tonal and broadband fan noise. Two other significant fan noise contributors should be pointed out too: the buzz-saw noise when shocks appeared at blade's supersonic tip speeds and the distortion-rotor interaction which is expected to increase with shortened intakes, open fan, and boundary layer ingestion architectures. The interested reader about description of all fan noise sources may refer to [66, 44]. The RSI mechanism is qualitatively explained through Fig. 6.

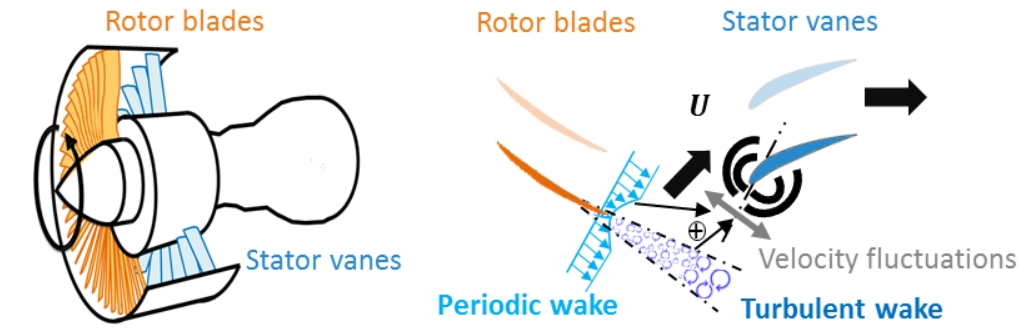


Figure 6: Sketch of the RSI noise mechanism.

The velocity fluctuations generated by the rotor wakes impact the leading edge of the stator vanes in the OGV stage, which generates high pressure fluctuations. In the far-field, these pressure fluctuations give rise to a tonal noise (associated with the periodic component of the wake and the Blade Passing Frequency (BPF)) and a broadband noise (associated with the turbulent part of the wake). One of the key challenges for future aeroengines is to design silent Fan-OGV stages by primarily reducing the RSI sources, which is the dominant source of noise on UHBR architectures and which should also be on open fan architectures [1]. There are two main challenges associated with the RSI mechanism. First of all, it is a matter of better predicting the RSI noise. URANS calculations have shown to be a very effective way of assessing the tonal part of the noise, whereas the evaluation of the broadband sources generated by the turbulent inflow remains more complex. It is also a question of proposing effective treatments for noise reduction. Several solutions have been investigated to reduce the tonal and broadband noises. However, the Technology Readiness Level (TRL) of devices targeting the broadband sources remains lower than for tones. In order to reduce the RSI noise, several technological innovations have been proposed in the literature as briefly discussed in the state of the art (Part I). One of them comes down to undulating the stator vane leading-edge. Such undulations are also found in the nature as portrayed in Fig. 7. They have enabled an evolutionary advantage, whether in terms of sound stealth or aerodynamic behavior (increased lift and reduced stall). First bio-inspired industrial applications have been implemented in wind turbines (qualitative example of trailing edge serrations is also provided in Fig. 7). More recently, serrations at the vanes leading-edge have been proposed to reduce the strength of the RSI mechanism in stator stages. ONERA has for example designed spanwise varying serrations in [144], which are depicted in Fig. 7.

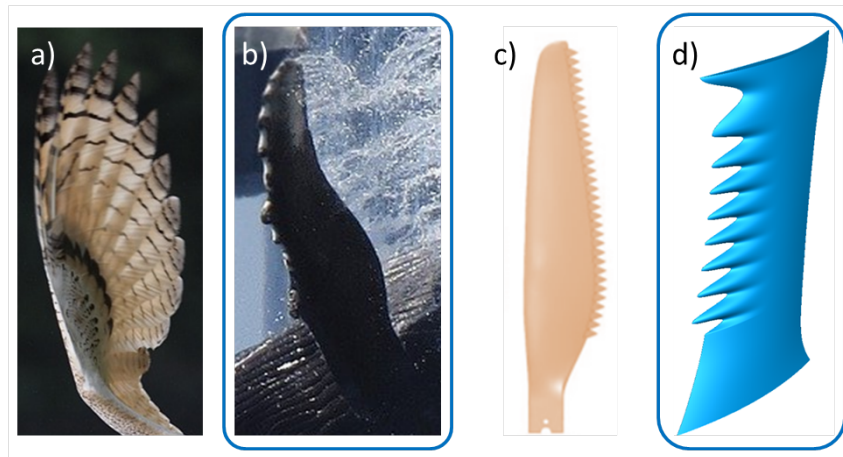


Figure 7: Illustrations of bio-inspired serrations, and leading-edge serrations circled in blue solid line.

In the framework of a new European project, Innovative STATor (InnoSTAT), ONERA is responsible for providing low-noise serrated geometries taking advantage of the experience gained in previous studies in collaboration with Safran and of the current work. A comparison of some active and passive treatments is made within the framework of the European project which aims at designing and evaluating promising solutions, proposed by the project's partners by focusing on broadband noise contribution, for future quiet aeroengines [7].

This PhD work, closely related to the InnoSTAT project, aims at the implementation and evaluation of suited prediction methodologies at different level of fidelity, for the turbulence-airfoil interaction noise assessment, as summarized in Fig. 8. Low-noise geometries with leading edge (sinusoidal) serrations are particularly studied. Fast analytical methods are required as guideline for the design (providing raw estimations), whereas numerical methods are able to provide more confident results but involving of course much higher CPU costs. Three approaches are investigated: (i) flat plate aeroacoustic response using a Wiener-Hopf formulation proposed by Ayton *et al.* [28], (ii) hybrid Computational Fluid Dynamics (CFD) and Computational Aero-Acoustics (CAA) with synthetic turbulence injection [144], (iii) high fidelity Lattice Boltzmann Method (LBM) [12]. These methodologies are applied on relevant turbulence-airfoil configurations proposed in InnoSTAT, involving low-noise serrated geometries designed through this thesis too.

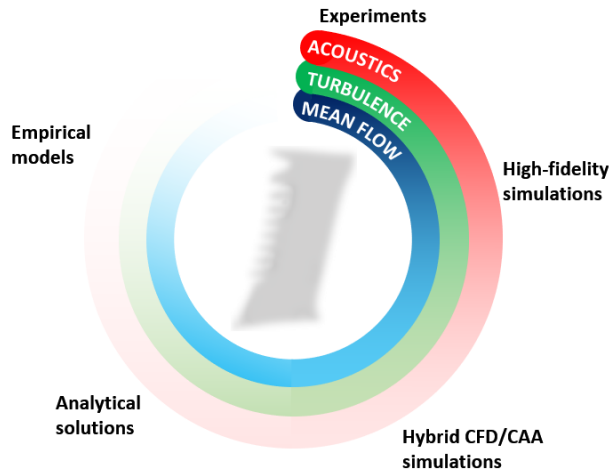


Figure 8: Multi-fidelity approaches for aeroacoustic assessment of turbulence-airfoil noise with leading-edge serrations.

As discussed later in Part II, leading-edge serrations have shown a great potential for RSI noise reduction on academic configurations, although the TRL at which they are fully validated remains relatively low. Indeed, the assessment of such passive noise concepts on turbofans remains both challenging and an open question, to at once greatly reduce noise and do not degrade the aerodynamic behavior. The latter aspect is addressed in the ONERA design process using RANS calculations. To increase the TRL, InnoSTAT project includes two main experimental campaigns: a first one on a rectilinear cascade impacted by a turbulent flow generated by a turbulence grid, on which the present work is mainly focused, and a second one on a realistic turbofan mock-up.

The dissertation is structured as follows.

Part I is devoted to a literature review on experimental, analytical, and numerical approaches for turbulence-cascade interaction noise assessment with a focus on serrated designs. Part I aims at getting a better sight of existing solutions both in terms of low noise concepts and prediction methodologies, along with the identification of remaining challenges. Part II deals more specifically with methods used during this thesis. A brief description of analytical tools and numerical approaches is provided. Moreover, the different test benches on which these latter methods are applied are described in this Part. There are three main test rigs of interest for this work: a rectilinear cascade in KCA test rig of Ecole Centrale de Lyon, a simplified turbofan benchmark case (NASA SDT) and the next turbofan mock-up in PHARE-2 ECL-B3 facility at Centrale Lyon too.

Turbulence modeling which is the physical source behind the RSI noise is introduced in Part III. First, main physical turbulence properties are reminded and useful notations used during this work are provided. Then, methodology of synthetic turbulence generation with Fourier modes decomposition is covered in detail for CAA simulations solving Linearized Euler Equations (LEE). A particular interest is given to obtaining a fully 3D turbulence field, more realistic than two-wavenumber turbulence structures previously taken into account at ONERA.

Parts IV and V are dedicated to the rectilinear cascade experiment. In Part IV, leading edge serrations are designed in preparation for the InnoSTAT test campaign, based on semi-empirical

criteria from literature. Acoustic behavior of this initial geometry is evaluated by a state of the art analytical solution [28] derived for a flat plate with wavy leading-edge by means of the Wiener-Hopf technique. In parallel, a correction is proposed to get rid of the infinite span hypothesis. Part V aims at evaluating numerically and experimentally the aeroacoustic behavior of the preliminary serrated geometry defined in Part IV. From CFD RANS calculations, a second geometry is proposed with reduced aerodynamic penalties. In parallel, the noise reduction is cross-validated through CAA taking into account a three-component-wavenumber synthetic turbulence field proposed in Part III. Following analytical and CAA approaches, the LBM simulations (using ProLB solver) are described and applied on the full cascade rig set-up and for baseline and two ONERA serrated geometries tested at Centrale Lyon. Cross comparisons of LBM solutions with previous prediction methods and experimental data are discussed. Finally, turbofan configurations are examined in Part VI. First, the CFD/CAA approach is revisited on a reference benchmark turbofan configuration proposed by NASA. Second, the design methodology of leading-edge serrations, introduced in Part IV and Part V and also evaluated throughout Part V, is extended to an OGV stage with realistic turbulence inflow. A preliminary concept is provided for the second InnoSTAT test campaign on this turbofan model.

Part I

State of the art

As stated in the introduction, the rotor-stator interaction (RSI) noise is one of the main physical mechanisms behind the tonal and broadband fan noise. More generally, the same phenomenon occurs when an object such as an airfoil is immersed in a non-stationary flow, such as a vortex street or a turbulent flow field. The unsteady inflow produces an unsteady lift response. The associated pressure fluctuations at the airfoil's surface radiate in the far-field. This acoustic source can be considered as a dipole located at the leading edge (LE) of the airfoil [85]. That is why, the RSI noise is often referred to as the leading edge noise. Below, several approaches for interaction noise assessment are presented with a focus on the leading edge serrations for broadband noise mitigation. It is worth mentioning that this review includes several studies which have been published during this PhD work.

Apart from the serrations, other RSI noise reduction (tonal and broadband) technologies can be mentioned. The most common is the swept and leaned OGV [71] focused on tone noise reduction. The idea is to increase the number of wake intersections per stator vanes, which results in a spanwise phase variation and thus a noise reduction in comparison with radially aligned vanes. Regarding passive treatment other than the LE undulations, porous media inclusion at the LE have been also studied [35, 34, 46]. Here, the idea is to make sure that the vortices which impact the airfoils are not brutally encountering a solid surface but rather slow down by porosity. In the same line of thought, perforated leading edges can be considered as in [83]. The smaller pressure jump across the airfoil induces a reduced noise radiation. As for porous media, wavy LE are often viewed as bio-inspired solutions. Several applications not detailed here, such as wire mesh screens, can be found in a specific review [174]. However, here again, the focus is on LE serrations.

Chapter I.1 is devoted to LE serration concepts for RSI noise reduction. Chapters I.2 and I.3 respectively highlight analytical and numerical tools for the RSI noise prediction in particular for the LE serrations assessment.

I.1 LE serrations for the RSI noise reduction

Considering the wavy LE option, a preliminary comparison has been performed between sinusoidal serrations and porous media in [158] along with analytical modeling. Nevertheless, the implementation of LE serrations, at the beginning sawtooth or sinusoidal, dates back to 1970s studies such as in [96] although the concept was not actually devoted to reducing the turbulence-airfoil mechanism in this study but mainly the self-noise in priority. There has been a renewed interest in this technology over the last 10 years and first relevant LE serration design aimed at reducing LE noise was firstly investigated by ONERA [142, 63] in the framework of the UE project FLOCON [6]. Many sensitivity studies conducted at ISVR on the amplitude and wavelength of the serration can be noted as in [135, 138]. Wavy LE shapes have been applied on flat plates impacted by a homogeneous isotropic turbulence (HIT), demonstrating a very high noise reduction, up to 14 dB. Serrations have also been investigated experimentally on isolated NACA airfoils. From experimental data, a semi-empirical model, based on the Strouhal number of the serrations, has been proposed by Paruchuri *et al.* in [55] along with the derivation of an optimal serration wavelength by modeling LE noise thanks to equivalent compact sources. Comparisons to the semi-empirical model have also been performed in [36] highlighting the same trend, especially when the LE edge noise is isolated from the self-noise. Complementary experiments including 3D sound field maps have been also investigated at Centrale Lyon [37]. In addition, the influence of turbulent inflow characteristics has also been investigated experimentally by several research teams [40, 138]. A broader statistical-empirical modeling of serration depending on set-up parameters has been proposed by Biedermann *et al.* [39]. Regarding LE serrations, a wide range of patterns can be adopted instead of sinusoidal patterns. In this regard, numerous patterns have been experimentally evaluated at ISVR on flat plates in [56], such as: double-wavelength, chopped-peak, slitted profiles. The key point is that contrary to sinusoidal serrations, for which the noise reduction is mainly based on a destructive interference between compact sources along the LE and filtering of oblique gusts [142], slit effects rely on an additional mechanism which is creation of secondary vortices at the slitted edge. These slitted geometries can offer a strong narrow-band noise reduction in the frequency domain, which seem promising for tone reduction of OGVs, the interested reader can refer to [50] for further details about the secondary vortices mechanism. However, in the present PhD work, the focus is made on sinusoidal serrations which are a more mature and easier solution to industrialize since there is fewer mechanical constraints and aerodynamic penalties. To end on the exploration of exotic noise reduction devices, thin curved LE serrations have been considered in [106]. Moreover, a blowing solution mimicking

sinusoidal LE edge serration has been proposed in [17], showing a good agreement in the low frequency region with their solid counterpart. In the field of aerodynamics, numerous studies have investigated wavy LE, here called tubercles, but few have considered both noise reduction and aerodynamic behavior. However, a recent study from Kim *et al.* [107] has investigated the benefit of LE serrations on the reduction of flow separation induced noise for airfoils at high angles of attack, which can hide the benefit from the LE noise decrease. Although the focus in this PhD is on the RSI noise, it is of importance to check how serrations modify the self-noise and aerodynamics as done in [115] for an airfoil at various angles of attack.

I.2 Dedicated analytical models

Analytical models have also been derived for the LE noise reduction. The most famous one is Amiet's solution which has been proposed in [19, 139] for an isolated flat plate in a uniform flow impinged by a HIT. A recent extension of Amiet's model to non-uniform mean flows has been proposed by Zhong *et al.* [179]. Analytical models are not limited to isolated flat plates. The acoustic response of a rectilinear or annular cascade has been also widely studied. The most used models in the industry today are Hanson's [95] and Posson's [149] models extended to swirling mean flows in [128]. A parametric study of the most advanced analytical solutions for fan broadband noise prediction has been proposed by Lewis *et al.* [122]. A collaborative benchmarking of RANS-informed analytical models for RSI broadband noise predictions has been conducted recently by DLR [92]. Aside from Hanson's and Posson's solutions, the mode-matching technique have also been investigated by Bouley *et al.* [45] for noise generation and propagation between fan and OGV. It should be noted that cascade response functions are usually restricted to flat plate vanes. However, in a recent study [31], the effect induced on interaction noise by airfoils with a small camber and thickness has been analyzed. Even if state-of-the-art models including cascade effects are available, they only account for straight LE. That is why, the focus here is more on models assuming an isolated flat plate which can be more easily compared with up-to-date analytical solutions derived for LE serrations (with this assumption). In order to account for wavy LE starting from Amiet's solution, two ways have been explored by Roger *et al.* [158]: a strip formulation which considers a locally swept straight airfoil and an exact formulation that takes advantage of a change of variables to get back to the classical straight LE framework. Unfortunately, this formulation (already implemented and tested by ONERA) failed in giving realistic quantitative predictions. More recently, analytical solutions accounting for varying LE have been also provided using the same change of variable but, solving the convective Helmholtz equations by means of the Wiener-Hopf (WH) technique, as proposed by Ayton *et al.* [28]. This formulation assumes an infinite flat plate with any piece-wise linear periodic LE in a uniform flow impinged by a HIT. It has to be noted that the WH approach has been extended to anisotropic turbulence in [94] only for straight (porous) LE. However, it is interesting to remark that in [131], a better agreement was found with the semi-empirical model than with the WH-based analytical solution in the mid-frequency range.

I.3 Dedicated numerical approaches

With the rise of High Performance Computing, numerical simulations have been proposed to assess turbulence-airfoil interaction noise in addition to the analytical approaches. An intermediate fidelity approach is based on hybrid CAA methods with an inviscid approximation. Most of the time, CAA codes solve the non-linear or linearized Euler equations (LEE) written in perturbation such as ONERA's code sAbrinA [156]. These hybrid approaches require the prescription of a so-called synthetic turbulent field. For the definition of such a field, four main techniques emerged: Fourier modes decomposition, synthetic eddy method, digital filtering, and proper orthogonal decomposition (POD). Although a large number of modes is required with POD for modeling small scale turbulence, this approach is very appealing for the representation of large and inhomogeneous turbulent structures for turbofan configurations as detailed in [125]. However, POD approach is still exploratory and not actually adopted in the aeroacoustic community. Fourier modes decomposition, synthetic eddy method, and digital filtering are addressed in more detailed in Part III, dedicated to turbulence modeling. The focus here is rather on their application for turbulence interaction and more particularly its reduction by LE serrations. A recent study from Kissner *et al.* [109], solving Euler equations written in perturbations, has compared two and three dimensional turbulence fields generated using the fast Random Particle Mesh method (which is based on the digital filtering of a white noise) for the prediction of RSI on a turbofan configuration. A three dimensional anisotropic turbulence field, halfway between digital filtering and synthetic eddy method, has been proposed by Gea-Aguilera *et al.* [15] for the evaluation of an isolated airfoil with LE serrations. This allows the study of the correlation between the turbulence length scales and the characteristic dimensions of the serrations. At ONERA, Fourier mode decomposition has been implemented and interfaced to the CAA code sAbrinA [61, 62] and used to assess acoustic response of vanes with spanwise varying LE serrations designed and published by Polacsek *et al.* [144]. The specificities of this recent study lies in the fact that the LE pattern has been adapted locally to account for radially variable turbulence length scale and thus to maximize the noise reduction. CFD RANS simulations were performed for the aerodynamic assessment of the low-noise design. These 3D hybrid CAA simulations [144] are probably the most advanced ones in terms of serration application to realistic turbofan configuration, even if they were limited to two dimensional turbulence fields. A preliminary extension to a more realistic three dimensional turbulence has been proposed by Cader *et al.* [47]. Moreover, the reader is invited to refer to [14] for comparison between synthetic turbulence approaches. It can be noted that full three-dimensional Euler equations have been employed in [173] to better understand the

noise reduction mechanism behind a wavy LE. For this purpose, a simplified configuration where a flat plate is impinged by a divergence free vortex has been considered. The main conclusion is that modeling of sinusoidal serrations needs to take into account downstream noise sources and not only rely solely on LE-based sources. The same framework has been further investigated for wavy and slitted LE in [49] emphasizing the role played by secondary vortices on noise reduction.

CAA methodologies discussed above require turbulent inflow prescription. In order to get rid of this constraint, a Large Eddy Simulation (LES) can be performed for broadband noise predictions. At first, approaches solving the classical Navier-Stokes (NS) equations are briefly reviewed before discussing lattice Boltzmann method (LBM) applications. Practically, WRLES (wall resolved LES) for simulating RSI is currently out of reach so that two kinds of strategies are practically adopted: hybrid RANS/LES (DES, ZDES) or WMLES (wall modeled LES). Furthermore, multi-sector calculations are performed instead of 360 degrees simulation to minimize the numerical cost. Usually, the number of vanes is modified to reach the lowest common denominator between rotor blades and stator vanes, which makes it possible to apply periodic boundary conditions. This approach is called blade reduction method (BRM). Otherwise, phase-lagged [132, 76] or profile transformation approach have to be considered, the latter generating spurious noise sources [2]. A WMLES with BRM has been performed with the TurboAVBP solver in [150] to assess the NASA Source Diagnostic Test turbofan configuration. A WMLES with BRM has also been applied on another turbofan configuration with TurboAVBP in [121] and compared with analytical solutions. This study has highlighted that flow separation can sometimes contribute more to the overall noise than RSI mechanism. An additional comparison between LES and analytical models can also be found in [16] for another turbofan configuration, the ECL5 fan/OGV stage. Within the high fidelity approaches based on NS, the Zonal Detached Eddy Simulation (ZDES) proposed by Deck *et al.* [68] has been intensively studied and currently applied at ONERA. The idea behind ZDES way is to resort to hybrid RANS/LES approaches in which the whole boundary layer is solved with RANS modeling. The ZDES presents similarities with the DDES from Spalart *et al.* [166] with the main difference concerning the choice of the characteristic mesh length. ZDES has been applied in [77, 145] for turbofan noise prediction on the same configuration ACAT1 than [120]. Regarding NS-LES for aeroacoustic assessment with serrated vanes, studies have been mostly restricted to isolated airfoil cases. For example in [57, 170], the rod-airfoil noise reduction by a wavy LE has been discussed. However, an LES simulation of a single stage axial fan with LE serrations has been recently investigated by Tong *et al.* [171] with a reduction of the broadband noise up to 4 dB. Although the focus for serration design is primarily on the RSI noise reduction, proposing aerodynamically efficient LE treatments is crucial. In this regard, the reader may refer to [151] where LES has been performed at University of Southampton to better understand the benefits of wavy LE for deep-stalled airfoils.

Finally, the LBM approach (still in the LES framework) seems to be unavoidable and maybe the most valuable strategy to simulate RSI noise and to assess LE serration performances on relevant configurations. The use of a LBM formalism (with stream and collide algorithm) is found to be much less dissipative than genuine NS solvers for acoustics, even though slightly more dispersive.

Again rod-airfoil interaction, here with straight LE, has been investigated in [172, 119] using the ProLB solver. For turbofan LBM applications, contrary to NS-LES, 360 degrees simulations are performed. Among those, several LBM simulations based on the PowerFLOW solver have been carried out on the NASA SDT benchmark case providing an impressive accurate solution compared to other numerical predictions from the aeroacoustic community. For instance in [89], the balance between rotor noise and RSI noise at intake and exhaust has been investigated. In [90], the authors have analyzed the turbulence properties between the rotor and stator stages. Those quantities are of prime importance for the RSI mechanism. In particular, the turbulence length scale plays a major role in the design of LE serrations as shown earlier by experimental data and CAA-LEE simulations [138, 15]. A final simulation on the SDT case has consisted in replacing the triggering instability devices in PowerFLOW by suited equations enabling natural turbulence transition [54]. In LBM simulations devoted to turbofan application, the Advanced Noise Control Fan (ANCF) configuration has been also investigated by the same teams using PowerFLOW and recently by ONERA using ProLB solver [67] with successful results. Several studies with the LBM approach have also been devoted to wavy LE. In Casalino *et al.* [53] and Teruna *et al.* [169], serrations and porous serrations for stator vanes have been respectively considered on the SDT case but, showing a rather small noise reduction and no particular study on aerodynamic penalties (apart for the configuration with porous serrations). More promising low noise designs with serration and/or porous media have been proposed in [168] for a rod-airfoil configuration.

With regard to this multi-domain (covering three topics) state of the art, two areas of improvement can be identified. First, a simultaneous significant reduction of the noise without altering the aerodynamic behavior remains to be demonstrated in particular on realistic turbofan configurations. Second, application/validation of prediction methods with different fidelity levels on more advanced experimental configurations (from cascade to turbofan test rigs) involving low-noise serrated geometries would give a further step towards the design of a future demonstrator. These are the main objectives of the present work.

Part II

Methods and Materials

The aim of this part is to present the analytical methods and numerical tools used during this work, along with experimental facilities on which these approaches have been applied.

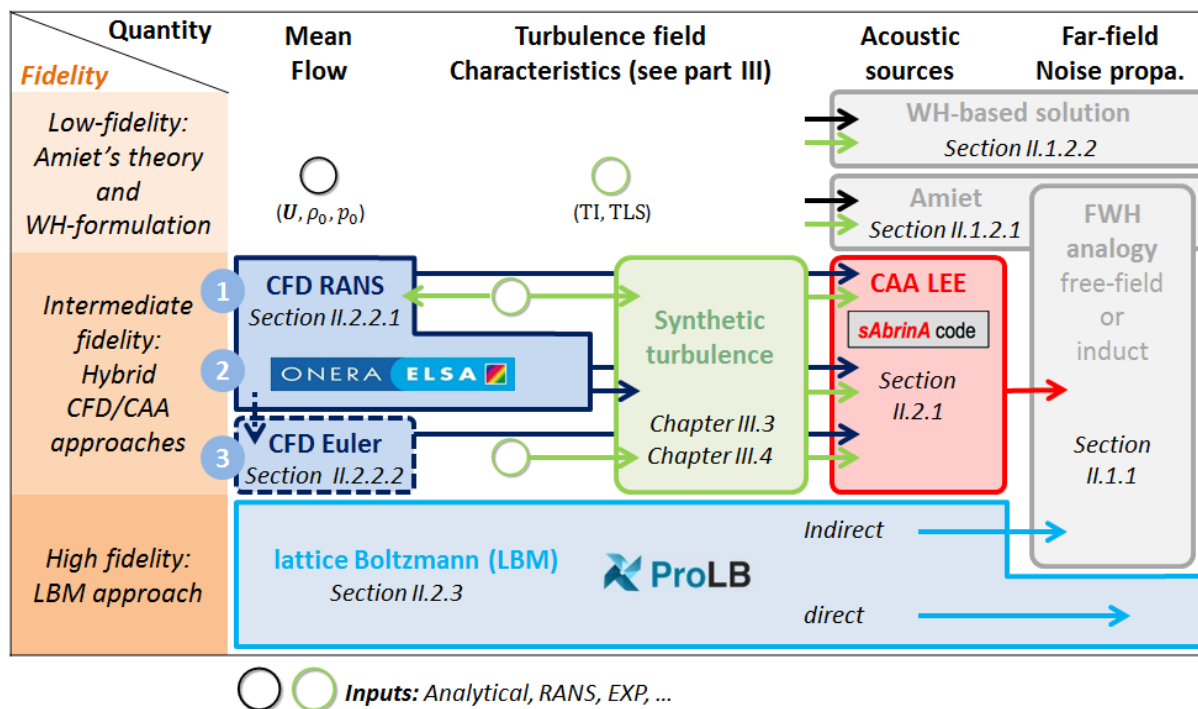


Figure II.1: Several approaches used in this thesis to predict broadband interaction noise.

As for aeroacoustic prediction methods, the focus is on broadband interaction noise. Figure II.1 illustrates the different methodologies, used during this work, depending on their level of fidelity. Low-fidelity approaches (Chapter II.1) consist in analytical solutions with geometrical approximations, where the aerodynamic inputs, mean flow and turbulence properties, have to be provided. Intermediate approaches (Chapter II.2) rely on fully numerical mean flow and acoustic sources computations. However, semi-analytical methodologies are mandatory for turbulence generation and noise propagation. The CAA (sAbrinA code) is presented in Section II.2.1 and the steady flow assessment required for CAA provided by CFD codes (RANS or Euler) in Section II.2.2. The high fidelity approach (Section II.2.3) relying on Large Eddy Simulation (LES) implemented in the lattice Boltzmann framework allows the simulation of all the physical mechanisms. Some of these approaches, from low to high fidelity, combine several tools based on usual acoustic analogies to calculate the acoustic response and the radiated sound field (in free-field or in duct). These ONERA tools derived from acoustic analogies briefly introduced too in the Section II.1.1. The more specific turbulence modeling is covered in a dedicated part, III.

Finally, Chapter II.3 of the present part is devoted to the presentation of the test rigs on which the previously mentioned methods are applied.

II.1 Semi-analytical methods for broadband interaction noise predictions

Semi-analytical methods for broadband interaction noise prediction are presented. First, a brief description of a central technique in aeroacoustics is provided: the Ffowcs Williams and Hawkings (FWH) analogy [74], which extends Lighthill theory [124] to account for solid surfaces. FWH is at core of aeroacoustic predictions, as it allows the computation of a given set of acoustic sources propagation in the far-field. Initially, confined to free-field cases, FWH has been extended by Goldstein to annular geometries [87]. In order to compute analytically the noise sources, theoretical approaches are focused on Amiet's solution to predict flat plate-turbulence interaction noise (Section II.1.2.1) and Ayton's solution [28] based on the Wiener-Hopf (WH) technique to assess interaction noise reduction from leading edge patterns (Section II.1.2.2). Some analytical models taking into account the cascade effect are also mentioned in Section II.1.2.3.

II.1.1 Acoustic analogy and dedicated ONERA codes (integral methods)

In the continuity of the work initiated by Lighthill [124], Ffowcs-Williams and Hawkings (FWH) [74] have proposed a general formulation to calculate radiation of acoustic sources (monopolar, dipolar, and quadripolar). Contrary to Amiet or WH-based analytical solutions, there is no model for the aeroacoustic response in FWH. Sources are supposed to be known. The main idea behind acoustic analogy consist in the rewriting of Navier-Stokes (NS) equations to derive an acoustic propagation equation. Indeed, Lighthill has shown that the acoustic field at a given observation point can be obtained by the convolution of an adequate Green function, satisfying the boundary conditions, with the acoustic solution to an impulse source. FWH have extended this idea by including solid surfaces inside the domain. Acoustic sources which are the input of FWH-based methods are usually provided by numerical simulation (CFD or CAA) but, can also be fully analytically defined. For instance, Amiet's solution presented in Section II.1.2.1, uses Curle's analogy [65], which is a particular solution of FWH method.

As previously mentioned, the FWH analogy consists in rewriting the fluid mechanics to make appear a wave propagation equation. The local formulation can be defined as follows, taking into account a uniform convecting mean flow:

$$\frac{\partial^2 \rho' H(S)}{\partial t^2} - c_0^2 \Delta [\rho' H(S)] = \frac{\partial(Q' \delta(S))}{\partial t} - \frac{\partial(F'_i \delta(S))}{\partial x_i} + \frac{\partial(T'_{ij} H(S))}{\partial x_i \partial x_j}$$

$$Q' = (\rho \mathbf{u} - \rho_0 \mathbf{U}) \cdot \mathbf{n}$$

$$F'_i = (p' \delta_{ij} + \rho(u_i - 2U_i)u_j + \rho_0 U_i U_j - \tau_{ij})n_j$$

$$T'_{ij} = \rho u'_i u'_j + (p' - c_0^2 \rho') \delta_{ij} - \tau_{ij}$$

τ_{ij} : viscous stress tensor

where δ denotes the Dirac function and H the Heaviside function. S is null on solid surfaces, positive outside and negative inside. \mathbf{n} is the normal to the considered surface. Different source terms appear in that equation:

- Q associated with the monopolar sources inside the domain,
- F_i denoting the surface forces imposed by the solid boundaries on the fluid. This is the main source of noise in the interaction noise mechanism. It corresponds to a dipolar source and is often called loading noise,
- T_{ij} the Lighthill tensor. It is associated with the deformations of the turbulent structures. It produces quadripolar noise sources.

In order to solve the wave equation with a source term, one may use a Green function which satisfies the following equation in the case the right-hand side source term is simply an impulse.

$$\left\{ \begin{array}{l} \left(\Delta - \frac{1}{c_0^2} \frac{\partial^2}{\partial t^2} \right) G(\mathbf{X}, \mathbf{Y}, t, \tau) = \delta(\mathbf{X} - \mathbf{Y}) \delta(t - \tau) \\ \mathbf{X} : \text{observer position} \\ \mathbf{Y} : \text{source position} \\ t : \text{reception time} \\ \tau : \text{emission time} \end{array} \right. \quad (\text{II.1})$$

Once the Green function is defined (taking into account the boundary conditions), the general solution is obtained by a convolution with the real source term (noted RHS, right-hand side):

$$p'(\mathbf{x}, t) = \int_{\mathbb{R}^3} \left(\int_{\mathbb{R}} \text{RHS}(\mathbf{Y}, \tau) G(\mathbf{X}, \mathbf{Y}, t, \tau) \right) d\tau d\mathbf{Y}$$

In the case of the FWH formulation in the frequency domain, the Fourier transform ($\tilde{}$) of the pressure satisfies:

$$\tilde{p}'(\mathbf{X}, \omega) = \int_S i\omega \tilde{Q}(\mathbf{Y}, \omega) \tilde{G}(\mathbf{X}, \mathbf{Y}, \omega) dS + \int_S \tilde{F}_i(\mathbf{Y}, \omega) \frac{\partial \tilde{G}(\mathbf{X}, \mathbf{Y}, \omega)}{\partial y_i} dS + \int_V \tilde{T}_{ij}(\mathbf{Y}, \omega) \frac{\partial^2 \tilde{G}(\mathbf{X}, \mathbf{Y}, \omega)}{\partial y_i \partial y_j} dV \quad (\text{II.2})$$

In the present work based on the turbulence-airfoil interaction mechanism, only the second dominant source term F_i (loading noise) is kept and Eq. (II.2) can be simplified as follows (velocity

terms are neglected on the solid surface):

$$\tilde{p}'(\mathbf{X}, \omega) = \int_S \tilde{p}'_i(\mathbf{Y}, \omega) n_i \frac{\partial \tilde{G}(\mathbf{X}, \mathbf{Y}, \omega)}{\partial y_i} dS \quad (\text{II.3})$$

Two in-house solvers used in this thesis to assess far-field radiated sound, provided by Eq. (II.3), are briefly presented in the following paragraphs. They relate respectively to two environments: free-field for the rectilinear cascade configuration (Section II.3.1) and confined for turbofan applications (Sections II.3.2 and II.3.3), by means of adequate Green functions. Both solvers, called MIA and FanNoise, rely on Fortran parallel routines. They are used in this thesis in the frequency domain, considering only a solid formulation, *i.e.* the dipolar interaction sources.

Free-field radiation: MIA code

To obtain the free-field noise propagation of acoustic sources starting from Eq. (II.3), the free-field Green function has to be used. It has the following expression, in the frequency domain:

$$\tilde{G}_f(\mathbf{X}, \mathbf{Y}, \omega) = \frac{1}{4\pi S_0} e^{-ik \left(\frac{S_0 - \mathbf{M} \cdot (\mathbf{X} - \mathbf{Y})}{\beta^2} \right)} \quad (\text{II.4})$$

with $\beta^2 = 1 - M^2$, $M = \|\mathbf{M}\| = \sqrt{M_x^2 + M_y^2 + M_z^2}$, and $S_0 = \sqrt{(\mathbf{M} \cdot (\mathbf{X} - \mathbf{Y}))^2 + \beta^2 \|\mathbf{X} - \mathbf{Y}\|^2}$.

In-duct propagation: FanNoise code

FanNoise relates rotating (rotor blades) or fixed (stator vanes) noise source terms to the radiated sound field in a ducted domain. For these configurations, the Green function has been derived for a simplified geometry representing a semi-infinite annular duct. The key definition of the associated Green function is provided below. The detailed definition of the Green function in the case of a ducted propagation can be found in [87, 152]. A semi-infinite annular duct, of radius r_{min} and r_{max} is considered, in which the mean flow is purely axial. Source terms in $\mathbf{Y} = (r_Y, \theta_Y, x_Y)$ radiate to an observer located at $\mathbf{X} = (r_X, \theta_X, x_X)$. The expression of the ducted Green function in the frequency domain is given by:

$$\tilde{G}_f(\mathbf{X}, \mathbf{Y}, \omega) = -\frac{i}{2} \sum_{m=-\infty}^{+\infty} \sum_{n=-\infty}^{+\infty} \frac{C_{mn}(r_X) C_{mn}(r_Y)}{\Delta_{mn} 2\pi r_{max}} e^{-im(\theta_X - \theta_Y + k_{mn}^\pm (x_X - x_Y))} \quad (\text{II.5})$$

with k_{mn} , the axial wavenumber. For additional explanation about the definition of terms in Eq. (II.5), please refer to [87, 152].

II.1.2 Analytical models for interaction noise predictions

Some models for analytical computation of acoustic sources, with different underlying assumptions, are presented below. They cover Amiet's solution for isolated flat plates and WH-based technique proposed by Ayton *et al.* for flat plates with leading edge serrations. A practical discussion about cascade effects is proposed in the end of this section.

II.1.2.1 Isolated flat plate with straight leading edge: Amiet's theory

Amiet's theory, introduced in [18], is the most famous model currently adopted for the leading edge noise prediction. Although the model is dedicated to an isolated (flat plate) airfoil, it can be considered for rectilinear and annular cascades by neglecting all the cascade effects (as done in this work and discussed in Section II.1.2.3). The brief overview provided here, only summarizes the main steps, which are detailed by Reboul [152] and Clair [61]. The model has several assumptions:

- the turbulence is supposed to be frozen, and represented by an isotropic spectrum model,
- the incoming turbulent structures are distributed over harmonic gusts,
- the mean flow is parallel to the chord,
- the airfoil is supposed to be flat without thickness.

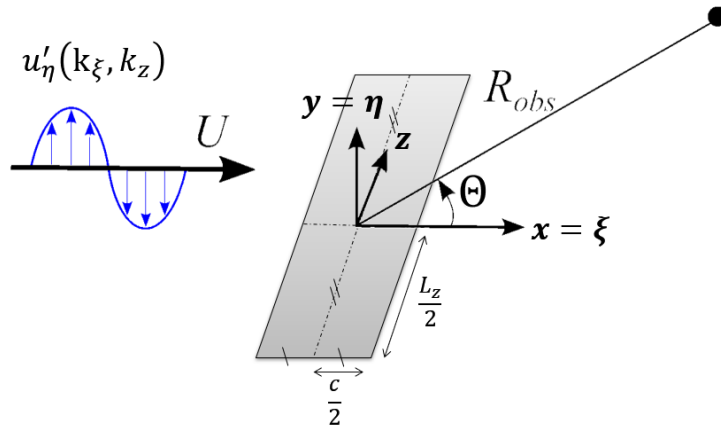


Figure II.2: Sketch illustrating Amiet's model configuration.

These assumptions are illustrated by Fig. II.2. The turbulence velocity, more precisely the component perpendicular to the chord, is supposed to be of the form, with A_η an amplitude:

$$u'_\eta = A_\eta e^{i(k_\xi \xi + k_z z - \omega t)} \quad (\text{II.6})$$

Thus, the pressure jump, across the flat plate, can be written as:

$$\Delta p' = 2\pi\rho_0 U A_\eta g(\xi, k_\xi, k_z) e^{i(k_\xi \xi + k_z z - \omega t)} \quad (\text{II.7})$$

where g is called the reduced lift function and is obtained via the Helmholtz convected equation. Moreover, the amplitude of the gust fluctuations can be related to the turbulence spectrum model. All the calculations done, the 2D spectral density of the radiated sound pressure has the following expression:

$$S_{pp}(\mathbf{X}, \omega, k_z, L_z) = \left(\frac{\omega \eta \rho_0 c}{2c_0 S_0^2} \right)^2 \frac{U L_z \pi}{2} \frac{\sin^2 \left(\frac{L_z}{2} \left(\frac{\omega z}{c_0 S_0} - k_\eta \right) \right)}{\pi \frac{L_z}{2} \left(\frac{\omega z}{c_0 S_0} - k_\eta \right)^2} |L(\xi, k_\xi, k_z)|^2 \varphi_{\eta\eta}^{2D}(k_\xi, k_z) \quad (\text{II.8})$$

with: L , the aeroacoustic transfer function, $\omega = k_\xi U$, $\varphi_{\eta\eta}^{2D}$ the planar turbulence spectrum (see Part III), M the Mach number, $\beta = \sqrt{1 - M^2}$, $S_0 = \sqrt{x^2 + \beta^2(y^2 + z^2)}$, c the chord, L_z the span, and ρ_0 the mean flow density. In Amiet's formulation presented here, two contributions are taken into account for L : the leading edge itself and the first order correction term due to the presence of the trailing edge. Two further simplifications are presented below to derive the 1D spectral density of the radiated sound pressure, *i.e.* depending only on the wavenumber $k_\xi = \omega/U_\xi$.

3D Amiet's formulation in the infinite span limit: $S_{pp}(\mathbf{X}, \omega, L_z \rightarrow \infty)$

First, Eq. (II.8) can be integrated over transverse wavenumbers k_z to obtain the 1D density of the radiated sound pressure:

$$S_{pp}(\mathbf{X}, \omega, L_z) = \left(\frac{\omega\eta\rho_0 c}{2c_0 S_0^2} \right)^2 \frac{U L_z \pi}{2} \int_{-\infty}^{+\infty} \frac{\sin^2 \left(\frac{L_z}{2} \left(\frac{\omega z}{c_0 S_0} - k_\eta \right) \right)}{\pi \frac{L_z}{2} \left(\frac{\omega z}{c_0 S_0} - k_\eta \right)^2} |L(\xi, k_\xi, k_z)|^2 \varphi_{\eta\eta}^{2D}(k_\xi, k_z) dk_z \quad (\text{II.9})$$

Equation (II.9) can be simplified further under certain hypotheses. If the span L_z is assumed to be infinite and the observer located in the mid span plane, *i.e.* $z = 0$, the pressure spectral density becomes:

$$\lim_{L_z \rightarrow \infty} (S_{pp}((\xi, \eta, 0), \omega, L_z)) = \left(\frac{\omega\eta\rho_0 c}{2c_0 S_0^2} \right)^2 \frac{U L_z \pi}{2} |L(\xi, k_\xi, 0)|^2 \varphi_{\eta\eta}^{2D}(k_\xi, 0) \quad (\text{II.10})$$

3D Amiet's formulation with a parallel gust inflow: $S_{pp}(\mathbf{X}, \omega, 0, L_z)$

Let us now consider a parallel gust formulation (*i.e.* $k_z = 0$) and an observer located in the mid span plane (*i.e.* $z = 0$). The pressure spectral density can be expressed as:

$$S_{pp}((\xi, \eta, 0), \omega, 0, L_z) = \left(\frac{\omega\eta\rho_0 c}{2c_0 S_0^2} \right)^2 \frac{U L_z \pi}{2} \frac{L_z}{2\pi} |L(\xi, k_\xi, 0)|^2 \varphi_{\eta\eta}^{2D}(k_\xi, 0) \quad (\text{II.11})$$

In order to recover the solution from Eq. (II.10), the spectral density from Eq. (II.11) has to be multiplied by $2\pi/L_z$:

$$\lim_{L_z \rightarrow \infty} (S_{pp}((\xi, \eta, 0), \omega, L_z)) = \frac{2\pi}{L_z} S_{pp}((\xi, \eta, 0), \omega, 0, L_z) \quad (\text{II.12})$$

In order to illustrate this point, a comparison of the solutions obtained using both formulations, corresponding to left and right-hand sides of Eq. (II.12), is plotted in Fig. II.3. They have been obtained with parameters close to InnoSTAT experiment discussed in Section II.3.1. A Liepmann planar turbulence spectrum, defined in Section III.1.3, has been considered here. Power spectrum is obtained by a weighted angular integral over half a circle downstream (used in FLOCON project [6], see for example equation (2.3) in [138]), following:

$$\text{PWL} = 10 \log_{10} \left(\frac{L_z R_{\text{obs}}}{\rho_0 c_0} \sum_{\text{mics in } \Theta} \text{SPL}(\Theta) \Delta\Theta \right) - 10 \log_{10} (W_{\text{ref}} = 10^{-12} \text{ W}) \quad (\text{II.13})$$

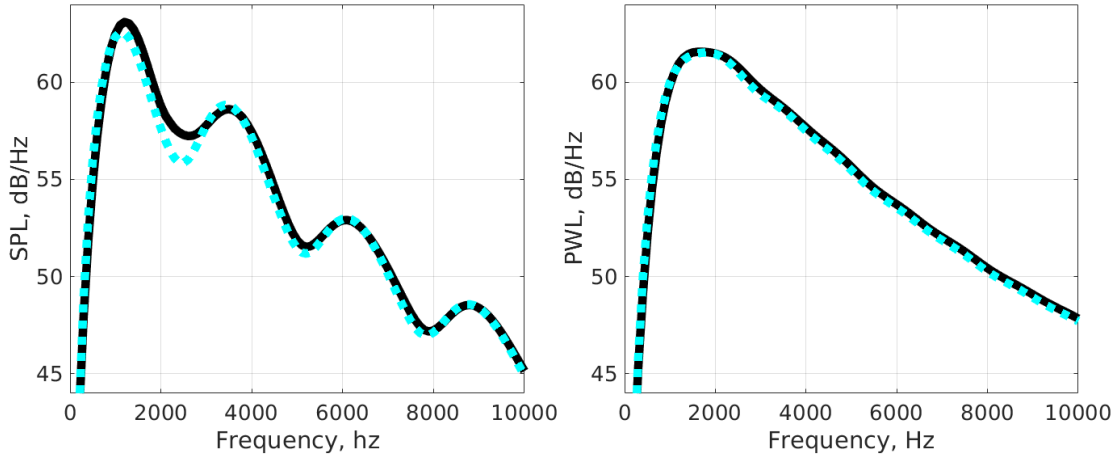


Figure II.3: SPL (at 90°) (a) and PWL (Eq. (II.13) integrated from -90° to $+90^\circ$) (b) spectra obtained from Amiet's solution. Eq. (II.12), computed with: $R_{obs} = 1.8$ m, turbulence intensity $TI=5\%$, integral length scale $L_l = 8$ mm, $M=0.3$, and $L_z=0.2$ m. Left-hand side of Eq. (II.12) — and right-hand side

This key result is particularly useful for CAA computations, when synthetic turbulence injection is restricted to structures with $k_z = 0$ (see discussions in Chapters III and V).

II.1.2.2 Isolated flat plate with a spanwise periodic leading edge pattern

This section presents an analytical solution, for turbulence noise interaction with a wavy leading edge. It has been originally proposed by Ayton and Kim in [30] and generalizes the ideas from Envia [70], whose study was restricted to a swept airfoil in a channel. Indeed, the solution provided by Ayton *et al.* takes into account infinite airfoils with periodically patterned leading edges. The notations of the solution have been slightly rewritten in [28]. The latter formulation has been implemented in Chapter IV.1. It has to be noted that a simplified solution has been proposed by Lyu *et al.* [126], in order to speed-up calculations by adequately approximating infinite integrals and sums by a single straightforward sum. Moreover, an optimization study of the leading edge pattern has also been performed by Lyu *et al.* [127].

This analytical solution based on the Wiener-Hopf technique enables the calculation of the far-field noise generated by a gust-plate interaction including LE serrations. The main specificity of this formulation is to take into account any serration shape with a periodic pattern. This is useful to estimate the broadband noise reduction associated with the sinusoidal LE serrations discussed in Chapter IV.2. The analytical model makes the following assumptions:

- a uniform convective velocity parallel to the chord,
- a semi-infinite plate (in the chordwise and spanwise directions),
- a periodically patterned leading edge,
- an acoustic perturbation potential satisfying the Helmholtz convective equation,
- a 2D planar wavenumber turbulence spectrum.

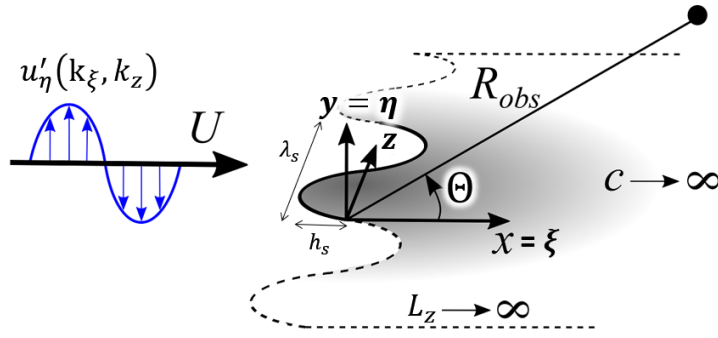


Figure II.4: Sketch of the configuration used by the analytical model.

Thus, the present problem can be depicted by Fig. II.4. A flat plate with a periodically patterned leading edge, here with a sinusoidal shape of amplitude h_s and length λ_s , is impinged by a HIT. The incoming gust is only represented by a single vector component normal to the chord u'_η . Indeed, this component primarily generates the noise. The key elements of the formulation are presented below. The governing equation to be solved assumes that the pressure perturbation can be derived from a scattered velocity potential, i.e. $p' = -\rho_0 D\phi/Dt$. The problem is sought for harmonic solutions of incoming harmonic gusts normal to the plate and assuming a frozen turbulence, which leads to the convective Helmholtz equation:

$$(1 - M^2) \frac{\partial^2 \phi}{\partial^2 \xi} + \frac{\partial^2 \phi}{\partial^2 \eta} + \frac{\partial^2 \phi}{\partial^2 z} + 2ikM \frac{\partial \phi}{\partial \xi} + k^2 \phi = 0 \quad (\text{II.14})$$

A detailed derivation of the analytical model using dimensionless variables is given in [30, 28, 127]. The main steps involve the use of convenient variable changes that are adopted to describe the serration over one wavelength with periodic boundary conditions. Then, a Fourier transform is applied on the main unknown function (h function in [30, 28]) and the solution to the governing equations is obtained using the separation variable technique. Finally, the system of equations obtained is solved by the Wiener-Hopf (WH) technique, and the acoustic field is deduced from an inverse Fourier transform in the infinite limit approximation of the observer distance to get an asymptotic expression for h . A more compact form is proposed by Lyu *et al.* [127], which relates the radiated sound pressure (in the far-field) as a response to a 2D gust $u'_\eta(k_\xi, k_z)$ associated to streamwise, k_ξ , and spanwise, k_z , wavenumbers. Considering an incoming gust u'_η of the form, $u'_\eta = Ae^{(k_\xi \xi + k_z z - \omega t)}$, where A is the gust amplitude, the dimensionless ($\hat{\cdot}$) far-field sound pressure can be written in a compact form.

$$\hat{p}'(\widehat{R}_{obs}, \widehat{\Theta}, \widehat{z}, \widehat{k}_\xi, \widehat{k}_z) = \mathfrak{L}(\widehat{R}_{obs}, \widehat{\Theta}, \widehat{z}, \widehat{k}_\xi, \widehat{k}_z) A(\widehat{k}_\xi, \widehat{k}_z) \quad (\text{II.15})$$

In Eq. (II.15), (R_{obs}, Θ) are the 2D polar coordinates of the observer from a compact source taken at z (for most practical applications z corresponds to the middle of the span and can be set equal to zero), and \mathfrak{L} is the aeroacoustic response function. The reader is referred to appendix A in [144], which summarizes the main steps of the analytical model (full derivation can be found in [30, 28, 127]). The broadband noise spectrum is obtained from Eq. (II.15) by integrating over the spanwise wave numbers k_z , and introducing a 2-wavenumber turbulence spectrum (such as those from von Karman or Liepmann models), $\varphi_{\eta\eta}^{2D}$, that is related to the upwash velocity disturbance

(see Section III.1.3). The dimensional Power Spectral Density (PSD) of the sound pressure in the wavenumber space takes the form:

$$|p'(R_{obs}, \Theta, k_\xi)|^2 = \rho_0^2 U^2 \int_{-\infty}^{+\infty} |\mathfrak{L}|^2 \varphi_{\eta\eta}^{2D}(k_\xi, k_z) dk_z \quad (\text{II.16})$$

The PSD in the frequency space, $S_{pp}(f)$ (in Pa^2/Hz), is given by:

$$S_{pp}(f, R_{obs}, \Theta) = \frac{2\pi}{U} |p'(R_{obs}, \Theta, k_\xi)|^2 \quad (\text{II.17})$$

The model implementation in MATLAB is discussed in Section IV.1.1 and a correction is proposed in Chapter IV.1 to take into account finite span airfoils.

II.1.2.3 Taking into account the cascade effect

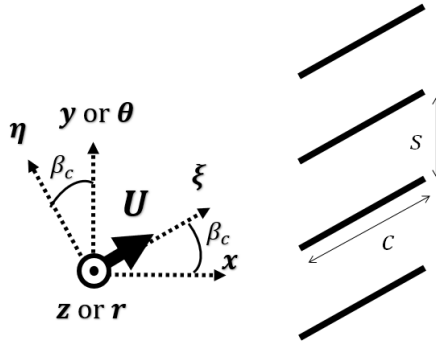


Figure II.5: Sketch of a cascade configuration.

Although, there is no analytical in-house tool at ONERA modeling acoustics of cascade configurations, illustrated in Fig. II.5, several approaches have been developed in the literature (for flat plates with straight leading edges only), some of which are highlighted below. Particular attention is paid to differences with isolated flat plate solutions. Indeed, a noise reduction is expected at low-frequencies (above a cut-off frequency) due to the cut-off modes, in particular for high-solidity cascades, *i.e.* small ratio s/c .

Two approaches used in the industry

A widely used approach by turbomachine manufacturers is the Hanson's model [95] which extends previous work from Glegg [86], from rectilinear to annular cascades. Although Hanson does not account for ducted mode propagation, he has included flat plate with non zero stagger, sweep, and lean angles. Moreover, a strip calculation can be performed in order to take into account spanwise varying conditions. More recently, Posson [148] has started from the Glegg's approach to obtain the analytical pressure jump at the blades. The acoustic sources are then radiated using Goldstein analogy [87]. Therefore, contrary to Hanson's solution, ducted mode propagation is taken into account. However, this result is achieved at the expense of the calculation cost. Hanson

and Posson models are both implemented in Optibrui, which is a solver own by Université de Sherbrooke, Ecole Centrale de Lyon, Airbus, Technofan and Valeo.

Comparison with isolated flat plate solution in an academic configuration

The aim of this paragraph is to provide some insight about expected differences between cascade and isolated solutions. In the literature, Blandeau *et al.* [41] compare an isolated flat plate solution to a rectilinear cascade model proposed by Cheong *et al.* [58]. A result from [41], with a solidity $s/c = 0.89$, is illustrated in Fig. II.6. The solidity is rather close to the one obtained for the InnoSTAT rectilinear cascade, for which $s/c \approx 0.71$.

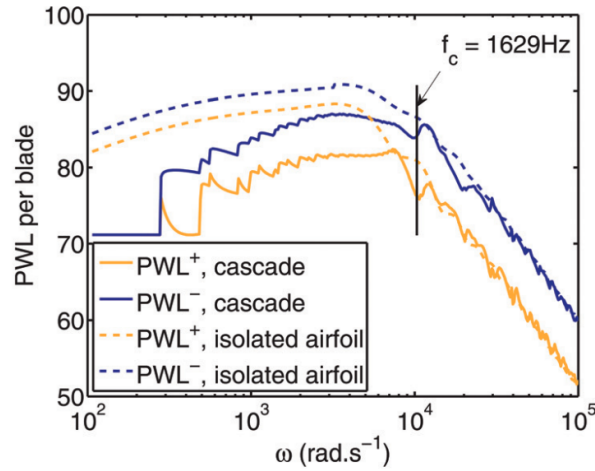


Figure II.6: Downstream PWL per blade predicted by the cascade and the isolated airfoil models, extracted from [41].

The critical frequency, under which the cascade effect is not negligible, is given by:

$$f_c = \frac{1 - M^2}{(1 - M_x^2)^{1/2} + M_y} \frac{c_0}{s} \quad (\text{II.18})$$

The latter critical frequency, can be evaluated in case of InnoSTAT for the different operating conditions and reported in Table II.1.

Mach	0.3	0.34	0.53	0.64
f_c (Hz)	3203	3077	2407	1828

Table II.1: Critical cascade frequency for various inflow Mach numbers (KCA rectilinear cascade configuration, Section II.3.1).

It has to be reminded that in case of the KCA rectilinear cascade (see Section II.3.1), thick cambered airfoils are considered, which might reduce the strength of the cascade effect.

Comparison with isolated flat plate solution in a turbofan configuration

As for cascade effect in a real turbofan configuration, a famous benchmark on turbofan broadband noise named NASA SDT has been performed. NASA SDT test-case is described in Section II.3.2

and computed in Chapter VI.1. In NASA-SDT baseline configuration (54 vanes), solidity and critical frequency can be respectively estimated at mid-span: $s/c \approx 0.61$ and $f_c \approx 9978$ Hz, which might explain the strong cascade effect visible in Fig. II.7.

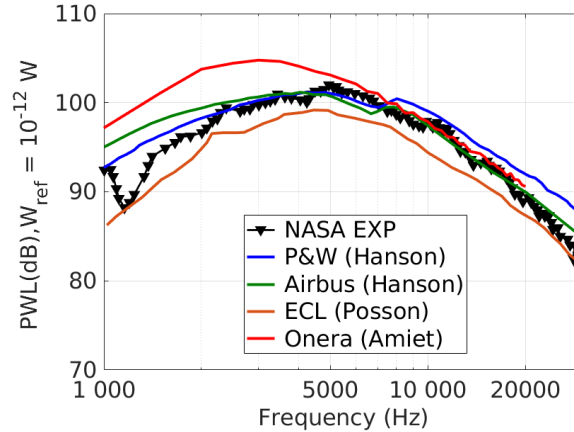


Figure II.7: Downstream broadband noise power spectra: experimental and analytical-based solutions.

Figure II.7 illustrates a comparison obtained during this benchmark between Hanson's, Posson's, and Amiet-based solutions. Amiet-based solution obtained with ONERA code TinA2D (Amiet's formulation extended to annular cascade [92, 152]) overestimates, as expected, the low-frequency levels, which is also pointed out by Blandeau *et al.* [41]. On the contrary, Posson's model (extracted from [120]) underestimates sound power levels at all frequencies. It is also interesting to note that even with the same Hanson's model, different solutions can be obtained depending on the parameters choice. It showcases the need for adequate setting of analytical models. Additional parametric studies with Hanson and Posson models applied to NASA SDT have been performed by Lewis [120].

Influence of the cascade effect on the noise reduction from serrations

When considering LE noise reduction treatments for fan OGV stages, it is interesting to consider whether the cascade effect can have an influence on the noise behavior. Mazella *et al.* [129] have carried out an experiment at the Institute of Sound and Vibration Research's (ISVR) open-jet wind tunnel facility, which provides some clarification on the previous question. This experimental set-up is close to the InnoSTAT rectilinear cascade: a seven flat plates rectilinear cascade is impinged by a turbulent inflow accelerated by a nozzle. A detailed description of the experiment at ISVR can be found in [129].

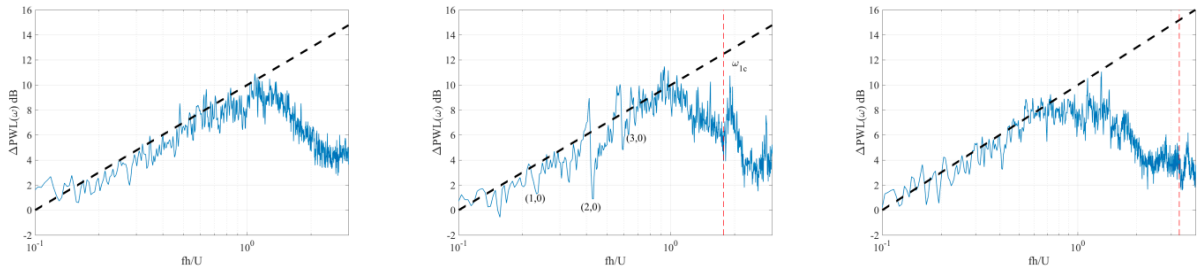


Figure II.8: Sound power reduction due to LE serrations in cascade configurations: isolated blade (left), 4 blades with $s/c = 1.2$ (center), and 7 blades with $s/c = 0.66$ (right). Extracted from [129].

Noise reductions obtained from sawtooth LE are compared in Fig. II.8 to a semi-empirical log-law proposed by Chaitanya *et al.* [55]. It depends on the Strouhal number of the serrations $St = fh_s/U_\xi$: $\Delta PWL = 10 \log(St) + 10$, in dB. The noise reduction in all three cases reproduced in Fig. II.8 match very well the log-law up to a frequency corresponding to $St = 1$. Indeed, the effectiveness of the noise reduction treatment is reduced by the self-noise of the blades in high frequencies. The LE noise mechanism is less efficient at these frequencies. Mazella *et al.* also note that peaks and dips visible in Fig. II.8 are linked with cutoff modes of the test section. This observation is also discussed in Chapter V.2. However, in all cases, it can be noted that a single airfoil experiment (or in Chapter V.2, a single airfoil simulation) is a cost-effective way of estimating the ability of a LE treatment to reduce broadband noise.

II.2 Numerical tools

Numerical codes applied during this thesis (reminded in Fig. II.9) are evoked, starting from the intermediate fidelity approach relying on CFD and CAA simulations. First, in Section II.2.1, an overview of the CAA code sAbrinA developed at ONERA is given. Based on Euler equations written in perturbations, it allows the computation of acoustic sources propagation for a given mean flow and turbulent field. Then, short reviews of two CFD codes, providing the aerodynamic input for sAbrinA are presented: in Section II.2.2, elsA developed by ONERA (3D RANS calculations here) and in Section II.2.2, a 2D open source code which solves the Euler equations. Finally, an overview of a high-fidelity approach is provided. The latter relies on the lattice-Boltzmann method implemented in the ProLB solver, presented in Section II.2.3. Contrary to the hybrid CFD/CAA methodology, all the physics are captured in the same calculation from turbulence generation to far-field acoustic propagation, even if, a FWH analogy can still be performed.

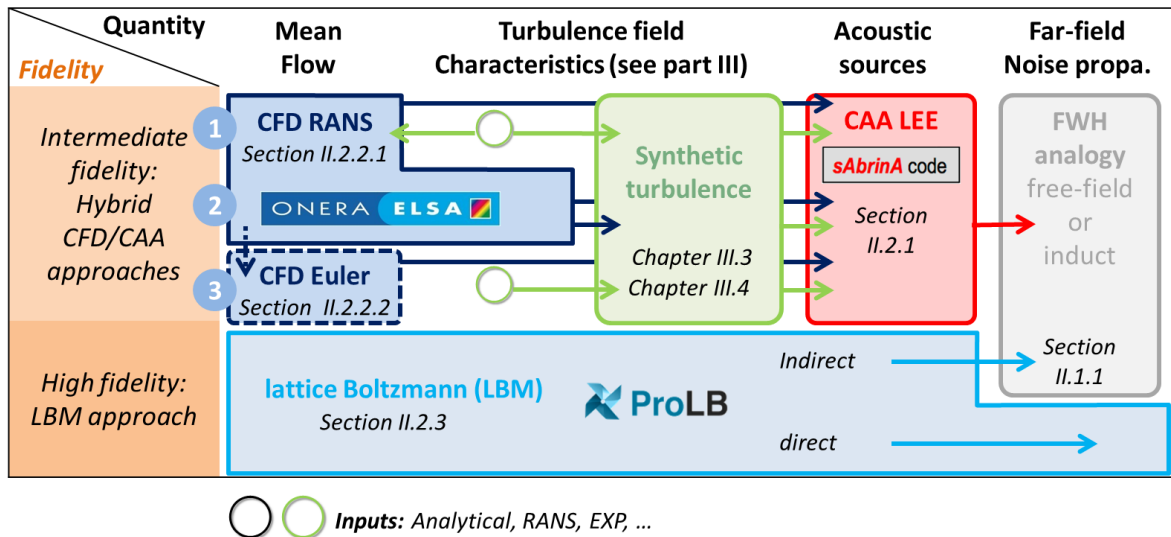


Figure II.9: Numerical approaches used in this thesis to predict broadband interaction noise.

As for the intermediate fidelity simulations, three sub-approaches can be distinguished in Fig. II.9.

1. The mean flow is computed around stator vanes by means of a CFD RANS code. But input turbulence for RANS has to be prescribed at the domain entrance. This sub-approach has

not been used for CAA mean flow calculation in this thesis. Indeed, the third sub-approach is more practical as discussed in Section II.2.2. However, RANS calculations have been performed to evaluate aerodynamic penalties of serrated designs in Chapter V.1.

2. This second sub-approach relying on a mixing plane method is currently adopted in fan-OGV calculations instead of expensive URANS simulations [144]. Basically, the CFD variables are circumferentially averaged over a cross-section (mixing plane) located at the interface between the rotating fan and fixed OGV domains. As discussed in Part VI and in [144], RANS mixing plane calculations provide the mean flow used by the CAA. Relevant turbulent fan wake parameters for the RSI noise are obtained from a fan alone RANS calculation by extending the mesh up to the OGV region, since the wakes are damped by the mixing process.
3. The mean flow is computed around stator vanes by means of a CFD Euler code in this third sub-approach. However, input turbulence properties have to be provided for synthetic turbulence generation. This sub-approach has been used to obtain the mean flow input for CAA simulations in Chapter V.2. This Euler-based mean flow methodology has also been used to obtain the mean flow around stator vanes in a turbofan application presented in Chapter VI.1.

II.2.1 CAA code solving the Euler equations written in perturbation form

The CAA simulations are achieved using the in-house parallelized time-domain code `sAbrinA`. It computes noise sources generation and propagation on multi-block meshes which are curvilinear and structured. It can solve both the non-linearized and linearized Euler equations written in a perturbation and conservative form, which are detailed in [156, 61]. The unsteady flow field is classically split into two parts, namely the mean flow, which has to be provided as an input, and the fluctuating part, which evolution is computed by the code. Regarding numerical schemes, `sAbrinA` uses a sixth-order finite difference scheme for the spatial derivatives and a third-order multistage explicit Runge–Kutta scheme for the temporal discretization. Specific treatments and boundary conditions (BC) are implemented, such as a tenth-order filter in order to remove high-frequency oscillations and Tam and Dong boundary conditions [167], which are used to allow both the exit and entrance of the fluctuations in the domain without generating spurious noise sources nor numerical reflections. The mean flow that advects the fluctuating variables is an input parameter of the CAA computations. Turbulent inflow generated through a stochastic process is injected at the entrance of the CAA domain using Tam and Dong’s non reflective boundary condition. The procedure developed to obtain the synthetic turbulence is detailed in the next part, III .

The general equations

The code solves Euler equations in a perturbation form. In order to obtain that system of equations, the starting point is to consider the Euler equations (conservative formulation).

$$\frac{\partial \mathbf{V}}{\partial t} + \frac{\partial \mathbf{F}}{\partial x} + \frac{\partial \mathbf{G}}{\partial y} + \frac{\partial \mathbf{H}}{\partial z} = \mathbf{0}$$

$$\mathbf{V} = \begin{pmatrix} \rho \\ \rho u \\ \rho v \\ \rho w \\ \rho E \end{pmatrix} \quad \mathbf{F} = \begin{pmatrix} \rho u \\ \rho u^2 + p \\ \rho uv \\ \rho uw \\ u(\rho E + p) \end{pmatrix} \quad \mathbf{G} = \begin{pmatrix} \rho v \\ \rho vu \\ \rho v^2 + p \\ \rho vw \\ v(\rho E + p) \end{pmatrix} \quad \mathbf{H} = \begin{pmatrix} \rho w \\ \rho wu \\ \rho wv \\ \rho w^2 + p \\ w(\rho E + p) \end{pmatrix} \quad (\text{II.19})$$

Then, from Eq. (II.19), the variables are decomposed as a sum of a mean part and a perturbative part. That allows to express the previous system as a combination of a mean flow (which is supposed to be known), a linear perturbative contribution (linear with respect to the fluctuating variable) and a non-linear perturbative part. The fully detailed set of equations is given in [155] and reminded in [61] (Appendix B).

As mentioned before, the sAbrinA code solves the non-linear Euler equations written in perturbation variables. However, in the current study, only linearized equations are solved for two different reasons. First, in the case of turbofan applications, the formulation written in cylindrical coordinates reveals cross terms (with non zero-divergence) if the non-linearized Euler equation is considered [63, 61] when u'_θ harmonic gusts are injected (because the fluctuating field does not satisfy the non-linear equations, which adds a source term). Second, Tam's boundary condition was derived under the framework of linearized Euler equations. If one performs non-linear Euler simulations without care, parasitic reflections could appear at the exit of the computational domain. The latter issue can be partially solved by the addition of a stretching zone at the exit of the domain, to dissipate the hydrodynamic modes and the acoustics before reaching the boundary condition. In any case, it is important to remind that the non-linearity has only an effect on the acoustic response for gusts of high amplitude, around 10% of the mean flow, as discussed in [88, 63, 61].

Tam's boundary conditions

The boundary conditions are defined using Tam and Dong formulation [167], which is based on an asymptotic expression of Euler equations in the far-field. The flow field perturbations are decomposed into three parts: acoustics waves (traveling at a speed equal to the sum of the flow and sound velocities), entropic waves and hydrodynamic waves (only convected by the flow). These conditions are written assuming the extension to the spherical coordinates system proposed by Bogey and Bailly [43], assuming that the center of the frame corresponds to the center of radiation. However, the solution is not very sensitive to that latter assumption, which also allows to consider various sources located at different points as far as they are enough close to each other compared to the size of the domain. In the case of an outflow boundary (the waves are leaving the domain), the boundary conditions are defined as follows:

$$\left\{ \begin{array}{l} \frac{\partial \rho'}{\partial t} + \nabla(\rho') \cdot \mathbf{U} = \frac{1}{c^2} \left(\frac{\partial p'}{\partial t} + \nabla(p') \cdot \mathbf{U} \right) \\ \frac{\partial \mathbf{u}'}{\partial t} + \nabla(\mathbf{u}') \cdot \mathbf{U} = -\frac{1}{\rho_0} \nabla(p') \\ \frac{1}{V_g} \frac{\partial p'}{\partial t} + \frac{\partial p'}{\partial r} + \frac{p'}{r} = 0 \\ V_g = \mathbf{U} \cdot \mathbf{e}_r + \sqrt{c_0^2 - (\mathbf{U} \cdot \mathbf{e}_\theta)^2 - (\mathbf{U} \cdot \mathbf{e}_\phi)^2} \end{array} \right.$$

Pressure fluctuations are supposed only associated with acoustic waves. As for inflow boundary (in our case the boundary in which are injected the turbulent gusts introduced in Part III), the formulation is (the subscript i denotes the known injected components):

$$\left(\frac{1}{V_g} \frac{\partial}{\partial t} + \frac{\partial}{\partial r} + \frac{1}{r} \right) \begin{pmatrix} \rho' \\ u' \\ v' \\ w' \\ p' \end{pmatrix} = \left(\frac{1}{V_g} \frac{\partial}{\partial t} + \frac{\partial}{\partial r} + \frac{1}{r} \right) \begin{pmatrix} \rho'_i \\ u'_i \\ v'_i \\ w'_i \\ p'_i \end{pmatrix}$$

More details about Tam conditions derivation can be found in [167] and about their implementation in sAbrinA in [61].

II.2.2 CFD solvers for stationary mean flow assessment

A 3D RANS code integrated to elsA solver

In order to perform CAA calculations using sAbrinA (presented in the latter section), a mean flow has to be prescribed or provided by a CFD calculation. To this end, RANS calculations are usually carried out. Moreover, these CFD simulations are required to evaluate the aerodynamic penalties of passive acoustic designs.

RANS calculations performed in Chapter V.1 and in Chapter VI have been carried out by means of the esLA code developed at ONERA. It computes internal and external flows around fixed and moving bodies, for which the domain is defined by a multi-block hybrid structured/unstructured and body-fitted mesh. esLA features a variety of turbulence models, ranging from Reynolds averaged Navier-Stokes (RANS) to Large Eddy Simulations (LES), and passing through Zonal Detached Eddy Simulations (ZDES). More general information about elsA capabilities and applications can be found in [48]. In Chapter V.1 and in Section VI.1.2, RANS simulations have been conducted by applying the Jameson spatial scheme and the $k-l$ Smith turbulence model. The $k-l$ Smith model is commonly used at ONERA and Safran Aircraft Engines (SAE) for turbofan applications. A comparison of several turbulence models on the ACAT1 Benchmark is provided in [110] in the framework of an EU project TurboNoiseBB [13].

A 2D and open source Euler mean flow solver

As mentioned in the previous section, a RANS calculation is currently performed to obtain a mean flow for CAA. However, in order to comply with the inviscid assumption of the CAA code, the boundary layers have to be filtered. Otherwise, numerical issues may occur, particularly

in the presence of serrations [144]. To avoid this correction step, the mean flow can also be obtained thanks to CFD solving the Euler equations, which intrinsically satisfies the inviscid assumptions of the CAA. Indeed, the solution provided by the Euler code is free of recirculation zones and boundary layers. However, unlike RANS simulation, the CFD Euler computations do not provide any information on turbulence properties. This is not a limitation for the first part of the InnoSTAT test campaign (see Section II.3.1 and Part V). Indeed, the turbulence properties are prescribed from pre-test conditions and then fulfilled experimentally by an adequately designed turbulence grid.

The mean flow Euler simulations performed here use an open source solver on 2D structured grid. The code is provided as a companion material to [42]. The required inputs are the total pressure and the total temperature at the inlet and the static pressure at the outlet. A dedicated grid generator is also provided with the CFD code. This solver has been used to obtain the mean flow around NACA airfoils in Chapter V.2. Note that this Euler code has also been applied to the NASA SDT turbofan case, with some adaptations discussed in Section VI.1.2. A comparison with RANS-obtained mean flow is carried out for CAA purpose.

II.2.3 High-fidelity lattice Boltzmann code

Aside from RANS and LEE CAA simulations, aerodynamic and aeroacoustic predictions are also achieved by means of a high fidelity approach based on the lattice Boltzmann method (LBM). Contrary to the traditional CFD solver relying on the Navier-Stokes (NS) equations, the lattice Boltzmann method originates from the kinetic theory of gases. The latter idea is illustrated in Fig. II.10. LBM approach is defined as mesoscopic, being situated halfway between particle methods and macroscopic conservative equation from NS. Indeed, in LBM, the fluid is described by probability distribution functions of fluid particles.

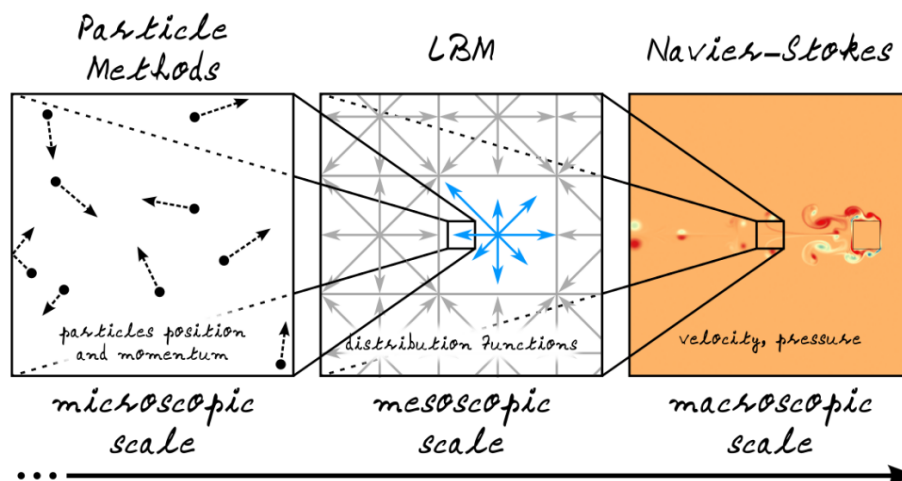


Figure II.10: From microscopic to macroscopic description of fluid mechanics, extracted from [100].

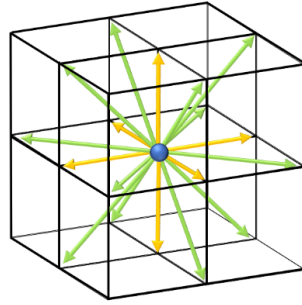


Figure II.11: Continuous Boltzmann equation to Discrete-Velocity Boltzmann Equation (DVBE) by a set of discrete velocities on a D3Q19 lattice.

In practice, the fluid velocities are discretized on a lattice, which acts as the mesh of the simulation. On this lattice, the LBM process is governed by a two-step operation often called "stream and collide" which allows to compute the evolution of the distribution function. Collisions take place locally and the streaming operation is performed following the octree lattice and is exact thanks to the Courant-Friedrichs-Lewy (CFL) equal to 1, which makes this step non-dissipative and its implementation very simple. A simple cubic octree mesh is illustrated in Fig. II.11. This basic idea behind LBM process explains the efficiency of the algorithm, in comparison with traditional NS solvers on parallel computers. Moreover, it offers a very low numerical dissipation suitable for aeroacoustic simulations. Additionally, immersed boundary conditions handle with ease complex geometries, even if the implementation of the boundary conditions on curved surfaces represents a challenge. For these reasons, LBM is a good candidate for simulating challenging aeroacoustics configurations. In the present work, LBM simulations are carried out here by means of the ProLB solver. It has been developed by a French consortium composed of universities, research institutes and industries [12]. In this study, the weakly compressible version of the solver has been used. The main variable in the lattice Boltzmann method is the distribution function, from which the density and momentum of the fluid are given by its statistical moments. For quasi-incompressible flows, the discrete distribution function involves nineteen components, also called D3Q19 as illustrated in Fig. II.11. The D3Q19 allows the computation of the athermal formulation of the NS equations with an error scaling with the Mach number to the third power [162]. This method is also referred to as isothermal LBM. In ProLB, an advanced collision model, the hybrid recursive regularized (HRR) operator is implemented, enhancing the stability of the scheme and reducing the spurious noise at mesh refinement transition [104, 21]. Indeed, the HRR scheme features some corrections to cancel $O(M^3)$ terms leading to a more robust code under $M=0.7$ [73, 91], while remaining athermal. As for the convection of the variables across grid refinements, a Direct Coupling (DC) cell-vertex algorithm is used [22, 23, 21]. It helps reducing spurious noise source generation at mesh transitions. Solid surfaces are represented by immersed boundary conditions, where the fluid boundary layer is resolved thanks to an advanced wall log-law taking into account the adverse pressure gradient and the curvature effect. Similarly to traditional CFD solvers, a Large Eddy Simulation turbulence model controls the unresolved turbulent dynamics. In the present case, the Shear-Improved Smagorinsky Model (SISM) [118] is employed as a subgrid-scale viscosity to model unresolved small-size eddies.

II.3 Experimental set-ups

The different experimental facilities, on which the previously mentioned analytical and numerical tools have been applied, are presented. This chapter covers:

1. The rectilinear cascade at Centrale Lyon used during the InnoSTAT project, in Section II.3.1. It aims at evaluating several treatments for interaction noise reduction, provided by the project partners. In preparation for this test campaign, ONERA has designed LE serrations in Part IV, which are assessed by numerical simulations, CFD/CAA and LBM, in Part V.
2. In Section II.3.2, the NASA Source Diagnostic Test (SDT) which is a scaled-down fan simulator at Glenn Research Center. It represents an international benchmark for turbofan broadband noise predictions. An assessment of the ONERA's CFD/CAA approach on this test-case is analyzed in Chapter VI.1.
3. Finally, in Section II.3.3, the ECL-B3 test rig, representing a 1/3 mock-up of a turbofan engine fan. This test facility will be used for the second part of the InnoSTAT project, in order to validate the successful acoustic treatments from the rectilinear-cascade test campaign on a bench which is more representative of a real turbofan. A first proposal of a LE serration design, adapted to this configuration, is discussed in Chapter VI.2.

II.3.1 Rectilinear cascade in KCA test rig of Ecole Centrale de Lyon



Figure II.12: Picture of the anechoic room at Centrale Lyon.

The experimental facility at Centrale Lyon used for the first test campaign of the InnoSTAT project is located in the main subsonic anechoic wind tunnel at Centrale Lyon. The flow is generated by a centrifugal fan powered by an 800 kW engine and the maximum mass flow rate is about 20 kg/s. The flow then passes through a series of absorbing acoustic treatments before reaching the 720 m³ anechoic room, depicted in Fig. II.12.

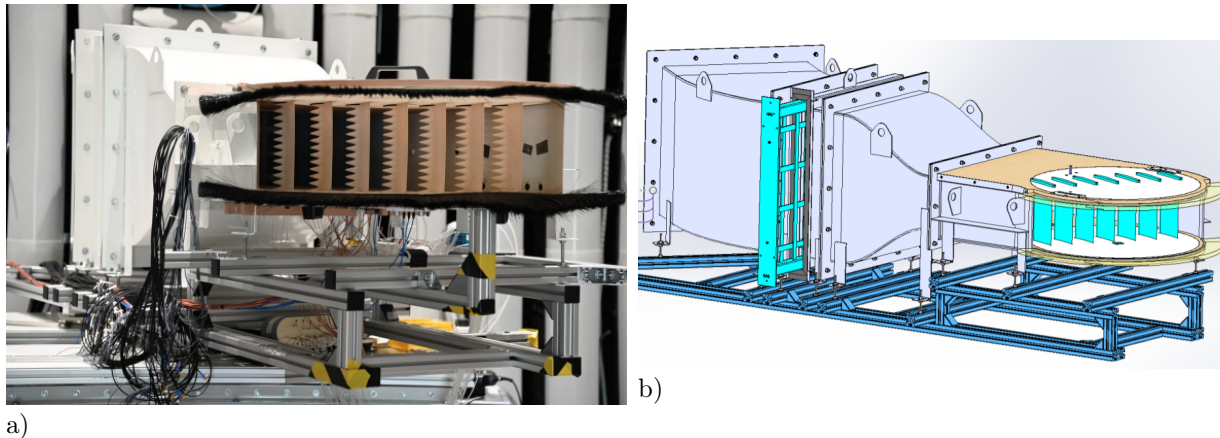


Figure II.13: Picture of the test facility at Ecole Centrale de Lyon (a). 3D geometric modeling of the bench (in light blue turbulence grid and vanes) (b).

A dedicated test section, presented in Figs II.13a, II.13b, and II.14 has been designed for this experimental test campaign. It consists of a rectilinear cascade as in similar [75]. A 0.5 m long contraction adapts the test section from $0.56 \times 0.56 \text{ m}^2$ to $0.56 \times 0.2 \text{ m}^2$. The nozzle accelerates the flow by this geometrical squeezing in order to reach the adequate mean flow between 45 m/s

and 180 m/s. In the thinner part of the test section, seven evenly spaced NACA7310 airfoils are mounted on a rotating disk to modify the cascade angle (between the incident flow and the normal to the cascade frontlines) around the nominal value $\beta_c = 34^\circ$, see Fig. II.15. The stagger angle is kept at a constant value $\chi = 13^\circ$ and the leading edge of the central vane is located at about 0.5 m downstream of the contraction. Vertical side plates guide the flow down to the trailing edge of the cascade, while the horizontal plates extend downstream of the cascade as a semicircle centered on the trailing edge of the central vane. The geometrical parameters can be visualized in Fig. II.15.

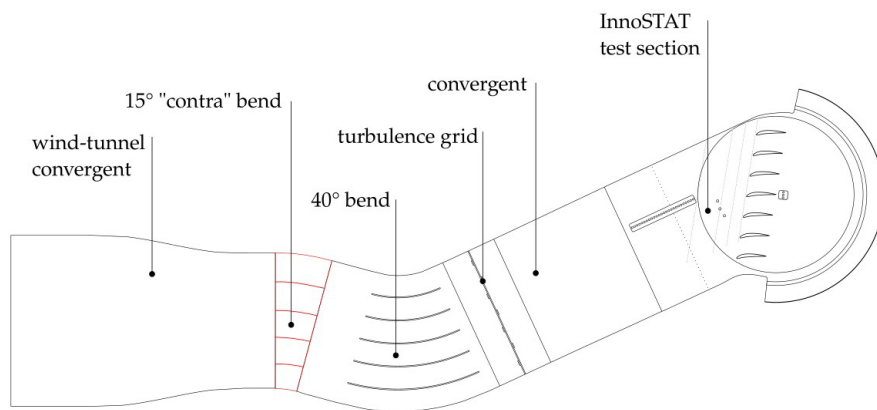


Figure II.14: Mid span cut of the complete test section geometry.

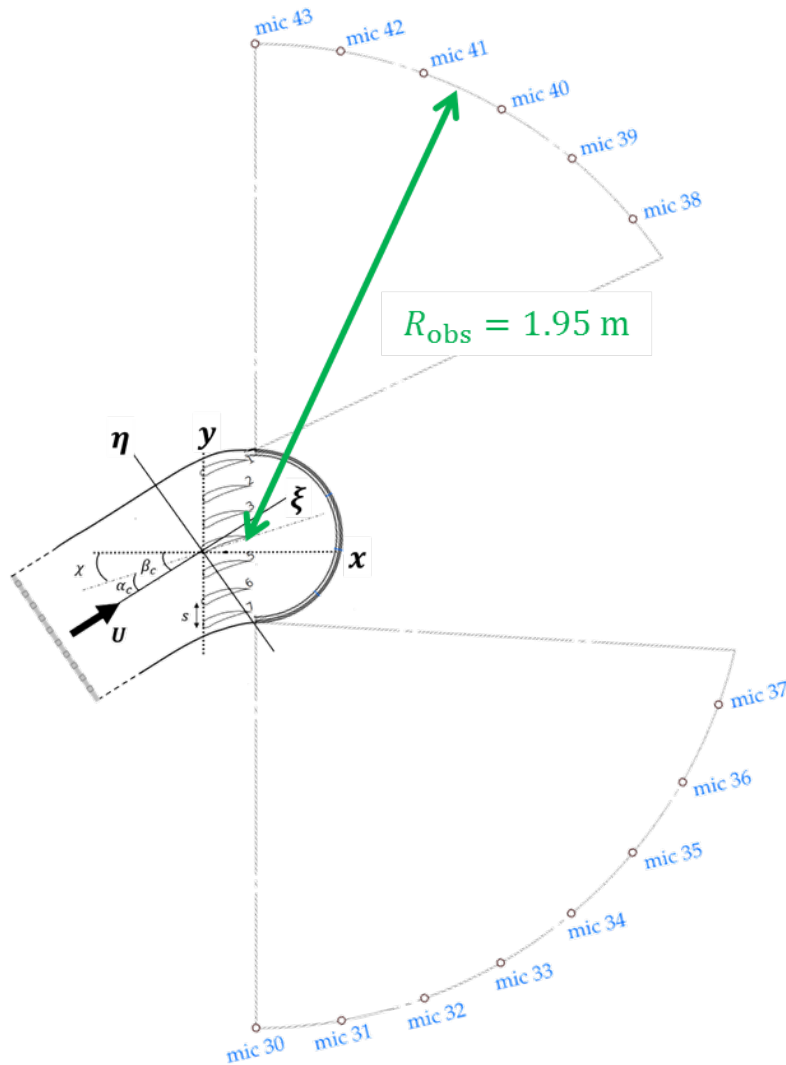


Figure II.15: Mid span cut of the test section geometry and definition of the coordinate systems. Location of the microphones downstream of the cascade.

The NACA profiles are impinged by a turbulent inflow, which is generated by a grid placed in the test section just upstream of the contraction. Initially, a turbulence grid previously evaluated in another test rig [36] (with a smaller test section), has been proposed during the InnoSTAT Critical Design Review (CDR). Its pattern generates a turbulence intensity (TI) of 4.5 % and an integral longitudinal length scale L_l of 9 mm, both quantities probed at 50 cm from the grid. However, due to a delayed experimental campaign, it has been decided to re-use another already available grid. Geometrical characteristics of both grids are compared in Table II.2. The analysis of turbulence obtained with this grid during the InnoSTAT test campaign is discussed in Section V.3.2. Table II.2 summarizes the main geometrical parameters of the experimental set-up.

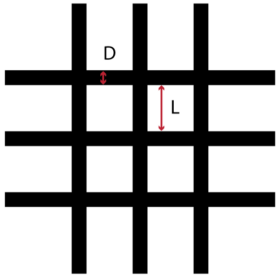
	Parameter	Value
Airfoil	shape	NACA7310
	chord c	12 cm
	span L_z	20 cm
	inter-vane space s	8.5 cm
Upstream flow	Velocity (U direction)	45 m/s to 180 m/s
	Angle between cascade and flow axis β_c	34° (nominal)
Turbulence grid (rectangular-section bars)		Early CDR grid [36]
		$D = 1$ cm
		$L = 4$ cm
		Final grid
		$D = 2$ cm
		$L = 5.5$ cm

Table II.2: Main parameters of the test campaign.

Regarding the instrumentation, static pressure probes which are flush-mounted in transverse direction are used to check the flow homogeneity. The latter might be influenced by the presence of bends along the test section, as shown in Fig. II.14. Hot wire anemometry at midspan characterizes the incoming turbulence, particularly the one component spectra at the blue circle location in Fig. II.16a. X wire probes also measure the velocity profiles along the red lines depicted in Fig. II.16a. Finally, airfoil chordwise probes are distributed at mid-span, over the pressure and suction sides of the reference middle vane (see Fig. II.16b), in order to measure the wall pressure coefficients.

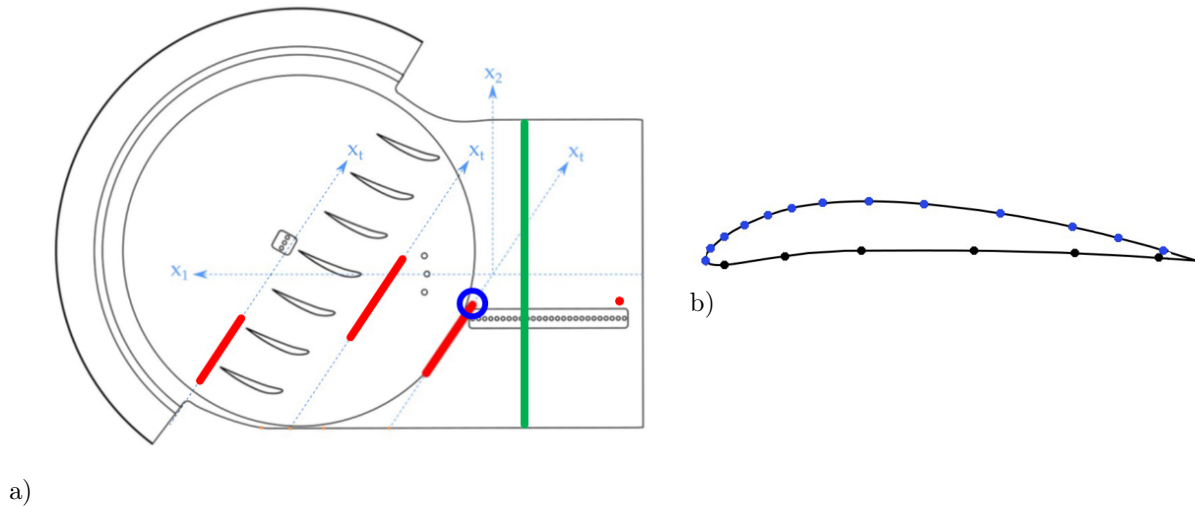


Figure II.16: (x, y) cut of the geometry and wire probes locations (a). Pressure probes at the vane surface (b).

Acoustic measurements are performed both upstream and downstream of the cascade. The positions of the 43 microphones are plotted in Fig. II.15. A linear array made of 26 microphones is located upstream of the cascade. This array can be used to separate the acoustic waves propagating in the upstream and downstream directions and thus isolate the upstream radiation from the cascade. Three microphones are located just downstream of the trailing edge of the central blade. A far-field circular array containing 14 microphones is centered on the trailing edge of the central vane with a radius of 1.95 m. The microphones are located in the mid-span plane, with an angular spacing of 10° from -90° to $+90^\circ$. No microphones are located in the turbulent wake of the cascade between -20° and $+40^\circ$. Acoustic predictions obtained in this PhD work are focused on this far-field antenna.

II.3.2 Source Diagnostic Test (SDT) turbofan model at NASA Glenn

The NASA Source Diagnostic Test (SDT) refers to a 22-inch fan rig simulator without core flow (illustrated by Fig. II.17) tested at the NASA Glenn Research Center [8]. A dedicated AIAA session took place in 2014 to discuss the turbofan broadband noise on this test-case. The main novelty associated with this test rig is that it represents a 3D simplified geometry including rotor and stator stages (without the primary flow) with a quasi-annular nacelle, well suited for benchmarking and code validation. The purpose of the test-case was primarily to compare methods for broadband noise prediction.

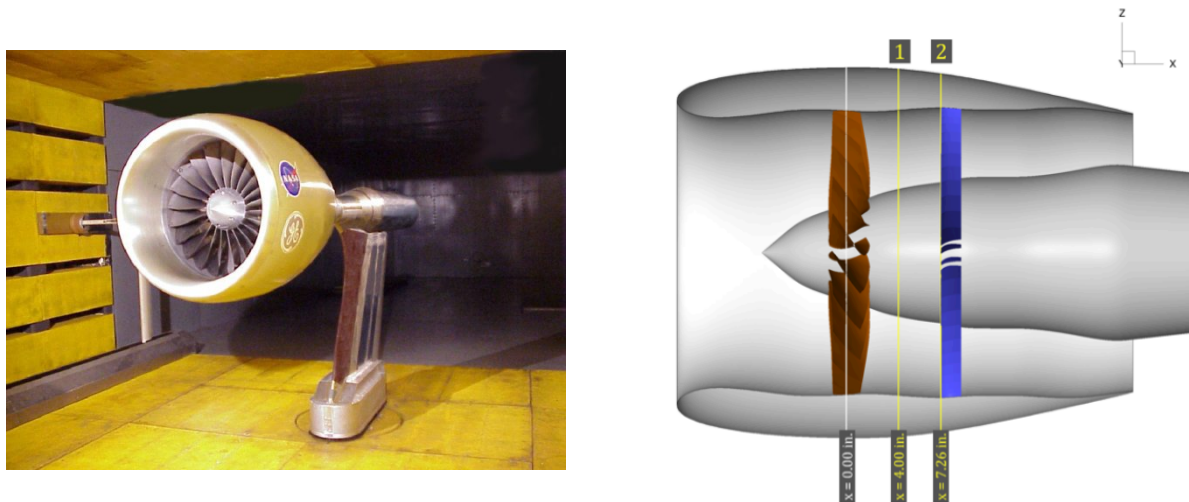


Figure II.17: NASA-SDT facility, picture extracted from [154] (a). Mean flow and turbulent velocities are provided for the positions 1 and 2 (b).

Three different stators have been tested: "baseline" (54 blades), "low count OGV" (26 blades) with a longer chord enabling the flow redirection, and "low noise OGV" with 26 inclined stator vanes in order to reduce passively the noise generation. The provided measurements cover the spanwise turbulence velocity components, the mean flow velocity, and the sound spectrum during the experiment (captured via a traversing microphone). In this work (simulations in Chapter VI.1), the focus is only on the "baseline" case at approach condition. In that configuration, the engine power is defined at 61.7 % of its nominal capacity. At this speed, the flow rate is 26, 29 kg/s and the flow is subsonic. Several data were acquired among which: hot wires to characterize the turbulent inflow at locations 1 and 2 in Fig. II.17 (right) [141], laser Doppler velocimetry, surface pressure probes, and in-duct and far-field noise microphones [177]. Additional details about the SDT project are given in [8].

II.3.3 PHARE-2 ECL-B3 turbofan test facility at Ecole Centrale de Lyon

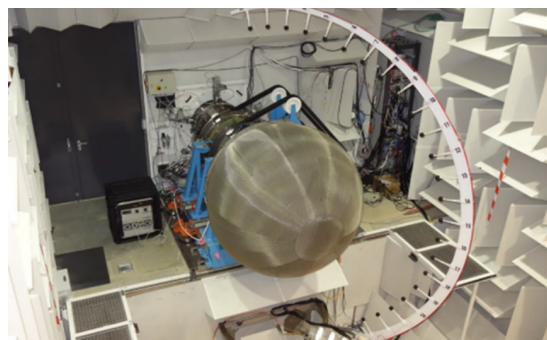


Figure II.18: Picture of the ECL-B3 anechoic chamber, fan stage mock-up with its windscreen and external microphone array reproduced from [140]

The ECL-B3 turbofan test rig, illustrated in Fig. II.18, is issued from an EquipEX investment program, called PHARE (Plate-forme machines tournantes pour la maîtrise des Risques Environnementaux), which has given rise to 3 test benches [10]. ECL-B3 aims at studying instability phenomena occurring in the fluid and the structure along with aeroacoustic sources generation and propagation.

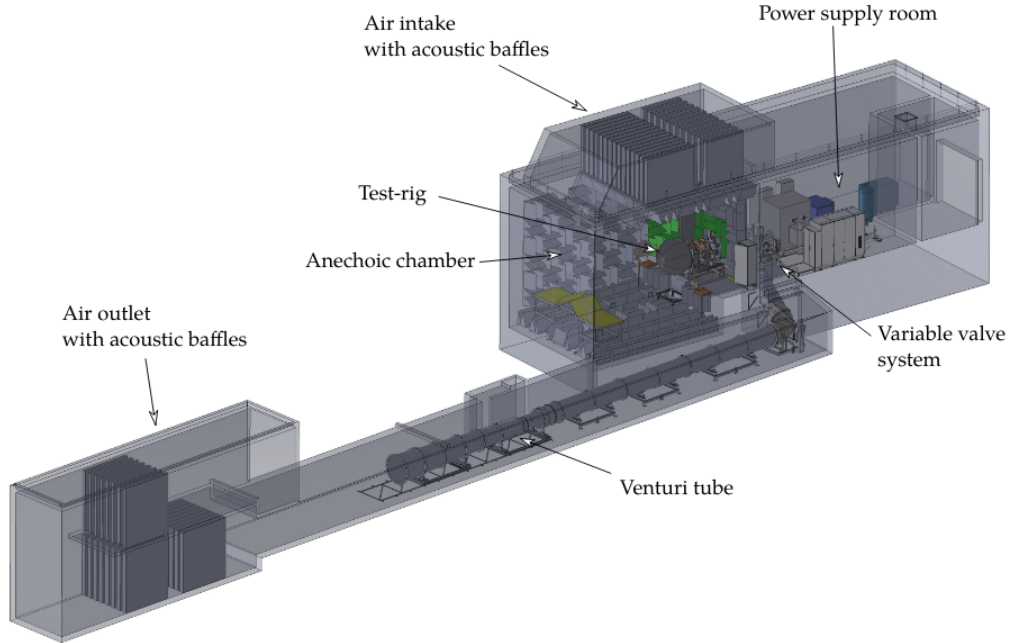


Figure II.19: 3D model of the building housing the ECL-B3 facility [159]

Located in a dedicated building at Centrale Lyon depicted in Fig. II.19, it represents a 1/3 scale fan stage co-designed with Safran Aircraft Engines. The particularity of the test rig lies in its modularity, which allows the testing of innovative concepts, such as low noise stators in the framework of the InnoSTAT project. The power of the facility is 3 MW.

With regard to the acoustic measurements, the fan mock-up is placed in an anechoic chamber. Upstream noise directivity can be characterized by a microphone array placed on a rotating stand as depicted in Fig. II.18. This allows the characterization of the acoustic waves over half a sphere. In-duct measurements are also made possible by 160 microphones adequately located to perform mode decomposition [140]. Further details about the acoustic instrumentation can be found in [159].

A second InnoSTAT test campaign at ECL-B3 is planned in 2023. Low-noise OGVs will be manufactured from the tests on the rectilinear cascade (Section II.3.1) and compared to a reference silent OGV, designed previously by ONERA and SAFRAN. However, the studied configuration in Chapter VI.2 comes from ENOVAL project [154], close to ECL-B3 and for which RANS data is available. Indeed, numerical simulations on PHARE ECL-B3 will be carried out in 2023 and are outside of the framework of the present thesis.

This page intentionally left blank.

Part III

Turbulence modeling

This third part, involving turbulence modeling, is divided into 5 chapters. The aim is to provide useful information for turbulence characterization and extend synthetic turbulence generation methods in preparation for the next parts dedicated to LE serration design and evaluation. In the first chapter, key theoretical background of turbulent fields representation is introduced. Its purpose is to provide mathematical expressions to characterize turbulence properties and explain how to compute them in practice. The second chapter deals with synthetic turbulence generation, three main techniques are discussed: Fourier modes decomposition, digital filtering, and Synthetic Eddy Method. Special attention is given to the generation method implemented at ONERA, in order to perform aeroacoustic computations. Third chapter presents turbulence generation framework put in place during this PhD to deal with the InnoSTAT rectilinear cascade experiment. In particular, the challenge of generating a 3-wavenumber turbulence while taking into account boundary conditions (periodicity and solid walls) is addressed. The extension to annular geometries is discussed in the fourth chapter. It is done in connection with previous work conducted at ONERA on synthetic turbulence generation for rotor-stator interaction noise assessment in turbofan configurations. Finally, numerical implementation of turbulence generation routines is addressed in Chapter III.5.

III.1 Characterization of turbulence fields

III.1.1 Geometrical notations and turbulent field definition

Geometrical notations

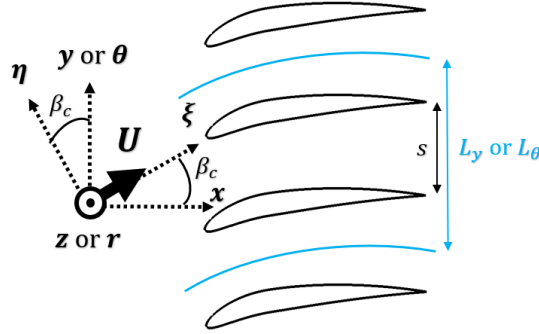


Figure III.1: Overview of the geometrical notations in cascade configurations

Figure III.1 provides the geometrical parameters considered in the following sections. The notations are given either in the Cartesian or annular coordinate systems. L_y and L_θ represent the width of the simulation domain (respectively for rectilinear and annular cascades). In annular coordinate systems, L_θ denotes the quantity $r\Delta\theta$, with $\Delta\theta$ the angular sector of the CAA domain. The spanwise length is denoted either by L_z in Cartesian coordinate systems (such as $z_{max} = z_{min} + L_z$) or L_r in annular configurations (such as $r_{max} = r_{min} + L_r$).

Reynolds decomposition

The starting idea to synthesize turbulence is based on an ergodic stochastic process. First, a set average $\langle \rangle$ can be applied on the velocity field in order to get a decomposition in a mean part and a fluctuating part,

$$\begin{cases} \mathbf{u} &= \mathbf{U} + \mathbf{u}' \\ \mathbf{U} &= \langle \mathbf{u} \rangle \\ \langle \mathbf{u}' \rangle &= 0 \end{cases} \quad (\text{III.1})$$

In case of squared fluctuating values, it can be easily demonstrated that:

$$\langle u'^2 \rangle = \langle u^2 - 2u \langle u \rangle + \langle u \rangle^2 \rangle = \langle u^2 \rangle - \langle u \rangle^2 \quad (\text{III.2})$$

The ensemble average can be seen as the expected value in the framework of the probability theory, with (n) a given realization. Hence,

$$\langle \mathbf{u} \rangle = \lim_{N_r \rightarrow \infty} \left(\frac{1}{N_r} \sum_{n=1}^{N_r} \mathbf{u}^{(n)} \right) \quad (\text{III.3})$$

To move from the discrete to the continuous formulation, the summation in Eq. (III.3) can be replaced by an integral, with $p_r(\mathbf{u})$ denoting the probability density function of \mathbf{u} ,

$$\left\{ \begin{array}{l} \int_{\mathbb{R}^3} p_r(\mathbf{u}) d\mathbf{u} = 1 \\ \int_{\mathbb{R}^3} \mathbf{u} p_r(\mathbf{u}) d\mathbf{u} = \langle \mathbf{u} \rangle \end{array} \right. \quad (\text{III.4})$$

Equation (III.4) provides the main properties of the probability density function.

Statistical stationarity

In case of stationary boundary conditions, the turbulence field is considered as statistically stationary, which provides for the probability density function:

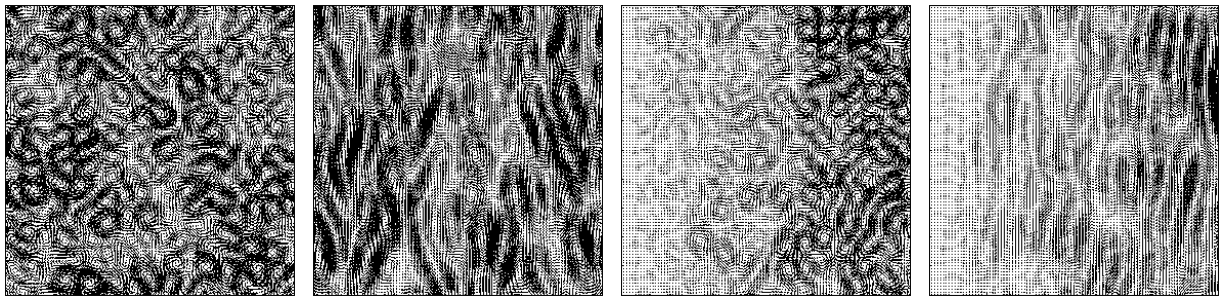
$$\frac{\partial p_r(\mathbf{u})}{\partial t} = 0 \quad (\text{III.5})$$

For an ergodic process, when the condition from Eq. (III.5) is satisfied, the expected value can be simply estimated by a time average:

$$\langle \mathbf{u} \rangle = \lim_{T \rightarrow \infty} \left(\frac{1}{T} \int_t^{t+T} \mathbf{u} dt \right) \quad (\text{III.6})$$

In practice, Eq. (III.6) is used to compute mean flow fields in simulations as well as in experiments.

Homogeneity and isotropy



a) Homogeneous and isotropic b) Homogeneous and non-isotropic c) Non-homogeneous and isotropic d) Non-homogeneous and non-isotropic

Figure III.2: Illustration of turbulence properties: homogeneity and isotropy (velocity vector plot)

Figure III.2 illustrates combinations of homogeneous and/or isotropic properties applied to

turbulent flows. The mathematical representation of these two properties is given below. If \mathbf{X} denotes the fluid particle position vector, and

$$\forall \mathbf{X} \in \mathcal{D}, \forall i \in \llbracket 1, 3 \rrbracket, \frac{\partial p_r(\mathbf{u}'(\mathbf{X}))}{\partial X_i} = 0 \quad (\text{III.7})$$

the probability density function of a homogeneous field inside a domain \mathcal{D} satisfies Eq. (III.7). The probability density function of two velocity components, u'_i and u'_j , is now considered.

$$\forall \mathbf{X} \in \mathcal{D}, \forall i, j \in \llbracket 1, 3 \rrbracket^2, p_r(u'_i(\mathbf{X})) = p_r(u'_j(\mathbf{X})) \quad (\text{III.8})$$

Likewise for isotropy, the condition defined in Eq. (III.8) has to be verified.

Frozen turbulence assumption: Taylor's hypothesis

The frozen turbulence assumption implies that turbulence structures are simply advected along streamlines by the mean velocity field.

$$\forall \mathbf{X} \in \mathcal{D}, \forall t_\xi, \mathbf{u}'(\mathbf{X}, t) = \mathbf{u}'(\mathbf{X} + \mathbf{U}t_\xi, t + t_\xi) \quad (\text{III.9})$$

The validity of the frozen turbulence hypothesis in Eq. (III.9) depends on characteristic times of turbulence and of the advection by the mean flow. They must satisfy $\tau_{turb} \gg \tau_{conv}$, that is, $u'/U \ll 1$. Furthermore, the frozen turbulence assumption requires in Fourier space that the angular frequency of the velocity fluctuations is directly related to the wavevector thanks to the following dispersion relation: $\omega = \mathbf{k} \cdot \mathbf{U}$.

III.1.2 Representation of turbulent velocity fields in Fourier space

Spatial Fourier transform

The turbulent velocity field is defined in the wavevector space through a Fourier transform TF (with $_s$ denoting the spatial domain),

$$\widehat{\mathbf{u}}'(\mathbf{k}) = \text{TF}_s(\mathbf{u}'(\mathbf{X}, t)) = \frac{1}{(2\pi)^3} \int_{\mathbb{R}^3} \mathbf{u}'(\mathbf{X}, t) e^{-i\mathbf{k} \cdot \mathbf{x}} d\mathbf{x} \quad (\text{III.10})$$

The double correlation tensor is considered in the case of steady and homogeneous turbulent flows, which is only a function of the separation in space and time,

$$R_{ij}(\mathbf{l} = \mathbf{X} - \mathbf{Y}, \tau = t - t_1) = \langle u'_i(\mathbf{X}, t) u'_j(\mathbf{Y}, t_1) \rangle \quad (\text{III.11})$$

The spectral tensor is defined as the Fourier transform of the double correlation tensor from Eq. (III.11).

$$\varphi_{ij}(\mathbf{k}) = \text{TF}_s(R_{ij}(\mathbf{l}, 0)) = \frac{1}{(2\pi)^3} \int_{\mathbb{R}^3} R_{ij}(\mathbf{l}, 0) e^{-i\mathbf{k} \cdot \mathbf{l}} d\mathbf{l} \quad (\text{III.12})$$

The spectral tensor defined in Eq. (III.12) will be described further in Section III.1.3. The reverse

mathematical operation can be applied to recover the double correlation tensor in the physical space.

$$R_{ij}(\mathbf{l}, 0) = \int_{\mathbb{R}^3} \varphi_{ij}(\mathbf{k}) e^{i\mathbf{k}\cdot\mathbf{l}} d\mathbf{k} \quad (\text{III.13})$$

Thus, the inverse Fourier transform is given by Eq. (III.13). It can be shown that:

$$\langle \widehat{\mathbf{u}}'_i(\mathbf{k}) \widehat{\mathbf{u}}'_j(\mathbf{k}) \rangle = \varphi_{ij}(\mathbf{k}) \quad (\text{III.14})$$

A more useful variant of Eq. (III.14) will be introduced in Section III.14, where spatial Fourier transform is replaced by Fourier transform in the time domain. In practice, it is also more convenient to deal with one-dimensional spectra, since they only require to perform calculations along one direction (in most cases aligned with the upstream mean flow direction ξ). 1D spectra are obtain considering that,

$$\varphi_{ij}^{1D}(k_\xi) = \text{TF}_s (R_{ij}(l_\xi, 0)) = \frac{1}{2\pi} \int_{\mathbb{R}} R_{ij}(l_\xi, 0) e^{-ik_\xi l_\xi} dl_\xi \quad (\text{III.15})$$

From Eqs. (III.13) and (III.15), one can deduce that:

$$\varphi_{ij}^{1D}(k_\xi) = \int_{\mathbb{R}^2} \varphi_{ij}(\mathbf{k}) dk^\perp = \int_{\mathbb{R}^2} \varphi_{ij}(\mathbf{k}) dk^y dk^z \quad (\text{III.16})$$

with k^\perp defined such as $\mathbf{k}^\perp = \mathbf{k} - \mathbf{k} \cdot \mathbf{k}_z \mathbf{z}$. The expanded form of Eq. (III.16) will be provided in Section III.1.3.

Temporal Fourier transform

The temporal Fourier transform with subscript t denoting the time domain is defined by:

$$\widetilde{\mathbf{u}}'(\mathbf{X}, f) = \text{TF}_t (\mathbf{u}'(\mathbf{X}, t)) = \int_{\mathbb{R}} \mathbf{u}'(\mathbf{X}, t) e^{-i2\pi ft} dt \quad (\text{III.17})$$

Let us introduce the double correlation tensor using time measurement at a single point. One can show that Eq. (III.11) becomes:

$$R_{ij}(\mathbf{0}, \tau) = \langle u'_i(\mathbf{X}, t) u'_j(\mathbf{X}, t + \tau) \rangle \quad (\text{III.18})$$

$$\varphi_{ij}^{1D}(f) = \text{TF}_t (R_{ij}(\mathbf{0}, \tau)) = \int_{\mathbb{R}} R_{ij}(\mathbf{0}, \tau) e^{-i2\pi f\tau} d\tau \quad (\text{III.19})$$

The 1D frequency spectrum in Eq. (III.19) is obtained by taking the temporal Fourier transform of Eq. (III.18).

turbulence hypothesis in Fourier space

Frozen turbulence assumption presented in Eq. (III.9) implies that:

$$\begin{aligned} \mathbf{u}'(\mathbf{X}, t) &= \mathbf{u}'(\mathbf{X} + \mathbf{U}t_\xi, t + t_\xi) \\ \Leftrightarrow R_{ij}(l_\xi, 0) &= R_{ij}(\mathbf{0}, \tau) \end{aligned} \quad (\text{III.20})$$

$$\Leftrightarrow \mathbf{k} \cdot \mathbf{U} = 2\pi f$$

Under the frozen turbulence hypothesis, there is an equivalence between correlation in space and time.

Therefore, one can deduce from Eqs. (III.18) and (III.20) (see demonstration in Appendix A, Eq. (VI.1)), the following relation:

$$\left\langle \widetilde{\mathbf{u}}_i^*(\mathbf{X}, f) \widetilde{\mathbf{u}}_j(\mathbf{X}, f) \right\rangle = \delta(0) \frac{2\pi}{U} \int_{\mathbb{R}^2} \varphi_{ij}(\mathbf{k}) dk^\perp \quad (\text{III.21})$$

with $\delta(0)$ denoting the Dirac function at 0. Equation (III.21) will be particularly useful for the post-processing. The quantity $\int_{\mathbb{R}^2} \varphi_{ij}(\mathbf{k}) dk^\perp$ is called $\varphi_{ij}^{1D}(k_\xi)$ (see Eq. (III.16)) and it will be expanded in Section III.1.3.

Expected value with a finite number of outcomes Particular attention has to be given to the set average operations. Indeed, in practice, only a finite number of outcomes can be used to perform the expected value operation. In cases simulated in Part V, the boundary conditions are time independent after a transient period. There is no moving parts nor variable boundary conditions (after a transient initialization). Turbulence can be considered as statistically steady over a certain time interval (see Eq. (III.6)). It implies that the set average operation can be replaced by a time integral.

For the set average operation in the Fourier space things are quite different. Three options can be examined in practice to obtain the expected (average) value.

1. One could run N_{simu} simulations of a time T_{simu} without the transient period and average the results. In practice, this option is not considered since multiple simulations are required.
2. A single simulation, with $T'_{simu} = T_{simu} \times N_{simu}$, could be run and the results cutted in N_{simu} pieces. An average is then applied as in 1). The choice of N_{simu} is discussed in [78].
3. Running a simulation with $T'_{simu} = T_{simu} \times N_{simu}$ and averaging results on frequency bands of width $1/T_{simu}$. This option has been compared to the first one in [61] p.66 or in [47], providing a similar output. In some cases in this manuscript, the band average is replaced by a moving mean average operation, in order to keep more point in the smoothed solution.

The two latter options are discussed in [82]. The tools presented above will be useful to either check injected synthetic turbulence properties or post-process turbulence fields from high fidelity LBM numerical simulations.

III.1.3 Modeling of main turbulent quantities and spectra

Turbulence energy analysis

The main quantity to interpret turbulent flows is the turbulent kinetic energy. This variable is defined as follows:

$$k = \frac{1}{2} \left(\langle u'_\xi{}^2 \rangle + \langle u'_\eta{}^2 \rangle + \langle u'_z{}^2 \rangle \right) \quad (\text{III.22})$$

From the turbulent kinetic energy in Eq. (III.22), the turbulent intensity can also be defined in order to easily compare the ratio of turbulence velocities to the mean flow magnitude $U = \|\mathbf{U}\|$.

$$\text{TI} = \frac{\sqrt{\frac{2}{3}k}}{U} \quad (\text{III.23})$$

In order to have a look at anisotropic flows, it can be interesting to define a quantity depending on each direction:

$$\left\{ \begin{array}{l} \text{TI}_\xi = \frac{\sqrt{\langle u'_\xi{}^2 \rangle}}{U} \\ \text{TI}_\eta = \frac{\sqrt{\langle u'_\eta{}^2 \rangle}}{U} \\ \text{TI}_z = \frac{\sqrt{\langle u'_z{}^2 \rangle}}{U} \end{array} \right. \quad (\text{III.24})$$

In case of an isotropic turbulence, one can recover from Eqs. (III.23) and (III.24) that:

$$\text{TI} = \sqrt{1/3 \left(\text{TI}_\xi^2 + \text{TI}_\eta^2 + \text{TI}_z^2 \right)} = \text{TI}_\xi = \text{TI}_\eta = \text{TI}_z.$$

Spatial analysis of turbulence fields

The other essential quantity for the computation of turbulence spectra (detailed in Section III.1.3) is the integral longitudinal length scale. More generally, the coherence of a turbulent field can be characterized in all directions of the space.

$$\mathfrak{r}_{ij}(\mathbf{X}, 2\mathbf{l}, t) = \frac{\langle u'_i(\mathbf{X} - \mathbf{l}, t) u'_j(\mathbf{X} + \mathbf{l}, t) \rangle}{\sqrt{\langle u'_i(\mathbf{X} - \mathbf{l}, t)^2 \rangle} \sqrt{\langle u'_j(\mathbf{X} + \mathbf{l}, t)^2 \rangle}} \quad (\text{III.25})$$

Equation (III.25) has been centered around 0, in comparison with the formulation given in [137]. A centered formulation is also provided page 109 in [147]. Indeed, in the case of a turbulent flow in a nozzle aligned with the axis $\boldsymbol{\xi}$ for example, the centered choice appears more relevant since the correlations at a point \mathbf{X} will be defined by taking contribution from upstream $\mathbf{X} - \mathbf{l}_\xi$ and downstream $\mathbf{X} + \mathbf{l}_\xi$ positions equally. The integral length scales $L_{ij,k}$ are then defined as follows,

$$L_{ij,k} = 2 \int_0^{+\infty} \mathfrak{r}_{ij}(\mathbf{X}, 2\mathbf{l}_k, t) dl_k \quad (\text{III.26})$$

It has to be noted that the implicit summation is never used in this work. In case of isotropic flows, one can derive the following relations:

$$\begin{aligned} \forall i \neq j, L_{ij,k} &= 0 \\ \forall i, \forall j, L_{ii,i} &= L_{jj,j} \\ \forall i \neq k, \forall j \neq k, L_{ii,k} &= L_{jj,k} \end{aligned} \quad (\text{III.27})$$

From Eq. (III.27), it can be deduced that for isotropic flows, turbulence is characterized by two quantities, namely the longitudinal integral length scale L_l and the transverse integral length scale L_t , with $L_t = 1/2L_l$ for isotropic flows. Under the frozen turbulence assumption (see Section III.1.2), the integral longitudinal length scale can also be obtained from the temporal Fourier transform of the velocities (see equation (6.213) in [147]):

$$L_l = L_{\xi\xi,\xi} = 2 \int_0^{+\infty} r_{\xi\xi}(\mathbf{X}, 2\mathbf{l}_\xi, t) dl_\xi = \lim_{f \rightarrow 0} \left(\frac{S_{u'_\xi u'_\xi}(f)U}{4 \langle u'^2_\xi \rangle} \right) \quad (\text{III.28})$$

In Eq. (III.28), $S_{u'_\xi u'_\xi}$ denotes the one-sided Power Spectrum Density (PSD) of the streamwise velocity component.

Liepmann turbulence spectra (1D, 2D and 3D) for CAA implementation The expressions of the turbulence spectra are detailed here to comply with the numerical simulations carried out in Chapter V.2 and Part VI, for which the geometrical notations are presented in Section III.1.1. In this study, the wavenumber spectra of turbulence are based on the definition proposed by Liepmann [123]:

$$E(k) = \frac{8\text{TI}^2 U^2 L_l}{\pi} \frac{(kL_l)^4}{(1 + (kL_l)^2)^3} \text{ with } k = \sqrt{k_\xi^2 + k_\eta^2 + k_z^2} \quad (\text{III.29})$$

where the subscript ξ still indicates the direction parallel to the mean flow, TI the turbulence intensity, and L_l the integral longitudinal length scale of turbulence (see Section III.1.3). From Eq. (III.29), the link with the autocorrelation velocity spectra can be made through, refer to equation (9.1.8) in [85],

$$\varphi_{ii}^{3D}(k_\xi, k_\eta, k_z) = \frac{E(k)}{4\pi k^2} \left(1 - \frac{k_i^2}{k^2} \right) \quad (\text{III.30})$$

To consider simplified cases with turbulence in a plane and also 1D spectra, an integration is performed over transverse wavenumber components.

$$\varphi_{ii}^{2D}(k_\xi, k_z) = \int_{-\infty}^{+\infty} \varphi_{ii}^{3D}(k_\xi, k_\eta, k_z) dk_\eta \quad (\text{III.31})$$

$$\varphi_{ii}^{1D}(k_\xi) = \int_{-\infty}^{+\infty} \varphi_{ii}^{2D}(k_\xi, k_z) dk_z \quad (\text{III.32})$$

The previous integrations in Eqs. (III.31) and (III.32) can be analytically performed to obtain explicitly $\varphi_{\xi\xi}$, $\varphi_{\eta\eta}$, and φ_{zz} which are of major interest for the implementations in the turbulence generation routines. They are listed in Table III.1.

2D planar spectra $\varphi_{ii}^{2D}(k_\xi, k_z)$	1D spectra $\varphi_{ii}^{1D}(k_\xi)$
$\varphi_{\xi\xi}^{2D}(k_\xi, k_z) = \frac{\text{TI}^2 U^2 L_l^2}{4\pi} \frac{1 + L_l^2(k_\xi^2 + 4k_z^2)}{\left(1 + L_l^2(k_\xi^2 + k_z^2)\right)^{5/2}}$	$\varphi_{\xi\xi}^{1D}(k_\xi) = \frac{\text{TI}^2 U^2 L_l}{\pi} \frac{1}{1 + (L_l k_\xi)^2}$
$\varphi_{\eta\eta}^{2D}(k_\xi, k_z) = \frac{3\text{TI}^2 U^2 L_l^4}{4\pi} \frac{k_\xi^2 + k_z^2}{\left(1 + L_l^2(k_\xi^2 + k_z^2)\right)^{5/2}}$	$\varphi_{\eta\eta}^{1D}(k_\xi) = \frac{\text{TI}^2 U^2 L_l}{2\pi} \frac{1 + 3(L_l k_\xi)^2}{\left(1 + (L_l k_\xi)^2\right)^2}$
$\varphi_{zz}^{2D}(k_\xi, k_z) = \frac{\text{TI}^2 U^2 L_l^2}{4\pi} \frac{1 + L_l^2(4k_\xi^2 + k_z^2)}{\left(1 + L_l^2(k_\xi^2 + k_z^2)\right)^{5/2}}$	$\varphi_{zz}^{1D}(k_\xi) = \varphi_{\eta\eta}^{1D}(k_\xi)$

Table III.1: Integrated autocorrelation spectra obtained from Liepmann spectrum in Eq. (III.29).

With the aim of simplification and with approximations discussed in Section II.1.2.1, one may choose not to consider the influence of the component k_z , with the subscript z referring to the direction aligned with the span of the studied airfoil or flat plate. Indeed, it has shown to be not significant for flat plates placed along the z axis, following Amiet's theory under certain hypothesis discussed in Section II.1.2.1 and [19, 63]. Thus, the spectra are not explicitly discretized along the latter direction since $k_z = 0$. To recover the expected magnitude of turbulence, a correction is required by multiplying the spectrum by a factor $\Delta k_z = 2\pi/L_z$, as proposed in [63]. Beyond the previous assumptions, the particular geometrical characteristics and CAA set-up of the rectilinear cascade facility, as depicted in Fig. III.1, must be considered. First of all, in order to limit the CPU cost, the test facility is not fully included in the CAA. Adjacent vanes are taken into account through periodic boundary conditions applied along the y direction. Multi-channel calculations can be performed, simply considering that $L_y = n_v \cdot s$. An example is given in Fig. III.1 (see Section III.1.1) for $n_v=2$. The fact that the cascade direction that is tilted from the normal axis to the mean flow, as shown by Fig. III.1, requires to be taken into account in the generation procedure since the gusts are injected in the coordinate system of the cascade (x, y, z) and not the one aligned with the test section and upstream mean flow (ξ, η, z) . Therefore, to ensure periodicity, all wavenumbers k_y have to be multiples of $2\pi/L_y$. Moreover, wall boundary conditions are taken into account for the CAA computations at both ends of the airfoil span. These slip flow boundary conditions considered for the CAA computations represent a major constraint for the generation of a fully 3D turbulence as it will be explained later in Section III.3.5.

III.2 Overview of synthetic turbulence generation methodologies

For CAA solvers based on linearized Euler equations, turbulence-interaction noise studies imply the injection of a synthetic turbulence in the domain (even though some CAA codes work in the frequency domain). Moreover, for high fidelity approaches such as LES and LBM, for which the turbulence can be directly generated by the geometry, it is often very convenient to inject a synthetic turbulence field. Indeed, it allows much more control over the turbulence properties and it avoid meshing adequately all the surfaces to properly generate turbulence. The reader may find more information about stochastic turbulence generation methods for CAA purposes in [116] or [14]. The main idea of the section is to provide some insight about these synthetic turbulence techniques, especially those recently applied to turbulence-cascade interaction noise or leading edge noise reduction from serrations. Moreover, a particular focus is put on the generation of isotropic divergence-free velocity fields, matching a target energy spectrum. The divergence-free constraint is of prime importance for CAA computations using LEE. Because, if unsatisfied, it may generate non-negligible spurious sources in the simulation domain which might overwhelm the physical acoustical sources. The latter point will be discussed in Chapter V.2. Finally, the key points of the generation processes used at ONERA, up to this PhD thesis, will be summarized. The challenging requirements with respect to the configurations studied in the InnoSTAT project will also be discussed.

III.2.1 Fourier modes decomposition

The general form of Fourier modes-based methods is given below.

$$\begin{aligned} \mathbf{u}' &= \sum_{\mathbf{k}} \mathbf{A}_{\mathbf{k}} \cos(\mathbf{k} \cdot \mathbf{X} - \omega t + \psi_{\mathbf{k}}) \\ \operatorname{div}(\mathbf{u}') &= - \sum_{\mathbf{k}} \mathbf{k} \cdot \mathbf{A}_{\mathbf{k}} \sin(\mathbf{k} \cdot \mathbf{X} - \omega t + \psi_{\mathbf{k}}) = 0 \Leftrightarrow \forall \mathbf{k}, \mathbf{k} \cdot \mathbf{A}_{\mathbf{k}} = 0 \end{aligned} \tag{III.33}$$

Turbulence fields are thus represented by a summation of sinusoidal functions with random phases. $\mathbf{A}_{\mathbf{k}}$ is the amplitude associated to the mode \mathbf{k} . A sufficient condition to ensure a divergence-free field verifies $\mathbf{k} \cdot \mathbf{A}_{\mathbf{k}} = 0$. Originally, these idea was introduced by Kraichnan [114] to produce a Gaussian energy spectrum. For instance, Huang *et al.* [102] proposed to adjust the amplitude of each mode, in order to make the energy spectrum fit any chosen shape. For these formulations,

the divergence-free formulation was practically achieved by taking \mathbf{A}_k of the form $(\mathbf{V} \times \mathbf{k})B_k$, with \mathbf{V} a vector and B_k an amplitude. However, an alternative approach has been proposed by Yu *et al.* [178]. Instead of applying the Fourier decomposition directly on the velocity field, as in Eq. (III.33), the velocity potential is obtained as a summation of sinusoidal weighted functions. By definition of the curl, the divergence-free property is therefore ensured.

Bechara *et al.* [38] developed a Stochastic Noise Generation and Radiation (SNGR) model to be used as a source term in linearized Euler computations. The key idea is to include a random phase term ψ in order to compute an isotropic, homogeneous, and more particularly here, a random velocity field at each time step of the simulations. The adequate temporal correlation is obtained by a filtering in the frequency domain in [38]. The idea of convected turbulent structures is evoked by Bechara *et al.* [38]. However, it is set up explicitly by Bailly *et al.* [33]. In order to allow the convection of the turbulent structures, a convection term is considered in Eq. (III.33). In practice, ω is replaced by $\mathbf{k} \cdot \mathbf{U} + \omega_{random}$. In case of a pure convection, *i.e.* under the frozen turbulence assumption, $\omega_{random} = 0$. First approaches using SNGR-like notations were devoted to the study of the jet noise. In these approaches [33], the amplitude of a particular velocity fluctuation was defined such as: $\mathbf{A}_k = \sqrt{E(k)\Delta k}\boldsymbol{\sigma}$, with $\boldsymbol{\sigma}$ a unit vector perpendicular to \mathbf{k} . Usually, the wavevector \mathbf{k} is sorted randomly over a sphere. A similar approach has been proposed by Niedoba *et al.* [136], as an inlet boundary for LES.

Another scope of application for SNGR methods, is turbulence-airfoil interaction noise. It has been highlighted in Section II.1.2, that the upwash velocity component plays the major role in the noise generation process. That is why, first calculations have only considered single velocity component driven solutions with a turbulence field invariant along the upwash and spanwise directions, as in Clair *et al.* [63], where the amplitude is defined via the autocorrelation spectrum of the upwash velocity component, *i.e.* $u'_\eta \propto \sqrt{\varphi_{\eta\eta}^{2D}(k_\xi, 0)\Delta k_\xi 2\pi/L_z}$. Gill *et al.* [84] have considered two and three velocity-components approaches. The two-velocity approach with a streamwise and upwash variations of the turbulence field is of particular interest for cascade configurations. Gill *et al.* have compared the different turbulent structures on isolated airfoils of different thickness and camber. The single velocity approach has shown to be sufficient for airfoils of a small camber or angle of attack. It is interesting to note that in these approaches the wavevector \mathbf{k} is not sorted randomly over a sphere of a radius k . In fact, each wavevector component, *i.e.* wavenumber k_i , is explicitly defined. This choice allows to compute turbulent fields in presence of periodic boundary conditions. For example, Gill *et al.* [84] and Rigall *et al.* [157] have considered discrete values of the spanwise wavenumber: $k_z = 2n\pi/L_z$, in order to ensure the spanwise periodicity.

Turbulence cascade applications have also been studied in the literature. Hixon *et al.* [98] have proposed a formulation to inject gusts in an Euler solver called BASS [97]. The turbulent gusts interact with rectilinear cascades configurations at zero-angle of attack. Preliminary computations have also been performed on cambered NACA airfoils [98]. As for annular configurations, several methods based on linearized Euler equations have been developed in the framework of a NASA benchmark proposed by Namba *et al.* [134], which consists of an annular flat plate cascade placed in a uniform axial mean flow. This test case was investigated by Hixon *et al.* [99] using the BASS code. Computing the acoustic response of an annular cascade placed in an

non-uniform swirling mean flow was studied by Atassi [27]. His method is based on the resolution of linearized Euler equations written in the frequency domain. He has accounted for 3-velocities and 3-components gusts. However, the radial velocity implemented had simply a shape of the form $\sin(\pi(r - r_{min})/(r_{max} - r_{min}))$, to ensure the zero velocity conditions at the walls. A similar methodology, when the radial velocity component is neglected, was obtained by Sescu *et al.* [161] and Hixon *et al.* [99]. The studies previously mentioned primarily focused on the prediction of a particular mode transmission. The ability to reproduce broadband noise spectra has been demonstrated by Atassi *et al.* [26, 24, 25]. These broadband noise calculations were performed on the NASA SDT (low count) configuration (see Section II.3.2).

One can notice from this overview of Fourier modes literature, that SNGR methods developed for turbulence-airfoil interaction noise often focus on accurately representing the upwash velocity component to the leading edge. In that case, axial and azimuthal velocity components are constructed such as the fluctuating velocity field is divergence-free.

Synthetic turbulence developed at ONERA for CAA calculations

Synthetic turbulence at ONERA has been studied and already implemented in the sAbrinA code (see Section II.2.1), which solves in the time domain the Euler equations written in perturbation. Tam's boundary conditions [167] were implemented, both to allow the exit and the entrance of fluctuations in the domain without generating spurious noise sources nor numerical reflections (see Section II.2.1). Broadband noise calculations have been performed in the framework of the European project FLOCON [6], dealing with an isolated baseline and serrated airfoil [62, 63]. Clair *et al.* [63, 61] have highlighted the importance of taking into account a non-uniform mean flow as close as possible to the real flow, instead of a uniform axial flow. In these computations, the synthetic turbulence is based on Kraichnan [114] and Bailly *et al.* [32], although only the upwash velocity component is represented. All the Fourier modes have the shape $u'_\eta(k_\xi, k_z) \propto 2\sqrt{\varphi_{\eta\eta}^{2D}(k_\xi, k_z)\Delta k_\xi\Delta k_z}$. However, for the NACA computations, the turbulence structure was limited to parallel gusts, *i.e.* $\varphi_{\eta\eta}^{2D}(k_\xi, 0)$. Although 3-wavenumber mode propagation has been studied by Clair in an annular configuration [63, 61, 143], broadband noise calculations were only performed considering planar turbulence structures: $u'_\eta(k_\xi, k_r) \propto 2\sqrt{\varphi_{\eta\eta}^{2D}(k_\xi, k_r)\Delta k_\xi\Delta k_r}$ [63, 61, 143]. Indeed, it would have been too expensive at that time to carry on a computation accounting for all 3 wavenumbers. The particularity of the planar turbulence simulation performed by Clair and Polacsek lies in the fact that the formulation accounts for the non-zero stagger angle and periodic boundary condition, similarly to [99]. These broadband noise predictions were achieved on an unloaded annular configuration for which the swirl was taken into account. The same configuration has been studied by Atassi and Vinogradov [26]). Reboul *et al.* [154] and Cader *et al.* [47] applied the previous methodology to assess realistic turbofan stages, respectively the NASA SDT benchmark (see Section II.3.2) and the AneCom AeroTest Rotor 1 (ACAT1) turbofan model [133]. In particular, they accounted for spanwise variation of the turbulence properties (intensity and length scale) and a realistic mean flow obtained from RANS simulations. Noise reduction achieved with serrated leading edges was also predicted using this methodology by Reboul *et al.* [154], and Polacsek *et al.* [144] in the framework of the European

project TurboNoiseBB [13]. Cader *et al.* [47] proposed to extend the 1-velocity driven turbulence with 2 wavenumbers to 3 wavenumbers turbulence fields. However, the generation process has shown to be very CPU demanding due to additional nested loops over the azimuthal coordinates and the azimuthal wavenumbers. Therefore, no acoustic post-processing was provided at that time. Moreover, as it will be shown in Chapters III.3 and III.4, this solution leads to very high fluctuations along the streamwise component in the low-frequency range. This might alter the numerical acoustic solution in case of thick airfoils.

III.2.2 Digital filtering

$$\left\{ \begin{array}{l} \mathbf{u}' = \nabla \times \psi \\ \forall i \in \llbracket 1, 3 \rrbracket, \psi_i = \int_{\Omega_s \in \mathbb{R}^3} A(\mathbf{X})G(\mathbf{X} - \mathbf{X}')W_i(\mathbf{X})d\mathbf{X}' \\ \forall \mathbf{X} \in \Omega_s, \text{div}(\mathbf{u}'(\mathbf{X})) = 0 \end{array} \right. \quad (\text{III.34})$$

Equation (III.34) presents the core idea of the digital filter family of methods. Although in practice the integral is replaced by a sum, the analytical integral notation has been kept here, in order to emphasize the fact that a white noise W_i is convoluted with a filter kernel G . A denotes the amplitude of the signal. The idea of filtering a white noise has been originally proposed by Careta *et al.* [51] to generate two dimensional HIT fields. By modeling the potential flow vector, the method is by definition divergence-free. A Langevin's equation, originally derived to describe motion of Brownian particles, is used to define the evolution of the turbulence field. The idea of filtering a white noise to obtain a synthetic Gaussian turbulence field for aeroacoustic applications was particularly studied by Ewert [72], who developed his Random Particle-Mesh (RPM) method. He derived the equations for a n-dimensional space. Equation (III.34) presents the 3D simplified solution. An extension to non-Gaussian spectra has been proposed by Siefert *et al.* [165] which consists in a summation of Gaussian kernels. In the aeroacoustic field, one should also mention Dieste *et al.* [69], who applied the digital filter method to study turbulence interaction noise with a flat plate. Their study provides filters precisely derived in order to obtain turbulence energy spectra such as von Karman or Liepmann. Moreover, they compared frozen turbulence hypothesis with a temporally evolving turbulence thanks to Langevin's equation.

Turbofan applications were also studied by means of the RPM method, extended to the suited fRPM-fan method [113, 112]. In particular, Wohlbrandt *et al.* [175] investigated how to take into account the effect of cyclostationarity. The synthetic turbulence generation process is coupled with a CAA code, PIANO, solving the linearized Euler equations [11]. These two-dimensional simulations were performed at midspan on the NASA SDT test rig (see Section II.3.2). The 2D approach was extended by Kissner *et al.* to 3D turbulent fields generation and applied on the turbofan test rig ACAT1 [112]. However, 3D turbulence calculations being very CPU demanding, the injection is only performed on one third of the span. Moreover, it has to be noted that the generation cost of the turbulence is reduced by taking a bigger time step for the RPM process than the one used for the CAA computation. The boundary conditions represent also a major challenge of these simulations, since the RPM methodology does not intrinsically take into account walls or periodicity. Therefore, particular treatment has to be applied at the limits of the source domain

to avoid spurious noise sources. The authors mentioned that contrary to simulations with 2D turbulence, the 3D cases were solved with the non-linear version of the PIANO code, although, this choice was driven by stability considerations rather than an influence on the generation of acoustic sources.

Finally, it has to be noted, that RPM methods usually require the discretization of the mean flow streamlines, which makes this noise prediction approach a mix between Lagrangian framework for the turbulence motion and Euler usual description for the noise sources computation and propagation. In that regard, it should be mentioned that an Eulerian divergence-free approach has been proposed by Cozza *et al.* [64].

III.2.3 Synthetic eddies methods

$$\left\{ \begin{array}{l} \mathbf{u}' = \nabla \times \psi \\ \forall i \in \llbracket 1, 3 \rrbracket, \psi_i = \sum_e A_{e,i} f_{e,i}(\mathbf{r} - \mathbf{r}_e) \end{array} \right. \quad (\text{III.35})$$

An alternative strategy for describing and generating turbulent flows has also been proposed. The key idea is based on the well-known Synthetic Eddy Method (SEM) is to consider the turbulent field as a sum of individual vortices. A generic form of such a turbulence field is given by Eq. (III.35), where the summation operation is performed over the eddies "e". $A_{e,i}$ is the amplitude of a given eddy and $f_{e,i}$ a function describing the shape of a given eddy, usually Gaussian or Mexican hat-like. From the initial study conducted by Jarrin *et al.* [105], who proposed three-dimensional synthetic turbulence to feed LES from RANS simulations, Poletto *et al.* [146] adapted the formulation to generate divergence-free fields. The divergence-free solution is derived by applying the methodology introduced by Jarrin to the vorticity instead of the velocity. The solution written in terms of velocity is analytical obtained by solving a Poisson equation under the incompressible flow hypothesis. Another way of achieving divergence-free turbulence fields is to model the vector potential. This approach was proposed by Sescu *et al.* [160] for aeroacoustic calculations. Hainaut *et al.* [93] proposed also a method based on the vector potential, in order to inject localized vorticity sources in the LEE code PIANO. They studied leading edge interaction noise. However, the limitation to 1D von Karman spectra leads to an overestimation of the decay slope at high frequencies for airfoils with an angle of attack. Kim and Haeri [108] proposed a way of extending the generation method to construct particular velocity spectra by superimposing various eddies. 15 parameters are taken into account for the definition of the field. A gradient-based approach is used to obtain a HIT following the von Karman spectrum. Their methodology handle periodic boundary conditions by duplicating the turbulence field adequately depending on the periodic distance of the CAA computations. Divergence-free condition is preserved since it is associated to the definition of an individual eddy. Finally, the synthetic turbulence field obtained by Kim and Haeri is applied to study turbulence-airfoil interaction noise.

In the SEM family, the advanced digital filter proposed by Gea-Aguilera *et al.* [79, 14] can be included. Although the mathematical framework corresponds to digital filtering, the numerical implementation is similar to the synthetic eddy method approach. The interesting feature of this approach is that less parameters are needed to reproduce a particular turbulence spectrum than in

[108]. This new approach is compared to Fourier modes in [79] and [80], to assess turbulence-airfoil interaction noise. Gea-Aguilera *et al.* also account for cyclostationarity in [81]. This work has been also extended to study serrated leading edges impinged by a 3D anisotropic turbulence [15]. Gea-Aguilera's formulation relies on a superposition of either isotropic or anisotropic Gaussian eddies, which implies that a set of parameters depending on the Mach number has to be derived for each simulation. Shen *et al.* [163] have proposed a new technique called Random Eddy Superposition (RES) which provides the general form of an anisotropic filter instead of relying on the Gaussian superposition. This work has been generalized in [164], and it is referred to as Direct anisotropic filter (DAF) method. In particular, it has focused on the link between isotropic and anisotropic filters and the exact derivation for Liepmann and von Karman spectra.

III.2.4 A few words about challenges in synthetic turbulence generation

From the previous non-exhaustive overview, one may notice that generating three-dimensional turbulence is still a challenging issue, in particular for turbulence-airfoil interaction noise studies on industrial applications. Recent works in Fourier modes [84, 47], RPM [112], and SEM [14] allowed the generation of 3D stochastic fields, while taking into account various turbulence properties (and other costly cyclostationarity, anisotropy,...). However, the ability of these approaches for industrial configurations remains non-trivial, whether in their use in CAA codes (RPM usually requires a dedicated mesh following the streamlines) or in the generation process (SEM requires several parameters to be optimized in order to recover a given spectrum). That is why, the classical SNGR framework with much more simpler Fourier-modes decomposition remains attractive and is adopted in this work for assessing full 3D configurations. The purpose of the following chapter is to derive in detail 1D, 2D, and 3D turbulence fields following approach used by Gill *et al.* [84] and previous work at ONERA on synthetic turbulence [63, 154, 47, 144]. The developments will focus on the way of enforcing a divergence-free field while taking into account simultaneously periodic and wall boundary conditions. As a first step, the generation approach will be presented in a Cartesian coordinate system in order to comply with the geometry of the rectilinear cascade from the InnoSTAT project (see Section II.3.1). A particular attention will be paid to boundary conditions: both periodicity and solid wall. Thus, the way of taking into account these boundary conditions should comply with the divergence-free conditions, in order to avoid spurious noise sources in the CAA computations. Subsequently, the generation of a three-dimensional turbulence in cylindrical coordinate system will be discussed in Chapter III.4 for turbofan applications.

III.3 Development of a 3D Fourier-mode synthetic turbulence in Cartesian coordinates

All the numerical applications in this chapter, are performed with the following flow parameters: $U = 102 \text{ m} \cdot \text{s}^{-1}$, $\text{TI} = 5 \%$, and $L_l = 8 \text{ mm}$.

III.3.1 ($k_\xi, k_z = 0$) turbulence structure

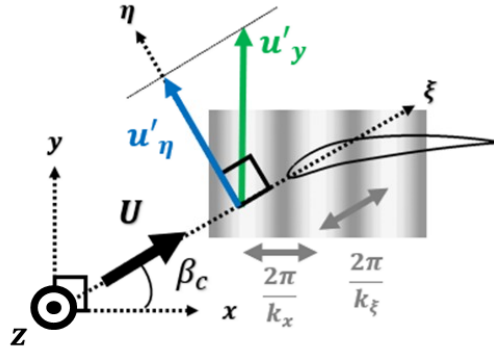


Figure III.3: Coordinate systems with associated wavenumbers and involved turbulent velocities for turbulence structures lying in the plane (k_ξ, k_z).

First of all, let us consider the simplest turbulence field for 3D geometries, namely parallel gust, for which $k_z = k_y = 0$, as illustrated in Fig. III.3. The divergence free condition leads to the simple condition $\partial u'_x / \partial x = 0$. This is ensured by setting u'_x equal to zero so that the overall turbulence velocity is driven by the one-component velocity u'_y . To recover the prescribed normal velocity, u'_η , we set $u'_y = u'_\eta / \cos(\beta_c)$. The angular frequency is independent of the considered reference frame, therefore $k_x = k_\xi / \cos(\beta_c) = \omega / U_x = \omega / (U \cos(\beta_c))$. The phase term simplification $k_\xi \xi = k_x x$ is obtained considering a flat plate aligned with the mean flow (all points of the flat plate being at a location $\eta = 0$, whereas, in the CAA, the airfoil thickness is considered. More details can be found in [61] (pages 132-134). The spatial discretization step is given by $\Delta k_{\xi,l} = \cos(\beta_c) \Delta k_{x,l}$ which can be associated with the angular frequency discretization through $\omega_l = 2\pi l \Delta f$. This equation allows to generate L modes equally distributed from $f_{min} = \Delta f$ to $f_{max} = L \Delta f$. For each mode l , a random phase ψ_l is also introduced. The autocorrelation spectrum of the upwash velocity component is defined by $\varphi_{\eta\eta}^{2D}(k_\xi, 0)$, refer to $\varphi_{\eta\eta}^{2D}(k_\xi, k_z)$ definition

in Table III.1. Since, the wavenumber k_z is set to zero, the turbulence spectrum has also to be weighted by $\Delta k_z = 2\pi/L_z$, in order to obtain the prescribed magnitude of the injected turbulence as mentioned in [63].

$$u'_y(\mathbf{X}, t) = \frac{2}{\cos(\beta_c)} \sum_{l=1}^L \sqrt{\varphi_{\eta\eta}^{2D}(k_{\xi,l}, 0) \Delta k_{\xi} \frac{2\pi}{L_z}} \cos(k_{x,l}x - \omega_l t + \psi_l) \quad (\text{III.36})$$

Since the synthetic turbulence defined by Eq. (III.36) depends only on the k_x wavenumber, the numerical results match exactly the analytical solution as depicted in Fig. III.4. Here, the 2D spectra $\varphi_{\eta\eta}^{2D} = \int \varphi_{ii}^{2D} dk_{\eta}$ multiplied by Δk_z are compared, since the wavenumbers along the spanwise direction are undefined, and thus set to zero.

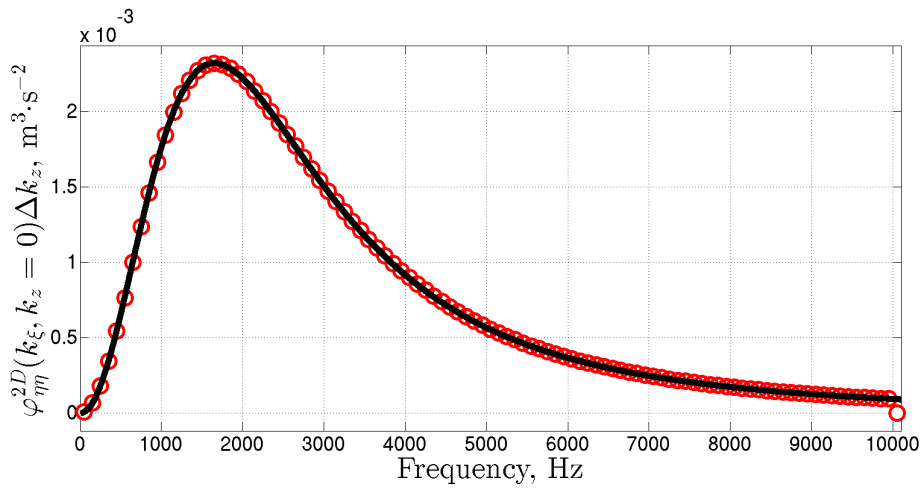


Figure III.4: Analytical spectrum of the upwash velocity component **—** and synthetic turbulence spectrum **—○—**, obtained with $\Delta f = 1$ Hz and averaged over 250 realizations.

III.3.2 (k_{ξ}, k_z) turbulence structure

For (k_{ξ}, k_z) turbulence, the same geometry and notations than previously are used as illustrated by Fig. III.3. The only difference is that the wavenumber k_z is no more equal to zero. Instead, the wavenumbers along the z direction are discretized following $k_{z,n} = n\Delta k_z$. Now, $L \times N$ angular phases ψ_{ln} are randomly selected. Fig. III.5 validates the correct implementation of this spanwise varying turbulence,

$$u'_y(\mathbf{X}, t) = \frac{2}{\cos(\beta_c)} \sum_{l=1}^L \sum_{n=-N}^N \sqrt{\varphi_{\eta\eta}^{2D}(k_{\xi,l}, k_{z,n}) \Delta k_{\xi} \Delta k_z} \cos(k_{x,l}x + k_{z,n}z - \omega_l t + \psi_{ln}) \quad (\text{III.37})$$

even if the k_z variation gives rise to statistical errors in PSD spectrum. Here, the comparison is performed on the 1D spectrum: $\varphi_{\eta\eta}^{1D}(k_{\xi}) = \int \varphi_{\eta\eta}^{2D}(k_{\xi}, k_z) dk_z$, since a single 1-point probe is required under the frozen turbulence assumption.

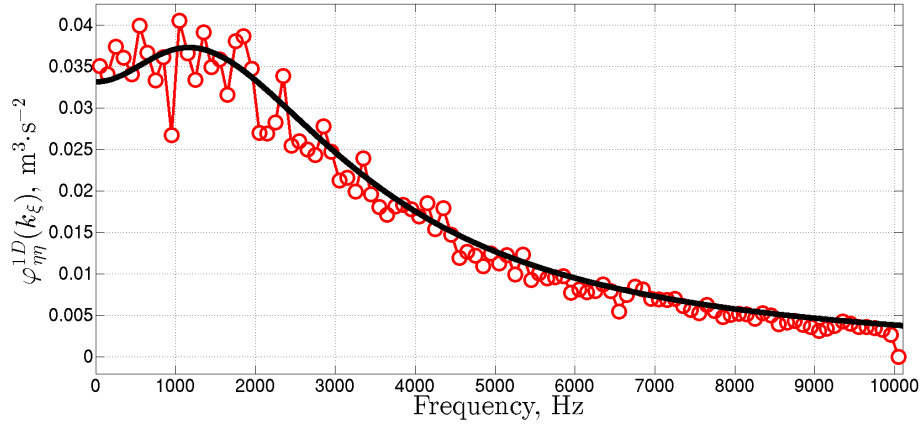


Figure III.5: Analytical spectrum of the upwash velocity component — and synthetic turbulence spectrum —○—, obtained with $N = 30$, $\Delta k_z = 2\pi/L_z$, $\Delta f = 1$ Hz, and averaged over 250 realizations.

III.3.3 ($k_\xi, k_\eta, k_z = 0$) turbulence structure

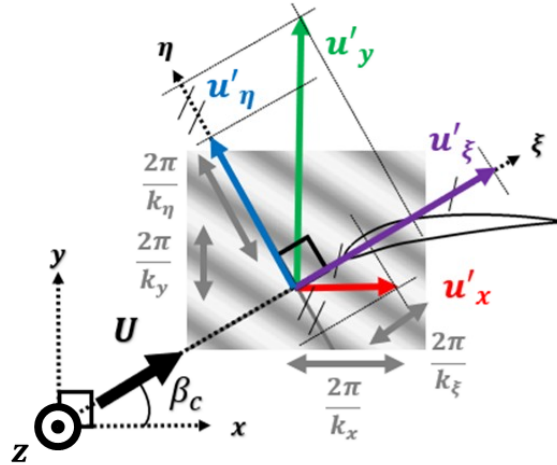


Figure III.6: Coordinate systems with associated wavenumbers and involved turbulent velocities for turbulence structures lying in the plane ($k_\xi, k_\eta, k_z = 0$).

The purpose of the structure ($k_\xi, k_\eta, 0$), is to take account for the pitchwise variations that should produce significant cascade effects in such rectilinear configurations. Fig. III.6 is helpful to follow the discussion. There are several ways to derive the equations for the injected velocities (u'_x, u'_y) or (u'_ξ, u'_η) depending on the coordinate system. Two of them are listed below. Contrary to the (k_ξ, k_z) turbulence for which the spectrum was integrated over k_η , the summation is explicitly defined here. Consequently, the u'_η component of the velocity is no more independent of the k_η wavenumber. To ensure a divergence free solution, a second velocity component must be considered and satisfies,

$$\frac{\partial u'_\xi}{\partial \xi} + \frac{\partial u'_\eta}{\partial \eta} = 0 \quad (\text{III.38})$$

Consequently, u'_ξ is defined by $u'_\xi = -k_\eta/k_\xi u'_\eta$, and furthermore, $\varphi_{\xi\xi}^{3D}(k_\xi, k_\eta, k_z = 0) = \varphi_{\eta\eta}^{3D}(k_\xi, k_\eta, k_z = 0)k_\eta^2/k_\xi^2$. The spectrum along the ξ axis is also correctly prescribed. Turbulence equations can also be obtained starting from the energy spectrum $E(k)$, as more usually done in SNGR models [38],

$$\mathbf{u}'(\mathbf{X}, t) = 2 \sum_{k=1}^K \sqrt{E(k^\perp) \Delta k^\perp} \frac{2\pi}{L_z} \cos(\mathbf{k}_k^\perp \cdot \mathbf{X} - \omega_k + \psi_k) \boldsymbol{\sigma}_k \quad (\text{III.39})$$

where k^\perp is defined such as $\mathbf{k}^\perp = \mathbf{k} - \mathbf{k} \cdot \mathbf{k}_z \mathbf{z}$, $\omega_k = \mathbf{k}_k^\perp \cdot \mathbf{U}$ and $\boldsymbol{\sigma}$ is a unit vector such as $\boldsymbol{\sigma} \cdot \mathbf{k}^\perp = 0$. Eq. (III.39) describes the discretized velocity for K modes distributed over a disk. As for $(k_\xi, k_z = 0)$ turbulence, a factor $2\pi/L_z$ has to be taken into account to recover the expected magnitude of the spectra. However, the turbulence modes are mapped on a rectangular box in the wavenumber space in the present work. This discretization proposed by Gill *et al.* [84] represents an original variant to the classical SNGR formulation [38, 136]. The wavenumbers relations are $k_{\xi,l} = 2\pi l \Delta f / U = k_{\xi,l} = \cos(\beta_c) k_{x,lm} + \sin(\beta_c) k_{y,m}$ and $k_{\eta,lm} = -\sin(\beta_c) k_{x,lm} + \cos(\beta_c) k_{y,m}$, which can be deduced from Fig. III.6.

$$\mathbf{u}'(\mathbf{X}, t) = 2 \sum_{l=1}^L \sum_{m=-M}^M \sqrt{\frac{E(\sqrt{k_{\xi,l}^2 + k_{\eta,lm}^2})}{\pi k}} \Delta k_\xi \Delta k_\eta \frac{2\pi}{L_z} \cos(k_{\xi,l} \xi + k_{\eta,lm} \eta - \omega_l t + \psi_{lm}) \boldsymbol{\sigma}_{lm} \quad (\text{III.40})$$

A similar equation is derived by Gea-Aguilera *et al.* [80]. The wavenumber decomposition along the spatial directions in Eq. (III.40) easily ensures the periodic boundary condition along the y direction by satisfying $k_{y,m} = \mathbf{k} \cdot \mathbf{y} = m2\pi/L_y$, with m an integer. The formulation coming from the autocorrelation velocity spectra can be recovered considering that $E(k) = \varphi_{\eta\eta}^{3D}(k_\xi, k_\eta, 0)4\pi k^4/k_\xi^2$, $E(k) = \varphi_{\xi\xi}^{3D}(k_\xi, k_\eta, 0)4\pi k^4/k_\eta^2$ and that $\sigma_{\xi,lm} = \pm k_{\eta,lm}/k$, $\sigma_{\eta,lm} = \pm k_{\xi,l}/k$. The gusts are then generated as follows,

$$\begin{aligned} u'_\xi(\mathbf{X}, t) &= -2 \sum_{l=1}^L \sum_{m=-M}^M \frac{k_\eta}{k_\xi} \sqrt{\varphi_{\eta\eta}^{3D}(k_{\xi,l}, k_{\eta,lm}, 0) \Delta k_\xi \Delta k_\eta} \frac{2\pi}{L_z} \cos(k_{\xi,l} \xi + k_{\eta,lm} \eta - \omega_l t + \psi_{lm}) \\ u'_\eta(\mathbf{X}, t) &= 2 \sum_{l=1}^L \sum_{m=-M}^M \sqrt{\varphi_{\eta\eta}^{3D}(k_{\xi,l}, k_{\eta,lm}, 0) \Delta k_\xi \Delta k_\eta} \frac{2\pi}{L_z} \cos(k_{\xi,l} \xi + k_{\eta,lm} \eta - \omega_l t + \psi_{lm}) \end{aligned} \quad (\text{III.41})$$

The numerical implementation is validated for both streamwise u'_ξ and upwash u'_η velocity components as plotted in Fig. III.7. Here, the 2D spectra $\varphi_{ii}^{2D} = \int \varphi_{ii}^{3D} dk_\eta$ multiplied by Δk_z are compared, since the wavenumbers along the spanwise direction are undefined and set to zero.

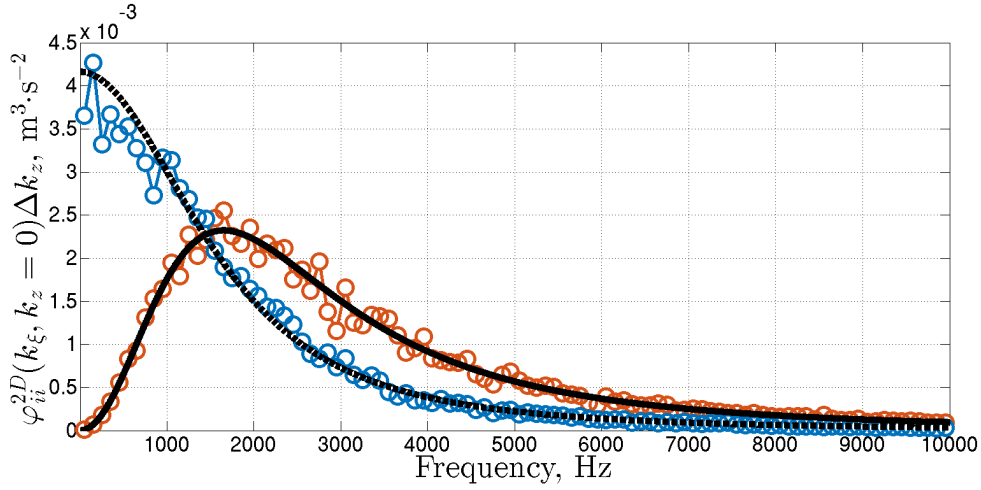


Figure III.7: Analytical upwash — and streamwise spectra. Synthetic upwash —○— and streamwise —○— spectra, with $M = 16$, $L_y = s = 8.5$ cm, $\Delta f = 1$ Hz, and averaged over 250 realizations.

III.3.4 Choice of a modeling suitable for 3D turbulence (k_ξ, k_η, k_z)

Let us see now how to obtain a fully three-wavenumber spectrum. The role of all the wavenumber components on the aeroacoustic response can thus be investigated for both the impinged baseline and serrated airfoils in a cascade configuration. As a preliminary step, it can be useful to underline the failure of a turbulent field built with only two components ($u'_\xi(k_\xi, k_\eta, k_z)$, $u'_\eta(k_\xi, k_\eta, k_z)$) defined as follows,

$$u'_\eta(\mathbf{X}, t) = 2 \sum_{l=1}^L \sum_{m=-M}^M \sum_{n=-N}^N \sqrt{\varphi_{\eta\eta}^{3D}(k_{\xi,l}, k_{\eta,lm}, k_{z,n}) \Delta k_\xi \Delta k_\eta \Delta k_z} \times \cos(k_{\xi,l}\xi + k_{\eta,lm}\eta + k_{z,n}z - \omega_l t + \psi_{lmn})$$

$$u'_\xi(\mathbf{X}, t) = -2 \sum_{l=1}^L \sum_{m=-M}^M \sum_{n=-N}^N \frac{k_{\eta,lm}}{k_{\xi,l}} \sqrt{\varphi_{\eta\eta}^{3D}(k_{\xi,l}, k_{\eta,lm}, k_{z,n}) \Delta k_\xi \Delta k_\eta \Delta k_z} \times \cos(k_{\xi,l}\xi + k_{\eta,lm}\eta + k_{z,n}z - \omega_l t + \psi_{lmn}) \quad (\text{III.42})$$

The autocorrelation spectrum of the u'_ξ component where the summation over the k_η wavenumber has been replaced by an integral is considered.

$$\frac{\partial u'_\xi}{\partial \xi} + \frac{\partial u'_\eta}{\partial \eta} = 0 \Rightarrow \varphi_{\text{pseudo},\xi\xi}^{2D}(k_\xi, k_z) = \frac{\text{TI}^2 U^2 L^2}{4\pi} \frac{1}{k_\xi^2} \frac{(k_\xi^2 + k_z^2)}{(1 + L^2(k_\xi^2 + k_z^2))^{3/2}} \quad (\text{III.43})$$

After integration, Eq. (III.43) is providing a so-called pseudo 2D autocorrelation spectrum. The 1D spectrum should be obtained from an integration over k_z . However, this $\varphi_{\text{pseudo},\xi\xi}^{2D}(k_\xi, k_z)$ tends asymptotically to $1/|k_z|$, which prevents the convergence of the integral with respect to k_z . Moreover, close to low frequencies the solution will diverge due to the $1/k_\xi^2$ term. That is why,

even if in practice u'_ξ is discretized over finite intervals and not over \mathbb{R}^2 , this formulation leads to very high values of the velocity component along the ξ axis. For a flat plate impacted by such gusts, u'_ξ plays absolutely any role and there is thus no issue. However, for a NACA airfoil with a non zero thickness, an issue may appear if the magnitude of u'_ξ is much higher in comparison with what it should be if turbulence had been properly defined. Consequently, the generated gusts have to include a non-zero component u'_z in order to match correctly the three components of the autocorrelation spectra.

Each velocity component is now defined through its spectral tensor following Eq. (III.30) with,

$$u'_i(\mathbf{X}, t) = 2 \sum_{l=1}^L \sum_{m=-M}^M \sum_{n=-N}^N \sqrt{\varphi_{ii}^{3D}(k_{\xi,l}, k_{\eta,lm}, k_{z,n}) \Delta k_\xi \Delta k_\eta \Delta k_z} \cos(k_{\xi,l}\xi + k_{\eta,lm}\eta + k_{z,n}z - \omega_l t + \psi_{lmn}) \quad (\text{III.44})$$

The turbulent field must satisfy the incompressibility condition in order to avoid the creation of spurious sources, which leads to,

$$\frac{\partial u'_x}{\partial x} + \frac{\partial u'_y}{\partial y} + \frac{\partial u'_z}{\partial z} = 0 \Leftrightarrow \sum_i k_i \sqrt{\varphi_{ii}^{3D}} = 0 \quad (\text{III.45})$$

When injecting $\varphi_{\xi\xi}^{3D}$ and $\varphi_{\eta\eta}^{3D}$ in Eq. (III.45), one can deduce that φ_{zz}^{3D} is inadequately prescribed. Namely,

$$\varphi_{\text{pseudo},zz}^{3D}(k_\xi, k_\eta, k_z) = \frac{1}{k_z^2} \frac{\left(k_\xi \sqrt{k_\eta^2 + k_z^2} + k_\eta \sqrt{k_\xi^2 + k_z^2} \right)^2}{k_\xi^2 + k_\eta^2} \varphi_{zz}^{3D}(k_\xi, k_\eta, k_z) \quad (\text{III.46})$$

The shape of the spectrum is strongly altered. Although the component $\varphi_{\eta\eta}$ plays a key role in the aeroacoustic response [15], non-negligible effects might be expected.

For this reason, the most reasonable path to obtain a fully 3D turbulence relies again on the usual SNGR formalism already initiated with $(k_\xi, k_\eta, k_z = 0)$ turbulence,

$$\mathbf{u}'(\mathbf{X}, t) = 2 \sum_{k=1}^K \sqrt{E(k_k) \Delta k} \cos(\mathbf{k}_k \cdot \mathbf{X} - \omega_k + \psi_k) \boldsymbol{\sigma}_k \quad (\text{III.47})$$

Eq. (III.47) is the general form of Eq. (III.39). However, it is not possible to take directly into account the periodic boundary conditions in the y -direction $k_y = m2\pi/L_y$. The present approach generalizes the key idea already probed with the $(k_\xi, k_\eta, 0)$ turbulence structure. The wavenumber space is no more discretized by spherical volumes of an equivalent radius k and thickness Δk , but by rectangular boxes with an elementary volume $\Delta k_\xi \Delta k_\eta \Delta k_z$. The relation between the two discretizations is given by $\Delta k \cong \Delta k_\xi \Delta k_\eta \Delta k_z / (2\pi k^2)$, and the velocity field is expressed as,

$$\mathbf{u}'(\mathbf{X}, t) = 2 \sum_{l=1}^L \sum_{m=-M}^M \sum_{n=-N}^N \sqrt{\frac{E \left(\sqrt{k_{\xi,l}^2 + k_{\eta,lm}^2 + k_{z,n}^2} \right)}{2\pi k^2}} \Delta k_{\xi} \Delta k_{\eta} \Delta k_z \cos(k_{\xi,l}\xi + k_{\eta,lm}\eta + k_{z,n}z - \omega_l t + \psi_{lmn}) \boldsymbol{\sigma}_{lmn} \quad (\text{III.48})$$

A similar decomposition has been proposed by Gill *et al.* [84]. The divergence free condition is now given by $\mathbf{k} \cdot \boldsymbol{\sigma}_{lmn} = 0$, with $\mathbf{k} = (k_{\xi,l}, k_{\eta,lm}, k_{z,n})^T$ and $\boldsymbol{\sigma}_{lmn}$, a unit vector. The direction of the turbulent velocity in Eq. (III.48) has to be determined. This is practically achieved by means of an efficient algorithm, similarly to [38], whose main steps are summarized in Appendix B. Finally, a piece of demonstration is given to show the consistency between this modified energy spectrum formalism proposed here and previous formulations in Appendix C.

III.3.5 Taking into account periodic and wall boundary conditions in case of 3D turbulence fields

The fully 3D turbulence formulation implies that a vertical velocity component u'_z has to be considered. This additional component must be damped near the wall boundaries in order to avoid spurious noise sources, which is a non-trivial issue. A window function $f_w(z)$ is applied to a stochastic velocity field, defined here for a single wavevector component in order to simplify the notations,

$$\mathbf{u}'(\mathbf{X}, t) = A f_w(z) \cos(\mathbf{k} \cdot \mathbf{X} - \omega t + \psi) \boldsymbol{\sigma} \quad (\text{III.49})$$

where A is the initial amplitude of this given fluctuation, such as the velocity tends to zero near the wall boundaries. The chosen windowing, without care on divergence, could be a gate function with half sinusoidal lobes on each side controlled by a length size L_w .

$$\left\{ \begin{array}{l} \forall z \in [z_{min}, z_{min} + L_w], \quad f_w(z) = \frac{1}{2} \left(1 - \cos \left(\pi \frac{z - z_{min}}{L_w} \right) \right) \\ \quad \quad \quad f'_w(z) = \frac{\pi}{2L_w} \sin \left(\pi \frac{z - z_{min}}{L_w} \right) \\ \forall z \in [z_{min} + L_w, z_{max} - L_w], \quad f_w(z) = 1 \\ \quad \quad \quad f'_w(z) = 0 \\ \forall z \in [z_{max} - L_w, z_{max}], \quad f_w(z) = \frac{1}{2} \left(1 + \cos \left(\pi \frac{z - (z_{max} - L_w)}{L_w} \right) \right) \\ \quad \quad \quad f'_w(z) = -\frac{\pi}{2L_w} \sin \left(\pi \frac{z - (z_{max} - L_w)}{L_w} \right) \end{array} \right. \quad (\text{III.50})$$

The function f_w proposed in Eq. (III.50) ensures a smooth, that is without discontinuity, transition to the zero velocity condition at wall boundaries due to the fact that f_w is C^1 (differentiable function whose derivative is continuous) everywhere on the interval $[z_{min}, z_{max}]$ and that $f_w(z_{min}) = f_w(z_{max}) = f'_w(z_{min}) = f'_w(z_{max}) = 0$.

$$\operatorname{div}(\mathbf{u}') = f'_w(z)A \cos(\mathbf{k} \cdot \mathbf{X} - \omega t + \psi) \sigma_z - f_w(z)A \sin(\mathbf{k} \cdot \mathbf{X} - \omega t + \psi) (\mathbf{k} \cdot \boldsymbol{\sigma}) = f'_w(z)A \cos(\mathbf{k} \cdot \mathbf{X} - \omega t + \psi) \sigma_z \neq 0 \quad (\text{III.51})$$

The divergence free property of the synthetic turbulence field is no more ensured when the windowing is introduced as demonstrated by Eq. III.51. The impact on the far-field acoustics will be discussed on the baseline numerical simulations in Part V.

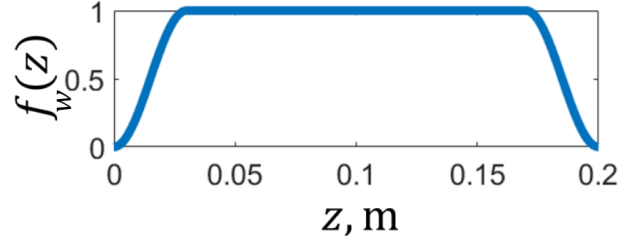
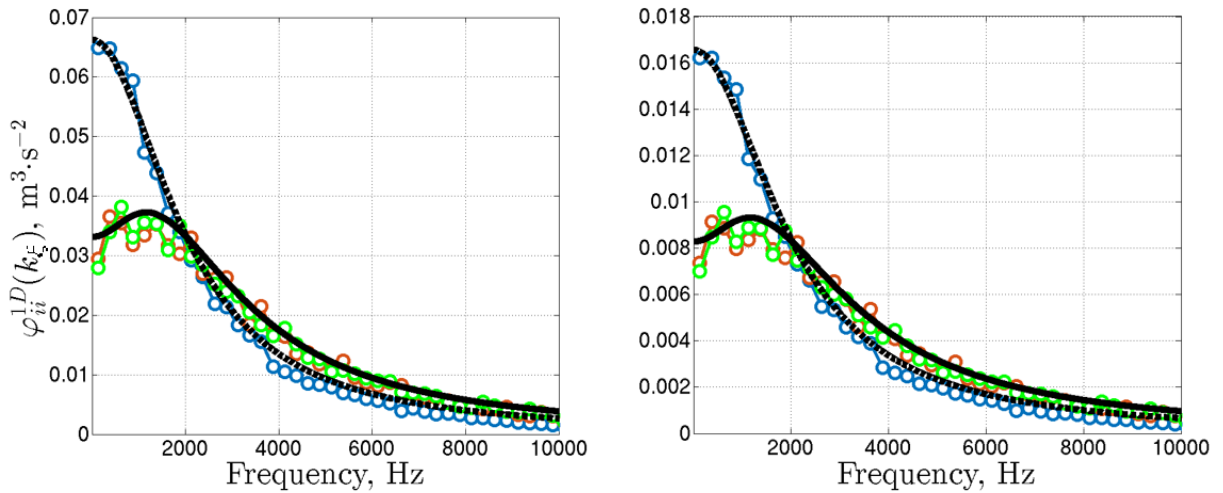


Figure III.8: $f_w(z)$ with $R_w = L_w/L_z = 15\%$ and $L_z = 0.2$ m.

An example of a window function is plotted in Fig. III.8 for a set of given parameters. Figs. III.9a and III.9b show respectively turbulence spectra at $z = 0$ (where $f_w(z) = 1$) and $z = 0.185$ (where $f_w(z) = 0.5$). They demonstrate a good agreement with the theoretical spectra, which validates the adapted formulation relying on the energy spectrum. Since the windowing consists simply in the multiplication of the turbulence fluctuations by a constant, the spectra amplitude at $z = 0.185$ are simply reduced here by a factor 0.5^2 as illustrated in Fig. III.9b.



a) Spectra at location $z = 0.1$ where $f_w(z) = 1.0$. b) Spectra at location $z = 0.185$ where $f_w(z) = 0.5$.

Figure III.9: Analytical upwash, spanwise — and streamwise spectra. Synthetic upwash —○—, spanwise —○—, and streamwise —○— spectra, with $N = 30$, $R_w = 15\%$, $M = 16$, $L_y = s = 8.5$ cm, $\Delta f = 1$ Hz, and averaged over 250 realizations.

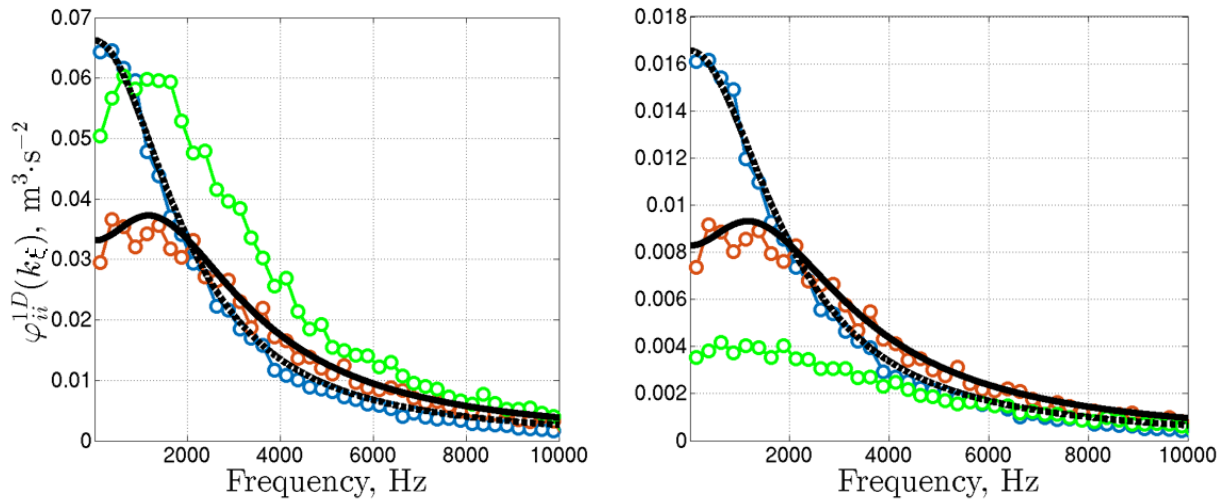
The choice has been made to only modify the component u'_z in Eq. (III.51) which plays a minor role in the noise source generation process: u'_z is replaced by $u'_z - g_w(z)A\sigma_z$, where g_w denotes the correction function.

$$\frac{\partial u'_z}{\partial z} = -f_w(z)A \sin(\mathbf{k} \cdot \mathbf{X} - \omega t + \psi) k_z \sigma_z + f'_w(z)A \cos(\mathbf{k} \cdot \mathbf{X} - \omega t + \psi) \sigma_z - g'_w(z)A \sigma_z \quad (\text{III.52})$$

Consequently, in order to cancel the additional spurious term appearing in Eq. (III.51) the derivative of u'_z is modified by means of a corrective function $g_w(z)$, as defined in Eq. (III.52). Other options would have been to alter all the components of the velocity. However, it would have led to less accurate acoustic predictions, especially, since the spectrum of the perpendicular component to the airfoils, u'_η would have been inevitably modified. Another option could have consisted in shifting phases to obtain a zero velocity at walls. However, it would have led to a complete loss of the spatial correlation and representativeness of turbulence length scales along the spanwise direction. The spatial correlation plays a major role regarding the noise reduction mechanism obtained with a serrated design. After some calculations ensuring $(f_w, g_w) \in C^1$ and specified boundary conditions, refer to Eq. (VI.10) in Appendix D, the following equality must be satisfied,

$$\begin{aligned} & \begin{cases} g_w(z_{min}) = g_w(z_{max}) = 0 \\ g_w(z_{min} + L_w) = g_w(z_{max} - L_w) \end{cases} \Rightarrow \\ & \cos\left(k_x x + k_y y + k_z z_{min} + \frac{k_z L_w}{2} - \omega t + \psi\right) \cos\left(\frac{k_z L_w}{2}\right) \\ & = \cos\left(k_x x + k_y y + k_z z_{min} + k_z L_z - \frac{k_z L_w}{2} - \omega t + \psi\right) \cos\left(\frac{k_z L_w}{2}\right) \end{aligned} \quad (\text{III.53})$$

There are two types of constraints which can be applied on k_z to ensure the equality coming from Eq. (III.53). Firstly, let us consider that $\cos(k_z L_w/2) = 0$, satisfying Eq. (III.53) which gives $0=0$. Under this assumption, $k_z = (2n+1)\pi/L_w$ with $n \in \mathbb{N}$. However, since $k_z \neq \pi/L_w$, as derived in Appendix D, this solution implies that the discretization cannot be uniformly spaced, since one cannot choose whatever integer $n \in \mathbb{N}$. Moreover, if L_w is chosen too small the discretization step tends to become very wide which could affect the precision of the solution. Another possibility is to consider $k_z = 2n\pi/(L_z - L_w)$, for which the left and right handside of Eq. (III.53) become $\cos(k_x x + k_y y + 2n\pi(z_{min} + L_w/2)/(L_z - L_w) - \omega t + \psi) \cos(2n\pi L_w/(2L_z - 2L_w))$. The case $R_w = 15\%$ provides the same envelope as for the non divergence-free scenario, but with a slightly shifted discretization of the k_z wavenumbers, $2n\pi/(L_z - L_w)$ instead of $2n\pi/L_z$. The generated spectra with the new implementation are compared with the analytical solutions in Figs. III.10a and III.10b. There is a good agreement for the streamwise and upwash components for all cases. The spanwise spectra are altered, which is linked to the choice of applying the correction on the u'_z component of the velocity.



a) Spectra at location $z = 0.1$ where $f_w(z) = 1.0$. b) Spectra at location $z = 0.185$ where $f_w(z) = 0.5$.

Figure III.10: Analytical upwash, spanwise — and streamwise spectra. Synthetic upwash —○—, spanwise —○—, and streamwise —○— spectra, with $N = 30$, $R_w = 15\%$, $M = 16$, $L_y = s = 8.5$ cm, $\Delta f = 1$ Hz, and averaged over 250 realizations.

III.4 Fourier-mode synthetic turbulence in cylindrical coordinates

Unless otherwise stated, the spectra are plotted in this chapter using the following parameters: $r_{min} = 0.2$ m, $L_r = 0.2$ m, $\Delta\theta = 40^\circ$, $\Delta f = 1$ Hz, $M = 30$, and $N = 30$. As for the mean flow definition, a simple form is considered: $U_x = 102$ m \cdot s $^{-1}$ and $U_\theta = 0$ m \cdot s $^{-1}$.

III.4.1 3D turbulence field (k_ξ, k_θ, k_r) with two velocity components

A framework to generate 3D turbulence fields for turbofan applications with spanwise varying turbulence and mean flow has been proposed by Cader *et al.* [47]. However, due to calculation cost induced by additional nested loops (azimuthal coordinate and wavenumber), the CAA calculation has not been completed. Optimization techniques have been implemented since then (please refer to Chapter III.5), which would allow such computations in a more reasonable time (days instead of weeks to generate turbulence on some hundred cores). Having only two non-zero components (u'_x, u'_θ) , is very appealing since there is no need to apply a correction on a term along \mathbf{r} (as in Sections III.3.5 and III.4.2). In that case, the divergence-free condition is simply achieved through the term $-k_\eta/k_\xi$ for each mode. Therefore, the solenoidal condition is ensured for any kind of spanwise varying mean flow and turbulence. However, the streamwise component u'_ξ is not accurately prescribed (see discussion in Section III.3.4). The turbulent velocity fields prescribed by Eq. (III.42) in a cylindrical coordinate system are written as:

$$\begin{aligned}
 u'_\eta(\mathbf{X}, t) &= 2 \sum_{l=1}^L \sum_{m=-M}^M \sum_{n=-N}^N \sqrt{\varphi_{\eta\eta}^{3D}(k_{\xi,l}, k_{\eta,lm}, k_{r,n}) \Delta k_\xi \Delta k_\eta \Delta k_r} \\
 &\quad \times \cos(k_{\xi,l}\xi + k_{\eta,lm}\eta + k_{r,n}r - \omega_l t + \psi_{lmn}) \\
 u'_\xi(\mathbf{X}, t) &= -2 \sum_{l=1}^L \sum_{m=-M}^M \sum_{n=-N}^N \frac{k_{\eta,lm}}{k_{\xi,l}} \sqrt{\varphi_{\eta\eta}^{3D}(k_{\xi,l}, k_{\eta,lm}, k_{r,n}) \Delta k_\xi \Delta k_\eta \Delta k_r} \\
 &\quad \times \cos(k_{\xi,l}\xi + k_{\eta,lm}\eta + k_{r,n}r - \omega_l t + \psi_{lmn}) \quad (\text{III.54})
 \end{aligned}$$

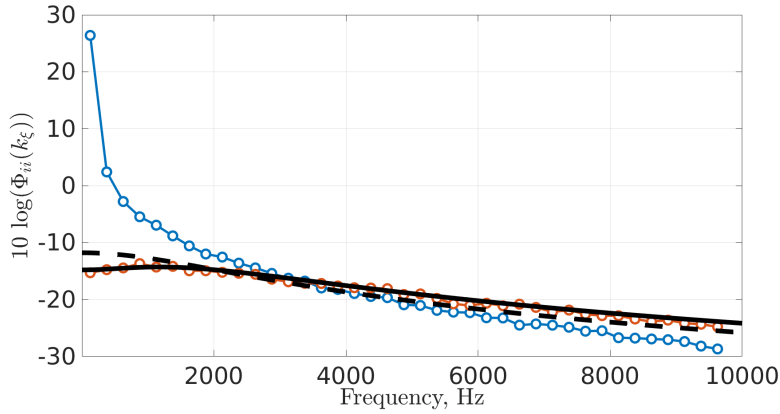


Figure III.11: Turbulence spectra obtained from Eq. (III.54). Analytical upwash — and streamwise - - - spectra. Synthetic upwash —○— and streamwise —○— spectra. Spectra plotted at $r = 0.2$ m and averaged over 250 realizations.

Hence, as shown in Fig. III.11, this method generates a very high amplitude of the velocity spectrum in the streamwise direction, particularly at low frequency due to the k_η/k_ξ term. This is the same issue than for the Cartesian framework presented in Section III.3.4. In case of flat plates without any camber, this would not be a matter. However, in case of real turbofan applications, the streamwise component might create spurious sources in the low frequency part of the acoustic spectrum. In order to tackle the latter issue, several solutions could be considered.

A first idea (1) could consist in limiting the wavenumber integration partially, depending on the frequency. The most obvious solution appears to be the limitation of the ratio k_η/k_ξ by means of a specific ranging to prevent undesirable amplification.

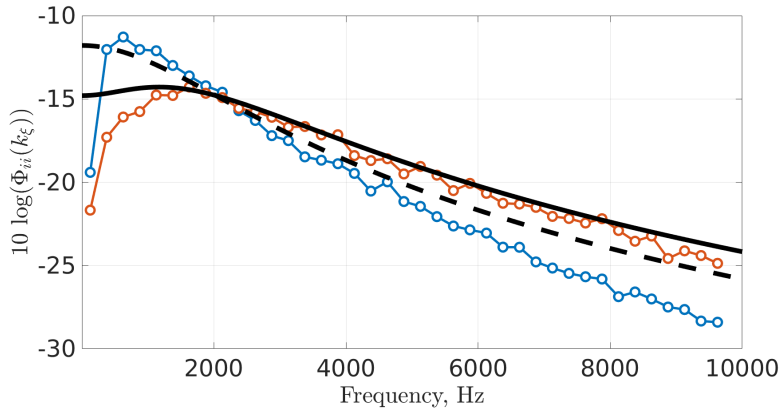


Figure III.12: Turbulence spectra obtained from Eq. (III.54) under the condition: $k_\eta < k_\xi/0.3$. Analytical upwash — and streamwise - - - spectra. Synthetic upwash —○— and streamwise —○— spectra. Spectra plotted at $r = 0.2$ m and averaged over 250 realizations.

Figure III.12 depicts an example of such a solution, obtained through a simple condition: $k_\eta < k_\xi/0.3$. The issue with this technique is that too much energy is lost on the upwash velocity component in the very low frequency range. A correction could be applied to the injected field to compensate for the loss. However, it implies the computation of the corrective term at each frequency of the integrated 1D spectrum of the upwash velocity component, which might increase

the generation time.

Instead of limiting the integration of the k_η wavenumbers as for idea (1), idea (2) limits the summation over the k_r wavenumbers with the constraint: $k_r < k_\xi/0.3$.

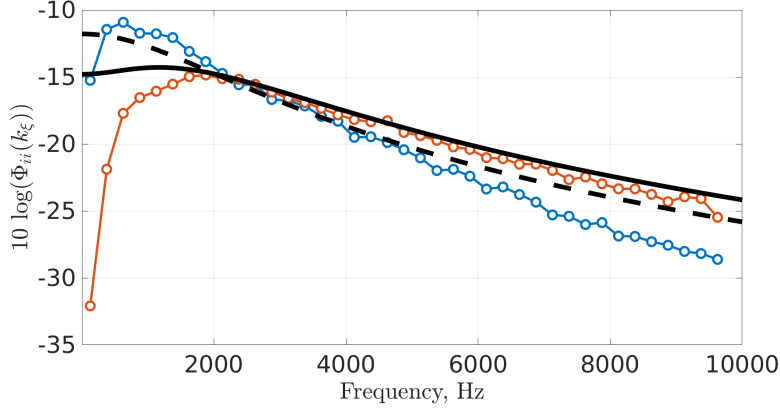


Figure III.13: Turbulence spectra obtained from Eq. (III.54) under the condition: $k_r < k_\xi/0.3$. Analytical upwash — and streamwise spectra. Synthetic upwash —○— and streamwise —○— spectra. Spectra plotted at $r = 0.2$ m and averaged over 250 realizations.

As shown in Fig. III.13, this solution also avoids the peak observed at low frequency in Fig. III.11. The advantages and disadvantages of this alternative method will be discussed later.

The option (3) could consist in splitting the turbulence generation process into two parts.

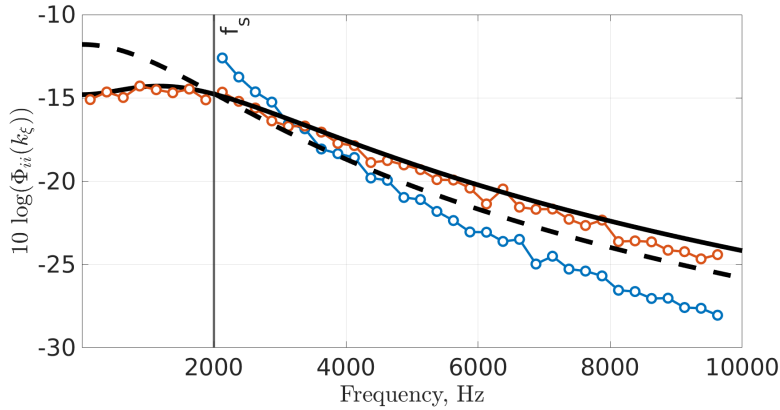


Figure III.14: Turbulence spectra obtained from Eq. (III.54) above the frequency f_s . Below the frequency f_s , the upwash spectrum is computed using $\varphi_{\eta\eta}^{2D}(k_\xi, k_r)$. Analytical upwash — and streamwise spectra. Synthetic upwash —○— and streamwise —○— spectra. Spectra plotted at $r = 0.2$ m and averaged over 250 realizations.

For frequencies in the range f_{min} to f_s , the turbulence would be generated using a shape $\varphi_{\eta\eta}^{2D}(k_\xi, k_r)$ (similarly to the Cartesian case, see Section III.3.2). From f_s to f_{max} , the turbulence field would be computed using the complete 3D spectrum $\varphi_{\eta\eta}^{3D}(k_\xi, k_\eta, k_r)$. This alternative choice is illustrated in Fig. III.14. The huge drawback of this option, is that it neglects the cascade effect which consists in the filtering of the k_η wavenumbers at low frequency [41].

The drawbacks of the three methods mentioned above are summarized in the Table III.2.

Type of calculation:	Overall noise (baseline)	Relative noise reduction (from serrations)
(1) limiting k_η	(A)	(B)
(2) limiting k_r	(C)	(D)
(3) Modification around f_s	(E)	(F)

Table III.2: Different uses cases for two-velocity driven 3D turbulence generation techniques

Some comments for the different cases, (A) to (F), are listed below.

- (A) A lack of energy in low frequencies may lead to an underestimation of the noise sources.
- (B) No significant influence is expected on the relative noise reduction since the transverse wavenumber k_η does not play any role in the theory of serrations. However, the difference in baseline spectra may change the Δ OAPWL estimations, since the contributions of the different parts of the spectrum are modified.
- (C) In Amiet's theory, under certain hypothesis discussed in Section II.1.2.1 and [19, 63]), the contribution of the spanwise wavenumber k_r is negligible.
- (D) A loss of accuracy in low frequencies is expected as concerns the relative noise reduction since the mechanism depends on the radial correlations of turbulence.
- (E) All the energy is preserved. However, since there is no variation of the turbulent field along the cascade direction, a loss of accuracy in low frequency is expected. Indeed, the cascade effect cannot be properly taken into account.
- (F) The relative noise reduction should not be influenced much by the loss of the spatial variation along the cascade direction. Indeed, the noise reduction mechanism is driven by the spanwise variation of turbulence, which is preserved here.

III.4.2 3D turbulence field (k_ξ, k_θ, k_r) with three velocity components

Obtaining a three wavenumber spectrum with all the three velocity components (u'_x, u'_θ, u'_r) is much more challenging in the case of turbofan engines. First, periodicity in the azimuthal direction implies that $k_\theta = (2\pi/\Delta\theta)m/r = m_g/r$, with m and $(2\pi/\Delta\theta)$ integers. Consequently, a spanwise dependence of the wavenumbers and velocity directivity σ appears contrary to the Cartesian case. Second, the trick of choosing a particular window function f_w as in the uniform Cartesian case, is not possible anymore, if a radially varying inflow (TI(r), $L_l(r)$, and $\mathbf{U}(r)$) is considered. The loss of this degree of freedom implies that an additional constraint (or correction) has to be applied to obtain a divergence-free turbulent field. It can be described as follows,

$$\mathbf{u}' = A(r) \cos(k_x x + m_g \theta + k_r r - \omega t + \psi) \boldsymbol{\sigma}(r) \quad (\text{III.55})$$

with $\boldsymbol{\sigma}$ denoting a unit vector perpendicular to the wavevector \mathbf{k} .

As for the 3D turbulence in Cartesian coordinates (please refer to Section III.3.5), the corrective functions $g_{w,x}$, $g_{w,\theta}$, and $g_{w,r}$ are applied in order to obtain a divergence-free field starting from Eq. (III.55). The key idea is to keep the upwash velocity component u'_η unchanged, therefore: $g_{w,\xi} = g_{w,x} / \cos(\beta_c(r)) = g_{w,\theta} / \sin(\beta_c(r)) \Rightarrow g_{w,\theta} = \tan(\beta_c(r)) g_{w,x}$.

$$\begin{aligned} \mathbf{u}' &= (\mathbf{u}'_\xi - \mathbf{g}_{w,\xi}) + \mathbf{u}'_\eta + (\mathbf{u}'_r - \mathbf{g}_{w,r}) \\ \Leftrightarrow \mathbf{u}' &= (\mathbf{u}'_x - \mathbf{g}_{w,x}) + (\mathbf{u}'_\theta - \mathbf{g}_{w,\theta}) + (\mathbf{u}'_r - \mathbf{g}_{w,r}) \end{aligned} \quad (\text{III.56})$$

The divergence of the corrected velocity defined by Eq. (III.56), can now be calculated.

$$\begin{aligned} \text{div}(\mathbf{u}') &= -A(r) \sin(\Delta) (\mathbf{k} \cdot \boldsymbol{\sigma}) \\ &\quad + \frac{1}{r} \frac{\partial r A(r) \sigma_r(r)}{\partial r} \cos(\Delta) - \frac{1}{r} \frac{\delta(r)}{\partial r} r A(r) \sigma_r(r) \sin(\Delta) - \frac{1}{r} \frac{\partial(r g_{w,r})}{\partial r} - \frac{\partial g_{w,x}}{\partial x} - \frac{1}{r} \frac{\partial g_{w,\theta}}{\partial \theta} \\ \Rightarrow \text{div}(\mathbf{u}') &= \frac{1}{r} \frac{\partial r A(r) \sigma_r(r)}{\partial r} \cos(\Delta) - \frac{1}{r} \frac{\delta(r)}{\partial r} r A(r) \sigma_r(r) \sin(\Delta) - \frac{1}{r} \frac{\partial(r g_{w,r})}{\partial r} - \frac{\partial g_{w,x}}{\partial x} - \frac{1}{r} \frac{\partial g_{w,\theta}}{\partial \theta} \end{aligned} \quad (\text{III.57})$$

It is expressed by Eq. (III.57), where $\Delta = k_x x + m_g \theta + k_r r - \omega t + \psi = \delta + k_r r + \psi$. It generalizes the Cartesian cases presented in Eq. (III.51). Let us discuss the derivative of the term $\delta = k_x x + m_g \theta - \omega t$. The periodic boundary conditions impose that m only takes discrete values. Two choices remain for the wavenumber discretization: either explicitly define k_x or k_ξ . Both choices implies that a term proportional to $x \times \sin(\Delta)$ or $t \times \sin(\Delta)$ will appear in Eq. (III.57). Yet, to keep a frozen turbulence field, the term $\delta(r)$ should be independent with respect to r . A solution consists in considering a rigid body movement for the mean flow: $\mathbf{U} = \mathbf{U}_x + r \boldsymbol{\Omega} \theta$. This assumption will be criticized later. Equation (III.57) is then multiplied by ζ , with ζ a dummy variable along the spanwise direction and integrated from r_{min} to r_{max} .

$$\int_{r_{min}}^{r_{max}} \frac{\partial \zeta A(\zeta) \sigma_r(\zeta)}{\partial \zeta} \cos(\Delta) d\zeta = \int_{r_{min}}^{r_{max}} \frac{\partial(\zeta g_{w,r})}{\partial \zeta} + \int_{r_{min}}^{r_{max}} \zeta \frac{\partial g_{w,x}}{\partial x} d\zeta + \int_{r_{min}}^{r_{max}} \frac{\partial g_{w,\theta}}{\partial \theta} d\zeta \quad (\text{III.58})$$

Wall boundary conditions are applied at r_{min} and r_{max} . The corrective term $g_{w,r}$ has to be canceled at these locations, in order to avoid a non-zero radial velocity at the walls. After an integration by part applied to the left hand side of Eq. (III.58), supposing A cancels at locations r_{min} and r_{max} , the equality becomes:

$$\int_{r_{min}}^{r_{max}} k_r \zeta A(\zeta) \sigma_r(\zeta) \sin(\Delta) d\zeta = \int_{r_{min}}^{r_{max}} \zeta \frac{\partial g_{w,x}}{\partial x} d\zeta + \int_{r_{min}}^{r_{max}} \frac{\partial g_{w,\theta}}{\partial \theta} d\zeta \quad (\text{III.59})$$

A possible solution to Eq. (III.59) is to set:

$$\begin{cases} g_{w,x} = -\cos(\beta_c) \frac{1}{k_\xi r} \frac{k_r}{r_{max} - r_{min}} \int_{r_{min}}^{r_{max}} [\zeta A(\zeta) \sigma_r(\zeta)] \cos(\Delta) d\zeta \\ g_{w,\theta} = -\sin(\beta_c) \frac{1}{k_\xi r} \frac{k_r}{r_{max} - r_{min}} \int_{r_{min}}^{r_{max}} [\zeta A(\zeta) \sigma_r(\zeta)] \sin(\Delta) d\zeta \end{cases} \quad (\text{III.60})$$

The definition of $g_{w,x}$ and $g_{w,\theta}$ given by Eq. (III.60) satisfies the condition $g_{w,\theta} = \tan(\beta_c(r))g_{w,x}$. In order to define the corrective function $g_{w,r}$, Eq. (III.57) is integrated from r_{min} to r . Then, an integration by part is applied at the left handside.

$$rA(r) \cos(\Delta) \sigma_r(r) + \int_{r_{min}}^r k_r \zeta A(\zeta) \sigma_r(\zeta) \sin(\Delta) d\zeta = \int_{r_{min}}^r \frac{\partial(\zeta g_{w,r})}{\partial \zeta} + \int_{r_{min}}^r \zeta \frac{\partial g_{w,x}}{\partial x} d\zeta + \int_{r_{min}}^r \frac{\partial g_{w,\theta}}{\partial \theta} d\zeta \quad (\text{III.61})$$

From Eq. (III.60), one can deduce that Eq. (III.61) becomes:

$$ru'_r + \int_{r_{min}}^r k_r \zeta A(\zeta) \sigma_r(\zeta) \sin(\Delta) d\zeta - \frac{r - r_{min}}{r_{max} - r_{min}} \int_{r_{min}}^{r_{max}} k_r [\zeta A(\zeta) \sigma_r(\zeta)] \sin(\Delta) d\zeta = \int_{r_{min}}^r \frac{\partial(\zeta g_{w,r})}{\partial \zeta} \quad (\text{III.62})$$

Finally, from Eq. (III.62), $g_{w,r}$ can be obtained:

$$g_{w,r} = u'_r + \frac{1}{r} \left(\int_{r_{min}}^r k_r \zeta A(\zeta) \sigma_r(\zeta) \sin(\Delta) d\zeta - \frac{r - r_{min}}{r_{max} - r_{min}} \int_{r_{min}}^{r_{max}} k_r [\zeta A(\zeta) \sigma_r(\zeta)] \sin(\Delta) d\zeta \right) \quad (\text{III.63})$$

The corrective functions defined by Eqs. (III.60) and (III.63) can be easily computed using for example a rectangular integration.

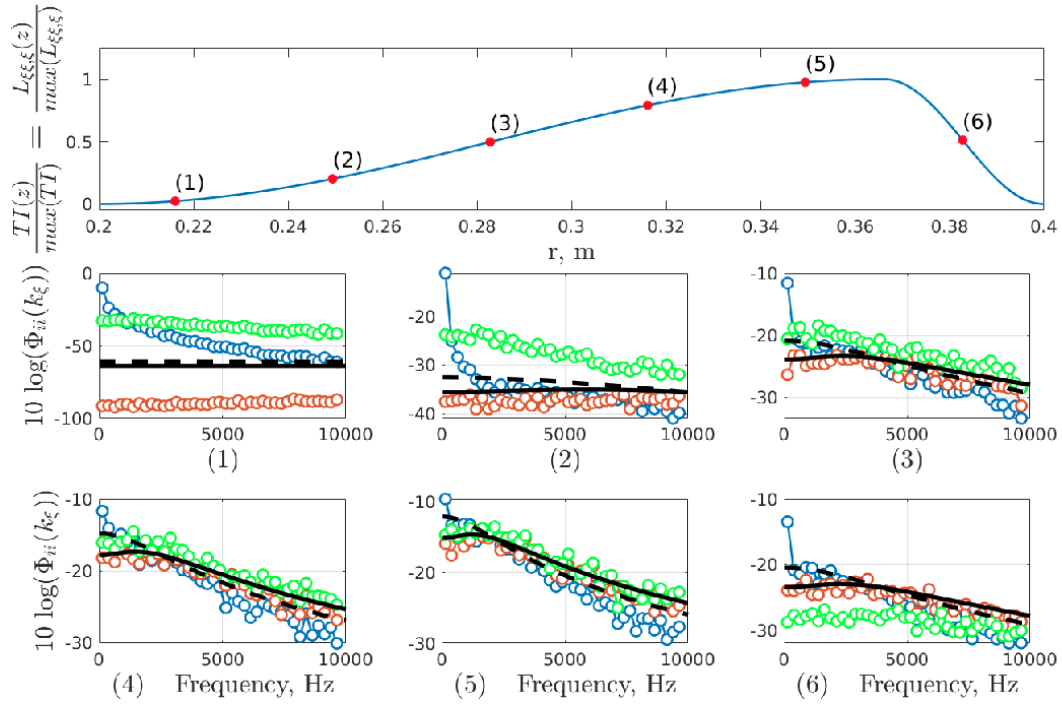


Figure III.15: Turbulence spectra obtained using the method defined in Section III.4.2. As illustrated by this example in the sub-figure at the top, turbulence intensity and integral length scale can be chosen to vary along the span. Analytical upwash, spanwise — and streamwise - - - spectra. Synthetic upwash $\text{-}\circ\text{-}$, spanwise $\text{-}\circ\text{-}$, and streamwise $\text{-}\circ\text{-}$ spectra. In practice, integrals are computed using Riemann sum with $\Delta r \approx 5.5 \times 10^{-4}$ m. Spectra obtained with $\Delta f = 10$ Hz and averaged over 25 realizations.

Figure III.15 compares numerical spectra with analytical solutions. Even if streamwise $\xi\xi$ and spanwise rr components are false due to corrective terms, they should not modify much the overall sound pressure level. Indeed, where the turbulence intensity is the highest, numerical spectra are close to the expected values. Moreover, elsewhere, the level does not seem to exceed much these latter values. This method also reveals a bump at low frequencies along the streamwise direction, although smaller than with the method from the Section III.4.1. Unfortunately, the major drawback of the framework proposed here is that the mean flow is supposed to have a simplified shape: $\mathbf{U} = \mathbf{U}_x + r\boldsymbol{\Omega}\boldsymbol{\theta}$. Whereas in a real turbofan jet engine, the tangential mean flow is drastically different, as shown in Fig. VI.28. However, the methodology proposed here might serve as a basis for future synthetic turbulence developments in case of turbofan applications.

III.4.3 Discussion about 3D turbulence field generation in cylindrical coordinate systems

Although the methodology presented to generate 3-velocity driven turbulence fields is appealing since it generalizes the Cartesian formulation, it is not suited for turbofan configurations apart from academic problems. Indeed, the rigid body movement is a too strong assumption, which is far from the real mean flow observed in turbofan engines.

Consequently, the best choice to generate turbulence in cylindrical coordinate systems appears to be the one or two-velocity driven methodologies, with either two or three wavenumbers depending on the CPU resources, which can be dedicated to turbulence generation. In the case of 3-wavenumbers turbulence fields, the best choice appears to be the limitation of the summation over transverse wavenumbers loops. However, particular attention has to be paid to the physical impact behind each assumption as discussed in Section III.4.1.

III.5 A few words about code optimization

A short discussion about the cost of generating turbulence for CAA simulations in Chapter V.2 is presented here. Several modifications have been made to speed up the generation process. First, the synthetic turbulence generation process has been implemented in a Fortran code. The previous routines used at ONERA for annular geometries [47, 144], have been rewritten in a Cartesian coordinate system. In parallel, several features have been added in order to reduce the CPU generation cost. Turbulence structures having an invariant axis are generated only on a line of the mesh and duplicated afterwards on all the injection plane. Turbulence equations have been decomposed as much as possible using trigonometric identities to factorize operations. In order to speed-up the generation process of a fully 3D synthetic turbulence, some additional optimization has been needed. It has been chosen not to generate turbulence over all the time steps of the simulation similarly to [112]. The missing time steps are recovered by a linear interpolation. For example, in this work, the synthetic turbulence field has been generated one time step over 10 on the baseline computations, still ensuring 40 points per period at the highest simulated frequency. For each 3 channels simulation, the 3D turbulence generation process has required only around 10 hours on one thousand cores, for which the CAA converged solution was obtained in about 30 hours on 1077 cores on the baseline geometry. The ratio between the CPU time dedicated to the turbulence generation and CAA simulations is presented in Table III.3 for various turbulent fields.

Simulations (cf. Chapter V.2)	Generation time of turbulence (on 100 cores)	Ratio with respect to CAA time (with $T_{simulation} = 3\Delta f$)
$(k_\xi, k_z = 0)$	≈ 20 minutes	$< 0.1\%$
(k_ξ, k_z)	≈ 40 minutes	$\approx 0.1 \%$
$(k_\xi, k_\eta, k_z = 0)$	≈ 2 hours	$\approx 0.3 \%$
(k_ξ, k_η, k_z) ($\Delta T_{gen} = 25\Delta T_{CAA}$)	≈ 100 hours	$\approx 15 \%$

Table III.3: Comparison of CPU times for turbulence generation and CAA calculations.

The generation time is negligible for one-dimensional and planar turbulent structures. However, if the fully 3D turbulence had been generated over all time steps it would have represented almost four times the CAA cost (around 2500 hours on 100 cores). The 3D turbulence field is instead

generated on sampled time steps without altering the quality of the solution since the characteristic time of the turbulence is much higher than the time step of the CAA calculation.

A flow chart representing the 3D turbulence generation is available in Appendix E.

Part IV

Design of vanes with leading edge serrations: a semi-analytical methodology

This part is devoted to the design and manufacturing of a low-noise rectilinear cascade in preparation for the first InnoSTAT test campaign at Centrale Lyon.

In a first step, an analytical Wiener-Hopf (WH) based solution introduced by Ayton *et al.* [30] (briefly described in Part II), to assess noise reduction from infinite flat plates with periodic leading edge patterns, is implemented in MATLAB. Then, a geometrical correction is proposed to deal with finite span airfoils and validated on various test-cases.

In a second step, from semi-empirical design rules and WH solution, a 2D sinusoidal LE pattern is proposed, fulfilling InnoSTAT's requirements. First assessment of the sound power level reduction is performed using the WH-based technique at various operating points corresponding to acoustic certification points. Then, after the definition of the 2D LE pattern, it is necessary to transpose it to the 3D NACA7310 geometry introduced in Section II.3.1. To this end, several methodologies are implemented in an in-house modeler at ONERA, which performs a morphing of the baseline geometry relying on the local chord variation along the span (LE serration pattern). Finally, the manufacturing process handled by National Research and Development Institute for Gas Turbines (COMOTI), a key partner of InnoSTAT project, is briefly discussed.

The aerodynamic and aeroacoustic behavior of the serrated geometry will be evaluated numerically and experimentally in the next Part V.

IV.1 Implementation of an analytical tool for the prediction of the leading edge noise

The main idea of this chapter is to implement and extend the analytical solution introduced in the Section II.1.2.2. The coding has been carried out on MATLAB following ongoing work of a previous PhD student (A. Cader). The code is decomposed into several routines in order to facilitate the implementation of the analytical method. The details about the coding are not provided here. The focus is on the extension of the methodology.

IV.1.1 Extension of the solution accounting for finite span

The formulation originally proposed by L. Ayton and J. W. Kim in [30] and relying on the Wiener-Hopf (WH) technique is written for an infinite span. A two-dimensional far-field noise propagation is assumed (in a similar way to a 2D Green's function), which varies as a function of $1/\sqrt{R_{obs}}$, where R_{obs} is the distance between the compact source and the observer. Some corrections (that are not explicitly stated in [30] and [127]) have to be introduced to account for finite span airfoils and 3D far-field radiation. These extensions are mandatory to assess SPL spectra, without any calibration on a reference case (as currently done) or without relying only on relative noise reduction available with an infinite-span solution.

From rather simple geometrical acoustic rules and using Taylor's expansion, it can be shown that such 2D to 3D corrections lead to a correction factor of L_z/R_{obs} , where L_z corresponds to the airfoil span. This factor L_z/R_{obs} seems consistent with the result found by Gea-Aguilera *et al.* [80], when applying 2D to 3D corrections for Amiet's theory. Thus, the 3D far-field sound pressure radiated from a centered point-source of the finite span airfoil, p_{3D} , that satisfies the assumption $L_z \ll R_{obs}$, can be related to the 2D asymptotic solution p'_{2D} , as $|p'_{3D}(L_z, R_{obs})|^2 \approx L_z/R_{obs} |p'_{2D}(R_{obs})|^2$. It should be noted that both solutions get identical $p'_{2D} = p'_{3D}$, when applying the condition $L_z \rightarrow \infty$, as detailed below in the derivation of these asymptotic limits. The derivation of these asymptotic limits is detailed below.

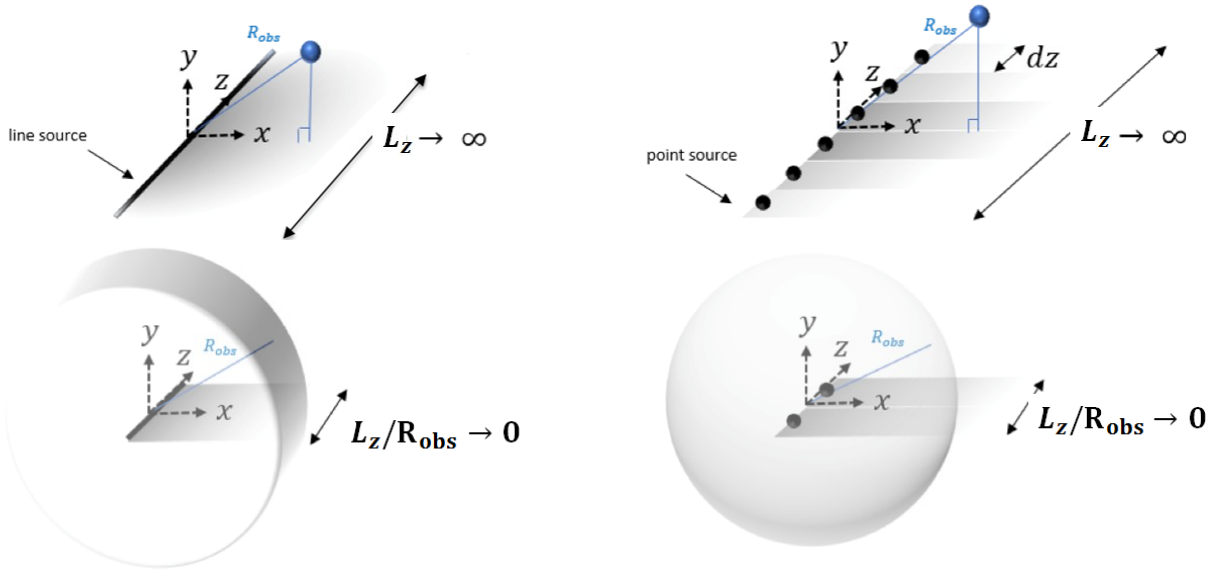


Figure IV.1: Diagrams of the different geometrical assumptions used to extend the WH formulation for finite span airfoils: line source (left) and equivalent distributed point sources (right) for asymptotic limits $L_z \gg R_{obs}$ (top) and $L_z \ll R_{obs}$ (bottom).

To account for finite span airfoils and to derive the term L_z/R_{obs} , a simple geometrical correction is applied in contrast with the reference model, which assumes an infinite span. Two asymptotic limits are considered: $L_z \gg R_{obs}$ and $L_z \ll R_{obs}$ (with R_{obs} the distance between the observer and the center of the airfoil). For a line-source (Fig. IV.1, left), the 2D Green's function is proportional to the inverse of the square root of the distance to the observer, which leads to $p'_{2D}(R_{obs}) \propto (A_{2D}/\sqrt{R_{obs}}) \exp(i(\omega t - kR_{obs}))$ (with A_{2D} an amplitude). Let us now decompose the span in a number $n = L_z/dz$ (with dz being a small interval of the span) of point sources (Fig. IV.1, top right). For each point source, $p'_{3D}(R_{obs}) \propto (A_{3D}/D) \exp(i(\omega t - kD))$. The 3D Green's function is proportional to the inverse of the distance D , where $D^2 = R_{obs}^2 + z^2$ and corresponds to a location in the spanwise direction. The two formulations must give the same intensity when an airfoil of an infinite span is considered, which leads to (using the Riemann sum approximation):

$$\begin{aligned}
 |p'_{2D}(R_{obs})|^2 &= \lim_{n \rightarrow \infty, dz \rightarrow 0} \sum_{i=1}^n = |p'_{3D}(dz, D_i)|^2 = 2 \int_0^\infty \frac{\lim_{L_z \rightarrow \infty} |A_{3D}(L_z, R_{obs})|^2}{R_{obs}^2 + z^2} dz \\
 \Rightarrow \lim_{L_z \rightarrow \infty} |A_{3D}(L_z, R_{obs})|^2 &= \frac{1}{\pi} |A_{2D}|^2 \quad (IV.1)
 \end{aligned}$$

When $L_z \ll R_{obs}$, the line-source tends to become compact. Let us consider two point sources infinitely close to each other from the observer point of view (Fig. IV.1, bottom right), and which are equivalent to a line-source. In order to keep a constant total radiated energy, one

should verify,

$$\begin{aligned} \lim_{\frac{L_z}{R_{obs}} \rightarrow 0} \left(\frac{1}{L_z} (L_z 2\pi R_{obs}) \frac{|A_{2D}|^2}{R_{obs}} \right) &= \lim_{\frac{l_z}{R_{obs}} \rightarrow 0} \left(\frac{1}{2} (4\pi R_{obs}^2) \frac{|A_{3D}(L_z, R_{obs})|^2}{R_{obs}} \right) \\ \Rightarrow \lim_{\frac{L_z}{R_{obs}} \rightarrow 0} \left(|A_{3D}(L_z, R_{obs})|^2 \right) &= |A_{2D}|^2 \end{aligned} \quad (IV.2)$$

Finally, for an airfoil with a finite span the integration in Eq. (IV.1) is performed only between $-L_z/2$ and $L_z/2$,

$$|p'_{3D}(L_z, R_{obs})|^2 = 2 \int_0^{L_z/2} \frac{|A_{3D}(L_z, R_{obs})|^2}{R_{obs}^2 + z^2} dz = 2 |A_{3D}(L_z, R_{obs})|^2 \frac{\tan^{-1} \left(\frac{L_z}{R_{obs}} \right)}{R_{obs}} \quad (IV.3)$$

In the case $L_z \gg R_{obs}$ (with R_{obs} fixed), Eq. (IV.3) becomes:

$$\begin{aligned} \lim_{L_z \rightarrow \infty} \left(|p'_{3D}(L_z, R_{obs})|^2 \right) &= \lim_{L_z \rightarrow \infty} \left(2 |A_{3D}(L_z, R_{obs})|^2 \frac{\tan^{-1} \left(\frac{L_z}{R_{obs}} \right)}{R_{obs}} \right) \\ &= \frac{2}{\pi} |A_{2D}|^2 \frac{\pi}{2R_{obs}} = |p'_{2D}(R_{obs})|^2 \end{aligned} \quad (IV.4)$$

Thus, the reference formulation for an infinite span is recovered. When $L_z \ll R_{obs}$, using a Taylor expansion of \tan^{-1} , one can show that

$$|p'_{3D}(L_z, R_{obs})|^2 \xrightarrow{\frac{L_z}{R_{obs}} \rightarrow 0} |A_{2D}|^2 \frac{L_z}{R_{obs}^2} \quad (IV.5)$$

Finally, the asymptotic limit of the radiated pressure through is given by:

$$|p'_{3D}(L_z, R_{obs})|^2 \xrightarrow{\frac{L_z}{R_{obs}} \rightarrow 0} \frac{L_z}{R_{obs}} |p'_{2D}(R_{obs})|^2 \quad (IV.6)$$

This extended finite-span formulation provided by Eq. (IV.6) is validated in Section IV.1.2 from:

- A comparison of broadband noise predictions (from both absolute SPL and PWL spectra) on straight LE airfoils using the present WH approach (with $h_s = 0$) and Amiet's solution;
- A comparison of broadband noise predictions from serrated LE airfoils using CAA and experimental results [63, 138].

Two additional analyses performed with the WH tool are provided in appendix:

- In Appendix F, accuracy and limitations of the model investigated through available experimental data from ISVR (Institute of Sound and Vibration Research) [138]. Parametric

studies are performed on serration's wavelength and amplitude.

- An evaluation of the noise radiated by a spanwise varying LE pattern on a turbofan stator vane, designed in the framework of TurboNoiseBB project [144], presented in Appendix G.

IV.1.2 Validation of the extended WH formulation

The extended WH formulation is applied to a well-documented test-case on the NACA 651210 airfoil [63, 135]. The main parameters are summarized in Table IV.1. The baseline and serrated LE configurations are considered here. First, a comparison is performed with Amiet's solution followed by a comparison with numerical and experimental data provided in the FLOCON project [6, 63, 135].

Chord (m)	L_z (m)	TI (%)	TLS (m)	h_s (m) (baseline / serrated)	λ_s (m)	Mach	R_{obs} (m)
0.15	0.45	2.5 %	0.006	0.000 / 0.005	0.01	0.18	1.2

Table IV.1: Parameters from FLOCON test-case for turbulence-airfoil noise predictions.

Comparison with Amiet's solution for the untreated case

The first validation step consists in the comparison of the noise level on a baseline configuration (straight leading edge) with respect to the reference Amiet's solution. Predictions of SPL at $\Theta=90^\circ$ and PWL spectra are compared. Sound power is computed by assuming cylindrical radiation, as defined in Eq. (II.13). Moreover, the turbulence comes from a planar Liepmann turbulence spectrum and it is supposed to be frozen, isotropic and homogeneous, as defined in the Chapter III.1.

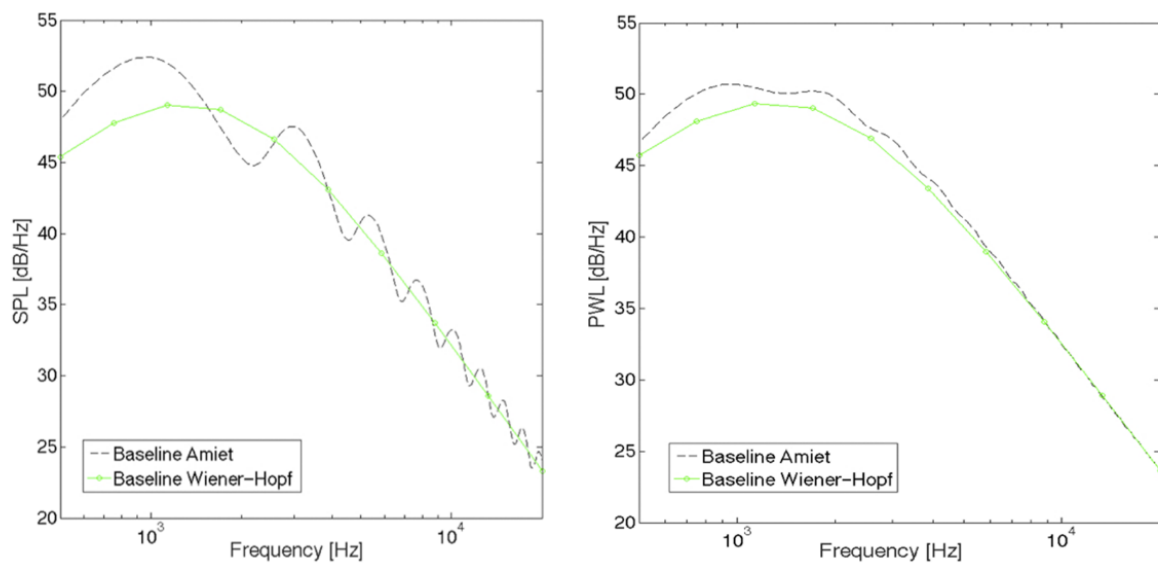


Figure IV.2: SPL spectra at $\Theta=90^\circ$ (left) and PWL spectra (right) from Amiet and WH solutions for the baseline LE flat plate.

Amiet's model exhibits strong oscillations in Fig. IV.2 (left) due to the interference between the leading edge and the trailing edge. This back-scattering effect is not present on the new analytical model. Indeed, this can be attributed to compactness effects along the chord, which cannot be accounted for in the present WH solution due to the semi-infinite chord assumption. However, both models provide the same overall trend of the radiated noise spectrum. Finally, the sound power level (PWL) is also compared in Fig. IV.2 (right). The spectra issued from the two formulations match quite well despite a slight level deviation, more significant at lower frequencies. Parametric studies, not detailed here, were performed (variation of the infinite velocity, the chord, and the distance to the observer), showing a pretty good agreement. The second step consists in validating the analytical model for serrated configurations, by considering solutions from CAA and results from experiment.

Comparison with numerical and experimental results for serrated cases

The WH formulation is applied to the LE serration case, and predictions are compared to available results from CAA and measurements [63, 135]. The SPL spectra at 90° are presented in Fig. IV.3 for both baseline and serrated LE cases. A quite good agreement is achieved although the WH solution tends to under-predict the noise levels at low frequencies. The acoustic performance of the LE serrations is confirmed by the WH approach in Fig. IV.4, which shows both Δ SPL and Δ PWL spectra to highlight the noise reduction. For the present case, the WH analytical model is able to reproduce the trends obtained from CAA and experimental results. The limited acoustic benefit at high frequencies (beyond 3-4 kHz) observed on measurements can be attributed to the TE noise. In Fig. IV.4, the self-noise contribution has been evaluated analytically following Howe's work [101] and added to the WH solution. This greatly improves the comparison with experimental results at high frequencies.

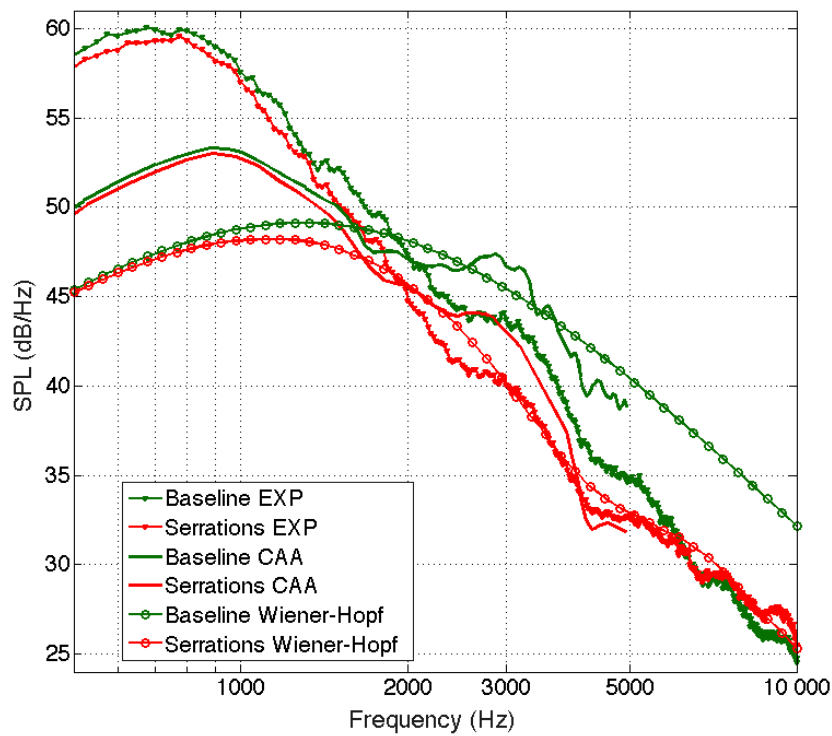


Figure IV.3: SPL spectra at $\Theta= 90^\circ$ for baseline and serrated LE cases from CAA solutions [63], the WH analytical model [28], and the experiment [135].

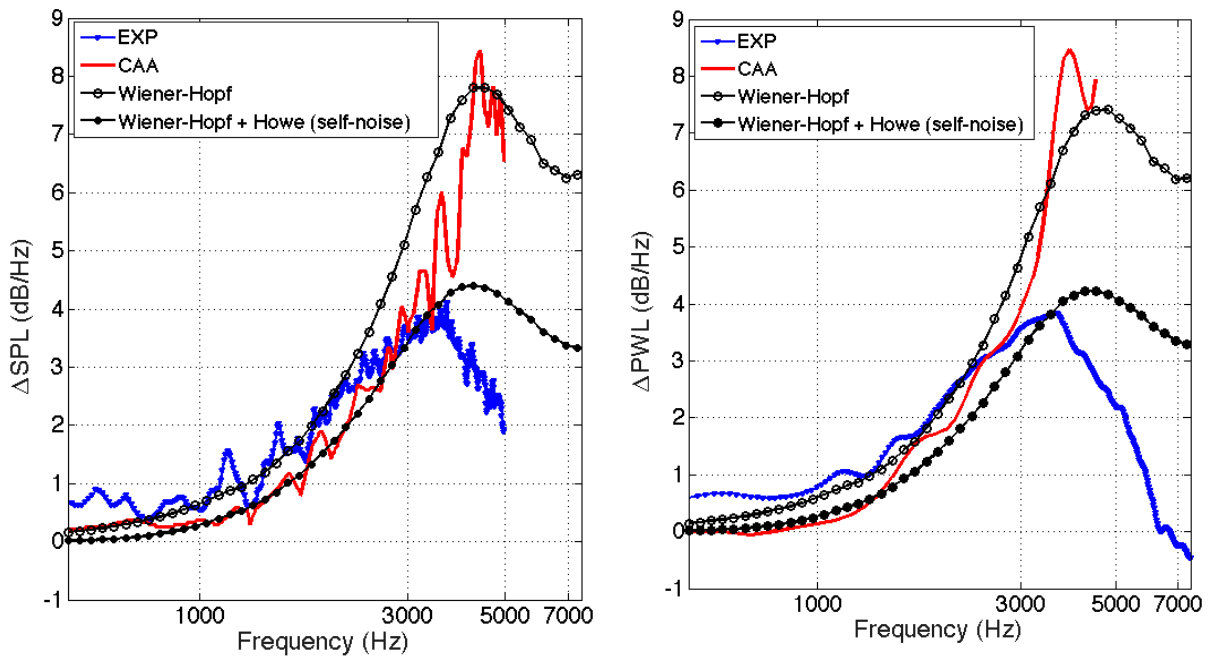


Figure IV.4: Delta SPL spectra at $\Theta= 90^\circ$ observer (left) and delta PWL spectra (right) from CAA solutions [63], from WH analytical model (with and without the self-noise contribution), and from experiment [135].

In the next chapter, this WH solution is used to assess a low-noise design, preliminary defined from semi-empirical design rules, in the framework on the InnoSTAT project.

IV.2 Design of a low-noise vane with leading edge serrations

In preparation of the cascade rig test campaign at Centrale Lyon, see Section II.3.1, ONERA has designed low-noise vanes by means of semi-empirical rules (presented in the following section) and WH-based solution presented in Section II.1.2.2 and extended in Section IV.1.1.

IV.2.1 Some background on noise reduction from sinusoidal leading edge serrations

In the last few decades, several works have studied the effects of leading edge serrations on noise generation. Some of the most relevant results in the field have been obtained from experimental investigations performed by ISVR on isolated airfoils. Based on previous publications from ONERA [63] and ISVR [135, 55], one can identify two major noise reduction mechanisms in the case of sinusoidal wavy patterns, as shown in Fig. IV.5. These noise reduction mechanisms are listed as follows:

- A reduction in the correlation between adjacent noise sources along the span, which is related to the transverse correlation length scale L_t and therefore, to the turbulence (longitudinal) integral length scale L_l ;
- A modification of the aeroacoustic response giving rise to a loss of efficiency in the acoustic radiation from incoming gusts. Clair *et al.* [63] proposed an explanation based on a simple reformulation of the dispersion relation in the presence of sinusoidal serrations (approximated by a sawtooth pattern), which shows a filtering of the incoming parallel gusts when the inclination angle of the serrations is close to 90° . This angle θ_s defined by $\theta_s = \tan^{-1}(4h_s/\lambda_s)$ highlights the role of the serration amplitude h_s and wavelength λ_s in the noise reduction mechanism. This finding has been confirmed by recent experimental [135, 55] and analytical studies [30].

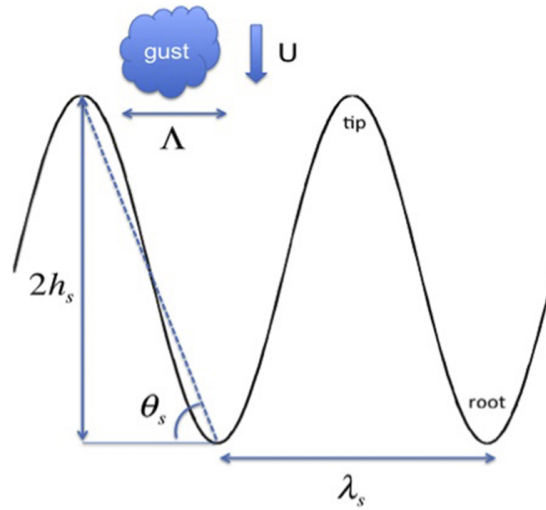


Figure IV.5: Sketch of sinusoidal LE serrations with main relevant design parameters, extracted from [144].

Based on the above observations, the best compromise for isotropic turbulence is to set the serration wavelength to $\lambda_s = 4L_t = 2L_l$. Another key parameter is the choice of a convenient ratio h_s/λ_s . Although the acoustic benefit could be improved by increasing h_s , a practical limitation is required to avoid a noticeable loss of aerodynamic performance for industrial applications, as discussed by Reboul *et al.* [154]. Hence, setting $h_s/\lambda_s = 1$ gives $\theta_s = 76^\circ$, which can be considered as a reasonable value close to the optimum design according to Narayanan *et al.* [135]. Another important result highlighted by Chaitanya *et al.* [55] is that the sound power attenuation ΔPWL which can be achieved by a single-wavelength serrated LE, is approximately proportional to the Strouhal number, $\text{St} = fh_s/U$, at the optimum serration wavelength, where U is the free stream velocity and f is the frequency. The following empirical law was proposed:

$$\Delta\text{PWL}(\text{dB}) = 10 + 10 \log(\text{St}) \quad (\text{IV.7})$$

In practice, a significant PWL reduction (≥ 3 dB) can be expected if $\text{St} \geq 0.2$ for isolated airfoils with leading edge serrations.

IV.2.2 Choice of a pattern addressing the InnoSTAT KCA configuration

Shaping based on the properties of the inflow turbulence

The leading edge serrations have been firstly designed on a 2D plane, applying background knowledge on LE serrations introduced in the previous section. The serration's pattern is depicted in Fig. IV.6. The theoretical optimal serration wavelength corresponds to twice the turbulence length scale. A pre-test value of 8 mm (roughly estimated from previous tests and adopted by the InnoSTAT Consortium as a target value) has been considered. The serration amplitude is defined directly in relation to the serration angle and so the ratio h_s/λ_s . To limit possible aerodynamic penalties, a threshold, $h_s/c \leq 0.15$ has been used in [154, 47, 144]. Hence, setting $h_s/\lambda_s = 1$

can be considered as a reasonable value close to the optimum design and verifying the previous constraint. In order to get an integer number of serrations along the span, the quantities have been slightly increased to end with $h_s = \lambda_s = 16.7$ mm, for the numerical computation.

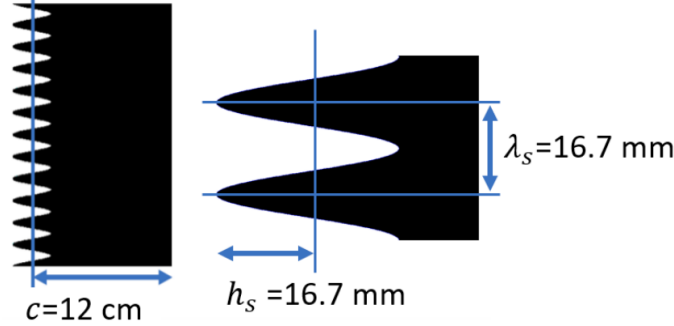


Figure IV.6: Main parameters of the LE serrations.

Parametric study of the noise reduction based on the inflow Mach number

Several ways have been considered in this project to try to assess the acoustic performances of the low-noise airfoil cascade, relying on empirical, analytical and numerical approaches. The empirical log-law evidenced by Paruchuri *et al.* [55] has been adopted to get a rough evaluation of the sound power level reduction Δ PWL in Eq. (IV.7). Additionally, a parametric study has been performed by means of the analytical solution discussed in Sections II.1.2.2 and IV.1.1. It aims at evaluating the acoustic performances at the three certification points: approach APP, cutback CUTB, and sideline SDL. The obtained results are plotted in Fig. IV.7. The prediction at $M=0.3$ (condition used for the CAA) is also given.

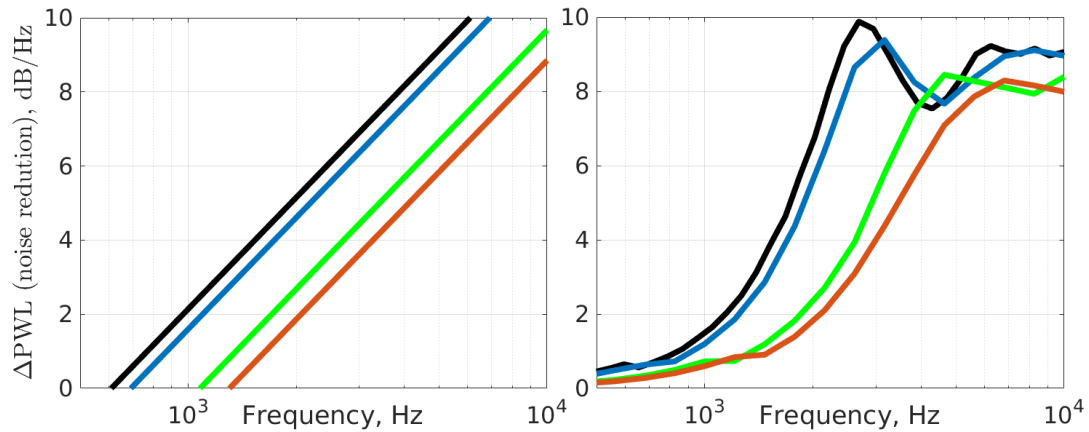


Figure IV.7: Log-law $10 \log(\text{St}) + 10$ (left) and Wiener-Hopf (right) solutions at 3 certification points: $M = 0.3$ —, APP ($M = 0.34$) —, CUTB ($M = 0.53$) —, and SDL ($M = 0.64$) —.

These results demonstrate that the noise reduction is shifted towards high frequencies. As already pointed out in [144], the peak-frequency of the PWL reduction roughly follows the one related to the noise emission spectrum, at respective regimes. By the way, the low-noise design remains efficient at low-speed and high-speed flows, and thus, well adapted for acoustic certification. Moreover, it can be noted that the empirical log-law and WH solution exhibit the same trend in

mid-frequencies. However, the log-law cannot predict the noise reduction for St below 0.1 and at high frequencies, where it does not reproduce the plateau visible in WH solutions.

IV.2.3 Application of the LE pattern to a NACA7310 airfoil

Once the 2D serration pattern is set, it is necessary to transpose it to the 3D geometry of the chosen airfoil for the InnoSTAT rectilinear cascade, presented in Section II.3.1. The latter is defined by a NACA7310 profile. To this end, two methodologies implemented in an ONERA in-house modeler *ersatzZ* are discussed.

A basic homothetic morphing

A first morphing methodology, used in [144], is applied. The skeleton of the vane is extracted at each 2D plane along the span. Then, a homothetic transformation of the airfoil shape is applied, while keeping a constant stagger angle and fixed trailing edge for all the surface deformations between the root and the peak of the serration. For all profiles, same camber law, same thickness law, and same relative thickness as the reference profile is retrieved. Figure IV.8 illustrates this deformation.



Figure IV.8: 2D deformations of the NACA7310 profile following a basic homothetic morphing.

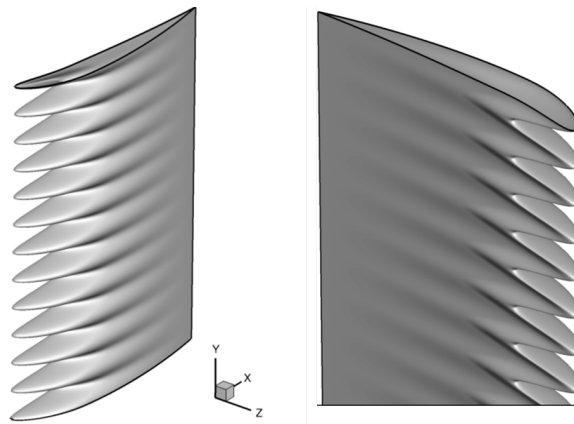


Figure IV.9: 3D deformation of the vane following a basic homothetic morphing.

The 3D geometry d_0 of the serrated vane is shown in Fig. IV.9. It has been obtained by means of a 3D ONERA's in-house modeler: *ersatzZ*. An aerodynamic evaluation of this serrated design, referred to as d_0 , is provided in Chapter V.1.

A camber/thickness lines based morphing

A second technique has been implemented by R. Barrier to deform the baseline geometry. The present 3D extension obeys to practical aerodynamic rules. The main idea is to keep all

the leading edge points aligned along the same line parallel to the mean flow. Moreover, the same angle of attack at all points of the leading edge is preserved. To that end, the camber and thickness laws of the NACA7310 airfoil are first extracted, similarly to the previous methodology, as illustrated in Fig. IV.10.

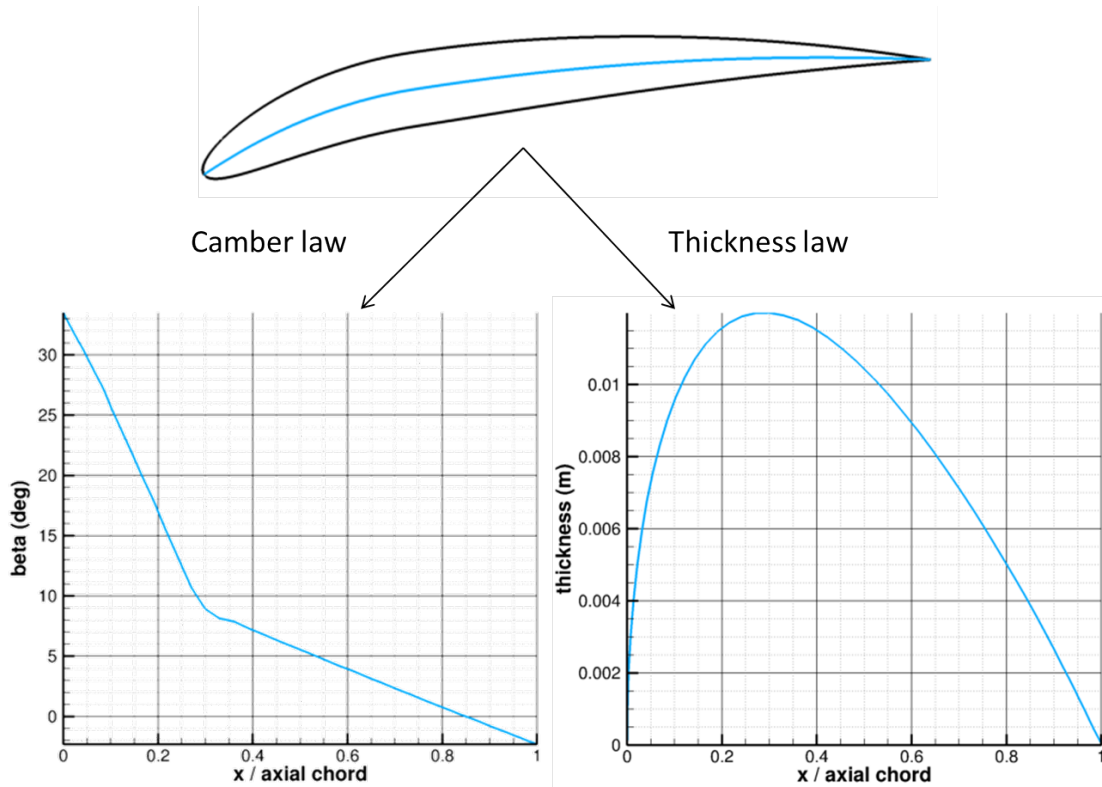


Figure IV.10: Extraction of camber and thickness laws from a NACA7310 geometry.

A homothetic transformation of these laws is performed to get the warped geometry in the planes at roots of the serrations (Fig. IV.11, left).

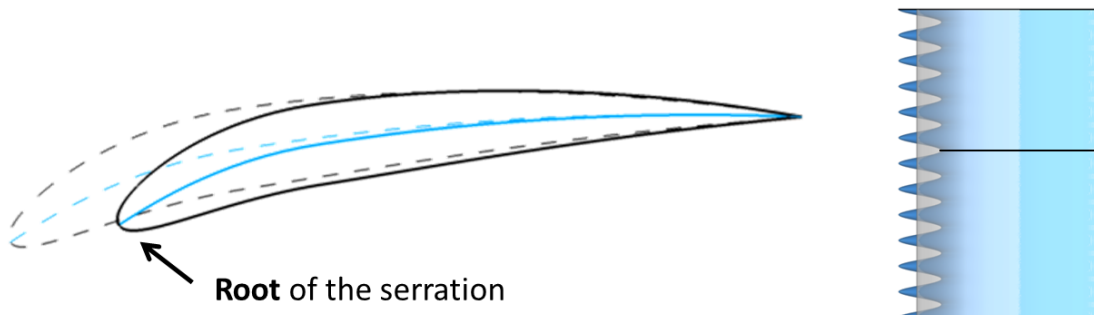


Figure IV.11: Definition of the deformed geometry at the roots of the serration.

Then, to assess the serration peaks, the reference LE is simply prolonged by keeping the angle constant, ensuring the same incidence angle with the upstream mean flow, as shown in Fig. IV.12 and in Fig. IV.13 (left). This choice leads in particular to a conservation of the reference beta angle at the LE, β_{LE} , to keep the same flow incidence, *i.e.* $\beta_c = \beta_{LE}$. Moreover, contrary to the previous methodology, for which the relative thickness was kept unchanged, here, a conservation

of the absolute maximum thickness ensures a safer choice for mechanical constraints. But this increase of the relative thickness (thickness/chord) which is generally correlated with a higher aerodynamic loss. The latter remark is challenged through RANS computations discussed in Chapter V.1.

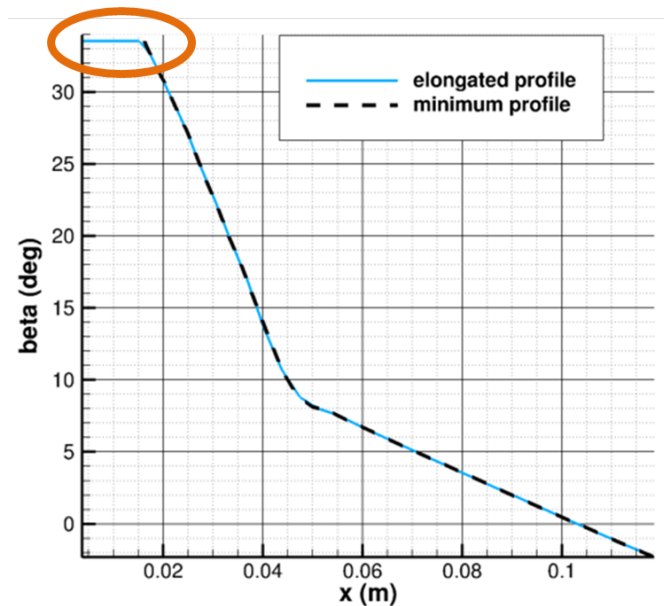


Figure IV.12: Constant extension of the camber law to define the LE profile at peaks of the serrations.

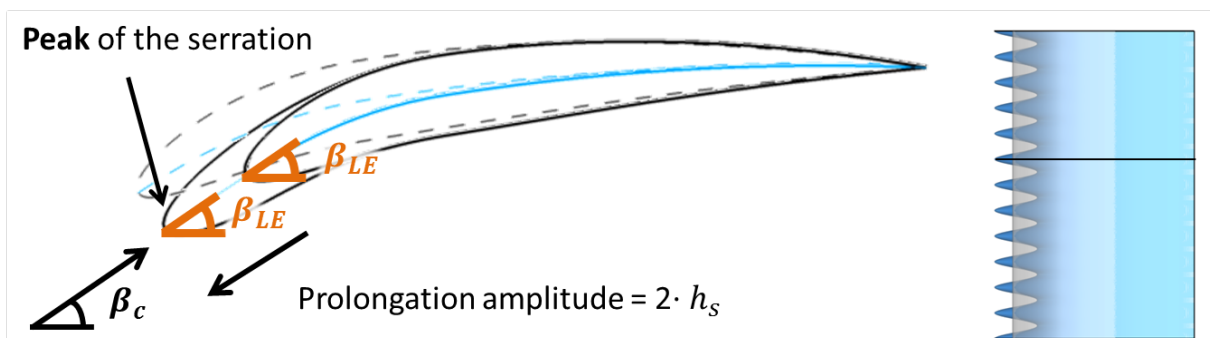


Figure IV.13: Definition of the deformed geometry at the peaks of the serration.

Pressure side and suction side views of the final 3D serrated geometry are shown in Fig. IV.14, middle and right, respectively. The surfaces of both pressure and suction sides are a much smoother than with the older methodology presented in Fig. IV.9. This is expected to improve the aerodynamic behavior analyzed in Chapter V.1, by preventing the generation of vortices from the grooves. This serrated design is referred to as d_1 .

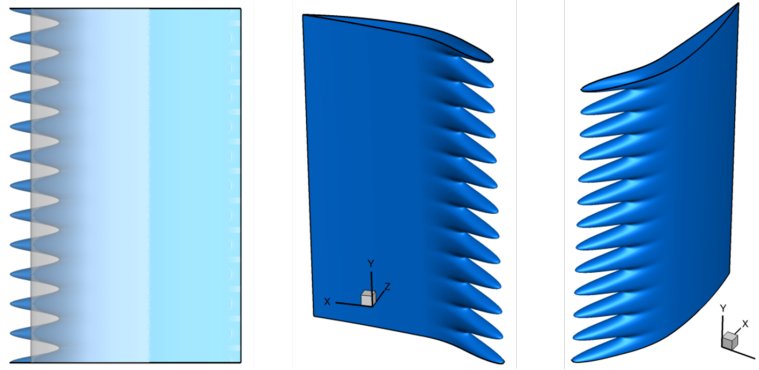
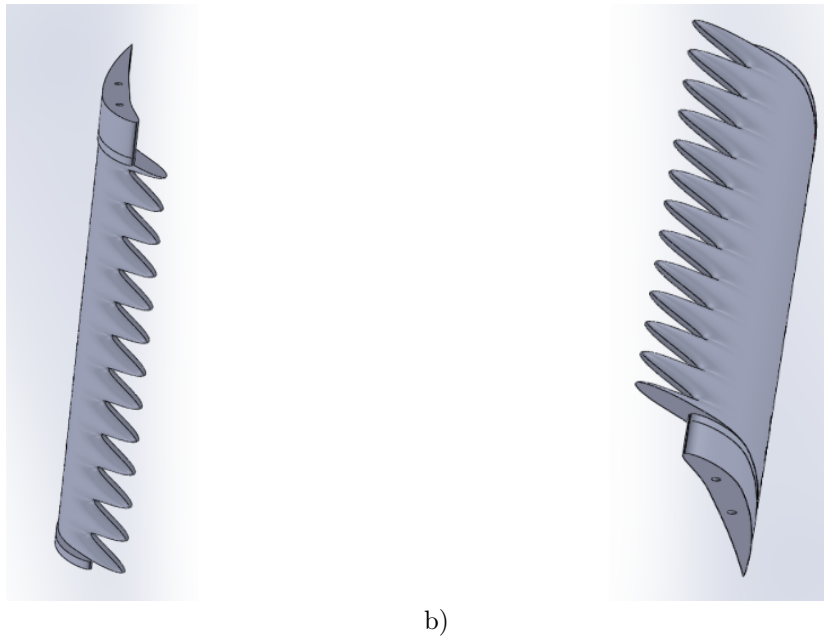


Figure IV.14: 3D deformation of the vane following the new morphing methodology.

IV.2.4 Manufacturing of the serrated vane

Some aspects of the manufacturing process are presented here. It has been overseen by the National Research and Development Institute for Gas Turbines COMOTI, which has printed 4×7 vanes (two COMOTI concepts and two ONERA concepts) in a high tensile resin. The two ONERA concepts are defined as d_1 and d_2 . d_1 design refers to Fig. IV.14 and d_2 to an optimized design proposed in Chapter V.1. The "basic" homothetic design d_0 , shown in Fig. IV.9, has been discarded due to high aerodynamic penalties discussed in Chapter V.1. The first step, in preparation for the manufacturing, has consisted in the addition of test rig adaptations to the CAD model, as illustrated in Fig. IV.15.



a)

b)

Figure IV.15: Addition of test rig adaptations to CAD model of the ONERA serrated vanes: d_1 design (a), d_2 design (b).

Then, the geometry has been printed by means of a Digital Light Processing (DPL) printer (LC Magna 3D). Contrary to filament printers, DPL technology provides a smoother result. However,

it requires two post-processing steps: solvent cleaning and curing (heat or UV oven) to harden the material. Moreover, a 1200 grit paper polishing under water jet has been applied at COMOTI. The manufacturing process and progress are illustrated in Fig. IV.16 and Fig. IV.17.

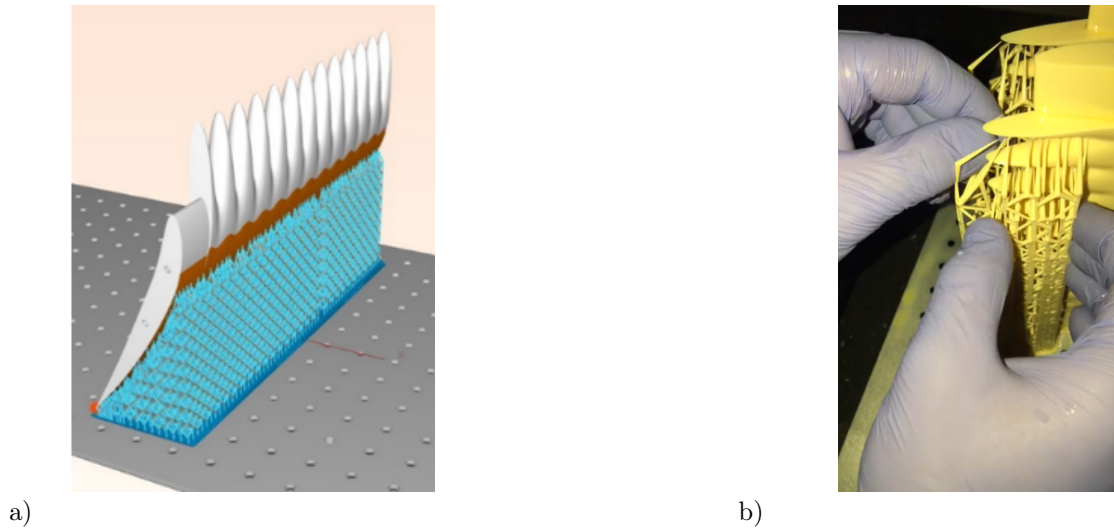


Figure IV.16: 3D model file for the printer (a) and vane at the print output (b) with support materials.



Figure IV.17: 3D serrated vane after support material removal and post-processing.

The final result for the d_1 design is illustrated in Fig. IV.17. Some of the testing to assess the printing quality and durability is presented in Appendix H.

In the next part, numerical simulations (RANS, CAA, and LBM) performed on baseline and low-noise design are compared both to analytical predictions and experimental results obtained during the InnoSTAT test campaign.

Part V

Aeroacoustic and aerodynamic study in a rectilinear cascade configuration: baseline and low-noise cases

Serrated designs d_0 (basic morphing) and d_1 (camber/thickness lines based morphing) have been proposed in Part IV, more precisely in Section IV.2.3, in preparation for the experimental campaign on the rectilinear cascade at Centrale Lyon, presented in Section II.3.1. Aerodynamic and aeroacoustic simulations to evaluate these serrated geometries are now discussed in this main Part V. They are based on intermediate and high fidelity approaches described in Part II - Chapter II.2.

First, aerodynamic penalties induced by serrations are compared to reference values in Chapter V.1. Through RANS simulations, comparisons are performed at two inflow speeds corresponding to approach condition and aerodynamic design point. Then, an improved design d_2 is also proposed in order to reduce aerodynamic penalties due to leading edge serrations.

In a second step, CAA calculations are performed to assess the noise reduction from design d_1 in Chapter V.2. Several parametric studies are performed on inter-vane spacing, vane count, and turbulence structure, to determine the influence of the different parameters on the far-field noise radiation.

An alternative to the hybrid CFD/CAA approach, is a high fidelity simulation based on the lattice Boltzmann method (LBM). It captures unsteady aerodynamics contrary to RANS simulations and actual turbulent flow generated by the turbulence grid (included in the numerical set-up) with no use of isotropic spectrum model as in the CAA. Moreover, LBM approach allows direct noise calculations taking into account installation effects. In Chapter V.3, LBM simulation are performed by mean of the ProLB solver presented in Section II.2.3. Numerical results provided by LBM simulation are compared to other prediction methods and experimental values.

To end this part, a trade-off between fidelity and cost (set-up and CPU) is discussed in Chapter V.4 for all methods.

V.1 Aerodynamic performance control through RANS simulations

Aerodynamic behavior of the serrated geometries designed in Part IV is evaluated by mean of RANS simulations relying on `esla` solver introduced in Section II.2.2.

V.1.1 RANS calculations on initial serrated designs d_0 and d_1

In addition to aeroacoustic evaluations, an aerodynamic assessment has been conducted through RANS calculations using ONERA code `esla` presented in Section II.2.2. The full span extension has been considered, with the use of adiabatic walls condition on the vane and end-walls and periodic boundary condition at vane channel sides. In the spanwise direction, 421 points are used, ensuring at least 30 points per serration wavelength. A view of the CFD grid, containing about 5 million cells, is shown in Fig. V.1a. For the serrated cases, the vane skin mesh shown in Fig. V.1b is trimmed using the in-house modeler `ersatz`.

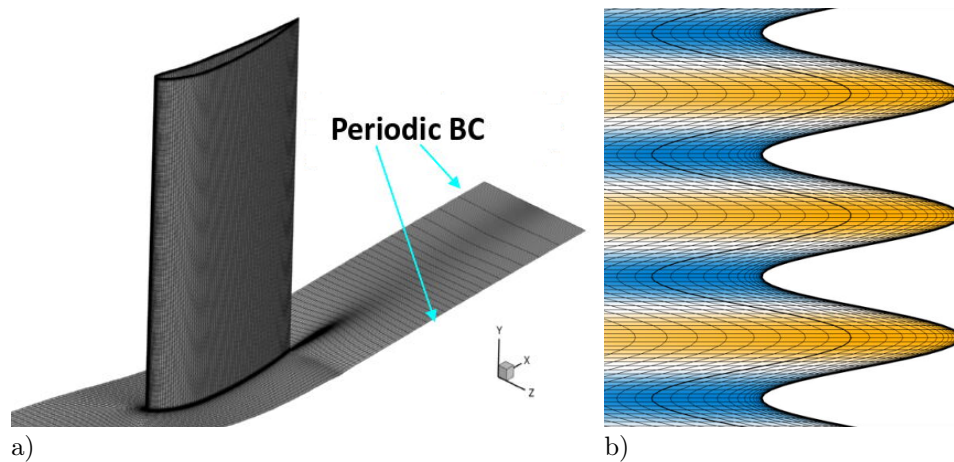


Figure V.1: 1-channel mesh of the baseline CFD geometry (a) and zoom view of the serrated mesh (b).

Two operating points are investigated, at approach (APP) and at the aerodynamic design point (ADP), with inlet Mach number respectively equal to 0.34 and 0.67, and inlet total pressure and temperature respectively equal to 101325 Pa and 288.15 K. The inflow turbulence intensity is set

equal to 4.5 %, the inflow angle β_c to 33° at APP and 32.7° at ADP (close to the target values from Safran specifications), and the normalized turbulent viscosity (μ_t/μ) of 0.01 is considered. The wall mesh size of 1×10^{-6} m ensures that $y^+ < 1$, as illustrated in Fig. V.2 for both baseline and serrated designs, here at APP condition.

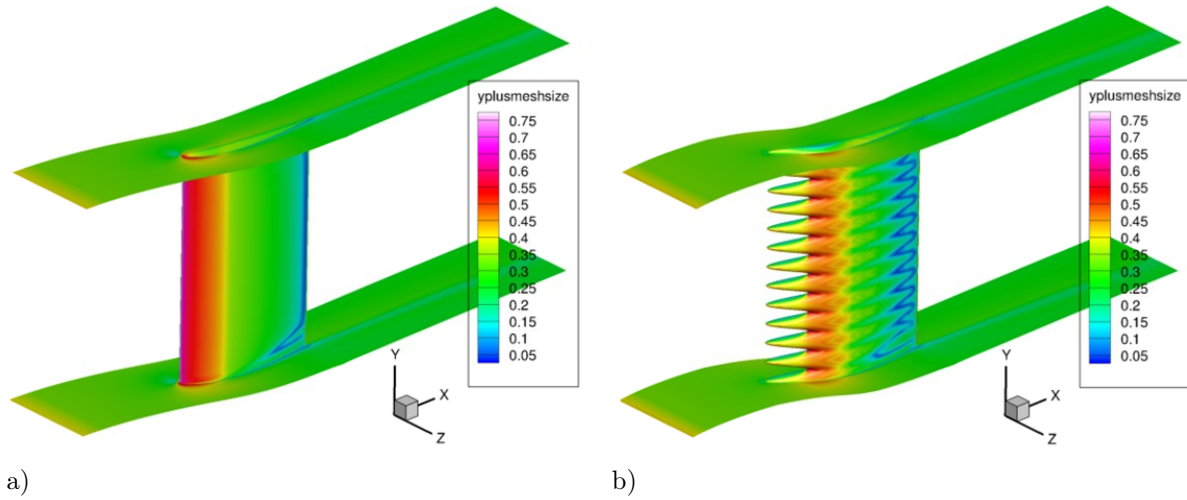


Figure V.2: y^+ at solid walls for baseline (a) and d_1 serrated designs (b).

At APP (selected condition for which the CAA simulations were performed), the d_0 design exhibits a huge flow detachment, as illustrated in Fig. V.4a (contour maps of Mach number) in the plane at the root level, contrary to the baseline airfoil in Fig. V.3. However, aerodynamic penalties at APP are found to be acceptable with the serrated design d_1 , as illustrated by Fig. V.4b and further below in Fig. V.8a, related to pressure loss coefficient. In Fig. V.3 and Fig. V.4b, comparisons of the cut views (taken at the roots of the serration) do not reveal significant changes with only a slight flow separation at the trailing edge suction side. This gives rise to a 0.14 p.p. (percentage points) deviation for total pressure loss coefficient and $+1.8^\circ$ deviation for outlet flow angle. Key results are gathered in Table V.1. For the reader information, pressure loss penalty associated with d_0 design is about -0.29 p.p., which explains why a new morphing methodology presented in Section IV.2.3 has been favored.

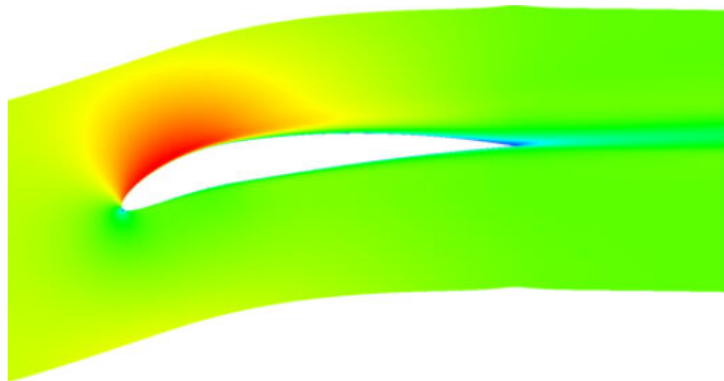


Figure V.3: Mach number (levels between 0.05 and 0.45) contour maps at APP for the baseline geometry.

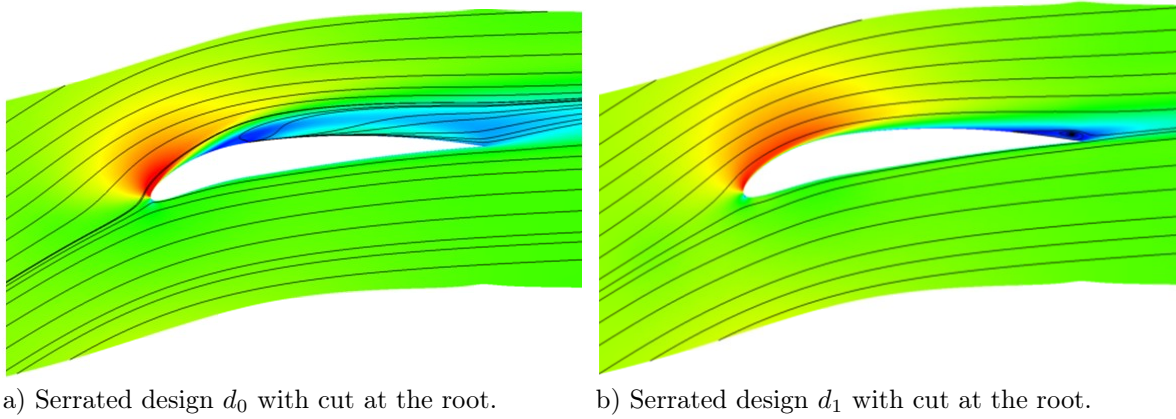


Figure V.4: Mach number (levels between 0.05 and 0.45) contour maps at APP.

A saturated contour map in Fig. V.5 shows the friction vector coefficient along x direction (perpendicular to the cascade). Usual corner flow separation appears near end walls. Around mid span, a small and uniform flow separation is visible near the trailing edge or the baseline case. However, on the treated d_1 case the separation is driven by the local chord. As expected from aerodynamic rules, the local chord length reduction is responsible of an increase of the penalties. Consequently, an elongation of the minimum chord has been suggested.

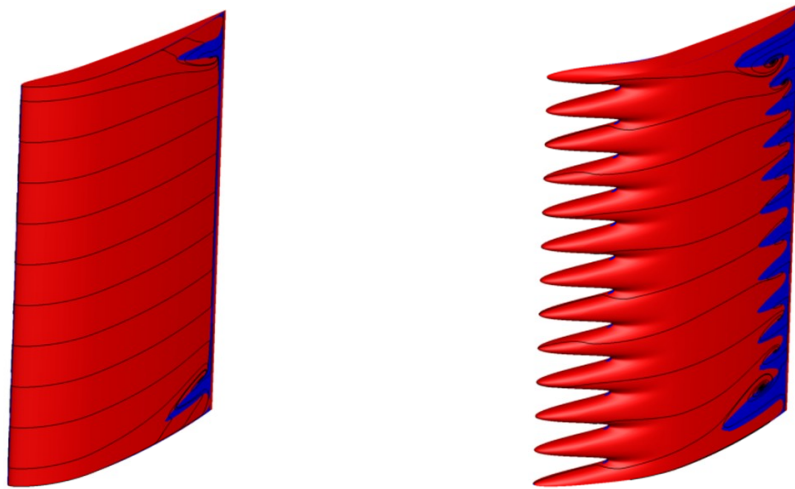


Figure V.5: Friction coefficient, x component, for the baseline (left) and d_1 geometry (right). Red area indicates a value over 1 and blue below 1.

V.1.2 Proposal of an improved serrated design d_2

Although the penalties obtained with design d_1 are not prohibitive at APP, at the ADP the aerodynamic performances are however significantly deteriorated compared to the reference geometry. Indeed, contrary to the previous observations from Fig. V.3, a strong flow separation is clearly shown in Fig. V.7b by comparison to the baseline solution in Fig. V.7a. This result has motivated the proposal of a second design, consisting in a basic modification of the initial serrated design for aerodynamic purpose only.

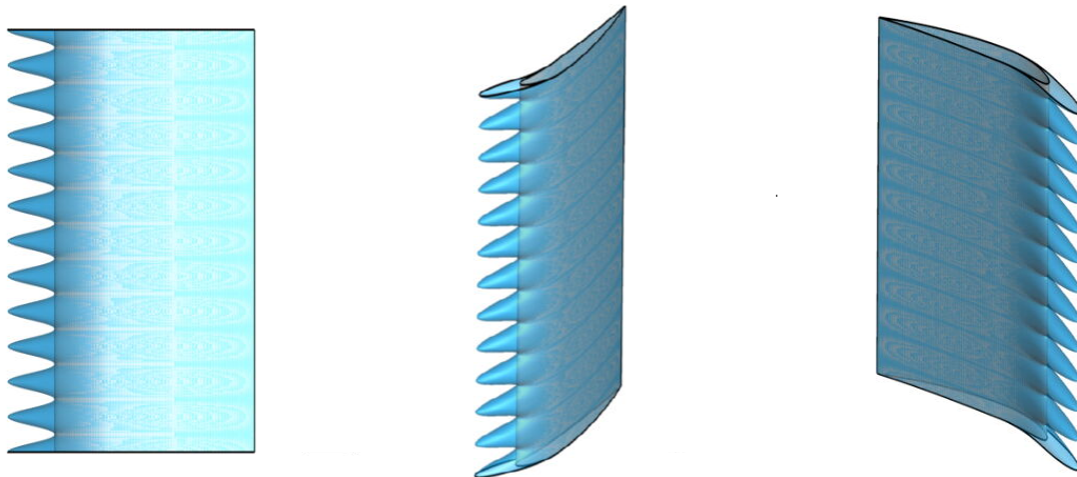


Figure V.6: Views of the baseline geometry (in grey) and the second serrated design (in blue).

In order to limit the aerodynamic penalties, more particularly of importance at ADP, a second serrated design with an increased averaged chord (the reference chord being set at the roots) has been simulated too. 3D views of this second serrated geometry are depicted in Fig. V.6. As the serration parameters (h_s, λ_s) are unchanged, this design d_2 should have almost no impact on acoustic performances assessed with the serrated design d_1 . Note that this modification of the averaged mean chord (compared to the baseline) has been practically validated by Safran. The following results address the aerodynamic performances obtained for both designs in comparison to the reference case.

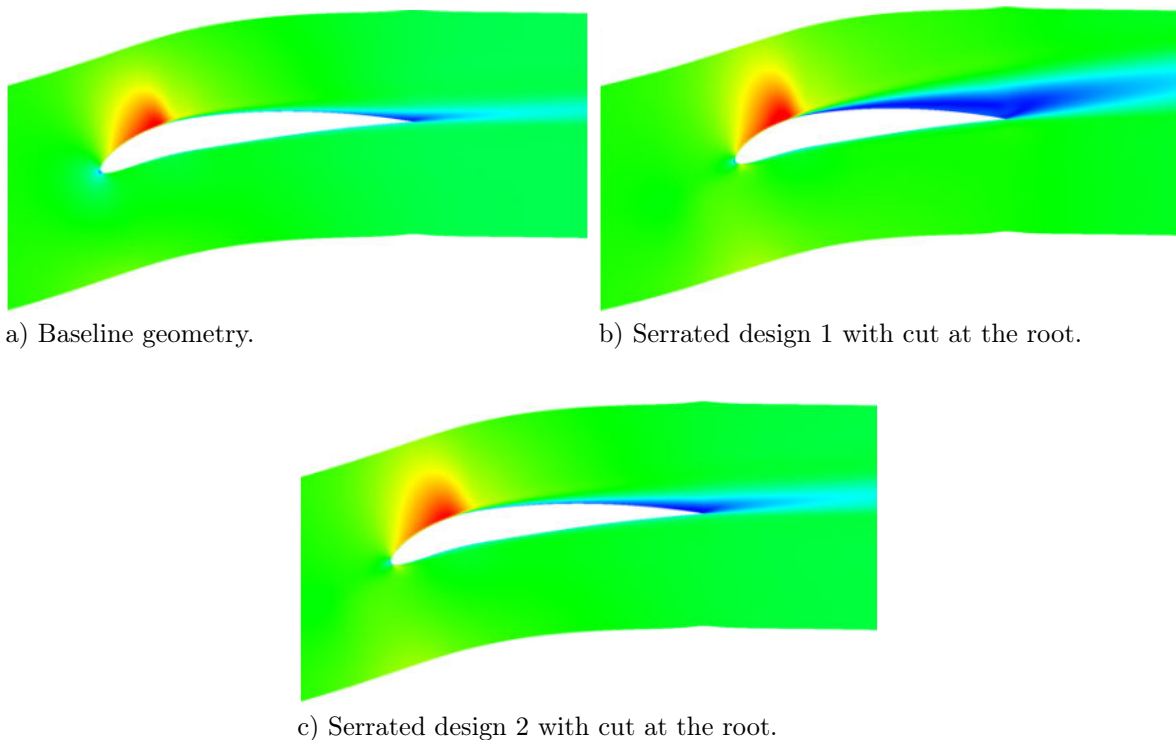


Figure V.7: Mach number (levels between 0.1 and 1.2) contour maps at ADP.

At ADP, the strong flow separation observed in Fig. V.7b is greatly reduced in the presence of

design d_2 . These positive effects are clearly pointed out on the spanwise profiles of pressure loss coefficient obtained for both designs, compared to the reference solution in Fig. V.8b at ADP.

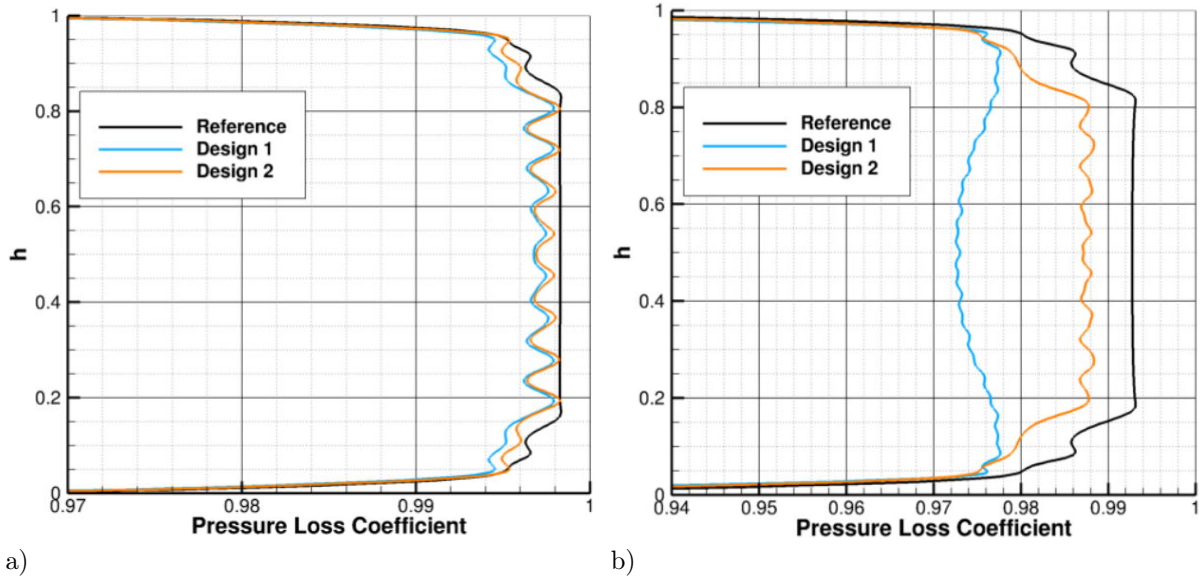


Figure V.8: Pressure loss distributions along the dimensionless spanwise coordinate $h = z/L_z$ at APP (a) and ADP (b).

The overall performances addressed in Table V.1 indicate a non-suitable penalty of -1.6 p.p. for total pressure loss coefficient and a flow angle deviation of $+3.8^\circ$ with design d_1 at ADP. These critical values are respectively reduced to -0.6 p.p. and $+0.8^\circ$ with design d_2 , which is a quite valuable improvement. At APP, the updated penalties for total pressure loss coefficient and outlet flow angle are found to be respectively reduced to -0.10 p.p. and $+0.5^\circ$ with design d_2 , as shown in Table V.1. The benefit of using an increased mean chord is clearly highlighted, the design d_2 being able to reduce the penalties all over the span, with much more acceptable deviations of the mean flow.

	baseline (reference)	design d_1	design d_2
Total pressure loss coefficient at APP	0.9970	0.9956 (-0.14 p.p.)	0.9960 (-0.10 p.p.)
Total pressure loss coefficient at ADP	0.9880	0.9720 (-1.60 p.p.)	0.9820 (-0.60 p.p.)
Outlet angle (remaining swirl) at APP	2.1°	$3.9^\circ (+ 1.8^\circ)$	$2.6^\circ (+ 0.5^\circ)$
Outlet angle (remaining swirl) at ADP	2.5°	$6.3^\circ (+ 3.8^\circ)$	$3.3^\circ (+ 0.8^\circ)$

Table V.1: Summary of the aerodynamic performances of baseline, serrated design d_1 , and design d_2 . Difference to the reference value in brackets.

V.2 CAA predictions

After having analyzed aerodynamic behavior of the serrated geometries in the previous chapter, noise reduction achieved by leading edge serrations is first evaluated by CAA through LEE simulations.

V.2.1 Inviscid mean flow calculation

In order to perform linearized Euler's simulations, determination of the mean flow variables is required. Here, the mean flow has been computed by means of a 2D open source Euler code presented in Section II.2.2. The inflow conditions are indicated in Fig. V.9.

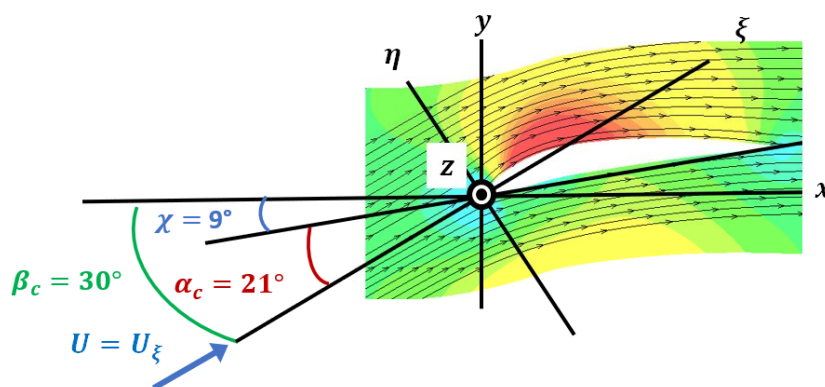


Figure V.9: U_x , axial velocity levels between 60 and 120 $\text{m} \cdot \text{s}^{-1}$.

A few iterations have been performed to reach the targeted upstream Mach number of 0.3. This has been done by adjusting the exhaust static pressure. This approach was shown to be an efficient alternative to previous RANS approach which requires some corrections near the solid boundaries in order to remove boundary layers and recirculation zones, incompatible with the inviscid assumption of the CAA code. A comparison between RANS and Eulerian mean flow based computations is conducted (not shown here for brevity) has shown a good agreement. Such comparisons are discussed in Part VI on the NASA SDT benchmark case. For the mean flow computation, a single channel simulation with periodic boundary conditions in the transverse directions has been considered. The obtained mean velocity field has been then duplicated and interpolated on the CAA mesh for acoustic multi-channel computations. The upstream Mach

number and the inlet flow angle used for the CAA have been chosen before the final values, corresponding to the pre-test values in Table II.2. It should not modify the conclusions drawn here.

V.2.2 CAA simulations set-up

The first set of simulations is performed on a single channel geometry ($s = L_y = 8.5$ cm) in order to limit the CPU time. Therefore, adjacent vanes are taken into account using periodic boundary conditions.

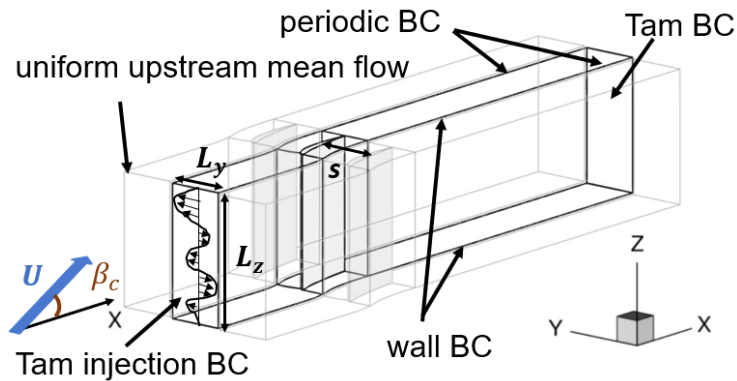


Figure V.10: CAA set-up used for the simulation.

The CAA mesh sizing is chosen following some criteria from previous studies [61]. In particular, the space discretization ensures at least 12 points per wavelength in all directions in which gusts are injected. Moreover, the grid density was chosen in order to control the energy loss in the injected velocity spectrum to less than 1 dB/Hz. Practically, the harmonic gusts above the cut-off frequency of the mesh are not injected. The CAA set-up is sketched in Fig. V.10 and numerical parameters are defined in Table V.2.

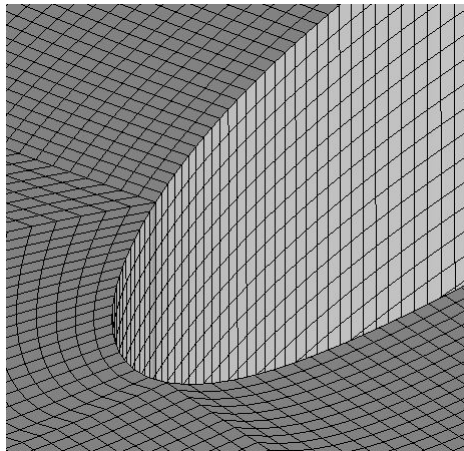


Figure V.11: CAA H-type pattern mesh at the leading edge.

Parameter	Value
Δx_{max}	8.5×10^{-4} m
Δy_{max}	4.3×10^{-4} mm
Δz_{max}	5.6×10^{-4} m
$\Delta x_{min}, \Delta y_{min}, \Delta z_{min}$	$\approx 4.0 \times 10^{-4}$ m
Δt	5.0×10^{-7} s
f_{max}	10 kHz

Table V.2: Numerical parameters.

Thereafter, a stretching zone is added at the exit of the domain coupled with a Laplacian filter to dissipate the hydrodynamic fluctuations impinging the exit boundary condition. The H support type pattern with a leading edge split is chosen in order to define the blocking. The mesh is designed to tolerate gusts of frequencies up to 10 kHz. The time step is chosen to ensure a CFL number lower than 0.8. A local view of the 3D grid is shown in Fig. V.11. The mesh has a total point number of 42 million.

V.2.3 Preliminary simulations of a single NACA7310 airfoil with periodic boundary conditions

Turbulent flow characteristics used in the synthetic turbulence (CAA) are not issued from CFD or measurements here, which is not a limitation in the scope of this study, but these turbulence properties were imposed using pre-test target values. In line with the previous studies carried out at ONERA on stochastic turbulence [63, 47, 144], the Fourier-mode decomposition was adapted from an annular to a rectilinear cascade problem, and practically achieved by considering a 1-wavenumber, 2-wavenumber, or 3-wavenumber isotropic turbulence spectrum model, focused to the upwash component (by analogy with Amiet's theory). For that, the latest generation and post-processing codes in cylindrical coordinates have been rewritten into Cartesian coordinates. Meanwhile, a numerical optimization of the Fortran routines has allowed a gain of about 20 on the time needed for the generation of the synthetic turbulence, as explained in Chapter III.5. First, the turbulence structures $(k_\xi, k_z = 0)$ and (k_ξ, k_z) defined in Chapter III.3 are considered. The wavenumber discretization along the z axis is chosen arbitrarily by setting $\Delta k_z = 2\pi / L_z$ and $N = 30$ (in order to also ensure 12 points per wavelength in the z direction, while injecting enough turbulent energy). As mentioned in Section II.1.2.1 and Chapter III.3, a factor $\Delta k_z = 2\pi / L_z$ is chosen to take into account the fact that the k_z wavenumber components are not defined for turbulence structure field where $k_z = 0$.

In order to avoid spurious sources at the injection plane occurring when a non-zero source term is imposed in the LEE simulation at time equals zero, a ramp in time is imposed during the starting

iterations of the simulation ($t_{\text{rampe}} = T_{\text{simu}}/3$). The benefit of this temporal ramp of the shape $\sin(t/t_{\text{rampe}}\pi/2)^2$, proposed during this work, is depicted in Fig. V.12.

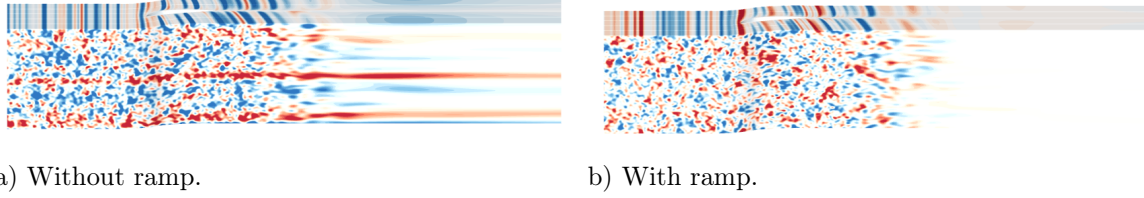


Figure V.12: Snapshots of u'_y [$\text{m}\cdot\text{s}^{-1}$] for the oblique gusts (levels between $\pm 10 \text{ m}\cdot\text{s}^{-1}$).

Although there is no influence on far-field acoustics associated with the ramp, synthetic turbulence snapshots in the CAA domain are improved and more representative. Indeed, the mean spurious values appearing without the ramp disappears when a ramp is added on the injected sources.

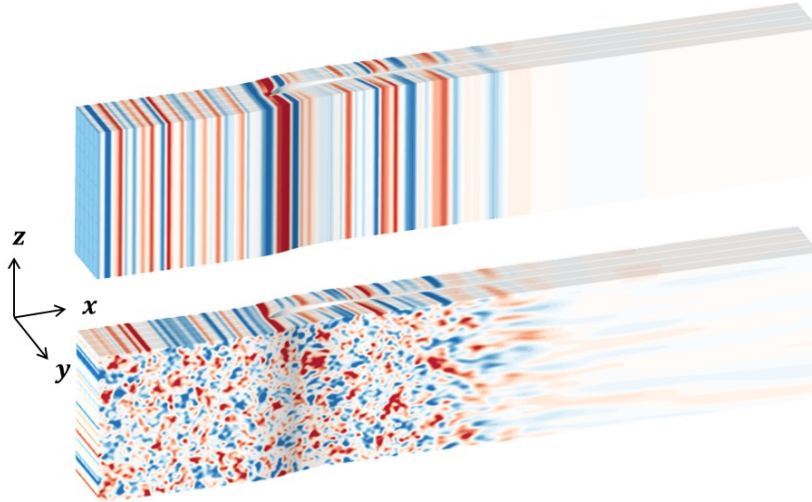


Figure V.13: Snapshots of u'_y [$\text{m}\cdot\text{s}^{-1}$] for the parallel (top) and oblique (bottom) gusts (levels between $\pm 2 \text{ m}\cdot\text{s}^{-1}$ for the $k_z = 0$ cases and $\pm 10 \text{ m}\cdot\text{s}^{-1}$ otherwise).

During CAA simulations with sAbrinA, snapshots have been taken at the end of the third period after the transient time and are gathered in Fig. V.13, highlighting the two structures of the injected turbulence. The unsteady pressure fields over the vane wall are then used as inputs to an in-house code (MIA), solving the loading noise term of the FWH (Ffwoes-Williams and Hawkings) equation with a free-field convected Green's function, in order to obtain the sound radiated in the far-field (Section II.1.1). As usually done, a simple angular integration of the quadratic pressure over a rearward half circle (centered in the mid plane) is adopted for the calculation of the downstream acoustic power (PWL spectra), as detailed in Eq. (II.13), similarly to [129] (appendix B). The observers are located at a distance of $R_{\text{obs}} = 1.8 \text{ m}$ (corresponding to the pre-test microphones positions in the Centrale Lyon test rig).

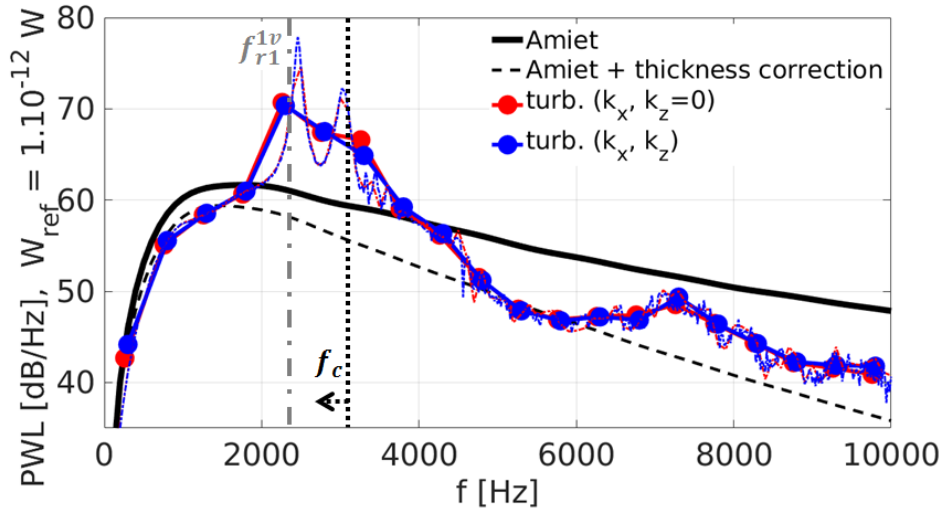


Figure V.14: Downstream PWL spectra obtained from numerical predictions and Amiet theory (isolated flat plate). Raw spectra in dashed lines and averaged (500 Hz bands) in solid lines.

The numerical results are compared to Amiet's formulation in Fig. V.14. It is important to stress that Amiet's solution does not take into account adjacent vanes. Therefore, the cascade effect mentioned in Section II.1.2.3 is not properly taken into account below a critical frequency f_c . Moreover, Amiet only considers a flat plate. In order to take into account thickness effect on the interaction noise mechanism, a correction has been applied from [138], following:

$$\Delta\text{PWL}(t, f) = 10 \log \left(-\beta(t) \frac{f c_0}{U} \right) \quad (\text{V.1})$$

with $\beta(t) = 1.369 \frac{t}{c_0} + 9.429 \left(\frac{t}{c_0} \right)^2$ and t the thickness of the NACA airfoil. First, regarding CAA results, a reduced radiated noise in lower frequencies which might be related to the cascade effect or thickness can be noted. A reduction is also observed in high frequencies which is due to the airfoil thickness. Acoustic spectra from both turbulence models are almost identical which can be theoretically explained, as detailed in Section II.1.2.1. Therefore, k_z has a little influence on CAA computations for the baseline case. Finally, two bumps appear in the spectra between 2000 and 4000 Hz whose such significant magnitude has not been observed in the literature [41, 14, 129], although peaks and valleys are clearly visible in similar cascade configuration. These particular peaks are not due to statistical errors, as it is clearly demonstrated by the comparison between spectra at $\Delta f = 100$ Hz (turbulence $(k_x, k_z = 0)$) and $\Delta f = 20$ Hz (turbulence (k_x, k_z)). These bumps might be linked to a resonance phenomenon amplified by the single channel computation with periodic boundary conditions. The associated resonance frequency is defined as:

$$f_{ri}^{jv} = \frac{ic_0}{2L_p^j} \quad (\text{V.2})$$

In Eq. (V.2), L_p^j denotes the periodicity distance depending on the number of vanes, $L_p^j = j \times s = L_y$. For the lower frequency at which resonance is observed, it is more accurate to take into account the airfoil's thickness. In consequence in Fig. V.14, the length $(L_p^1 - t)$ is considered instead of L_p^j to compute Eq. (V.2). In order to better understand the origin of these parasitic

sources, a parametric study is performed in the next section on a simplified flat plate geometry.

V.2.4 Parametric study of the channel spacing for a flat plate rectilinear cascade

To better understand the resonance phenomenon, a simpler configuration with flat plates at zero stagger angle is considered instead of NACA airfoils. This choice reduces the number of variables related to the physical mechanism at stake. The parametric study is based on the pitching spacing between the flat plates. Two meshes are introduced: a uniform grid (coarse mesh) and a highly refined grid around the edges (fine mesh) following criteria discussed in [61]. The different simulation domains are illustrated in Fig. V.15.

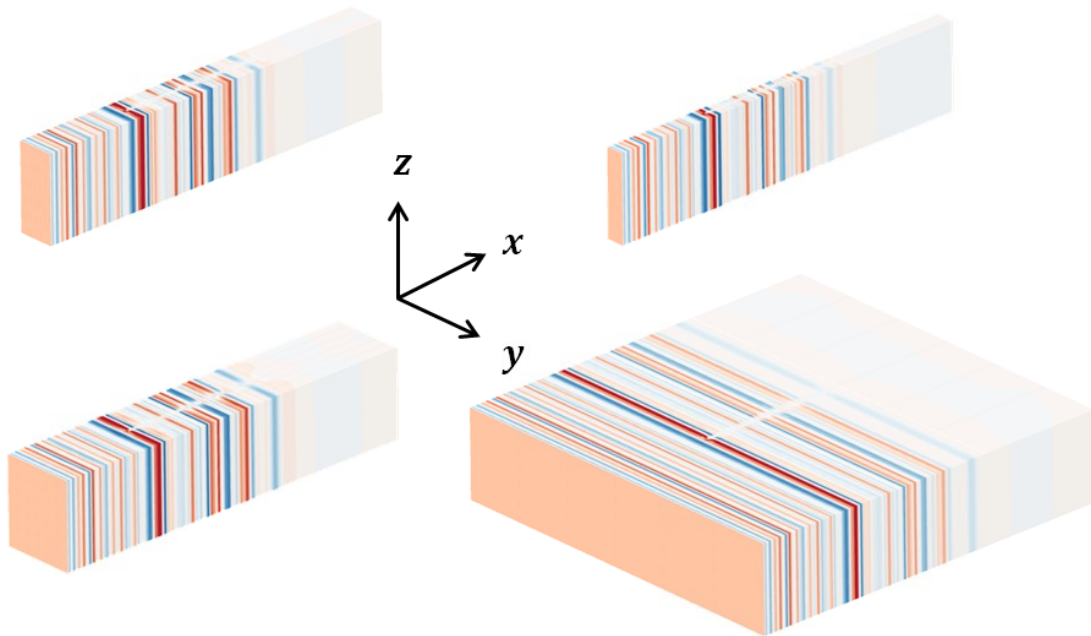


Figure V.15: Snapshots of u'_y [$\text{m}\cdot\text{s}^{-1}$] (levels between ± 2) for various channel widths: top left ($s = 8.5$ cm, actual cascade value), bottom left ($s = 17$ cm), top right ($s = 4.25$ cm) and bottom right ($s = 85$ cm, used to mimic free-field boundary conditions).

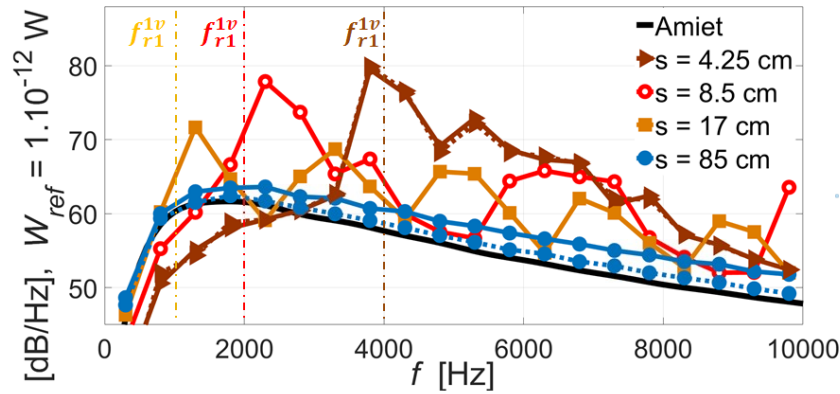


Figure V.16: Downstream sound power spectra obtained from CAA with various channel widths s . Fine meshes (for the cases $s = 4.25$ cm and $s = 85$ cm) in dashed lines. Spectra averaged on 500 Hz bands.

The power spectra in the far-field are plotted in Fig. V.16. First of all, the consistency of the results is observed with Amiet's solution, that is retrieved for the maximum spacing value considered ($s = 85$ cm). The more the spacing is reduced, the more the bumps are getting pronounced with a peak shifted to a higher frequency. This phenomenon can be attributed to resonance effects, as outlined by the resonance frequencies $f_{r1}^{1v} = c_0/(2s)$ superimposed in Fig. V.16 and close to the peaks. Hence, one can say that the present methodology cannot be applied using a single vane channel with periodicity conditions, in particular for $s = 8.5$ cm (corresponding to the present cascade configuration). The next section is devoted to two main extensions proposed in order to get more realistic predictions:

- (i) A possible decorrelation of the turbulence in the transverse y direction through the use of a 3-wavenumber turbulence spectrum (with $k_z = 0$);
- (ii) Simulations over multi channels using a 2-wavenumber or 3-wavenumber turbulence spectra.

V.2.5 Parametric study on the vane count in the CAA domain and influence of the blade to blade acoustic correlation in FWH analogy

In addition to taking into account several vanes for the CAA calculation, the k_x and k_y wavenumbers are also taken into account. The k_z wavenumber has indeed shown to be of little importance in the case of non-leaned and non-swept vanes in Section V.2.3. Nevertheless, its influence on serrated airfoils will be discussed in Section V.2.6. The $(k_x, k_y, k_z = 0)$ wavenumber formulation, detailed in Section III.3.3, is considered here. As a result of the boundary conditions along the y axis, it is necessary to satisfy the following relation $k_y = n2\pi / L_y$ (with L_y the width of the domain). Validation of the implementation is demonstrated through the velocity autocorrelation spectra in Fig. V.17. The spectra are more chaotic in Fig. V.17 than in Fig. III.7, since a larger Δf is used. However, Fig. V.17 demonstrates that turbulence is advected in a satisfactory way by probing the signal near the LE of NACA airfoils.

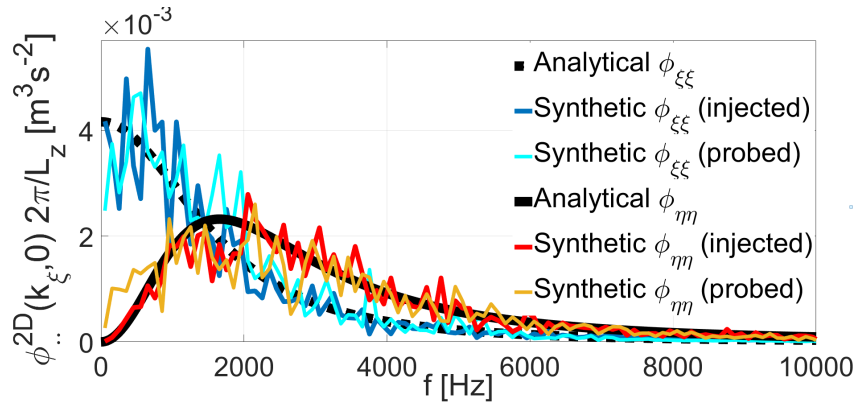


Figure V.17: Velocity autocorrelation spectra (synthetic turbulence generated with a $\Delta f = 10$ Hz and averaged on 100 Hz bands). Probe is located near the leading edge.

Several simulations have been performed with different vane counts. All new computations within this section are carried out with $\Delta f = 10$ Hz and averaged over 100 Hz bands. The new turbulence implementation has been used not only for a single channel domain but also for a domain containing several vanes, as 7 for example in Fig. V.18.

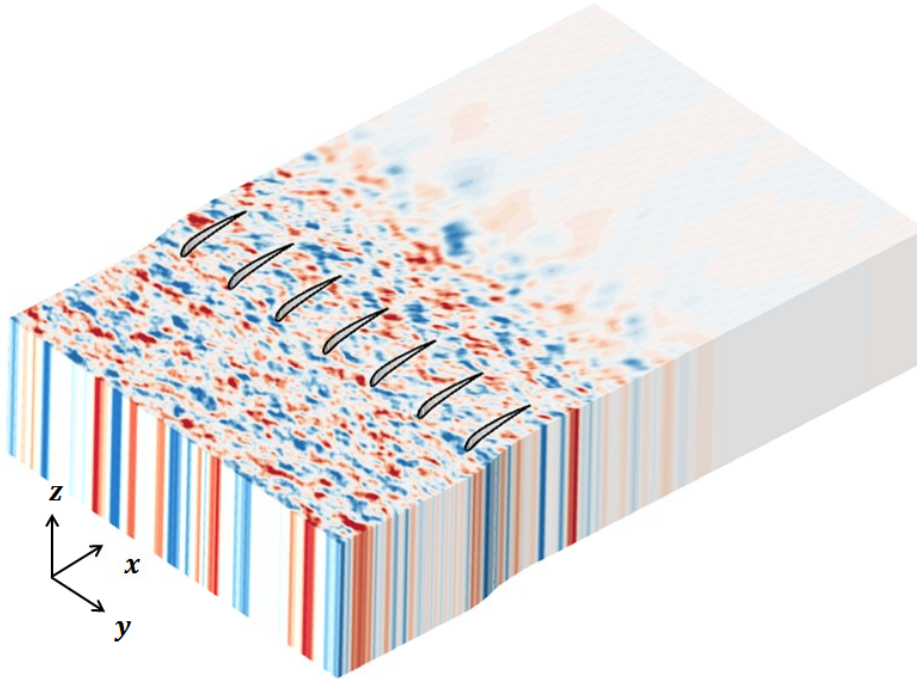


Figure V.18: Snapshots of u'_y [m·s⁻¹] for the 7 vanes configuration (levels between -2 and 2).

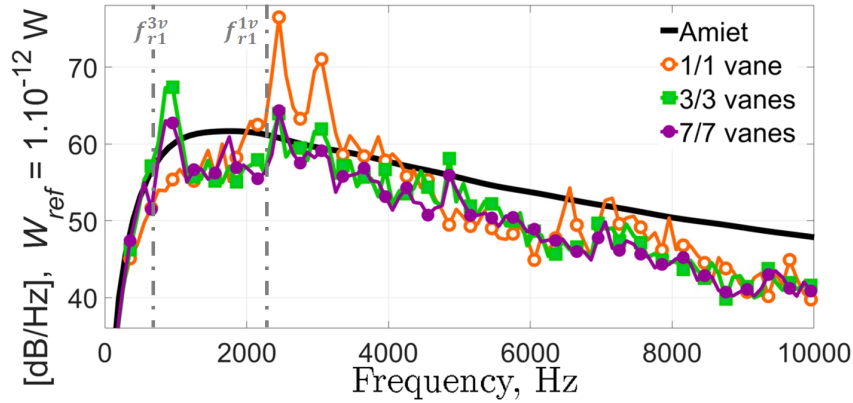


Figure V.19: Downstream PWL spectra using CAA with different vane channels.

In Fig. V.19, all the vanes of the CAA are considered for the FWH calculation. There is a gap between whether or not one or several channels are considered. The greater the distance L_y is, the more there are modes k_y that are not multiples of $2\pi/s$. For 1-channel simulation in Fig. V.19, since all k_y are multiples of s , the results obtained with $(k_x, k_z = 0)$ and (k_x, k_z) turbulence structures from Fig. V.14 are recovered. However, a decrease in the acoustic level is observed for the peaks in medium frequency for multiple channels simulations. In addition, one or several additional peaks appear in low frequency which seems to be due to a resonance associated with the distances sub-multiples of s . Their amplitude decreases as the number of vanes is increased (see Fig. V.19). In [14], it has been proven that for a 20-channels computation they almost disappear. However, such a computation is too expensive. A compromise between computational cost and fidelity seems to be achieved when at least three vanes are considered.

Vane-to-vane correlation effects on far-field acoustics

Figure V.20 allows us to assess the role played by the phase dependency (considering uncorrelated or correlated vanes in the FWH integration) on the acoustic spectra. In particular, there is a noticeable shift in the area of the resonance bumps in medium frequency when the correlation is not taken into account for the far-field calculation. It is therefore important to consider all the vanes dependently in the FWH integral method.

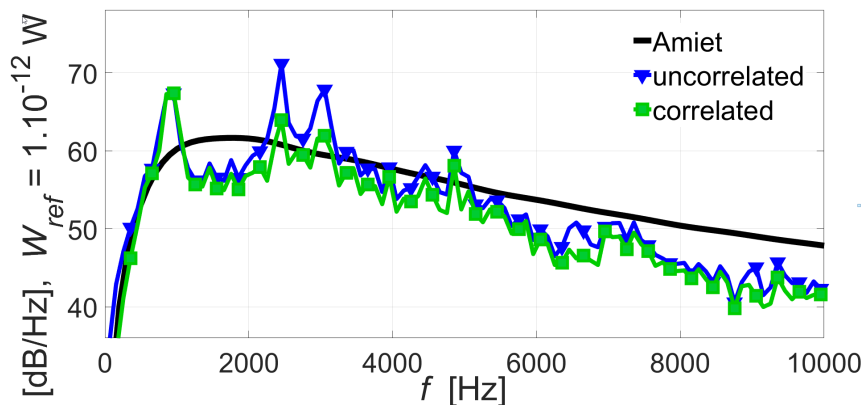


Figure V.20: Downstream PWL spectra per vane. CAA for a 3 channels computation.

V.2.6 Evaluation of the radiated sound depending on the structure of the injected turbulence

Choice of the CAA set-up

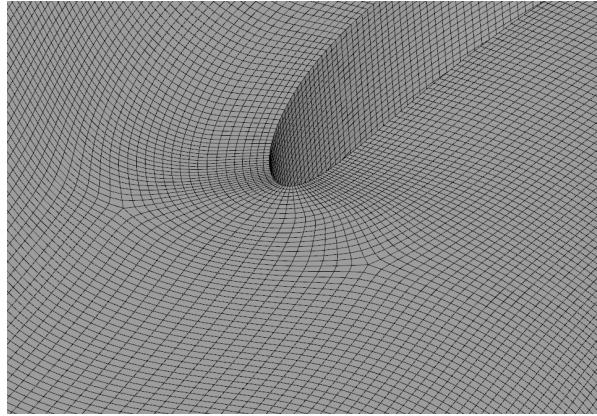


Figure V.21: CAA OH-type pattern mesh at the leading edge.

The CAA simulation set-up uses the boundary conditions presented in Figs. V.10 and V.9. Except for the one channel computations and the parametric study on the vane count in Section V.2.5, which are performed on a H pattern grid, the whole CAA grid is designed using an O-H pattern. This choice facilitates the generation of the 3D mesh for the serrated geometry. Indeed, the mesh is practically designed using the in-house tool *ersatzZ* which allows to apply suitable 3D deformations on the reference skeleton to obtain the serrated shape and to extend them within the grid volume. Both meshing, O-H (Fig. V.21) and H (Fig. V.11) give almost the same result as it is illustrated in Fig. V.22. Only a small difference can be observed in high frequencies, which is consistent with the fact that the new mesh is a bit more dissipative along the y axis.

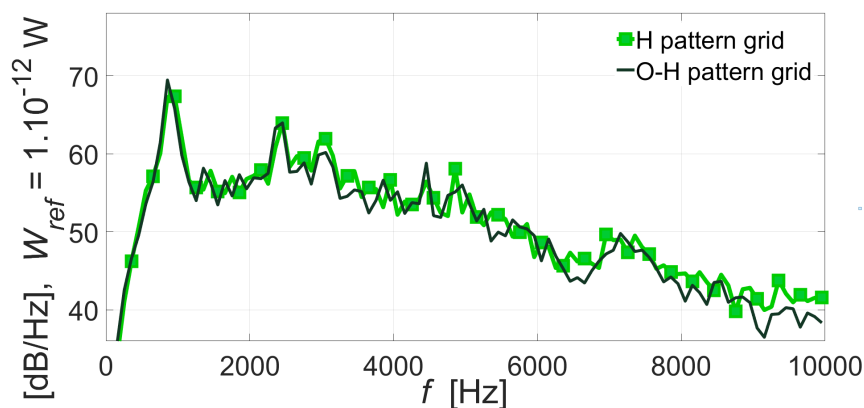


Figure V.22: Downstream PWL spectra per vane of a 3 channels computation (baseline geometry) for the H and O-H pattern meshes. Averaging over 100 Hz bands.

The main conclusion from CAA computations in previous sections, is that multi-channel computations are mandatory to avoid spurious resonance phenomena in the mid frequency range resulting from periodic boundary conditions and requiring including at least 3-vane channels in the CAA domain. A typical result from these parametric studies is depicted in Fig. V.19.

CAA computations for various turbulence inflows

All the simulations discussed in the next paragraphs are carried out using 3-vane channels and the first CAA solutions are completed using fully 3D turbulence modeling detailed in Section III.3.5. The parameters used for the generation of the 3D synthetic turbulence are the following: $L_y = 0.255$ m, $M = 48$, $N = 30$, and $\Delta f = 100$ Hz. In Fig. V.23, snapshots of synthetic turbulent flows related to the transverse velocity (u'_y) are clearly exhibiting the different patterns issued from 1D (a), 2D (b) and (c), and 3D (d) injected turbulence. Note that 1D (parallel gust), 2D (planar), and fully 3D structures are respectively linked to the number of velocity components (1,2 or 3) [84] and then to the non-zero wavenumbers involved in the present turbulence models. All the turbulence formulations are detailed in Chapter III.3.

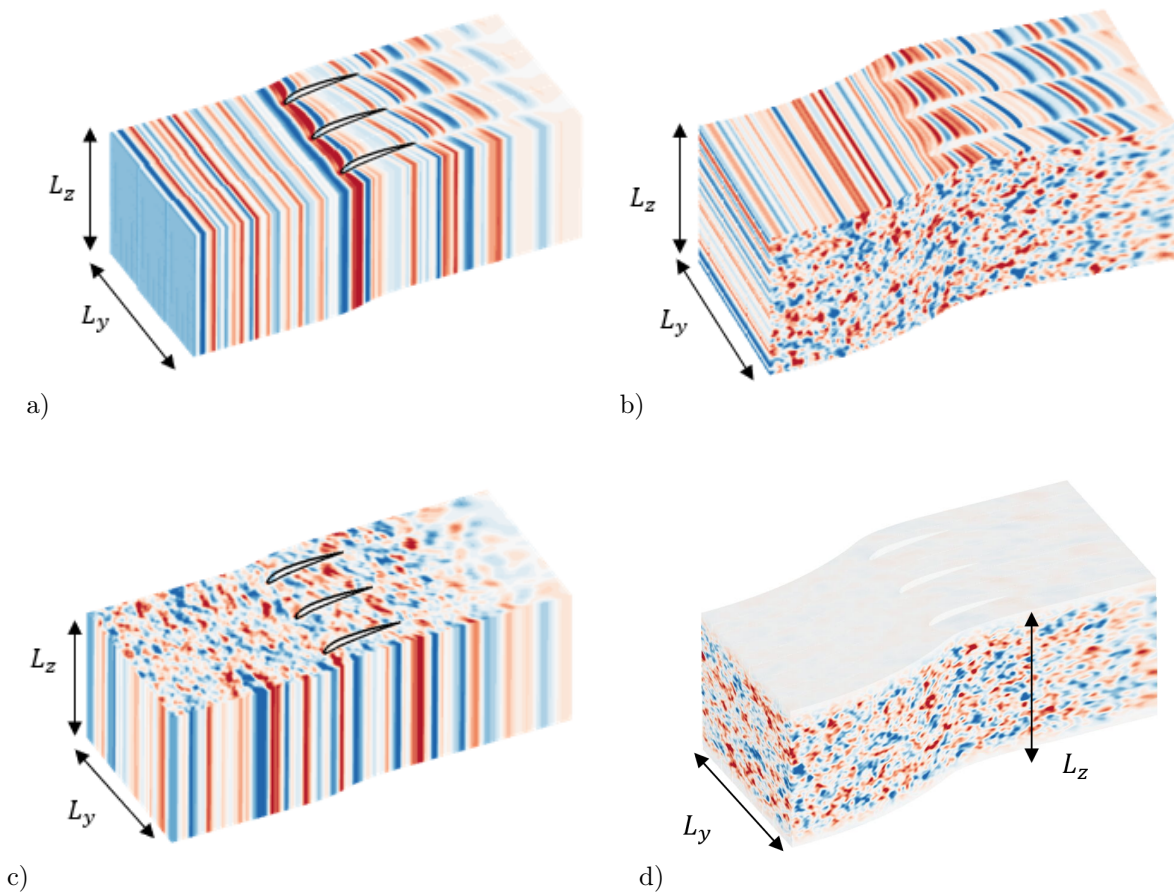


Figure V.23: Turbulent-like u'_y snapshots (levels between ± 2 m \cdot s $^{-1}$ for the $k_z = 0$ cases and ± 10 m \cdot s $^{-1}$ otherwise). Turbulence structures from (a) to (d): $(k_\xi, k_z = 0)$, (k_ξ, k_z) , $(k_\xi, k_\eta, k_z = 0)$, and (k_ξ, k_η, k_z) .

The pressure fluctuations are extracted at the vane skin and radiated in the far-field using the in-house code MIA. The power spectra are obtained by a weighted angular integral over half a circle downstream of the cascade, as performed in Eq. (II.13). In order to compensate the lack of energy input due to the window function $f_w(z)$ (presented in Section III.3.5 and visible in Fig. V.23d), with $R_w = 0.15$, a simple correction is applied to the acoustic spectra, $+20\log(1/(1-R_w))$. These numerical spectra are compared to Amiet's solution for an isolated flat plate in Fig. V.24. Please note that a cascade model as proposed in [86, 95, 41] might be used to get a reliable reference

solution, so that the Amiet-based spectrum is only giving a biased estimate by neglecting the cascade effect. At high frequencies, Amiet's model is over-predicting the acoustic spectra because it does not take into account any airfoil thickness. As a result, a thickness correction from Eq. (V.1) is applied again. For $(k_\xi, k_z = 0)$, (k_ξ, k_z) , and (k_ξ, k_η, k_z) turbulent structures, the computations have been performed with $\Delta f = 100$ Hz and with $\Delta f = 20$ Hz for $(k_\xi, k_\eta, k_z = 0)$ turbulence.

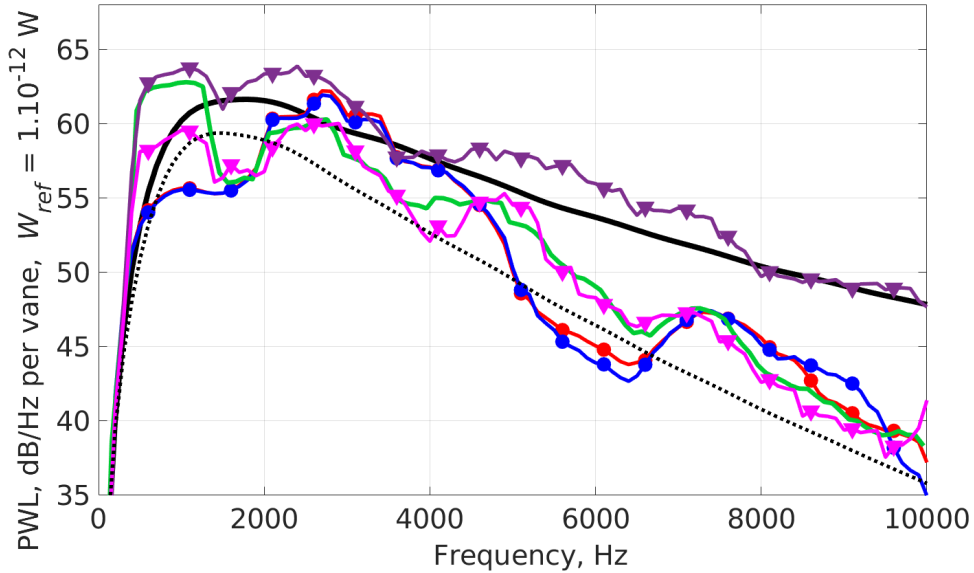


Figure V.24: Amiet's solution without — and with ⋯⋯ thickness correction. Numerical spectra with a 1 kHz moving average: $(k_\xi, k_z = 0)$ $\text{—}\bullet\text{—}$, (k_ξ, k_z) $\text{—}\bullet\text{—}$, $(k_\xi, k_\eta, k_z = 0)$ $\text{—}\bullet\text{—}$, (k_ξ, k_η, k_z) with $\text{div}(\mathbf{u}') \neq 0$ $\text{—}\blacktriangledown\text{—}$, and (k_ξ, k_η, k_z) with $\text{div}(\mathbf{u}') = 0$ $\text{—}\blacktriangledown\text{—}$.

Regarding the numerical spectra associated with $(k_\xi, k_z = 0)$ and $(k_\xi, k_\eta, k_z = 0)$ turbulence fields, one may notice that taking into account k_η provides a more constant slope at medium and high frequency range. However, the bump (around 800 Hz) due to a numerical amplification using periodicity conditions over 3-vane channels instead of 7 is stronger when a turbulence with a varying k_η is injected, see Fig. V.19. Regarding the comparison between CAA results and Amiet's solution, the levels are definitely over-estimated by the isolated flat plate approximation, without the thickness correction. Even if the non-zero divergence turbulence is the closest solution to Amiet's one, it represents in fact the worst numerical prediction. Indeed, following literature [14, 41], a few decibels reduction is at least expected at low frequencies due to the cascade effect and at high frequencies due to the non-zero thickness of the airfoils [138]. Looking at the divergence free result, taking into account the k_z wavenumber seems not to modify the spectra (green vs. pink curves) except for the resonance bump at low frequencies (link with the 3-channel periodicity), which is in accordance with previous numerical simulations comparing $(k_\xi, k_z = 0)$ with (k_ξ, k_z) and also, with Amiet's theory (see Section II.1.2.1).

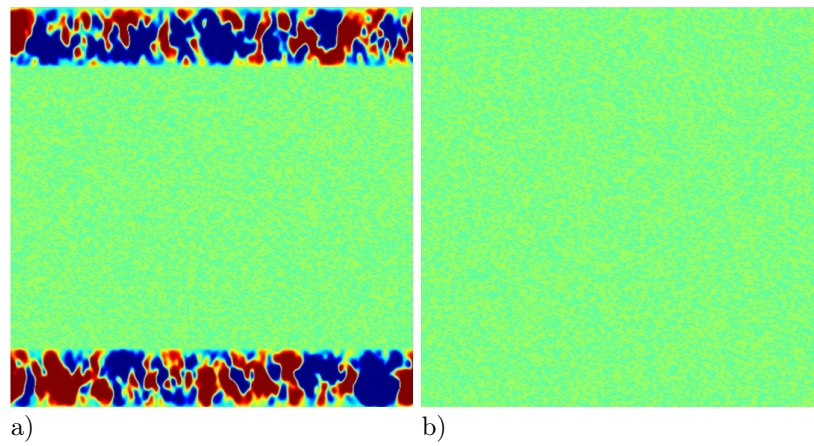


Figure V.25: $\text{div}(\mathbf{u})$ (levels between $\pm 100 \text{ s}^{-1}$) over the injection surface. Fully 3D turbulence with non-zero divergence (a) and with divergence free formulation (b).

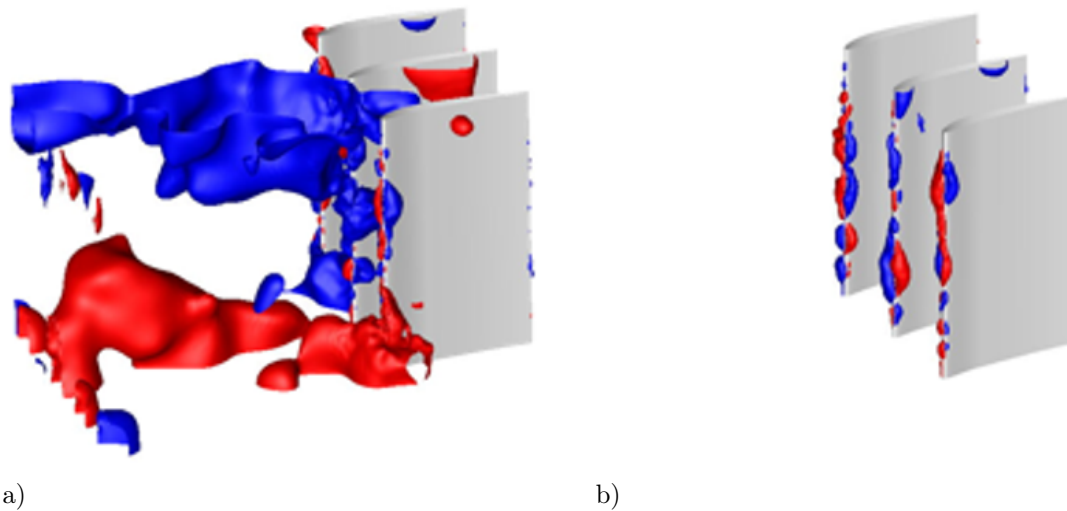


Figure V.26: Isosurfaces of p' at $\pm 200 \text{ Pa}$. Turbulence (k_ξ, k_η, k_z) with non-zero divergence (a) and (k_ξ, k_η, k_z) with divergence free formulation (b).

Snapshots of the turbulent-like velocity divergence are plotted in Fig. V.25, at the injection plane. In the non-zero divergence case plotted in Fig. V.25a, the divergence amplitude is non-negligible in the region where the window function derivative is maximum. On the contrary, with the divergence-free formulation, the issue disappears as illustrated in Fig. V.25b. As clearly visible on iso-surfaces of fluctuating pressure in Fig. V.26, the non-zero divergence formulations (Fig. V.26a) gives rise, close to areas of maximum divergence in Fig. V.25a, to local intense spots extending through the CAA domain and interacting with the vanes, and responsible for some spurious noise. On the contrary, the solution obtained with the divergence-free formulation (Fig. V.26b) is found to be much cleaner without the generation of artificial pressure waves.

V.2.7 Noise reduction as a function of the injected turbulence

The leading edge serrations have been defined in Chapter IV.2, and aerodynamically assessed in Chapter V.1. From this aerodynamic study, the d_0 design has been discarded and a d_2 design improved from aerodynamic point of view has been proposed. The aeroacoustic simulations are only performed on the low-noise design d_1 .

Mean flow and CAA computation

To obtain the mean flow around the new geometry with the 2D Euler open-source code, the computation was performed on z planes, from which the velocity field has been then interpolated on the 3D CAA mesh. Thus, U_z is set equal to zero in the overall domain, which is a proper approximation. Indeed, the vertical (radial) component of the mean flow velocity has shown to be almost negligible in comparison with the other velocity components by RANS solutions discussed in Section VI, and also consistent with previous studies on realistic turbofan configurations [144]. The resulting Eulerian mean flow fields, in terms of axial velocity maps and streamlines visualization, are plotted in Figs. V.27a and V.27b, respectively for planar cuts at root and peak of the serration. The streamlines are perfectly aligned to the airfoil geometry for these two tricky positions, which should allow to properly assess the turbulence-airfoil sources and sound propagation in the CAA.

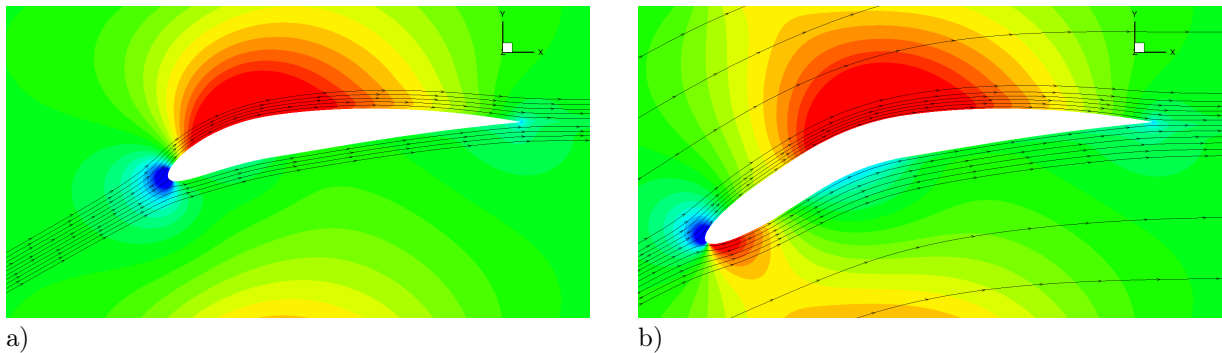


Figure V.27: Isocontour maps of U_x (levels between 60 and $120 \text{ m} \cdot \text{s}^{-1}$) with streamlines. Cuts at the root (a) and peak (b) of the serration.

In order to obtain the CAA mesh for simulations on the d_1 design, the ersatzZ modeler which has been used in Chapter IV.2 to apply morphing to the baseline NACA7310, is also able to extend the skeleton deformations to the cells of the volume mesh, as illustrated in Fig. V.28.

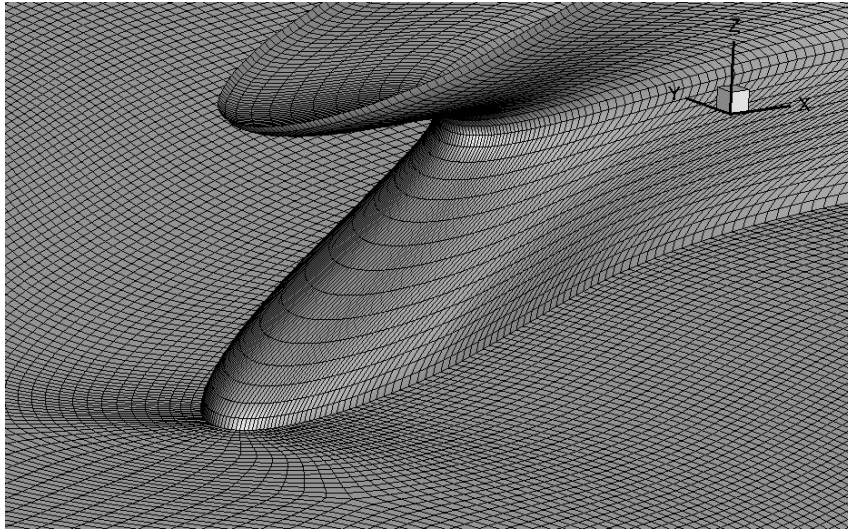


Figure V.28: Views of the skin CAA mesh and z slice at the peak of the serration.

The contour maps of the RMS pressure fluctuations from CAA on the vane skin are plotted in Fig. V.29. Moreover, the strongest pressure sources are located at the roots and peaks of the serrations in accordance with the literature [14, 144]. Finally, the pressure fluctuations are equally distributed over the 3 vanes, in agreement with the prescription of periodicity conditions (enforced in the transverse direction), indicating the good convergence of the CAA computation.

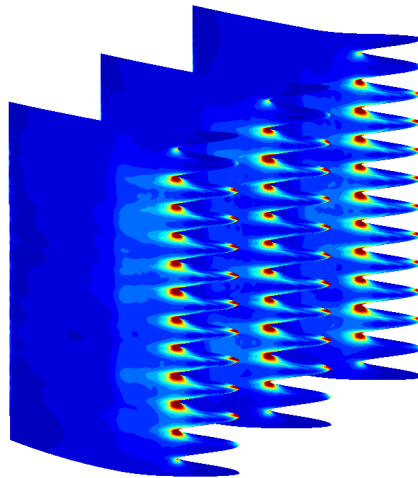


Figure V.29: RMS wall pressure p'_{rms} , Pa (levels between 0 and 500 Pa).

Sound Power Level reductions (Δ PWL) from CAA and analytical solutions

The noise reduction assessed in terms of Δ PWL spectra are summarized in Fig. V.30. The numerical predictions with the different synthetic turbulence injections are compared with both an analytical solution and a semi empirical law proposed by ISVR [138]. The analytical solution presented in Section II.1.2.2 satisfies the Helmholtz advective equation and is obtained from a the Wiener-Hopf technique for any piecewise leading edge geometries. It has been slightly modified for applications to finite span airfoils in Section IV.1.1. The semi-empirical law from [138] provides the optimal noise reduction occurring when $\lambda_s = 2L_{\xi\xi}$, for a single-wavelength geometry in terms

of the Strouhal number, $\Delta\text{PWL}=10\log(St)+10$. There is a good agreement between the different solutions in the medium frequency range especially in comparison with the semi-empirical law. As discussed in previous numerical studies [61], omitting the spanwise turbulence variation leads to an over-prediction of the noise reduction particularly at high frequencies. The 3D turbulence numerical prediction (in pink) exhibits a slightly smaller noise reduction at high frequencies compared to other CAA computations in particular the 2-wavenumbers (k_ξ, k_z) formulation (in blue). Hence, it is remarkably close to the WH solution. Practically, this study highlights that the (k_ξ, k_z) turbulence model is a good compromise in terms of accuracy against CPU time for the noise reduction prediction. In particular, the ΔPWL spectra achieved in this case is found to be almost identical when using 1-channel or 3-channels simulations, which makes this approach very attractive. However, the latter conclusion should be nuanced, since it is limited to a rectilinear cascade set-up.

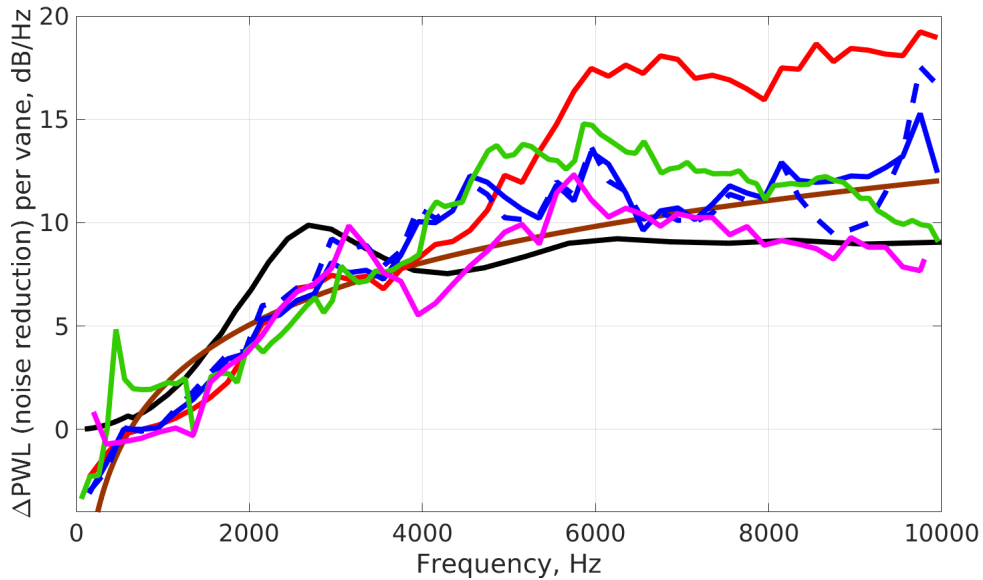


Figure V.30: Wiener-Hopf — and semi-empirical log-law — . Numerical spectra with a 1 kHz moving average: $(k_\xi, k_z = 0)$ — , (k_ξ, k_z) — (1-channel —), $(k_\xi, k_\eta, k_z = 0)$ — , and (k_ξ, k_η, k_z) — .

The expected acoustic performances from numerical, analytical, and semi-empirical approaches are gathered in Table V.3. A good agreement is found between the trends drawn from Fig. V.30 and the average noise reduction provided in Table V.3. However, drawing conclusions from the overall sound power level noise reductions (ΔOAPWL) is a bit tricky, since it is influenced by the shape of the baseline noise spectra. Indeed, due to resonance phenomenon associated with periodic boundary conditions, some bumps appear in the spectra which tend to over-predict the noise emission around 500 to 1000 Hz, for the 3-channel set-up. The later bump is a bit less visible on a multi-channel computation with a turbulence invariant along the cascade directions, as shown in Fig. V.24. Consequently, in order to give a better idea of the overall noise reduction for the multi-channel computations, the frequency range 1300 Hz to 9800 Hz is also considered. In any case, a significant ΔOAPWL (noise reduction) around 6 dB is expected for all the methods.

	Avg. Δ PWL, 0.2-9.8 kHz	Δ OAPWL, 0.2-9.8 kHz	Δ OAPWL, 1.3-9.8 kHz
WH	7.3	5.5	6.8
$10 \log(St) + 10$	7.5	4.9	6.1
CAA ($k_x, k_z = 0$)	11.0	5.2	6.2
1-vane CAA (k_x, k_z)	8.7	6.7	7.1
CAA (k_x, k_z)	8.6	5.4	6.4
CAA ($k_x, k_y, k_z = 0$)	9.0	3.9	5.3
CAA (k_x, k_y, k_z)	7.2	3.5	5.7

Table V.3: Average Δ PWL and Δ OAPWL, [dB].

V.3 Lattice Boltzmann simulations

High fidelity LBM simulations with the ProLB software introduced in Section II.2.3 are now carried out on the full experimental rectilinear cascade test rig. This high fidelity LBM approach is expected to provide quantitative results closer to experimental data than a CAA modeling. Section V.3.1 is focused on the description of the numerical set-up and parameters, the grid definition, and the convergence achievement. Aerodynamic and acoustic analyzes are discussed in Section V.3.2 devoted to the comparisons with other prediction approaches and the experimental data. It can be noted that these LBM simulations are performed in blind, ahead of the test campaign.

V.3.1 Set-up of lattice Boltzmann simulations

V.3.1.1 Overview of the iterative set-up process

Contrary to previous CFD RANS and CAA LEE simulations, the turbulence grid and test section are explicitly taken into account in LBM. Geometrical components can indeed be easily modeled by means of immersed boundary conditions in ProLB.

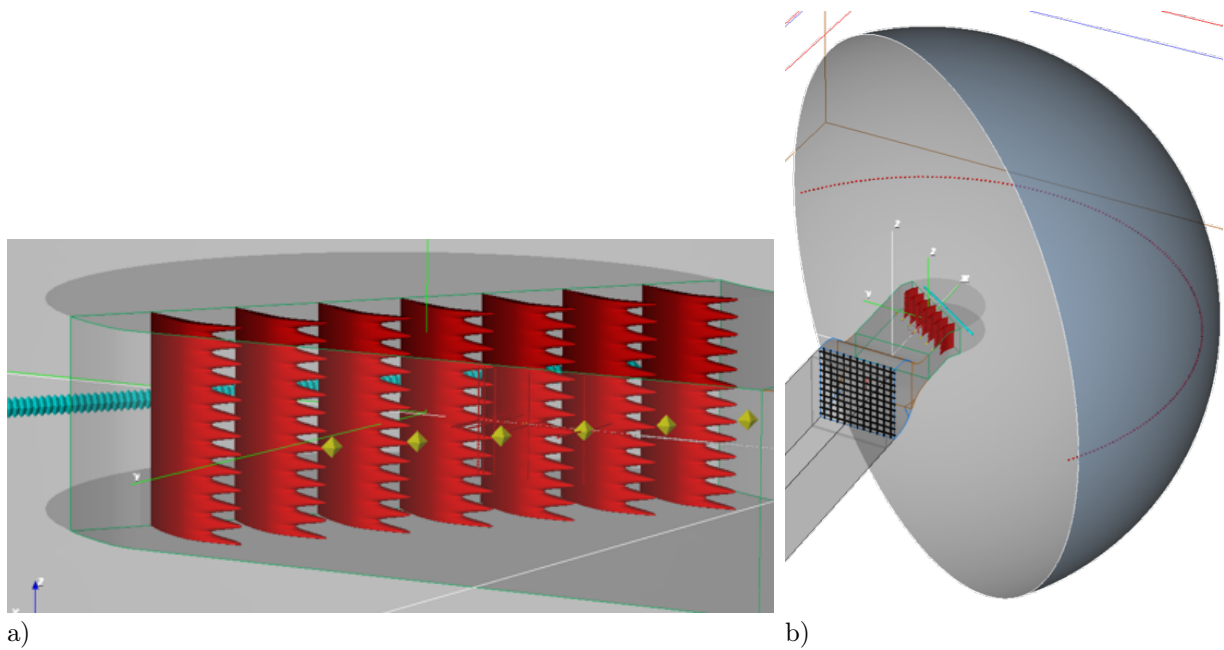


Figure V.31: View of the cascade geometry with serrations (a) and of the test rig geometry (b).

Typical views of the geometry from the graphical user interface of ProLB are reproduced in Fig. V.31. The test section is represented with the nozzle and the grid, along with the seven vanes cascade, here depicted with LE serrations. Far-field point probes are also visible (red dots placed in half-circle), they materialize the experimental microphones array, as presented in Section II.3.1. Two methodologies are considered for acoustic propagation: a direct calculation of the far-field noise obtained from these probes located at microphones locations in the simulation domain and a FWH-based approach for which the unsteady pressure is extracted at vanes' skin and radiated in the far-field (as for CAA modeling). Simulations are carried out at approximately the approach (APP) operating point, corresponding roughly to $M=0.34$. Only results provided with the final set-up referred to as "fine mesh" are detailed in the next sections. However, in order to achieve the final numerical implementation, numerous intermediate simulations have been necessary. Between these various simulations, the main difference consists in adjusting the octree mesh discretization. The zones of interest for the definition of the refinement levels are displayed below.

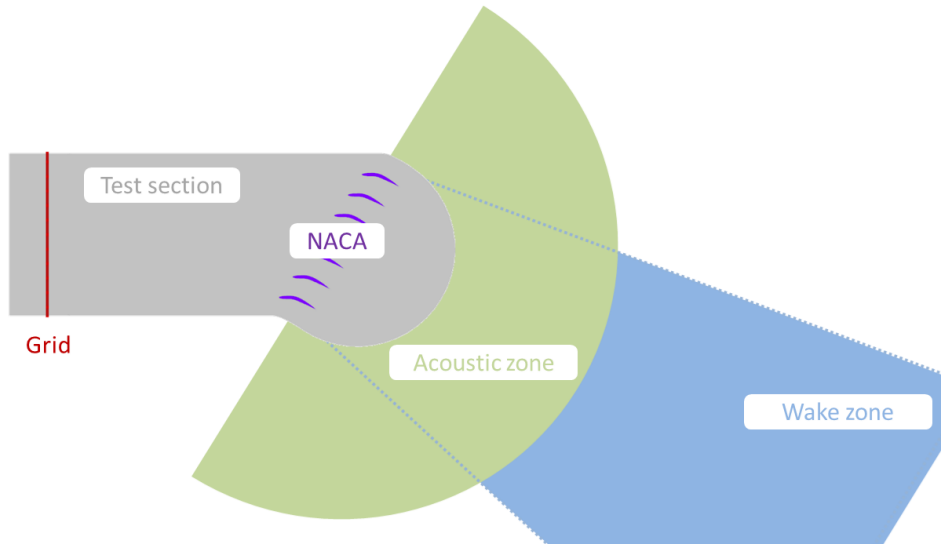


Figure V.32: Areas of interest for the definition of the mesh refinement levels.

Figure V.32 illustrates several zones of prime importance for the definition of the octree mesh refinement levels: turbulence grid, NACA airfoils, test section, acoustic propagation zone and wake zone. The definition of the mesh discretization is a key parameter of the numerical set-ups definition process, which is summarized in the following. The total number of points for each set-up is indicated along with the number of fine equivalent points. The latter quantity consists in weighting the number of points present in each refinement level (noted r_l) by the mesh size ratio compared to the finest mesh dimension. The number of fine equivalent points is given by the following formula.

$$\text{fine equivalent points} = \sum_{r_l=0}^{N_{r_l}-1} (\text{points in level } r_l) \times \left(\frac{1}{2}\right)^{r_l} \quad (\text{V.3})$$

In Eq. (V.3), at each octree transition the mesh size is doubled. Thus, the local time step is twice bigger, which halves the number of temporal iterations (CFL=1 by construction in LBM). Thus, the fine equivalent number of points is a good indicator of CPU cost, whereas the total number of points is mainly limited on ONERA's cluster by the Random-Access Memory (RAM). That is why, adjusting each refinement area is a key parameter of the LBM set-up definition. In the following table, summarizing set-up process, the points are indicated in million. As a reminder, DC denotes the Direct Coupling cell-vertex algorithm used in ProLB, which helps reducing spurious noise sources at mesh transitions.

case	DC	pts (eqv fine)	geometry	comments and highlights
coarse <i>v1</i>	no	170 (133)	baseline	Coarse mesh set-ups are used to perform parametric study to define the velocity condition at the test section entrance to reach the adequate Mach number in front of the cascade, here $M=0.34$. No acoustic area is considered.
coarse <i>v2</i>	no	244 (138)	baseline	The wake zone (cf. Fig. V.32) has been expanded to facilitate the evacuation of the large turbulent structure due to transient period.
medium <i>v1</i>	no	411 (144)	baseline	In medium mesh set-ups, the mesh is twice finer everywhere compared to coarse mesh configuration. Moreover, an acoustic zone (cf. Fig. V.32) is added. The idea of all medium mesh set-ups is to perform first analysis of turbulence grid properties and far-field acoustics.
medium <i>v2</i>	no	550 (237)	baseline	After analysis of turbulent flow properties provided by the medium <i>v1</i> simulation, alteration (dissipation and partial transfer towards larger vortices) of the turbulent field appeared at the mesh transitions inside the test section. Indeed, previous set-ups considered a variable discretization in the test section to account for variable mean flow velocity and thus minimize the number of points. In this medium <i>v2</i> configuration, it has been decided to remove these transitions in the test section and to relocate them at the exit of the test section. This choice avoids undesirable changes in turbulence properties from the grid up to the NACA airfoils. However, the number of fine equivalent points has been increased, in comparison with medium <i>v1</i> case, which has impacted the CPU cost.

medium <i>v2</i>	yes	550 (237)	baseline	The same calculation has been performed with the Direct Coupling cell-vertex algorithm in order to minimize parasitic noise radiation coming from turbulent wake while passing through mesh transitions. However, no clear difference has been observed. Indeed the DC algorithm is particularly efficient when mesh transitions are aligned with mesh directions, which is not the case with the medium set-ups. The latter point is improved with the "fine mesh" configuration.
medium <i>v3</i>	no	948 (263)	baseline	In the previous medium <i>v2</i> set-up, a parasitic noise source was appearing in the simulation domain at the mesh transition between acoustic and wake areas (cf. Fig. V.32). It has been decided to remove this transition, by keeping a constant discretization between acoustic and wake zones. This has been done at the expense of the total number of points. However, a negligible effect on overall performance has been observed since the equivalent fine number of points has not changed so much.
medium <i>v3</i>	yes	948 (263)	baseline	Again, no clear difference in the far-field acoustics with the Direct Coupling enabled. Indeed, in this set-up mesh transitions at the exit of the test section are not aligned with the mesh coordinates. Yet, DC is more efficient at avoiding parasitic noise at mesh transitions crossed by a turbulent wake when these transitions are non-oblique or curved. The "fine mesh" configuration improves the latter point by considering straight mesh transitions.

medium $v3$	no	954 (262)	serrated d_1	A first simulation with the serrated d_1 geometry has been performed in order to assess the noise reduction. A maximum 4 dB reduction at mid-frequencies has been obtained with the FWH integral method. However, with direct noise evaluation, almost no noise reduction was observed (0.5 dB).
fine	yes	1 790 (338)	baseline	Two major modifications are introduced with respect to the medium $v3$ configuration. First, an additional layer of refinement around the airfoils is added in order to improve acoustic source capture and aerodynamic predictions. Moreover, the mesh transitions between the test section and the acoustic area are spaced and aligned with the mesh direction. The aim is to reduce the strength of turbulent wakes crossing mesh transitions along with a better working of the DC algorithm due to straight transitions.
fine	yes	1 803 (350)	serrated d_1	The key point is the evaluation of the far-field noise reduction (with the low-noise geometry d_1) both with indirect (integral method) and direct acoustic calculations. Aerodynamic behavior is compared to reference RANS calculation from Chapter V.1. Significant noise reduction of 4 dB is now observed with the direct prediction.
fine	yes	1 819 (365)	serrated d_2	Due to a larger mean chord with the d_2 design, the number of points is slightly increased in comparison with d_1 set-up. The possible impact of serrated design d_2 on noise reduction is assessed. Again aerodynamic behavior in terms of Cp profile is compared to the reference RANS solution.

Table V.5: Overview of the main numerical configurations for LBM simulations.

Main LBM set-ups investigated through these laborious but necessary iterative simulations (in order to get an accurate solution) are provided in Table V.5. Although small changes which occurred during different trials are not listed, three main highlights from the Table V.5 are illustrated below.

1. Initially, mesh transitions were located inside the test section to limit the number of points by taking advantage of the flow acceleration induced by the nozzle. But it led to the turbulent structures alteration with a partial transfer of the energy towards larger vortices. Keeping a constant discretization from grid to cascade has solved the issue as illustrated in Fig. V.33.

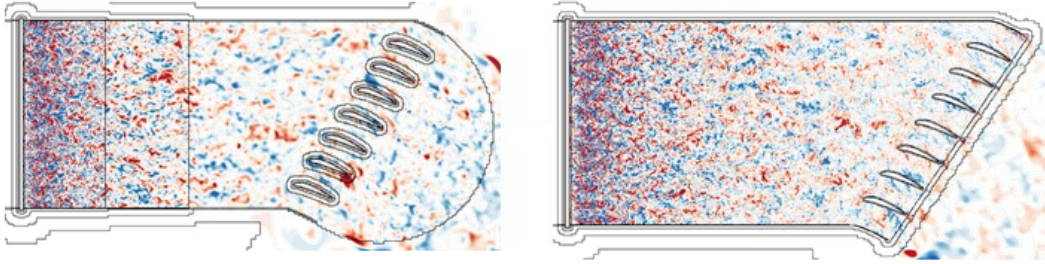


Figure V.33: $u'_z \pm 10$ [m/s] velocity fluctuations for two set-ups: medium $v1$ (left) and medium $v2$ (right).

2. In medium set-ups, a 300 points per chord discretization have been considered around the airfoils, whereas with the fine mesh configurations, there are 600 points per chord. Increasing the total number of points has significantly reduced additional pressure sources at the trailing edge and at mid-chord, which is expected to help better distinguishing the leading edge noise mechanism as depicted in Fig. V.34.

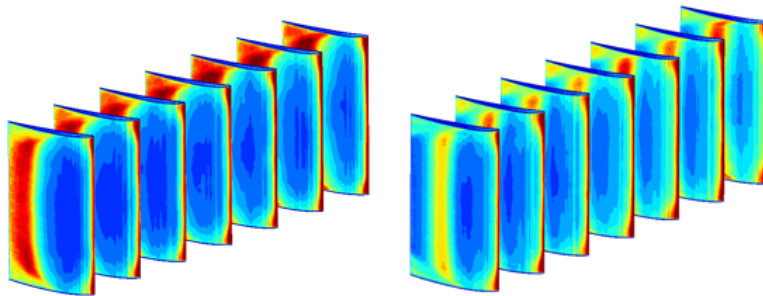


Figure V.34: p'_{RMS} 0 to 500 [Pa] for two set-ups: medium $v3$ (left) and fine (right).

3. A parasitic noise source was appearing with the medium $v2$ when the turbulent wake was crossing the curved mesh transition in Fig. V.35 (left). Removing the latter in the medium $v3$ set-up has solved the issue. However, three tilted mesh transitions remained in the medium $v3$ configurations. With the final fine mesh set-up, these mesh transitions have been aligned with the mesh axis, as illustrated in Fig. V.35. Moreover, the Direct Coupling (DC) algorithm has been used, the latter being particularly efficient at the reduction of parasitic noise sources occurring with straight mesh transitions. While almost no noise

reduction with direct calculation (far-field probes in the numerical domain) was achieved when comparing baseline and serrated geometries with the medium $v3$ set-up, a reduction of few decibels was obtained with the fine mesh. This might be a combination of straight separated mesh transitions in combination with the DC algorithm, and a finer mesh around the airfoils in Fig. V.34.

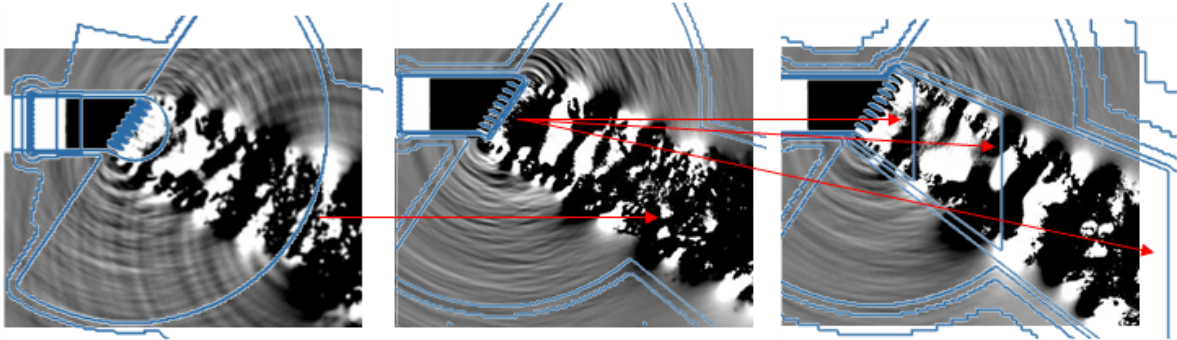


Figure V.35: $p - p_\infty \pm 25$ [Pa] pressure fluctuations for three set-ups: medium $v2$ (left), medium $v3$ (center), and fine (right).

A detailed presentation of fine mesh set-up definition is given in the following section.

V.3.1.2 Fine mesh refinement

It can be pointed out that simulations on the fine mesh configurations have been made possible thanks to a unique availability of the ONERA supercomputer during a special event called "Young Researcher Challenge".

Parameter / Geometry	baseline	serrated d_1	serrated d_2
CPU cores	≈ 4000	≈ 4000	≈ 8000
solver restitution time (days)	≈ 3.5	≈ 3.5	≈ 2
CPU core time (hours)	≈ 300 k	≈ 320 k	≈ 400 k

Table V.6: HPC characteristics of LBM simulations on ONERA's supercomputer Sator.

Main HPC features of these simulations are presented in Table V.6. In particular these LBM simulations provide an opportunity to test ProLB scalability up to 8000 cores. With 8000 cores, the restitution time has been approximately accelerated by a factor 1.6. Regarding the octree mesh definition, Figs. V.36 and V.37 show where the separations between different mesh refinement levels are located.

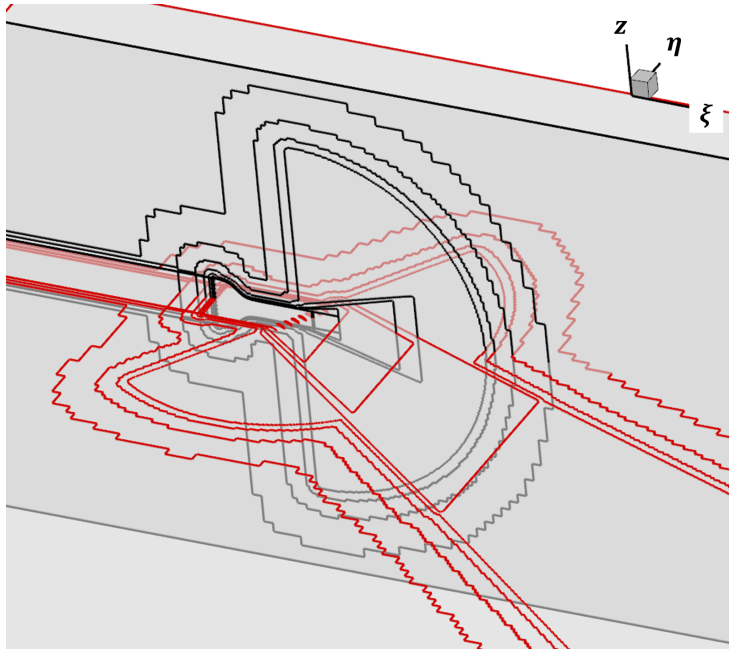


Figure V.36: Sketch showing mesh transitions in planes $z = 0$ and $\eta = 0$.

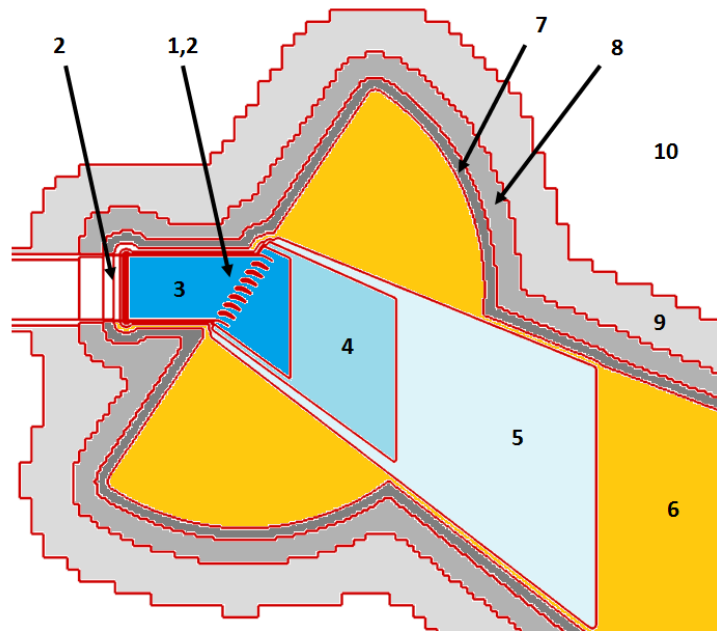


Figure V.37: Mesh refinement levels in the plane $z = 0$.

The number of points and the number of fine equivalent points for each discretization region are indicated in Table V.7, in terms of percentage to the overall point number (total or fine equivalent). The zone index corresponds to the numbering introduced in Fig. V.37. With this distribution, 14 points per wavelength are ensured for the turbulent flow in front of the cascade. In the acoustic area at 10 kHz there is only 5 point per wavelength whereas from the LBM community the recommended value is around 8 point per wavelength at minimum, which is satisfied up to about 6.5 kHz in the acoustic area.

zone n°	1	2	3	4	5	6	7	8	9	10
mesh size (mm)	0.2	0.4	0.8	1.6	3.2	6.4	12.8	25.6	51.2	102.4
points in zone (%)	≈ 6	≈ 3	≈ 34	≈ 14	≈ 11	≈ 29	≈ 1	≈ 0	≈ 0	≈ 0
eqv. fine points in zone (%)	≈ 31	≈ 8	≈ 44	≈ 9	≈ 4	≈ 5	≈ 0	≈ 0	≈ 0	≈ 0

Table V.7: Mesh characteristics at each discretization level.

Table V.7 indicates that discretization inside the test section (for convection of turbulence structures) is the main contributor to both the CPU cost and RAM usage. The second major component of the CPU cost is the NACA airfoils. Moreover, increasing the mesh cut-off frequency in the acoustic area n°6, from approximately 6.5 to 13 kHz, has been prevented by limited RAM capabilities. Indeed, the number of points in the acoustic region n°6 would have been multiplied by 8, which an increased contribution to 77% of the total number of points. XY cuts of the octree meshes around a turbulence grid bar and close to the NACA LE are presented in Fig. V.38. Two successive layers of mesh of 8 points (above the minimum recommended value of 6) protect the airfoil's geometry, with a resolution of nearly 600 points per chord at the finest level.

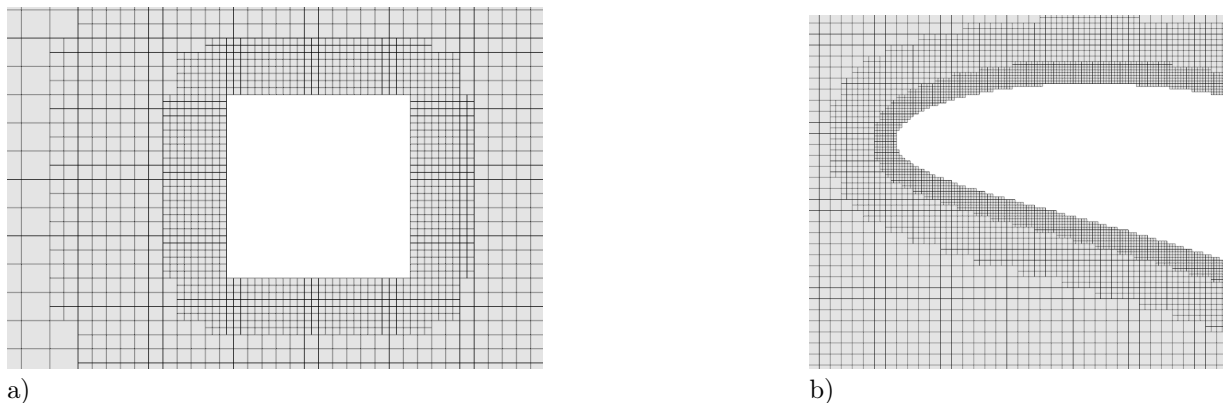


Figure V.38: Octree mesh for the "fine mesh" configuration around a grid bar (a) and a NACA airfoil LE (b).

Numerical parameters of the fine mesh set-up are gathered in Table V.8. The operating condition is driven by velocity injection in a plane upstream of the turbulence grid. The law defining the inflow velocity is also given in Table V.8. Finally, some absorbing layers are added in the far-field to damp waves in addition to the octree mesh de-refinement.

Parameter	Value and comment
dx_{min}	2 mm
Reference c_0	343 m/s
Time step	3.36 e-7
Number of It.	1 200 k
Simulated Time	0.404 s
SISM cut-off frequency	15 kHz
Inflow conditions	$U_{injection} = 38.0*(It/200000)*(It < 200000) + 38.0*(It \geq 200000)$

Table V.8: Numerical parameters of the simulations. SISM refers to the Shear-Improved Smagorinsky Model. $U_{injection}$ denotes the velocity conditions imposed at the entrance of the test section.

V.3.1.3 Validation of the set-up and mean flow convergence study

The choice of the discretization around the grid and NACA profiles is partially validated by the $y+$ non-dimensional distance to the wall plotted in Fig. V.39.

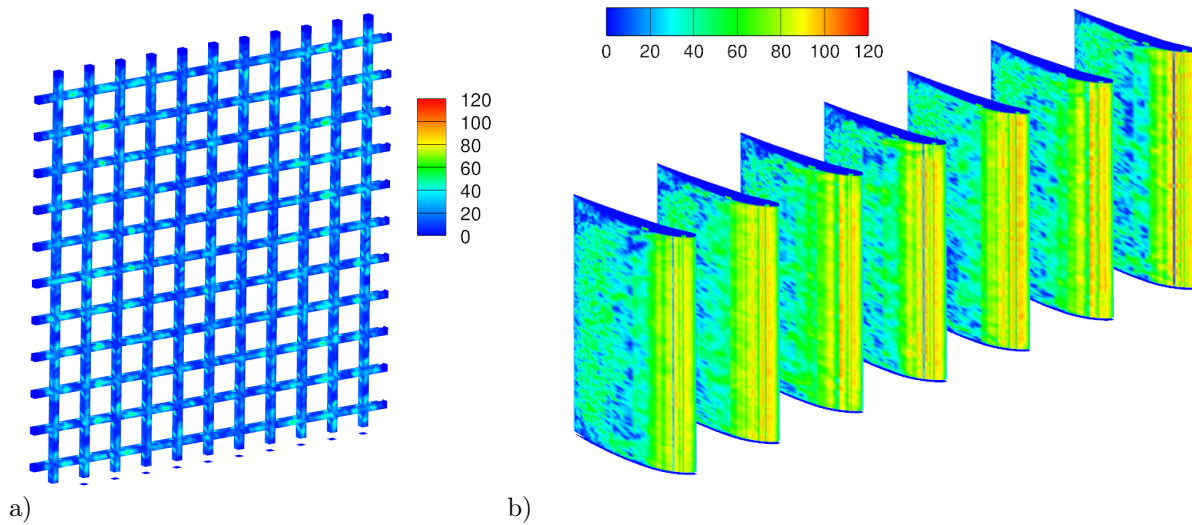


Figure V.39: Average $y+$ at the turbulence grid surface (a) and at the airfoil skin (b).

Figure V.39 shows that $y+$ values are under 300 which is a threshold value for LBM simulation with a wall log-law model. In addition to the surface outputs, several lines of probes are included in the LBM simulation domain, apart from those materializing the half-circle microphone array (plotted in Fig. V.31b).

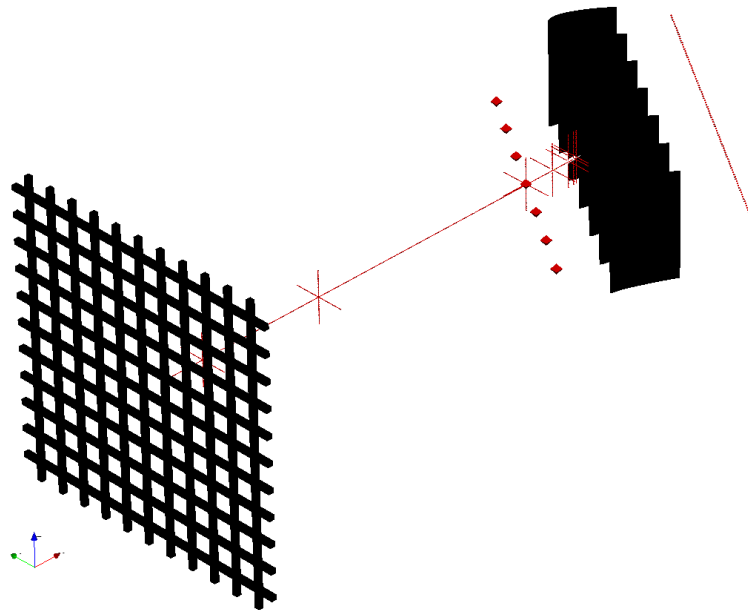


Figure V.40: Sketch of probes arrays (red lines) in the test section.

Temporal signals are recorded at locations displayed by red dots in Fig. V.40. Regarding the convergence toward the experimental operating point, the target inflow speed regime has been measured at a distance of one chord in front of the vane cascade at the center of the test section. The transient time has been reduced along with an improved stability of the computation by considering a time ramp on the inflow velocity condition. Without this ramp, an overshoot of the velocity could lead to a crash of the simulation.

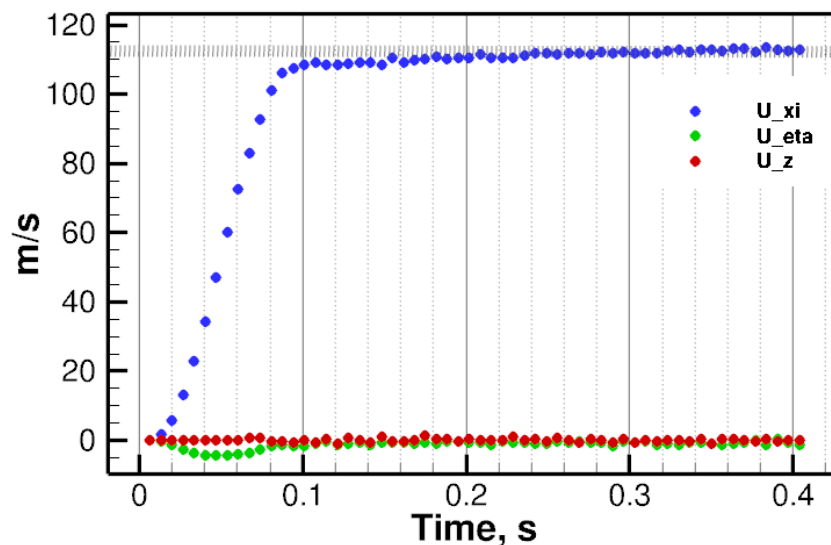


Figure V.41: Mean flow convergence along each space direction.

A rather good convergence of the mean flow properties is obtained after a transient time of approximately 0.2 s, as demonstrated in Fig. V.41.

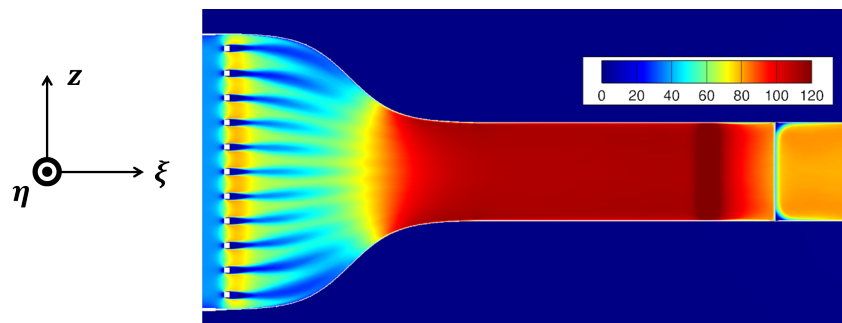


Figure V.42: Axial mean flow velocity U_ξ (m/s) at the end of the simulation. Values averaged on 66 advection chords in the plane $\eta = 0.025$ m.

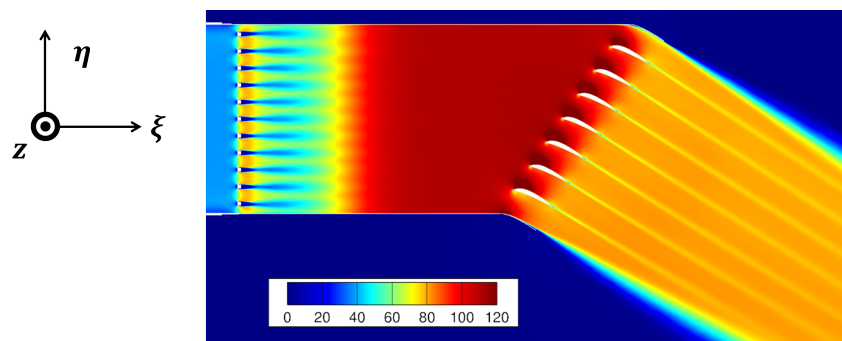


Figure V.43: Axial mean flow velocity U_ξ (m/s) at the end of the simulation. Values averaged on 66 advection chords in the plane $z = 0.025$ m.

Figures V.42 and V.43 illustrate the mean flow U_ξ velocity. The squeezing effect of the nozzle on the mean flow is clearly visible, the mean flow is only homogenized at the exit of the nozzle. The blocking effect of the grid is also observable.

V.3.2 LBM solution analyzes and cross-comparisons with other predictions and experimental data

Aerodynamic and aeroacoustic results mainly provided by the LBM simulations are compared to experimental data from the InnoSTAT test campaign on the rectilinear cascade. Experimental data and ready-user files have been provided to ONERA by E. Salze and V. Clair from Centrale Lyon who are gratefully thanked. Additional details about the measurements are presented in Section II.3.1. Comparisons are also performed here with analytical solution (WH model) and hybrid CFD/CAA computations discussed in the previous part. As discussed previously when introducing LBM simulations, preliminary convergence studies were performed on the "medium mesh" configuration introduced in Table V.5 and continued with the "fine mesh" configuration.

V.3.2.1 Basic aerodynamic validation of the baseline and serrated vanes

First, a comparison between LBM simulations and reference RANS calculations is performed. It has to be noted that the RANS computations consist in a 1-vane computation with periodic boundary conditions (see Chapter V.1 for more details), whereas for the LBM simulations, the

full set-up is considered. The mean flow properties are extracted at mid-span for RANS and LBM. The central vane is taken into account for LBM aerodynamic extractions since it is the less influenced by the side plates.



Figure V.44: Contour maps of mean Mach number for RANS (left) and LBM (right) computations. Levels between 0 and 0.5.

Figure V.44 illustrates the mean velocity field, in terms of mean Mach number, provided by RANS and LBM computations, where small differences appear. For instance, the boundary layer thickness near the TE (at the suction side) is slightly greater with the RANS. The wall pressure coefficient C_p is also compared. It is assessed experimentally as well on the reference vane at mid-span, for a flow speed of 117 m/s, and compared to RANS and LBM predictions in Fig. V.45. The C_p has been computed as follows:

$$C_p = \frac{p - p_{\text{ref}}}{\frac{1}{2}\rho_{\text{ref}}U_{\text{ref}}^2} \quad (\text{V.4})$$

where subscript $_{\text{ref}}$ denotes mean reference value measured half chord upstream of the airfoil.

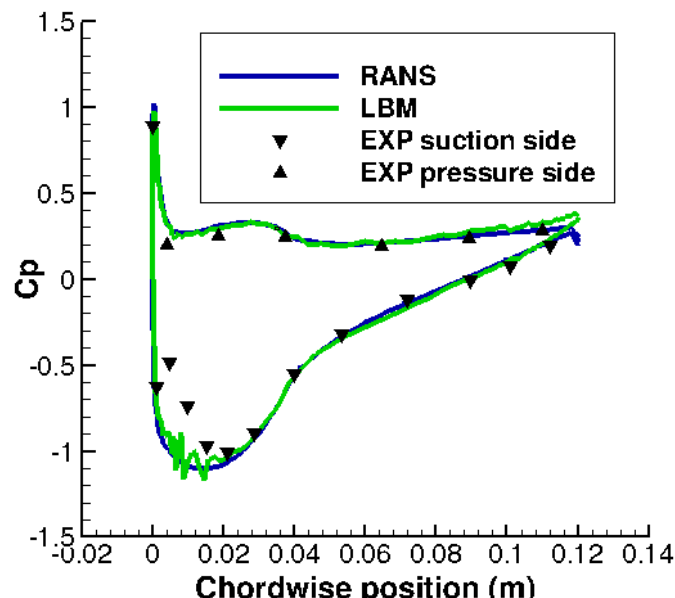


Figure V.45: C_p profile of the central vane at mid-span for the baseline configuration at $M=0.34$.

A fairly nice agreement is pointed out between the three approaches. However, small oscillations on the suction side are visible on the LBM results. Indeed, in this region, large curvature induces steep geometrical variations of the intersection between the immersed boundary conditions and

the octree mesh, which may produce some oscillations in the boundary solution.

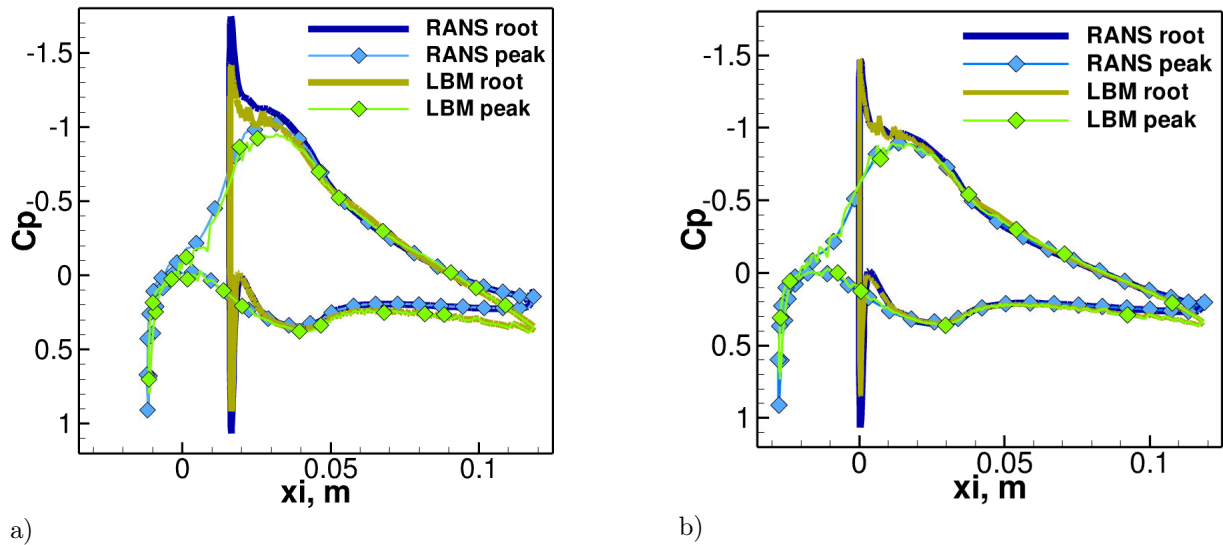


Figure V.46: C_p profile of the central vane at mid-span for the serrated d_1 (a) and d_2 (b) configurations at $M=0.34$.

The C_p profiles for the serrated geometries d_1 and d_2 are illustrated in Fig. V.46. The mean pressure has been extracted at peak and root locations around mid-span. Again, a good agreement is found with the RANS solutions, even if a larger deviation can be observed near the TE in particular for the d_1 calculation compared to the baseline and d_2 cases. Similar comparisons on C_p profiles have been performed at CERFACS [59], but at a higher inflow ($M = 0.53$) demonstrating a good agreement with the RANS solution again.

V.3.2.2 Characterization of the turbulent inflow

The interaction noise radiated from the cascade of airfoils is directly related to the upstream turbulent flow generated by the turbulence grid. Thus, a reliable capture of the main turbulence characteristics is required to check the pre-test conditions, which are of prime importance for the serrated designs d_1 and d_2 definition discussed in Part IV. Instantaneous fluctuating velocity (u'_η) field in the mid-planes of the test section are depicted in Fig. V.47.

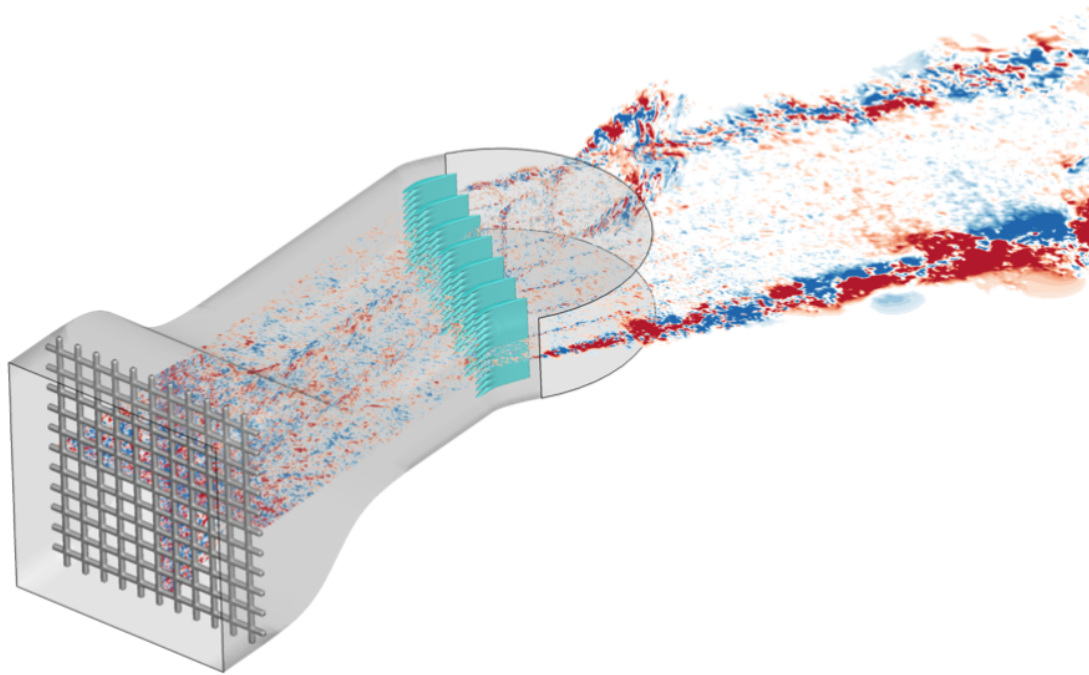


Figure V.47: Snapshot of the fluctuating velocity field at mid-planes of the section.

Turbulent wakes generated by lateral plates at the exit of the test section are also reproduced in Fig. V.47. More generally, the whole test bench is represented from the grid to the exit of the test section. A quantitative analysis of turbulence properties generated by the grid can be performed from time signals recorded during LBM simulations on a line of point probes placed in the middle of the section. Turbulence is statistically stationary after the transient period due to the temporal ramp on the velocity injection defined in Table V.8.

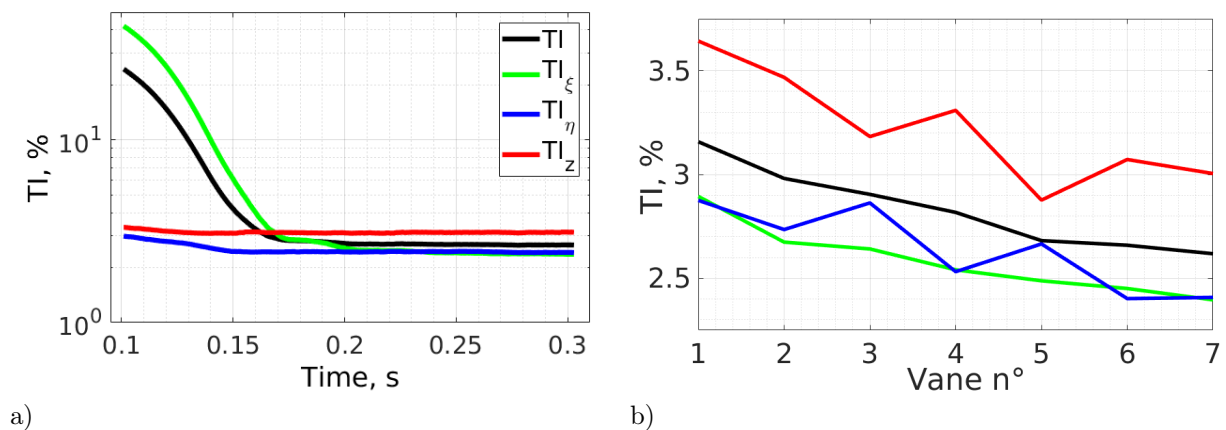


Figure V.48: Temporal evolution of turbulence intensities (a) defined in Chapter III.1 (a moving average of width 0.2 s is applied, resulting in a signal from 0.1 s to 0.3 s) and turbulence intensities in front of each NACA airfoil (b).

Again, convergence is achieved after a transient time of approximately 0.2 s, as illustrated in Fig. V.48a for the fluctuating velocities expressed in terms of directional turbulence intensity. It is interesting to note an amplification of the z-component, which might be due to the fact that the

contraction of the test section is very strong (ratio 2.8) and only along this z-direction. As a result, the turbulence field is not perfectly isotropic. In Fig. V.48b, the variation of turbulent intensities is plotted along the cascade direction. It indicates that the blades are not uniformly impacted by the turbulent inflow, which is therefore not perfectly homogeneous. In the following, the focus is put on turbulence properties analysis based on velocity spectra. The single component turbulent velocity spectra, $S_{u'_\xi u'_\xi}(f)$, obtained from a single wire hot-wire probe at the location circled in blue in Fig. II.16a are presented in Fig. V.49 for two incident flow velocities, $U_\xi = 45$ m/s and 95 m/s (the higher reachable speed for a reliable use of the hot-wire data without vibration issues). They are compared to the standard Liepmann isotropic model (in blue) calibrated by experimental values for TI and L_l deduced from theoretical expressions, discussed in Chapter III.1. Here, the turbulence intensity is deduced from the formulation in the frequency domain, and reads

$$\langle u'_\xi{}^2 \rangle = \int_0^{+\infty} S_{u'_\xi u'_\xi}(f) df \quad \text{and} \quad \text{TI} \approx \text{TI}_\xi = \frac{\sqrt{\langle u'_\xi{}^2 \rangle}}{U} \quad (\text{V.5})$$

where $U = U_\xi$ upstream of the cascade. The Parseval's identity ensures that Eq. (V.5) obtained in the frequency domain provides the same result for $u'_\xi{}^2$ than a standard estimation performed from a temporal signal as done in Chapter III.1. However, it can be more relevant to consider Eq. (V.5), than its temporal counterpart, especially for post-processing when the very low frequency response is not perfectly converged. The turbulent length scale L_l is computed from the turbulence velocity spectrum following

$$L_l = \lim_{f \rightarrow 0} \left(\frac{S_{u'_\xi u'_\xi}(f)U}{4 \langle u'_\xi{}^2 \rangle} \right) \quad (\text{V.6})$$

as written in a similar fashion in Eq. (III.28) from Chapter III.1.

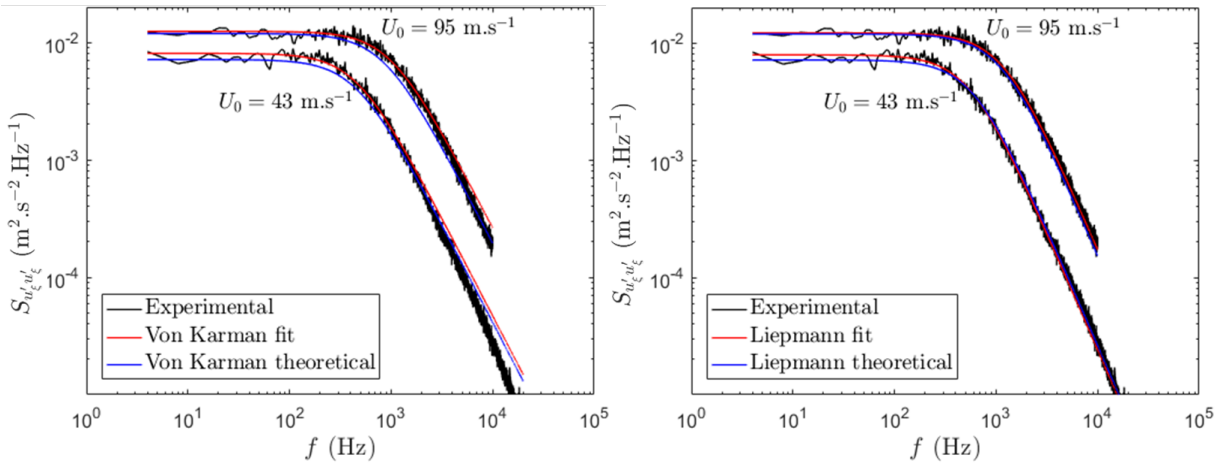


Figure V.49: Turbulent velocity spectra of the axial velocity component obtained during the experimental test campaign.

Another solution to compute turbulence properties has been proposed during the experimental data post-processing which relies on a least square fitting method. It is also plotted in Fig. V.49 (in red). The values of TI and L_l are also given in Table V.9. Note that for $U_\xi = 95$ m/s, the experimental spectrum was only used up to 10 kHz because of vibration issues.

	$U_\xi = 43 \text{ m/s}$		$U_\xi = 95 \text{ m/s}$	
	TI (%)	L_l (mm)	TI (%)	L_l (mm)
Theoretical	6.1	11.2	4.9	13.3
Liepmann least square fit	6.5	11.2	5.0	12.6
von Karman least square fit	6.5	11.2	5.4	11.4

Table V.9: Turbulent intensity and length scale deduced from experimental velocity spectra

Overall, Liepmann's model provides a very good fit to the experimental data, with a decay slope in better agreement than von Karman's model. The values of TI and L_l deduced from the theoretical expressions and from the least square fits are consistent with one another, and there seems to be some variations in these values between the two incident flow velocities considered. The theoretical and the least square fits expressions are also deduced from the LBM results at the same location than in the experimental set-up, around 20 cm in front of the vane cascade.

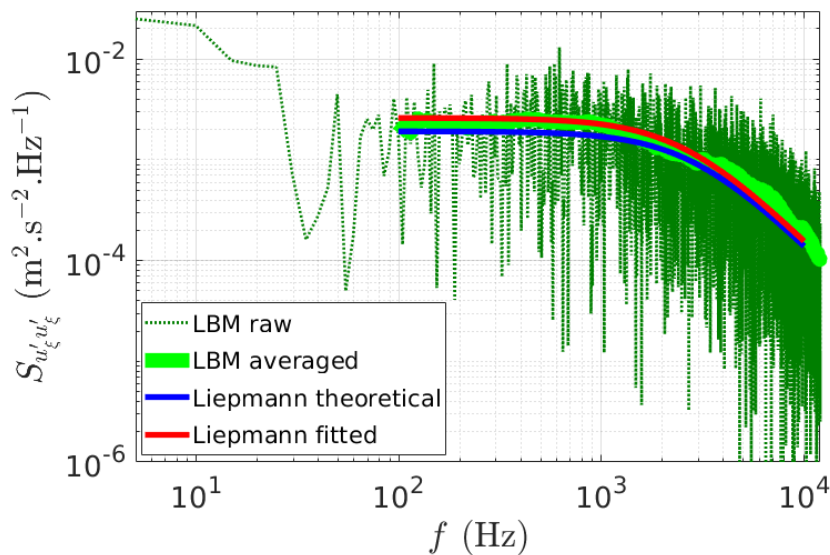


Figure V.50: Turbulent velocity spectra of the axial velocity component obtained from LBM simulations.

In order to avoid a poor definition of spectra in the low frequency range, the post-processing frequency range is restricted to 100 Hz - 10 kHz as illustrated in Fig. V.50. As a reminder, the LBM results are acquired on 0.2 s contrary to experimental values obtained from a 60 s signal, which explains the higher convergence in Fig. V.49 in the low frequency range. Thus, Eq. (V.5) is particularly useful since it allows to discard the very low-frequency contributions. A turbulent intensity TI and an integral length scale L_l of approximately 2.8% and 7 mm are obtained for both the theoretical and least square methods. There is a clear gap with experimental values from Table V.9. It must be emphasized that LBM simulations have been carried out using a pre-test grid geometry with square bars of 1 cm side and a pattern of 4 cm whereas a different grid of 2 cm side bars and 5.5 cm pattern has been actually considered in the experimental test campaign. This mismatch was tardily informed by Centrale Lyon (when numerical simulations were completed).

A simple correction based on the energy spectrum has been proposed by ONERA to solve this problem, where $U = U_\xi$ is the mean velocity upstream of the cascade.

$$S_{u'_\xi u'_\xi}^{\text{LBM, corr}}(f) = S_{u'_\xi u'_\xi}^{\text{LBM}}(f) \times \frac{\varphi_{\xi\xi}^{1D}(f, U^{\text{exp}}, \text{TI}^{\text{exp}}, L_l^{\text{exp}})}{\varphi_{\xi\xi}^{1D}(f, U^{\text{LBM}}, \text{TI}^{\text{LBM}}, L_l^{\text{LBM}})} \quad (\text{V.7})$$

Spectra with frequency correction from Eq. (V.7) are plotted in Fig. V.51 with: $U^{\text{exp}} = 95$ m/s, $\text{TI}^{\text{exp}} = 5\%$, $L_l^{\text{exp}} = 12.6$ mm, $U^{\text{LBM}} = 95$ m/s, $\text{TI}^{\text{LBM}} = 2.8\%$, and $L_l^{\text{LBM}} = 7$ mm.

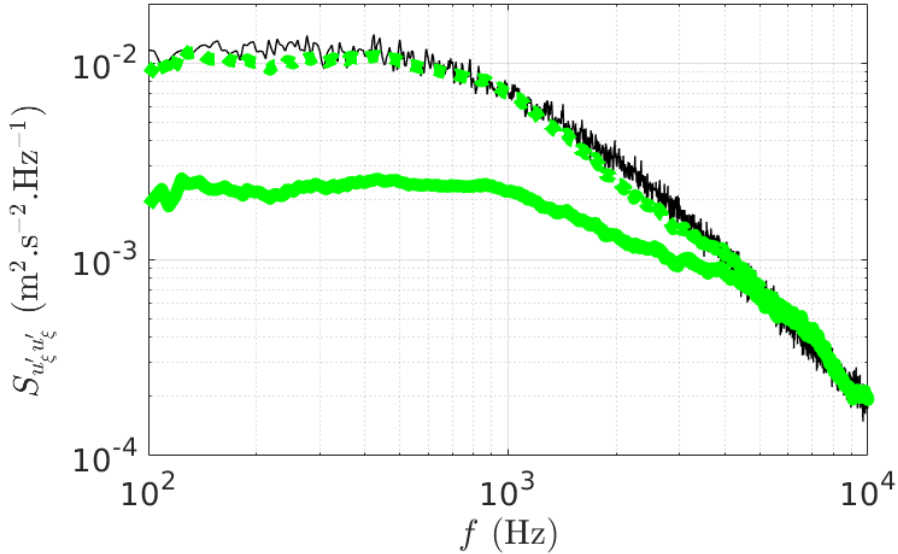


Figure V.51: Turbulent velocity spectra of the axial velocity component obtained from experimental (—) data and LBM simulations with (.....) and without correction (—).

A very good matching is observed between experimental and adjusted spectra from LBM simulation. Indeed, with the theoretical method, a value of $\text{TI} \approx 4.6\%$ and $L_l \approx 12.6$ mm is now obtained from the corrected LBM spectrum (very close to those from Table V.9). This correction is also applied in the next section to far-field acoustic spectra obtained from LBM simulations. Some additional analysis of turbulent flow properties along the test section, from grid to NACA airfoils, are discussed in the following.

Figure V.52 shows the evolution of the turbulence intensity between the grid and the LE of the vanes. The very low frequency part of the spectrum has been discarded for post-processing. One may observe that there is a rather good agreement with the experimental data from an older experimental data. Yet, it has to be reminded from Section II.3.1 that these data have been recorded in another test rig [36], using the same turbulence grid, but with a smaller test section than during the InnoSTAT test campaign (30 cm x 15 cm vs 30 cm x 20 cm). Its pattern generates a TI of 4.5% and an L_l of 9 mm, both quantities probed at 50 cm from the grid.

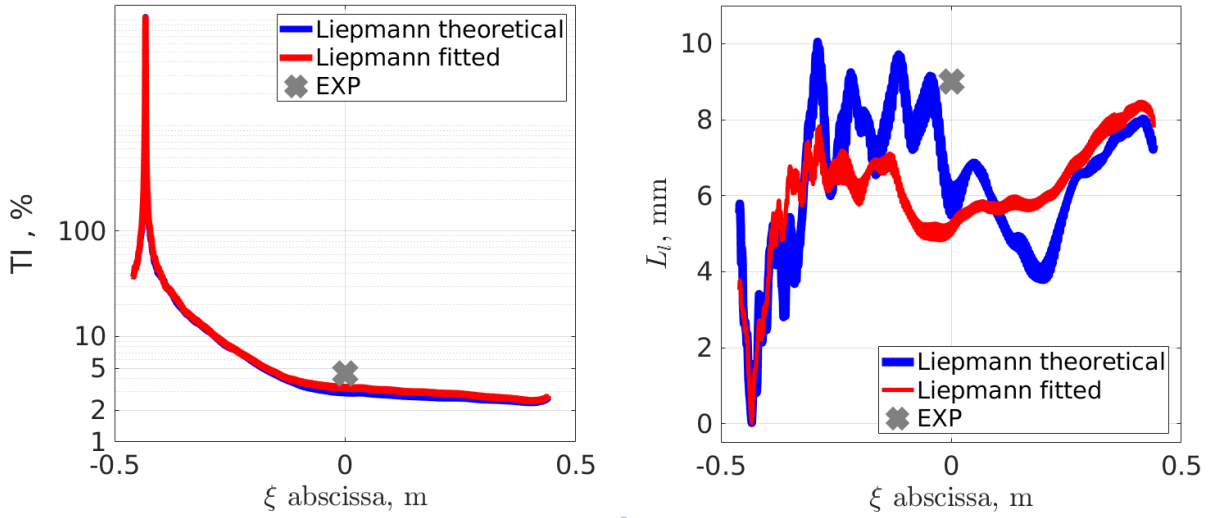


Figure V.52: Evolution of turbulent intensity TI (left) and length scale L_l (right) from the grid to NACA airfoils. $\xi=0$ corresponds to the nozzle exit. Experimental data from [36].

Previously, the turbulent length scale L_l has been obtained from the longitudinal velocity spectrum. Another available option consists in deducing turbulent length scales $L_{ij,k}$ from spatial correlations, as presented in Eq. (III.26). To that end, crossed lines of probes from Fig. V.40 are considered, located half a chord upstream of the central vane.

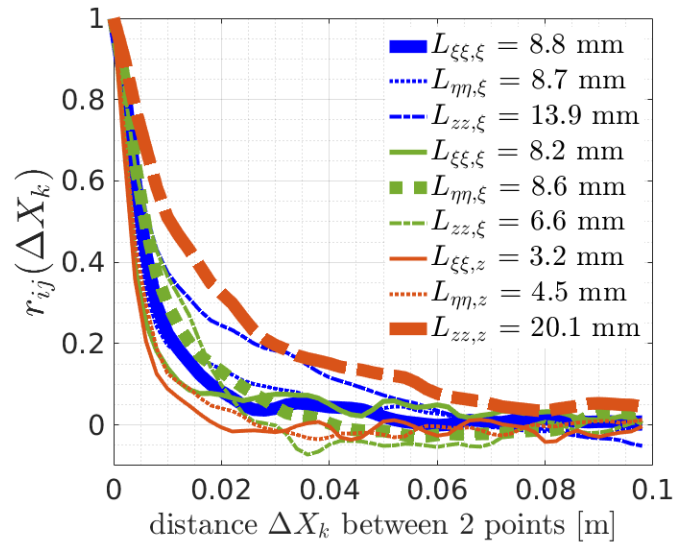


Figure V.53: Turbulent length scales $L_{ij,k}$ evaluated at a half chord upstream of the central vane.

Oscillations in Fig. V.53 demonstrate that the turbulent length scale post-processing from spatial correlations remains very challenging. However, several key aspects can be deduced from Fig. V.53. A strong anisotropy of turbulence is present which is not consistent with analytical models and synthetic turbulence assumptions. Nevertheless, it is interesting to note that $L_{\eta\eta,z}$ which corresponds to the spanwise correlation length of the upwash velocity component (theoretically equal to half the longitudinal integral length scale L_l) is close to the serration design parameter $L_t = 4$ mm. Indeed, serrations wavelength $\lambda_s = 4L_t$ has been chosen accordingly in order to

maximize the noise reduction. Unfortunately, the L_t value with the turbulence grid used in the KCA tests is larger (12.5 mm instead of 8 mm) so that the serration design is not fully suited.

V.3.2.3 Far-field acoustic spectra and sound power reductions

The acoustic field primarily generated by the interaction between the grid turbulence and NACA airfoils is now analyzed. Figure V.54 shows a snapshot of the fluctuating pressure in the plane $z = 0$. The mean pressure field p_0 has been subtracted to the pressure field p . Acoustic waves emitted from the cascade can be observed in the domain, outside of the turbulent wake. Figure V.54 does not show any spurious noise source, in particular at refinement mesh transitions crossed by the turbulent wake. Moreover, shear boundary layers at the side plates are also reproduced.

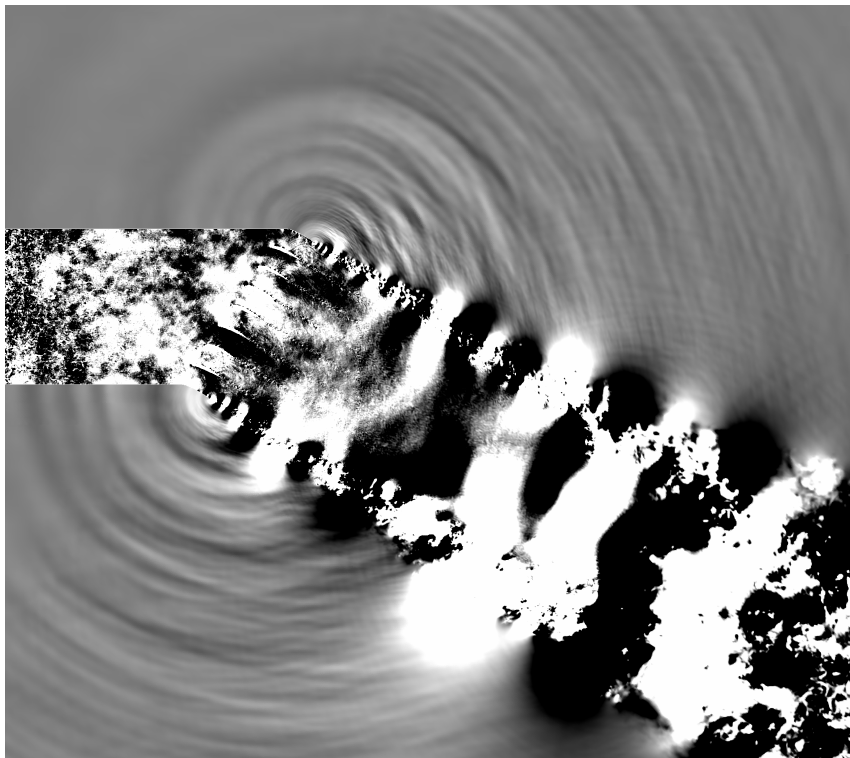


Figure V.54: Visualization of the fluctuating pressure (p' , levels between ± 20 Pa) at mid-span in the simulation domain - $M=0.34$

In order to outline the serration effects on acoustic sources on the vanes, the fluctuating pressure has been extracted at the vane skin. The root mean square (RMS) fluctuating pressure (p'_{RMS}) contour maps are plotted in Fig. V.55 at $M=0.34$.

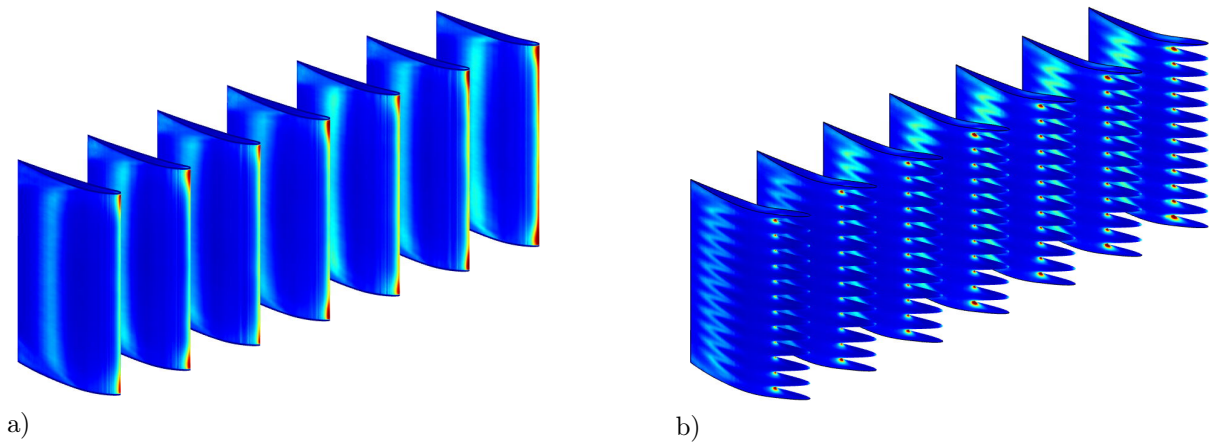


Figure V.55: p'_{RMS} on the vane skin (levels between 0 and 1000 Pa). Calculations on the baseline (a) and serrated d_1 (b) geometries.

Two major areas of fluctuating pressure are visible on the baseline geometry. A primary area of high pressure fluctuations is located at the LE and is caused by dipolar noise sources from the turbulence-airfoil interaction noise. A secondary high pressure fluctuation band is noticeable near the mid chord. These two locations of the noise sources (LE and at mid-chord) are also found in the work by Lewis [120] (see pages 140-141, in particular). The secondary source in this work is partly associated with a laminar-turbulent transition. It can be noted that the wall law used is ProLB is supposing a stationary turbulent boundary layer. Therefore, this boundary layer transition cannot be properly resolved in ProLB. More broadly, turbulent sources at mid-chord can also be linked to flow detachment at LE of stator vanes at the considered operating condition, as shown by ZDES simulations and which could generate secondary sources as discussed by François *et al.* [77] and Polacsek *et al.* [145]. As expected from the literature [138, 15], the LE pressure sources are concentrated at the roots and tips of the serrations in the low noise design configurations in Fig. V.55b. The shape of the secondary noise source is also modified by the presence of serrations. These additional sources, might also limit the efficiency of the LE treatment.

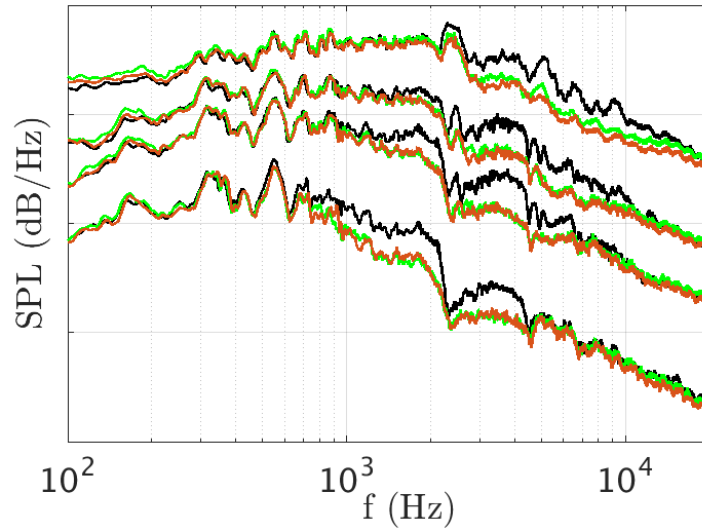


Figure V.56: Measured SPL at microphone 33 and various flow speeds for baseline (in black), design d_1 (in green), and design d_2 (in orange). 20 dB step between y-ticks.

The following analyzes are devoted to the comparisons of SPL spectra at selected microphones of the far-field antenna used during the test campaign in Fig. II.15 from Section II.3.1. The spectra at microphone 33 for the baseline and d_1 cases are plotted in Fig. V.56, for all speed flows ($U = U_\xi$) of the test matrix, from $U_\xi = 45$ m/s (bottom curve) up to $U_\xi = 182$ m/s (top curve). As expected, as long as U_ξ is increased, the SPL are increased, and the peak levels are shifted to higher frequencies. A significant level reduction can be observed for all speeds, and the cut-on frequency of treatment efficiency roughly varies linearly with U (according to the Strouhal number $St = f \times h_s / U$). An assessment in terms of far-field noise reduction is also achieved at locations corresponding to the microphone antenna. A first solution consists in the extraction of the pressure sources at the vane skin and performing a FWH integral method. Pressure temporal evolution is recorded on the same mesh than for the pre-processing during 0.2 s which results in a frequency step of ≈ 5 Hz. The signal is extracted every 64 time steps, which corresponds to a sampling frequency of 46 kHz. Then, a Fourier transform is applied to obtain the wall pressure fluctuations in the frequency domain required as inputs to the MIA code. As a reminder, the calculation is performed considering the solid surface FWH formulation (restricted to the loading noise term) with a free-field Green function. A second solution, more straightforward, consists in computing acoustic spectra directly from probes placed at the microphone location (see Fig. V.31b) also sampled at 46 kHz. It can be observed that in the acoustic region a 46 kHz extraction corresponds to an extraction every two time steps. Moreover, to perform the calculation, it is of prime importance, as in the experimental set-up to exclude regions crossed by the turbulent wake, which would otherwise pollute the acoustic signature in particular in the low frequency range. Numerical predictions provided by CAA and LBM are compared to measurements in Fig. V.57 (a) and (b), for microphones 33 and 40 respectively.

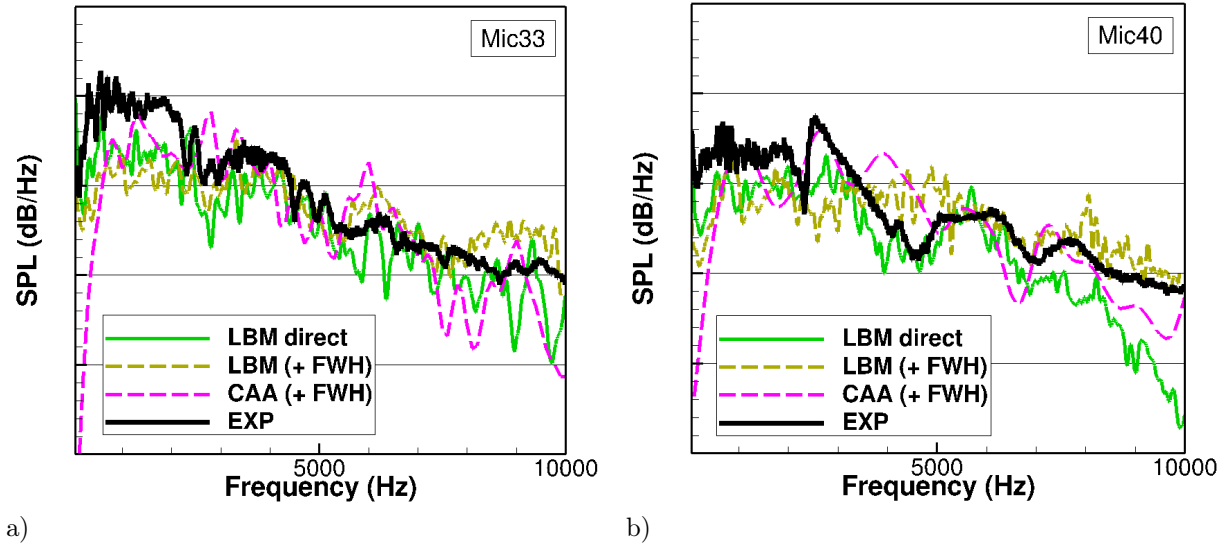


Figure V.57: SPL comparisons on baseline case: numerical simulations vs. experiment at Mach 0.34 for mic. 33 (a) and mic. 40 (b). A moving averaged has been applied to smooth the spectra. 10 dB step between y-ticks.

The agreement is reasonable for all methods despite the fact that different inflow turbulent conditions have been considered: $TI = 5\%$ and $L_t = 8$ mm for the CAA (prescribed values), $TI = 2.8\%$ and $L_t = 7$ mm for the LBM, $TI = 5\%$ and $L_t = 12.6$ mm for the experimental data. It can be pointed out that sawtooth variations sometimes visible on the experimental spectra (Fig. V.57 (b)) are fairly well captured by the LBM direct calculation, despite of the numerical dissipation effects of the mesh beyond 6.5 kHz. Indeed, the direct LBM calculation is the only numerical approach taking into account installation effects on the overall radiated noise. In what follows, a correction is applied to the LBM direct acoustic spectra to take into account discrepancies related to the difference in turbulence grid dimensions, as already pointed out when analyzing turbulence properties. The following equation provides the corrected spectra:

$$SPL^{LBM, \text{corr}}(f) = SPL^{LBM}(f) + 10 \log \left(\frac{\varphi_{\xi\xi}^{1D}(f, U^{LBM}, TI^{LBM}, L_t^{LBM})}{\varphi_{\xi\xi}^{1D}(f, U^{\text{exp}}, TI^{\text{exp}}, L_t^{\text{exp}})} \right) \quad (\text{V.8})$$

It has to be noted that contrary to Eq. (V.7), in Eq. (V.8) the equality $U^{LBM} = U^{\text{exp}}$ holds. Indeed, the experimental acoustic spectra have been also obtained at the same regime of $M=0.34$ than in LBM. Correction from Eq. (V.8) is then applied to LBM direct acoustic spectra as shown in Fig. V.57.

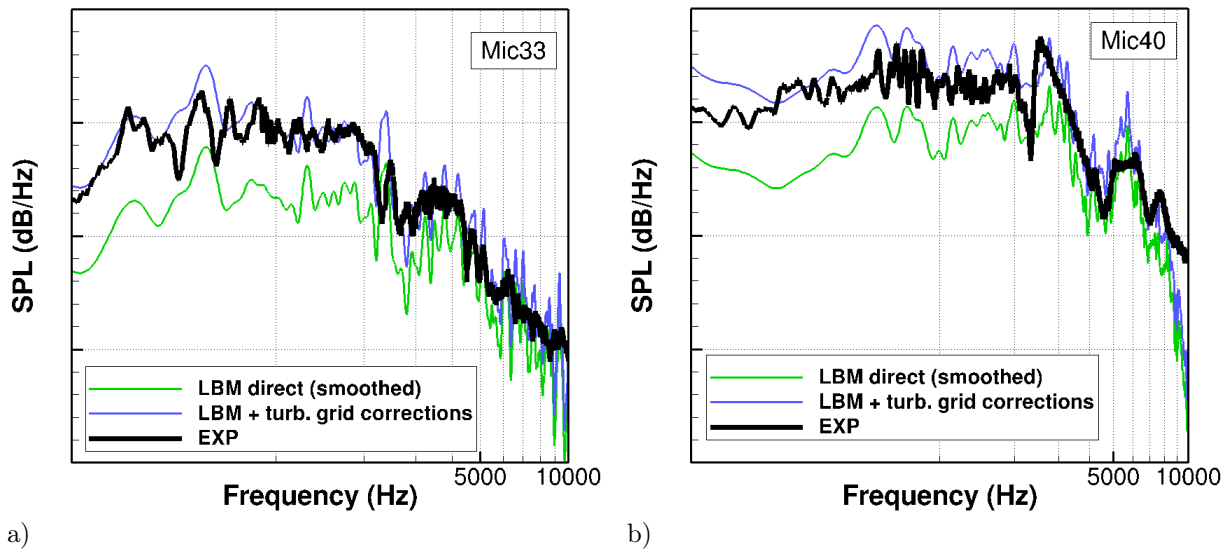


Figure V.58: SPL comparisons on baseline case: direct LBM results (with and without correction) vs. experiment at Mach 0.34 for mic. 33 (a) and mic. 40 (b). 10 dB step between y-ticks.

With the proposed correction, a very good agreement is observed between the experimental and numerical solutions. This demonstrates the relevance of the correction introduced in Eq. (V.7) to compensate for the discrepancy in turbulence grid geometries. Moreover, Fig. V.58 confirms the ability of LBM simulations with ProLB to perform quite accurate direct noise predictions taking into account all installation effects. A comparison of noise directives in terms of OASPL is also provided. This time experimental data has been corrected to account for grid geometry difference, similarly to Eq. (V.8).

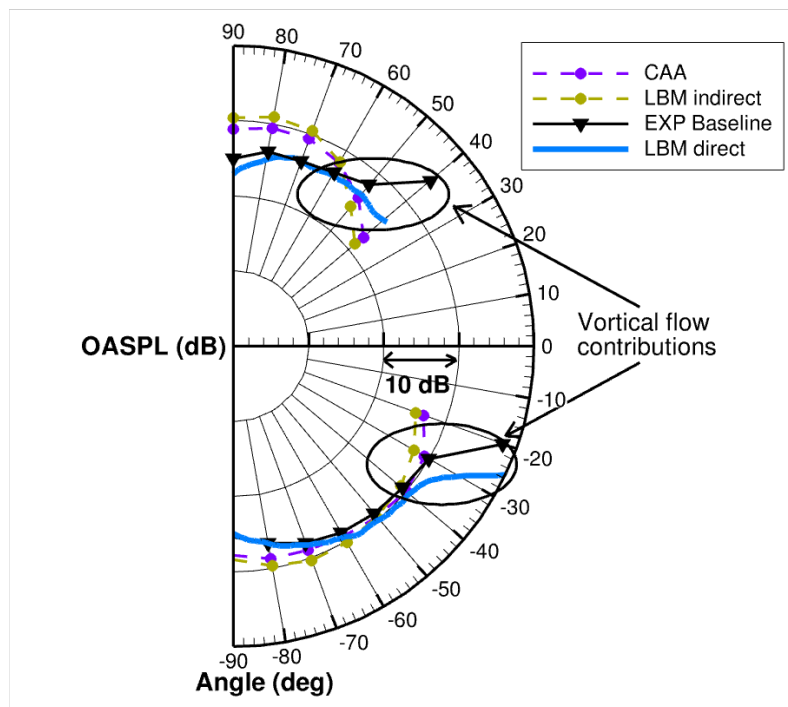


Figure V.59: OASPL (from 100 Hz to 10 kHz) noise levels from CAA, LBM, and experimental data.

OASPL directivities are plotted and cross-compared in Fig. V.59. Aside from microphones in the vicinity of to the turbulent wake, LBM direct prediction matches the experimental data, which strengthens the conclusion already pointed out on SPL spectra from Fig. V.58. In addition to the radiated noise predictions with the reference geometry, noise reduction predictions are achieved for both d_1 and d_2 serrated designs. To get a general view of the noise reduction, an angular summation of the acoustic spectra (avoiding the turbulent wake) is performed using the following approximation:

$$\Delta\text{PWL} = 10 \log_{10} \left(\sum_{mics} \text{PSD}_{\text{baseline}} \right) - 10 \log_{10} \left(\sum_{mics} \text{PSD}_{\text{serrated}} \right) \quad (\text{V.9})$$

Due to the log functions difference, additional terms of Eq. (II.13) (such as the surface) disappear. Note that for the same reason, turbulence grid corrections applied to LBM solutions are not required when assessing noise reduction.

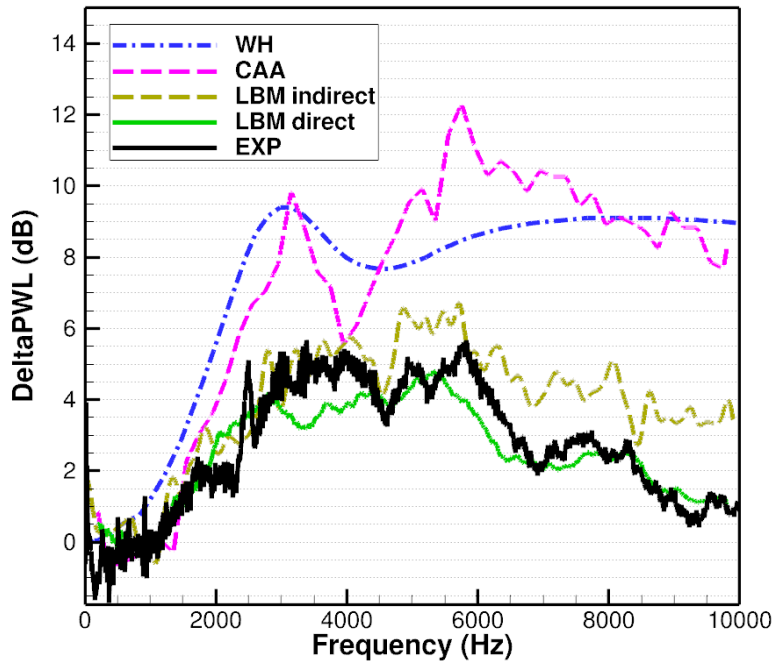


Figure V.60: Noise reduction assessment at the approach condition ($M=0.34$)

ΔPWL spectra provided by all available methods on design d_1 at Mach 0.34 (Mach 0.3 for CAA) are compared to experimental data in Fig. V.60 (using a linear frequency scale). The WH and CAA solutions are close together. But both are exhibiting an over-prediction of the noise reduction. The LBM predictions are fairly well matching the measurements, and more particularly the direct LBM solution. Indeed, with the indirect calculation (FWH analogy), only the noise sources at the vanes surfaces are radiated in the far-field. Any other sources present in the test rig cannot be properly taken into account. However, it is interesting to note that even with the indirect calculation, as done for CAA simulations, noise predictions is much lower with LBM. Two explanations are plausible. First, a perfectly homogeneous and isotropic turbulence is considered in CAA which matches the optimal design of the serrations as detailed in Chapter IV.2. Second, LBM simulation is inherently able to capture some (under-resolved here) contribution

of the self-noise (source generation mechanisms issued from the turbulent boundary layer effects and vortices convected along the wall and not related to the LE noise) of the airfoils, contrary to CAA approach that has been designed for LE noise assessment only. This can be checked by comparing the RMS pressure at vane's skin in Fig. V.29 (CAA solution) and Fig. V.55b (LBM solution). Additional sources captured by LBM in the rear chord region are much more intense compared to CAA. As mentioned earlier, these noise sources might be related to laminar-turbulent boundary layer transition, although in ProLB this phenomenon cannot be accurately predicted by the stationary turbulent wall law. In order to assess the impact of secondary sources (apart from the LE region) on noise reduction differences between CAA and LBM, a limitation of the integration surface in FWH to the LE region of the airfoils is proposed. Moreover, bottom and top regions have been discarded in order to avoid corner flow effects in LBM simulations. The limitation of the surface integration is illustrated in Fig. V.61a.

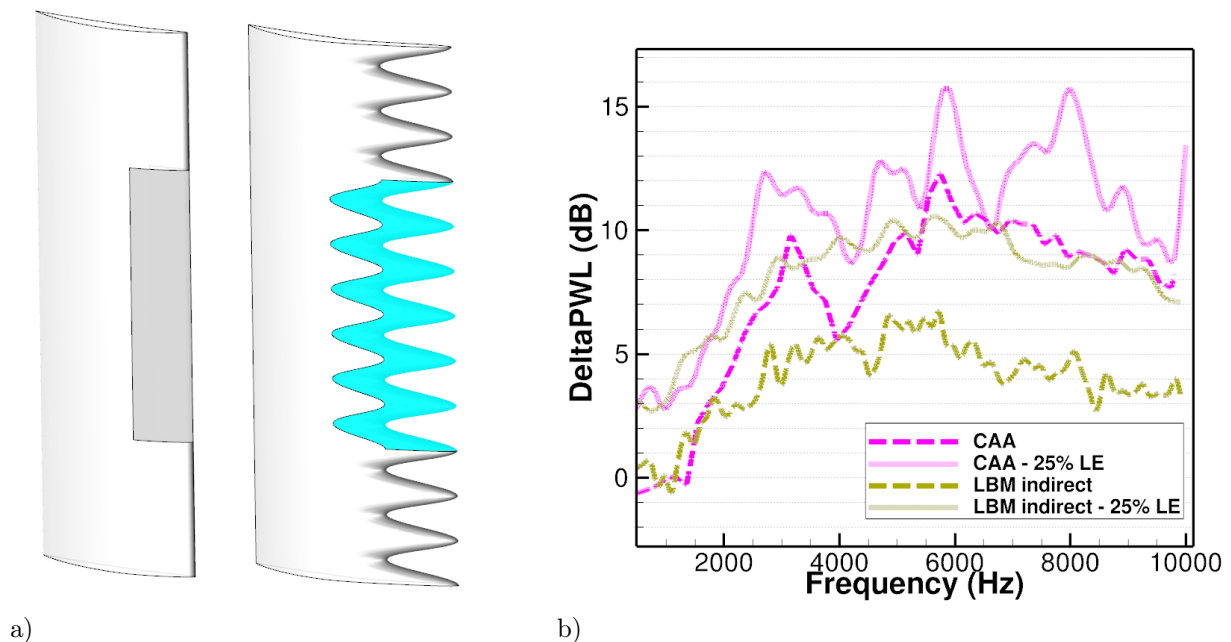


Figure V.61: Sketch showing the MIA integration surface limited to 25 % of the LE and discarding top and bottom sides (a). Noise reductions obtained with MIA from CAA or LBM data (b).

In both cases, CAA and LBM, noise reduction is increased by the limitation of the noise sources integration. Yet, the difference appears larger with LBM as illustrated in Fig. V.61b and a better agreement is observed between CAA and LBM indirect solutions. This may partially explain why CAA leads to higher noise reductions. The other explanation previously pointed out is that a perfectly homogeneous and isotropic turbulence is injected in the CAA domain. Moreover, the remaining difference might be partly linked to secondary vortices at the LE [56] and which are better captured by the LBM, although these secondary vortices are usually supposed to be negligible in the case of single-wavelength serrations.

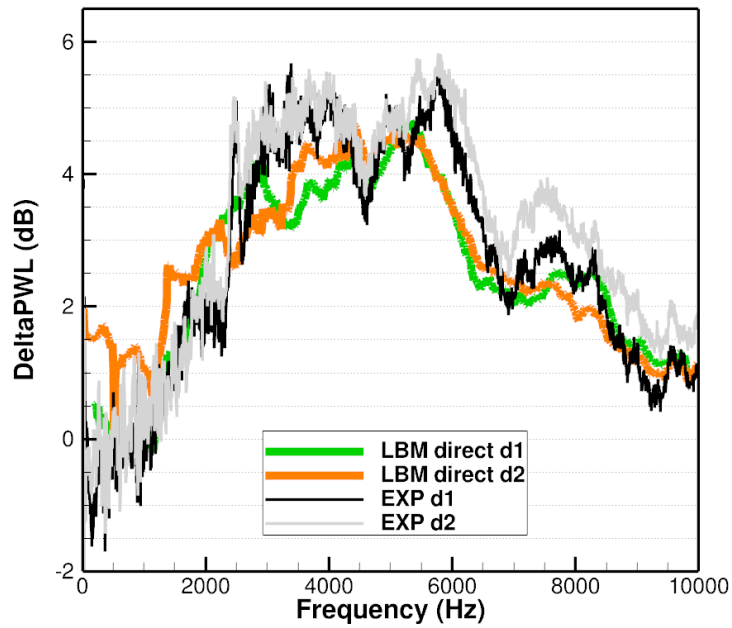


Figure V.62: Noise reduction assessment at the approach condition ($M=0.34$)

Finally, the Δ PWL spectra provided by the direct LBM calculations at Mach 0.34 for designs d_1 and d_2 are compared to the experiment in Fig. V.62. The good accordance between numerical and experimental spectra is quite remarkable. Furthermore, it confirms the almost identical acoustic performances of both designs at this regime. This reinforces the interest of the second design improved from the aerodynamic point of view, as proposed in Chapter V.1, showing almost no penalty on acoustic performances and even a slight increase of Δ PWL. Comparison with experiment also highlights the rather low sensibility of the noise reduction to the turbulent inflow properties with respect to the integral length scale. Indeed, the serrations wavelength $\lambda_s \approx 16.7$ mm is slightly off the optimum, which would have been $2L_l \approx 25$ mm. Experimental sensitivity analysis to inflow parameter can be found in [138].

As a last result, complementary power reduction spectra obtained during the test campaign for various inflow speed regimes are analyzed.

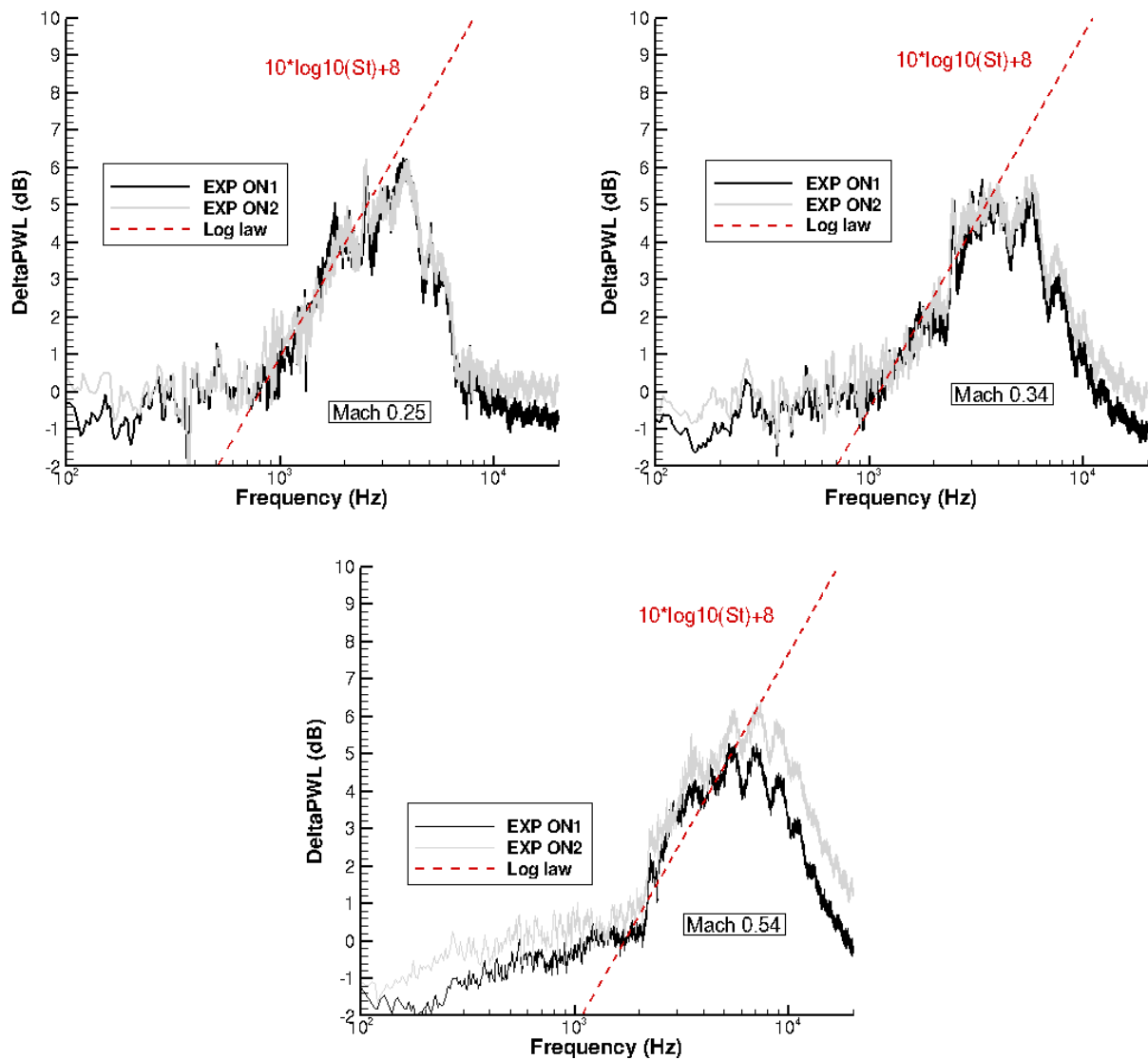


Figure V.63: Δ PWL measured for d_1 and d_2 designs at 3 regimes: Mach 0.25 (left top), Mach 0.34 (right top), Mach 0.54 (bottom).

The Δ PWL spectra obtained from the measurements are plotted in Fig. V.63 for three flow regimes: $M=0.25$, $M=0.34$ (already discussed in Fig. V.62), and $M=0.54$. A significant level reduction up to 6 dB can be observed with a peak frequency linked to the speed flow. Moreover, acoustic performances are found to be close with a slightly higher reduction for d_2 , particularly at higher speed ($Mach = 0.54$). A significant level reduction can be observed for all speeds, and the cut-on frequency of treatment efficiency roughly varies linearly with U (according to the Strouhal number $St = f \times h_s/U$). The semi-empirical log-law from the literature is confirmed to be a reliable indicator too, when the constant term is modified to better fit the present experimental results: $PWL \text{ (dB)} = 10 \log(St) + 8$.

V.4 Comparison of the trade-off between cost and fidelity of the different approaches

The purpose of this chapter is to provide some elements to feed the discussion about the pros and cons of the different modeling approaches: analytical solution, hybrid CFD/CAA, and LBM. The focus is made on the physical representativeness of the underlying assumptions and associated CPU cost for each approach. Main pros and cons of each numerical approach are summarized in Table V.10. Advantages and disadvantages of each approach are discussed according to a thematic splitting: aerodynamic loads calculation, mean flow representatives, turbulence characterization (both in terms of 1D properties such as TI and L_t and unsteady turbulence field representation, and acoustic far-field prediction). Another aspect, in terms of manpower effort dedicated to the numerical set-up should be considered too, since the mesh constraints are different from CFD, CAA to LBM simulations. Lastly, the CPU consumption required for each approach is evoked.

The reader may note that analytical (Amiet or WH) solutions are not detailed in the Table V.10. Indeed, they both focus on the acoustic predictions only, with strong assumptions: finite or semi-infinite flat plate in a uniform mean flow with all turbulent flow properties being prescribed. However, these analytical approaches can provide acoustics predictions on large array of microphones in a very short period of time (few minutes), which allows fast parametric studies.

method	Hybrid CFD (RANS 3D + Euler 2D) / CAA LEE + FWH		LBM
Variant	(k_ξ, k_z) (1-channel CAA)	(k_ξ, k_η, k_z) (3-channel CAA)	Weakly compressible
aero. loads	+	RANS 3D: accurate determination of aerodynamic penalties and loads.	All stationary and unsteady aerodynamic quantities are computed.
	-	Euler 2D: no assessment of aerodynamic performances.	Steady aerodynamic loads calculation slightly less accurate than with RANS body fitted mesh simulations.
mean flow	+	Euler 2D: mean flow calculations satisfying inviscid CAA assumption and thus well suited to mean flow inputs for CAA.	Mean flow computed inside and outside of the test section.
	-	RANS 3D: requires removal using in-house routines (not fully automatized and not user friendly).	
turb. prop.	+	RANS 3D: relatively accurate estimation of kinetic energy and able to provide a rough value of the turbulent length scale estimation.	Fully resolved turbulence characteristics up to the cut-off frequency.
	-	RANS 3D: reliable computation of the turbulent length scale remains challenging. Euler 2D: no assessment of turbulence characteristics.	Advection of turbulence is quite expensive.
turb. field	+	The turbulence spectrum can easily be changed.	All turbulence unsteady field simulated up to the cut-off frequency
	-	Boundary conditions and divergence free conditions can be hard to achieve.	Expensive advection of turbulence.
acou.	+		3D turbulence noise sources taken into account.
	-	Cascade blade to blade interaction not perfectly taken into account. No installation effects. Self-noise not properly modeled.	No installation effects. TE edge noise not properly modeled.
Other	CFD and CAA mesh generations take. But slight geometry changes can be easily handled by the ersatzZ modeler.		Limited to the approach operating regime (weakly compressible version). Definition of refinement zones can take time. But geometry easily exchangeable.
T= 1/ Δf	100 Hz	100 Hz	5 Hz
Cost per ΔT	$\approx 7k$ hours	$\approx 30k$ hours	$\approx 160k$ hours

Table V.10: Comparison of analytical and numerical approaches regarding fidelity and CPU cost.

From Table V.10, it can be deduced that both numerical approaches respond to two different philosophies. The hybrid CFD/CAA approach is efficient at improving a given design, without taking into account the installation effects. Indeed, RANS 3D is very accurate at aerodynamic load prediction and CAA perform very well at capturing LE noise. For this relative comparison purpose between two designs, the 1-channel CAA computations with (k_ξ, k_z) turbulence is the most effective. The 3-channel approach with (k_ξ, k_η, k_z) enables more accurate absolute noise levels predictions, as it reproduces better cascade effects and blade to blade interactions. In the long run, 1-channel CAA with (k_ξ, k_z) seems appealing for shape optimization process. However, for the CFD/CAA approach, turbulence properties usually have to be experimentally provided since the length scale computation from RANS remains challenging, as discussed in [111] for turbofan applications. In the present the simulations, the turbulence properties were not at all computed by RANS but, provided as an input.

LBM approach offers several benefits. First, no input data is required for turbulence calculation. Indeed, the turbulence grid is included in the simulation domain, which provides a more representative velocity fluctuation field, accounting for inhomogeneity and anisotropy. Second, LBM provides accurate absolute acoustic level predictions as it takes into account installation effects with direct noise capability. Moreover, additional noise sources (apart from interaction noise) are also modeled. Third, once a set-up has been properly defined, LBM is a user-friendly approach considering its ability to easily modify the considered geometry associated with quasi automatic re-meshing of the octree mesh. From that perspective, it is also an appealing approach for choosing between several designs. The main difficulty in LBM set-up lies in the definition of mesh transitions, in particular for a direct noise prediction. The present fine mesh set-up could be further improved by replacing the acoustic half-sphere with a thick disk and halving the mesh size in this region, which would increase the cut-off frequency above 10 kHz. Although, in this study the ProLB version is limited to weakly compressible flows, CERFACS has been carrying out computations on the same rectilinear cascade, but with a compressible version of the solver [59].

For a same output signal length $T = 1/\Delta f$ (without transient), CAA and LBM requires similar CPU resources. However, LBM computations require a longer transient time to convect the information from the grid to far-field probes (to perform direct calculation). Furthermore, it should not be forgotten that CAA represent a more research oriented approach. Indeed, the synthetic turbulence enables a more in depth study of interaction noise mechanism, for example depending on the turbulent field structure. From that perspective, synthetic turbulence injection in LBM could represent a way forward, although boundary conditions represent a major constraint for the generation of a divergence-free field as discussed in Part III.

For the first turbofan application presented in the next chapter, the CAA approach has been retained.

Part VI

Application to realistic turbofan configurations

This part aims at presenting the extension of the CAA numerical approach to turbofan configurations. First, calculations on a reference benchmark case are performed. This reference case is based on the NASA SDT test rig introduced in Section II.3.2, and the present study relies on a CAA numerical set-up previously assessed at ONERA. First numerical simulations have indeed been carried out by Cader [154], using the sAbrinA solver coupled to a synthetic turbulence. Available results, numerical set-up, and turbulence generation routines have been fruitfully re-used here. The essential points are recalled before proposing new studies including a focus on the mean flow influence and the number of vanes taken into account for acoustic post-processing.

A final chapter is devoted to the future InnoSTAT test campaign on the ECL-B3 turbofan. As the test parameters are not definitively fixed, this work is based on a very similar configuration from a previous project [154]. Drawing on the methodology developed in Parts IV and V, the serration design process is transposed from a rectilinear cascade with a uniform inflow to an annular configuration with a spanwise variation of the turbulent inflow, as already done in Appendix G. Then, preliminary assessment is performed using the Wiener-Hopf technique [28] already implemented in Part IV and Appendix G. Due to delayed InnoSTAT test campaign, no CFD/CAA or LBM simulations are performed under the scope of this thesis. In addition, as for LBM, the ProLB version used during this thesis is limited to weakly compressible flows ($M < 0.7$). The possibility of carrying LBM simulations on such turbofan configurations with the new compressible version of the code is addressed in the perspectives part of the thesis.

VI.1 CAA simulations on the NASA SDT benchmark

In order to assess the prediction of the broadband noise radiated by a turbofan, a benchmark case namely the NASA SDT, was proposed. The 3D numerical approach here is based on the CAA code sAbrinA. The work consists in a follow-up of a simulation which was previously carried out at ONERA coupled with a 2D turbulence (k_x, k_r) injection similar to the process used in Part V for the rectilinear cascade configuration but written in a cylindrical coordinate system. This previous simulation led to a higher predicted noise level than the experimental data (see the NASA SDT section of [154]). In the former study, the mean flow field was provided by a RANS simulation with inadequately prescribed operating conditions. This wrongly defined mean flow field has been suspected to generate an unrealistic vorticity field in the CAA resulting in the higher noise levels for the CAA computation. A CAA simulation with a new RANS mean flow, recently obtained with elsA code, is conducted here.

VI.1.1 Set-up of the CAA simulation with a RANS mean flow

A reminder of the main steps required to obtain the numerical prediction and to compare with the experimental data is proposed.

1. A RANS simulation over the full fan-OGV stage using a mixing plane approach is carried out. The mixing plane is defined at the rotor outlet/stator inlet, where the data are averaged in the circumferential direction on both the rotor outlet and the stator inlet boundaries. This allows to solve a steady-state problem. It provides the mean flow for the CAA simulation. The RANS simulation domains are illustrated in Fig. VI.1.

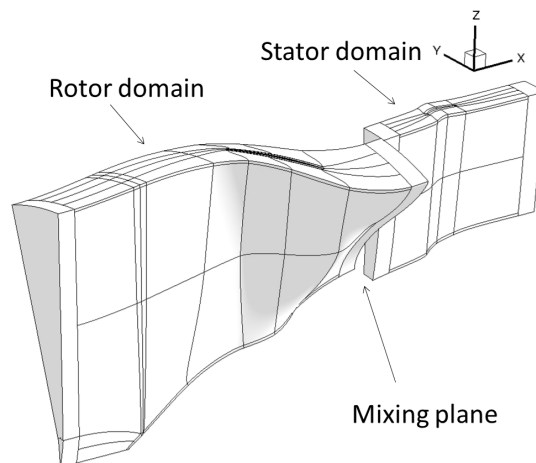


Figure VI.1: Rotor and stator computational domains of the single channel.

- (1 bis). A RANS simulation is performed on the isolated rotor blade (in the rotating frame attached to the blade), in order to get the turbulence characteristics (L_l and TI). The radial profile is obtained by averaging the quantities over the pitchwise direction. To get the turbulence characteristics up to the LE of the OGV, the outflow boundary of the isolated blade domain is extended beyond the OGV plane. In the present study, the turbulence profiles used to calibrate the isotropic turbulence spectrum model are directly provided by the experimental measurements, available from the data package delivered in the framework of the NASA SDT benchmark [8].
2. The mean flow for the stator stage is interpolated on the CAA grid.
 3. The flow is then filtered in order to satisfy the non-viscous assumptions of Euler's equations solved by the CAA. Indeed, unsupported strong velocity gradients in the wall boundary layers are likely to generate unrealistic vorticity and give rise to numerical artefacts. This can result in spurious additional noise sources. Moreover, the CAA calculation may become locally unstable with the uncorrected RANS mean field, as demonstrated in [47]. To perform the CAA simulation, the boundary layers and recirculation bubbles have to be removed from the mean flow. To this end, the mean flow is modified in the latter zones in order to keep a minimal positive axial velocity, which avoids an over-accumulation of the acoustic energy.
 4. A pre-processing module is run to simulate the injected synthetic turbulence field at each time step to be stored over a specific zone (rows of cells involved in the Tam's injection boundary condition). A 2D axi-symmetric turbulence of the shape $(u'_x(k_x, k_r), (u'_\theta(k_x, k_r)))$ is considered. Further details can be found in [154]. This description is similar to the (k_x, k_z) model used in Parts III and V but expressed in cylindrical coordinates.
 5. The CAA computation is performed. The wall pressure fluctuations on the blades are extracted throughout time. A post-processing unit computes the harmonic loadings on the blades, which are the Fourier-transformed pressure fluctuations, as done for the cascade simulations.

6. Then, the harmonic loadings or sources terms are radiated in a ducted domain thanks to an-house code FanNoise (introduced in Section II).
7. The in-duct sound spectrum provided by the simulation is compared to experimental values. It should be noted that the PWL spectra issued from the experiments are obtained from a free-field antenna so that the in-duct power spectrum is assumed to be close to the radiated one.

In this case, a three channel domain is considered. As illustrated in the simulation carried out in [154], there is a more reliable cascade effect impacting the radiated acoustic spectrum if several adjacent vanes (at least 3) are taken into account in the simulation domain instead of just one. The domain used for the CAA simulation is described in Fig. VI.2. In previous simulations carried out at ONERA on the NASA SDT configuration, only the central vane has been considered for the FWH analogy. This choice, which is proved to be a salient point during this work, is challenged later.

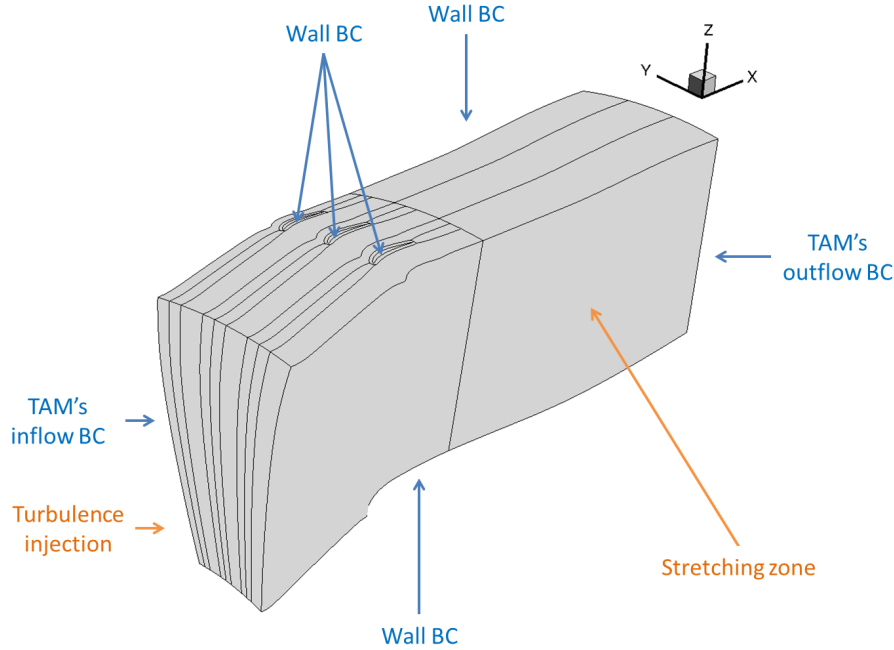


Figure VI.2: Description of the CAA computation domain with specific boundary conditions.

Additional details concerning the set-up of the simulation can be found in [154]. Only the main elements are summarized here. The three channels mesh has 18 blocks and a total of approximately 19,2 million points. The mesh size was chosen to ensure the propagation of the velocity and pressure fluctuations. Thus, the cell size must satisfy $\Delta l < \frac{\lambda_{min}}{10}$ (l denoting the characteristic dimension of a cell), with λ_{min} the shortest turbulent or acoustic wavelength. Moreover, only a finite range of wave frequencies can be adequately computed. The maximal frequency f_{max} is determined by the axial discretization Δx . The minimal frequency f_{min} is determined by the time of one period of the simulation $T = 1/50$ s. Thus, the synthetic turbulence can be generated within a range of frequencies between 50 Hz and 20 kHz using Liepmann's spectrum model with a step of 50 Hz. The radial wavenumber varies between $\pm 900 \text{ m}^{-1}$ with a

step of 10 m^{-1} . A convergence study was performed in the framework of [154], in order to select the proper radial mesh size. It has been shown that about 160 points over the radial direction are required to get a reliable solution. Finally, the time-step was chosen in order to ensure a local CFL number lower than 0.8: $\text{CFL} = \min_i \left(\frac{(|u| + c)_i}{\Delta x_i} \right) < 0.8 = \text{CFL}_{\max}$, with i denoting the considered spatial direction. The parameters used for the synthetic turbulence generation match here by the experimental data and prescribed radial profiles are plotted in Fig. VI.3. The blue curve denotes the absolute velocity, practically used to set the turbulence inflow convection velocity $U = U_\xi$, and the red curve denotes the absolute flow angle.

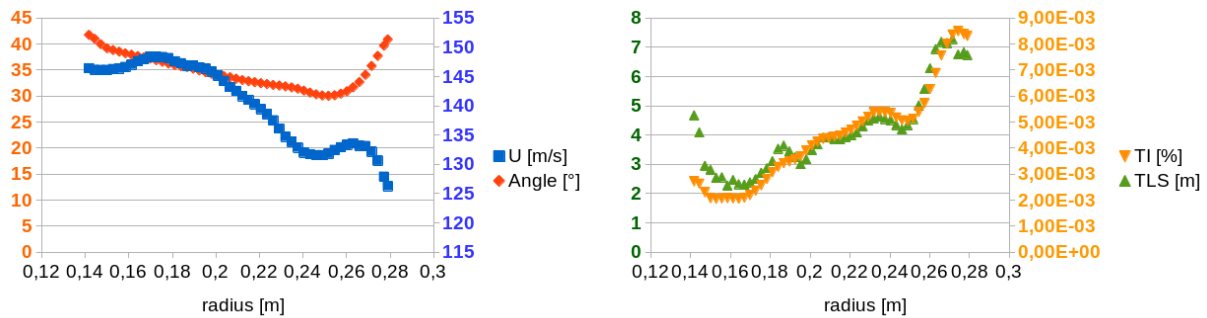


Figure VI.3: Radial profiles of the mean flow absolute velocity and angle β_c (left) and the turbulence characteristics (right) at the OGV plane (HW2 location) issued from experiment.

It was also checked in [154] that the turbulence velocity spectrum, picked-up upstream of the vanes in CAA, was in good agreement with the prescribed Liepmann spectrum model of the injected synthetic turbulence (see figure 10 in [154]).

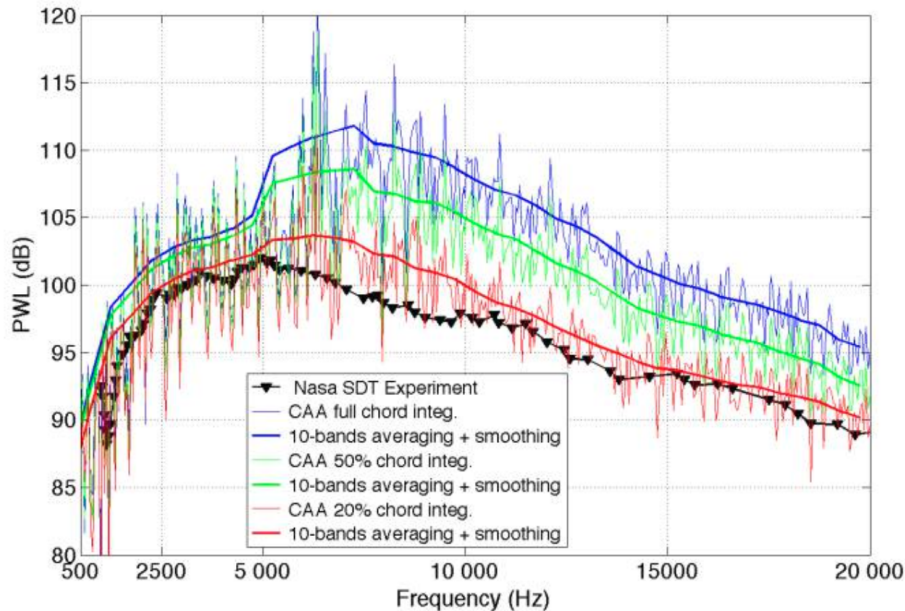


Figure VI.4: Predicted PWL spectra in the bypass duct (extracted from [154]).

In the previous simulations [154], the results have shown a shift in frequency and amplitude of the simulated spectrum compared to the experimental result, as plotted in Fig. VI.4. As pointed

out in this figure, limiting the FWH integration in the chordwise direction to the region of the LE reduces the generated noise and thus the gap between numerics and experiments is drastically reduced. One of the suspected reasons is that the RANS mean flow used at that time (2016) was not correct due to wrong profiles (total temperature and total pressure) imposed at inflow infinite boundary conditions. It was checked that the updated RANS solution obtained later in 2019 was closer to the aerodynamic performance targets at the operating point (61.7% N) and that the flow detachment on the OGV suction side detected in 2016 RANS solution was no more observed. Therefore, it could be the origin of extra acoustic sources probably due to some excitation of hydrodynamic modes impacting boundary conditions and overwhelming the physical acoustic field. The first task in this chapter consists in investigating if an improved new mean field will allow to obtain a reduction of the radiated noise to better match the experimental data while integrating FWH over the full chord. A new RANS calculation matching the experimental operating was performed at ONERA on the NASA SDT configuration using elsA solver. The main differences are visually highlighted in Figs. VI.5, VI.6, and VI.7. Generally, the velocity contour map comparisons highlight that with the new RANS flow, the velocity fields are more homogeneous with streamlines better aligned to the airfoil and re-circulations zones are less pronounced. Moreover, the angle of incidence is more adequate. Finally, the operating design point is better achieved for the new CFD computation.

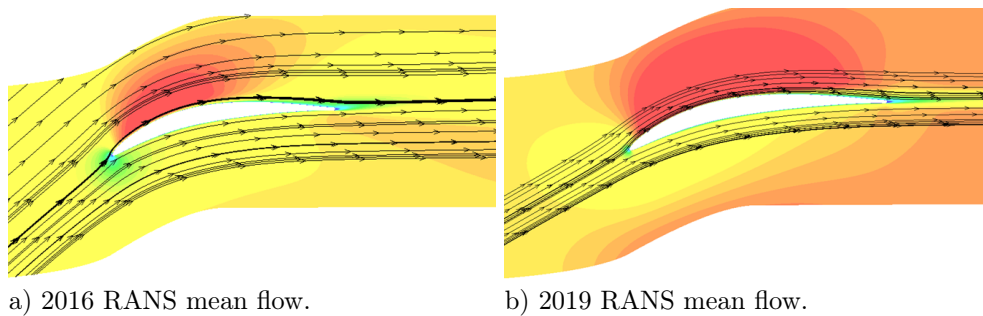


Figure VI.5: Axial velocity field comparison at radius 0.26 m. Levels between 20 and 130 m/s.

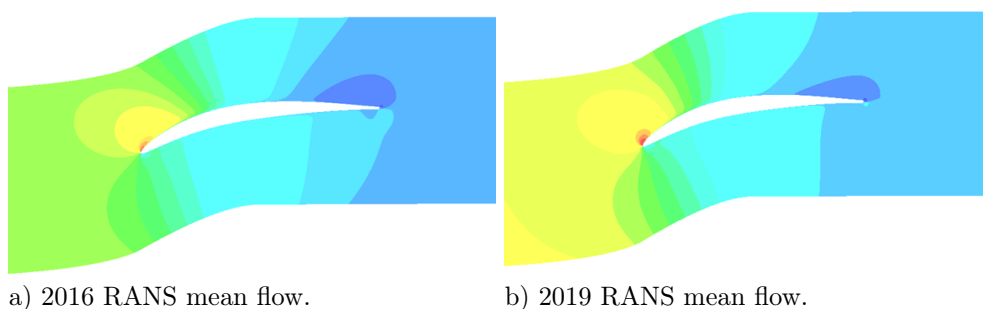


Figure VI.6: Tangential velocity field comparison at radius 0.26 m. Levels between -10 and 120 m/s.

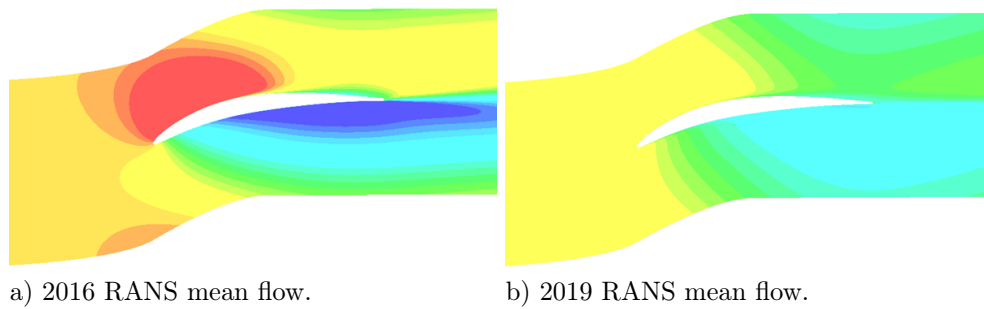


Figure VI.7: Radial velocity field comparison at radius 0.26 m. Levels between ± 10 m/s.

A new CAA computation is then performed with this new RANS flow field. Figure VI.8 shows how the injected velocity fluctuations are convected by the mean flow. It outlines the 2D-axi shape of the synthetic turbulence which is adopted.

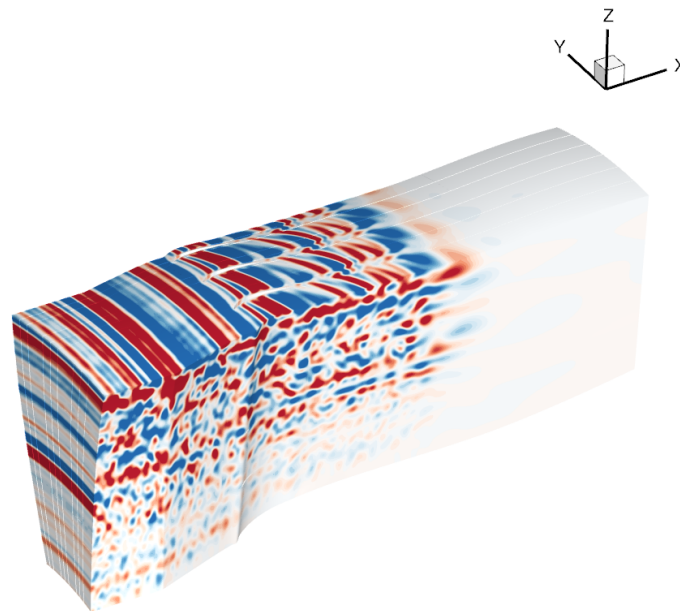


Figure VI.8: Instantaneous view of the advected gusts: u'_θ between ± 10 m/s.

One may also notice that the fluctuations are less intense in the hub region than in the casing region, which is directly related to the TI profile plotted in Fig. VI.3. After one period of converged signal, corresponding to 300 000 time steps or $\Delta f \approx 50$ Hz, the p'_{rms} (pressure root mean square) over the vane surface is compared in Fig. VI.9 to previous solution obtained with the older RANS mean flow.

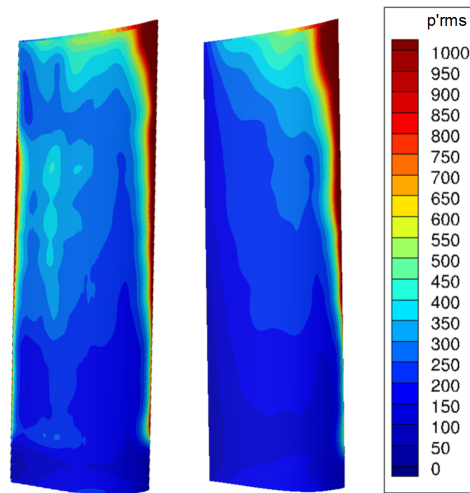


Figure VI.9: p'_{rms} on the blade surface: previous (left) and updated (right) CAA.

The use of a new RANS mean flow leads to a smoother distribution of the pressure. Moreover, the noise sources near the TE are removed. Finally, the FWH integration is performed using FanNoise code in order to assess the in-duct sound field radiated by the turbulent-like sources on the vanes. The resulting PWL spectrum is plotted in Fig. VI.10.

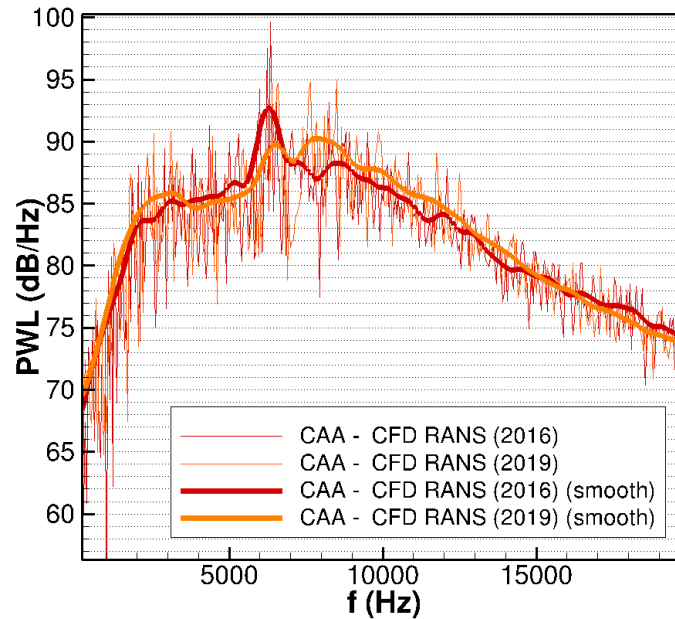


Figure VI.10: Comparison of the downstream PWL spectra provided by the CAA computations with the two RANS mean flows.

Despite of the improvements observed on the p'_{rms} maps in Fig. VI.9, the PWL spectra obtained with the new mean flow input are roughly unchanged. This result is quite disappointing and it seems to prove that other reasons are responsible for the present overestimation of the acoustic levels. In the following sections, two other explanations are investigated.

VI.1.2 Impact of inviscid or RANS mean flow on acoustic predictions

Even if the new RANS mean flow provides a cleaner field for CAA, it still requires a filtering step in order to treat the boundary layers and re-circulation zones. Indeed, it does not intrinsically satisfies the inviscid assumption used in the CAA. That is why, a mean Euler flow simulation is proposed as an alternative. To perform this CFD computation, an open source Euler 2D code is considered, which has already been used to obtain the mean flow around the InnoSTAT rectilinear cascade. The idea is to perform a 2D CFD simulation at each radius of the CAA domain. To this end, the CAA domain is slightly deformed as shown in Fig. VI.11, since the duct has originally not a perfectly annular shape with a constant cross section.

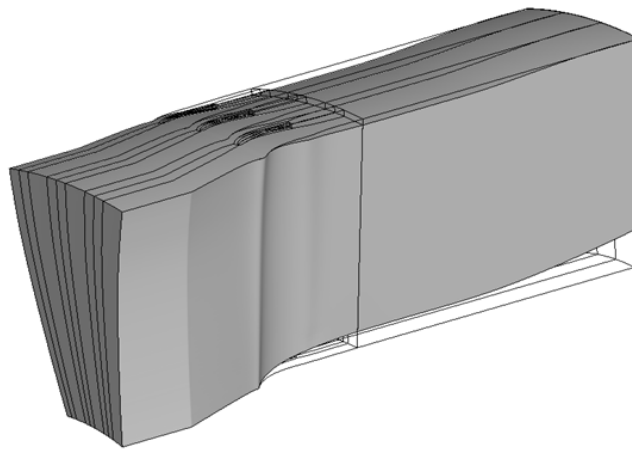


Figure VI.11: Deformation of the CAA domain toward a perfectly annular geometry.

At each radius of the CAA mesh, the geometrical boundaries are extracted (step (1)). From there, a CFD mesh is build using a MATLAB code (step (2)). The mean flow boundary conditions for the 2D Euler code is provided by the RANS simulations, except for the boundary layers at hub and casing which are discarded. In order to achieve the same operating conditions than for the RANS, the outflow static pressure of the Euler computation is adjusted. After having computed the mean flow field for each slice associated to each constant radius (step (2)), a routine is merges the planar data to recreate a 3D field (step (3)). This 3D field is then deformed to match a cylindrical coordinate system and it is interpolated on the CAA mesh (step (4)). The previously mentioned steps are schematized in Fig. VI.12.

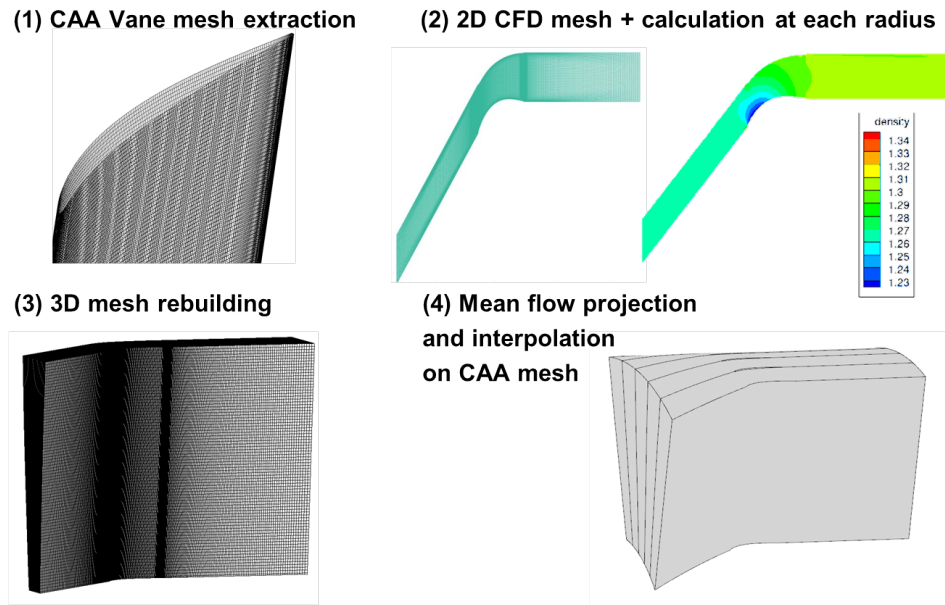


Figure VI.12: Illustration of the workflow set-up to obtain to a mean flow field for CAA calculations with a 2D Euler CFD code.

The following figures compare the RANS (2019) and Eulerian mean flow fields. A very close distribution of axial velocity is observed, which is of prime importance for accurate advection of turbulence structures.

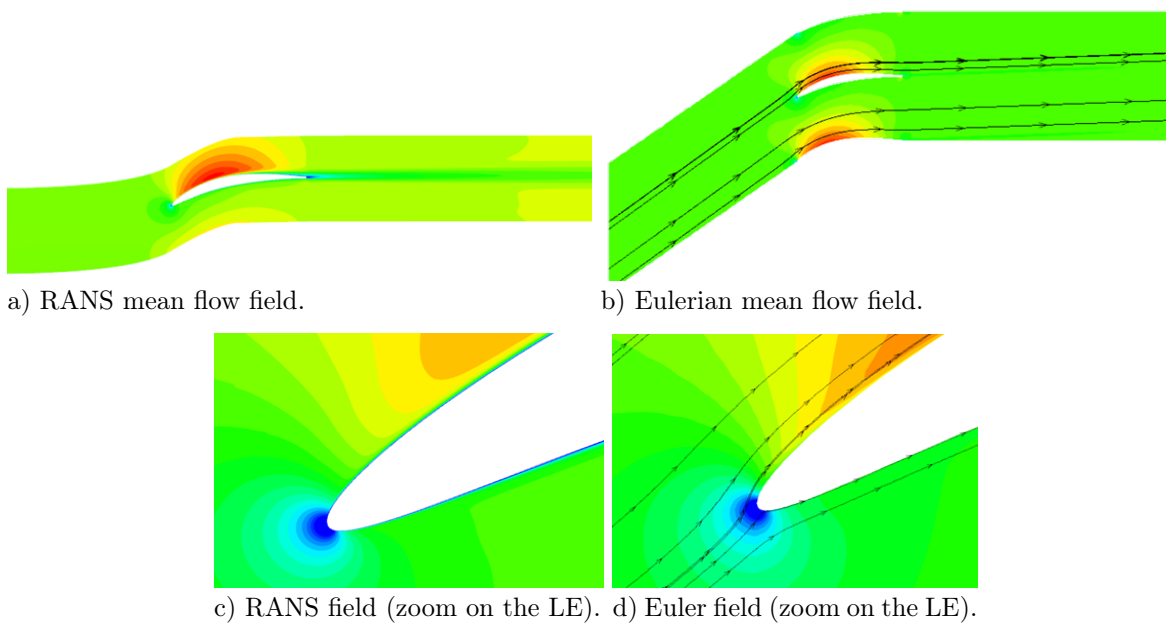


Figure VI.13: Axial velocity field U_x between 40 and 160 m/s.

A huge difference however appears for the static pressure field. In order to get the same operating point than for the RANS computation, the static pressure at the outflow boundary has been adjusted in the Euler simulations. Figure VI.14 compares static pressure fields. The deviation relative to the static pressure field is assumed to have a negligible impact with respect to the flow

convection effects and the source generation. An error of 2.2% on the mass flow rate is obtained between the 3D RANS and multi-slice 2D Euler solutions.

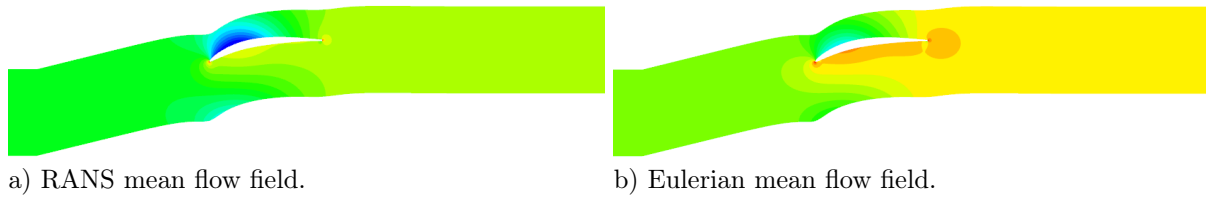


Figure VI.14: Static pressure p_0 extracted at $r = 0.26$. Levels between 95k and 115k Pa.

A CAA simulation is then performed with the Eulerian mean flow. The same synthetic turbulence is injected than with previous CAA with a RANS mean flow. The resulting fluctuating vorticity advected by RANS and Eulerian mean flow fields are illustrated in Fig. VI.15.

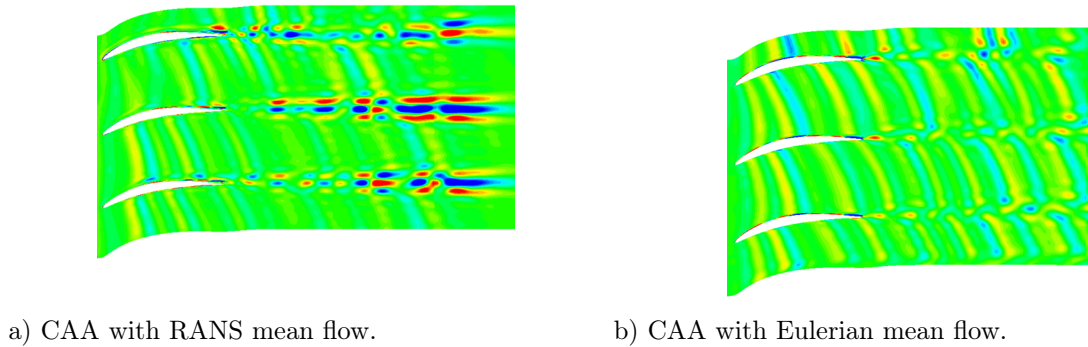


Figure VI.15: Vorticity ω'_z at $r = 0.21$ m, levels between $\pm 10k$ s^{-1} .

A weaker vortex shedding is observed in Fig. VI.15 when an Eulerian mean flow is used. This might reduce spurious acoustic sources. As for the previous CAA simulations, the fluctuating pressure distributions over the vanes are then extracted.

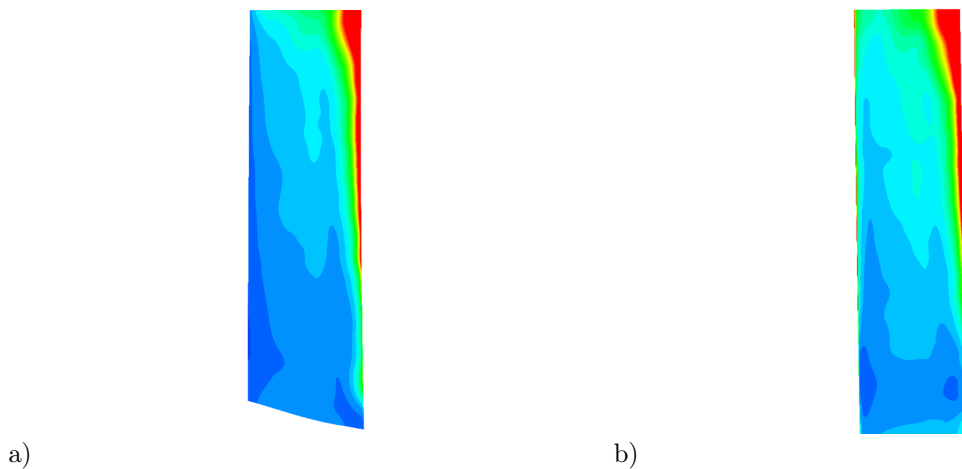


Figure VI.16: Distribution of p'_{RMS} (levels between 0 and 1000 Pa) over the vanes skin. CAA with RANS (a) and Euler (b) mean flows.

Surprisingly, RMS pressure contour maps in Fig. VI.16 do not reveal a major modification of p'_{RMS} distribution between the RANS and Euler based CAA simulations. Pressure sources are only slightly stronger with the Euler-based solution. This qualitative observation is confirmed by the comparison of the PWL spectra. No significant difference is observed indeed in Fig. VI.17 between the two CAA and FWH combining solutions.

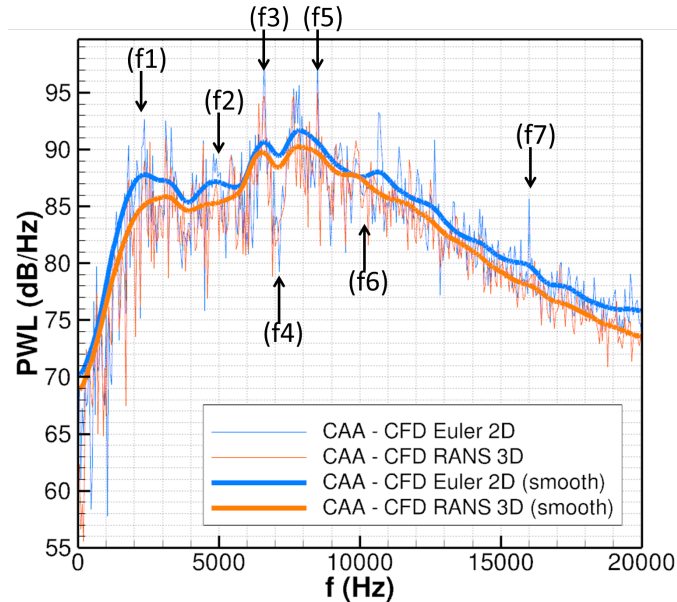


Figure VI.17: Downstream PWL spectra obtained with RANS and Eulerian mean flows.

Two conclusions can be drawn. First, Euler-based simulation is very appealing since it is rather easy and fast to perform multiple light 2D CFD Euler simulations, for which there is no need to filter boundary layers. That is especially a good point regarding acoustic simulations on serrated designs. Indeed, LE serrations create strong recirculation which might be tricky to handle as in [144]. That is why, Euler CFD has been used for the InnoSTAT rectilinear cascade configuration presented earlier in Chapter V.2. Second, a perfectly annular geometry represents a rather good approximation to the first order of a realistic OGV duct in the view of CAA broadband noise predictions. However, stronger peaks are visible in the Euler-based spectrum, which tend to increase the levels on the smoothed spectra. To deeper explore the later observation, the squared pressure is extracted on the vane skin at several frequencies indicated in Fig. VI.17.

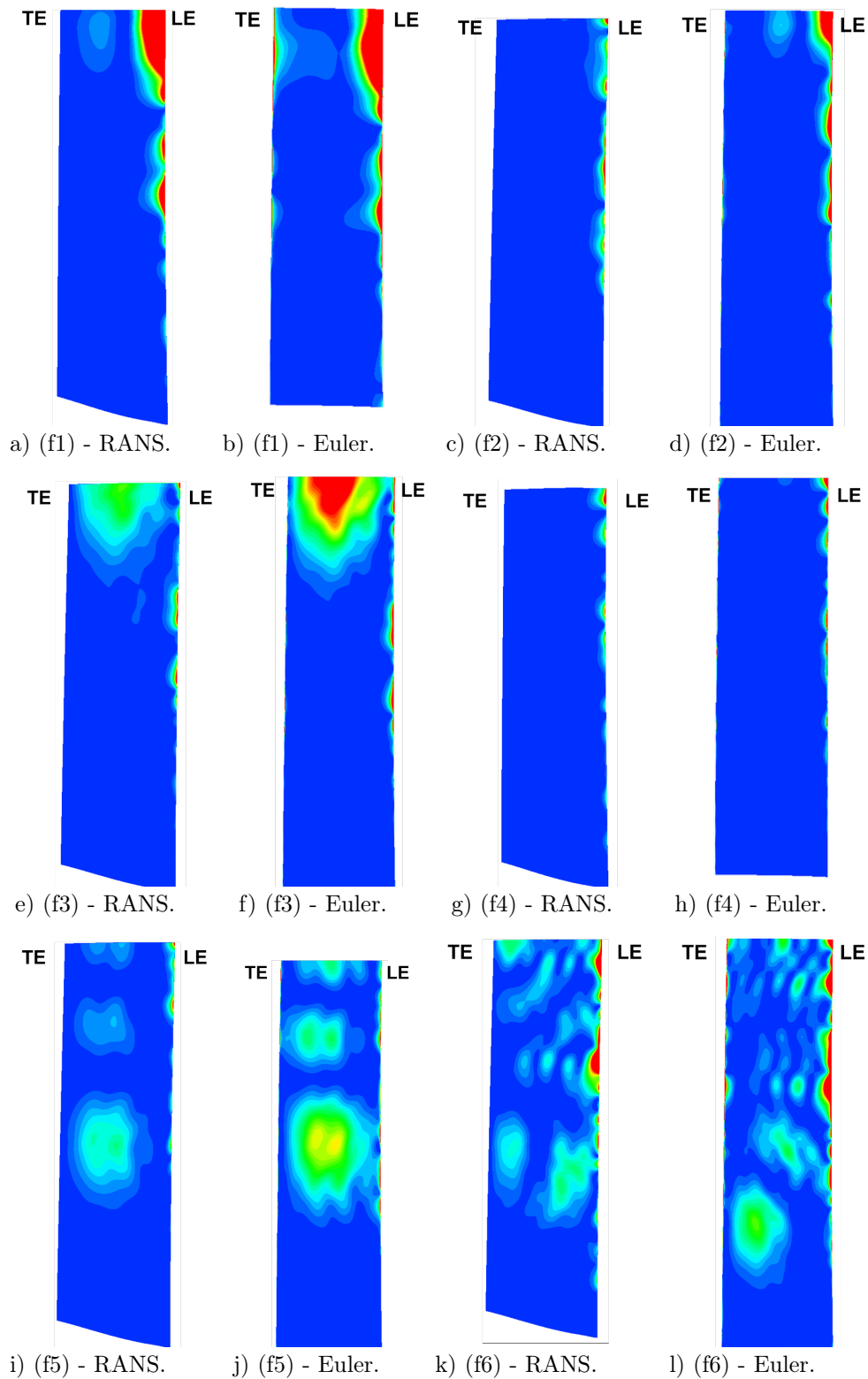
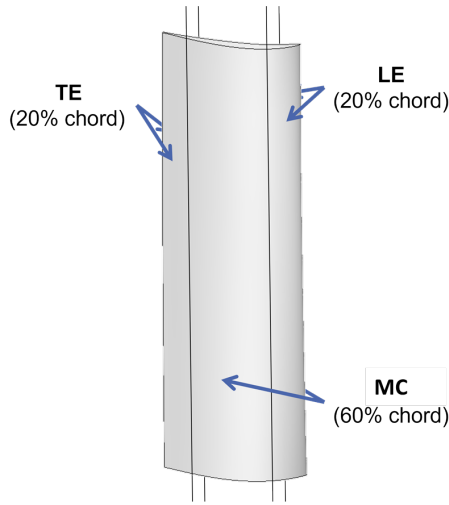


Figure VI.18: For frequencies (f1) to (f6) (cf . Fig. VI.17), the squared pressure fluctuation p'^2 on the vane skin is plotted.

Aside from the peaks in the spectra from Fig. VI.17, RANS and Euler based CAA provide very comparable pressure maps. At the peak locations, the pressure sources are stronger with the Eulerian mean flow, as shown by RANS/Euler comparisons in Fig. VI.18. In addition to Fig.

VI.18, the squared pressure is integrated over three different areas defined in Fig. VI.19. The relative contribution of each area in terms of p'^2 is also provided in the adjacent table.



(f1) 2350 Hz			(f2) 5000 Hz		
TE	MC	LE	TE	MC	LE
1/18	14/11	85/71	1/14	9/10	90/76
(f3) 6600 Hz			(f4) 7150 Hz		
TE	MC	LE	TE	MC	LE
5/10	67/69	28/21	3/22	24/7	73/70
(f5) 8500 Hz			(f6) 10200 Hz		
TE	MC	LE	TE	MC	LE
7/10	75/77	18/18	9/23	42/37	49/40

Figure VI.19: Considered surface of integration. Table VI.1: At each frequency from Fig. VI.17, the relative contribution (in percentage) of each area represented in Fig. VI.19 is provided. Left value corresponds to RANS based simulation and right to the Euler based CAA.

From Table VI.1, the LE is the major contributor to p'^2 at all frequencies except at the peak frequencies 6600 Hz (f3) and 8500 Hz (f5). Overall, peaks are more intense with the Eulerian mean flow field. This is certainly due to the perfectly annular geometry of the duct which emphasizes cutoff effect of acoustic modes at the Green's function singular frequencies. Moreover, the TE sources are stronger with the Euler based simulations. This might be due to the filtering of the boundary layers near the TE with the RANS field. Indeed, the filtering of the RANS induces a stronger axial mean flow at the TE than the one observed with the Eulerian mean flow. However, for both RANS and Euler based CAA, strong sources may appear at mid-chord (MC). In order to visualize the influence of these sources at TE and MC on far-field spectra, a limitation of the sources integration in FanNoise code is performed, as already done in [154].

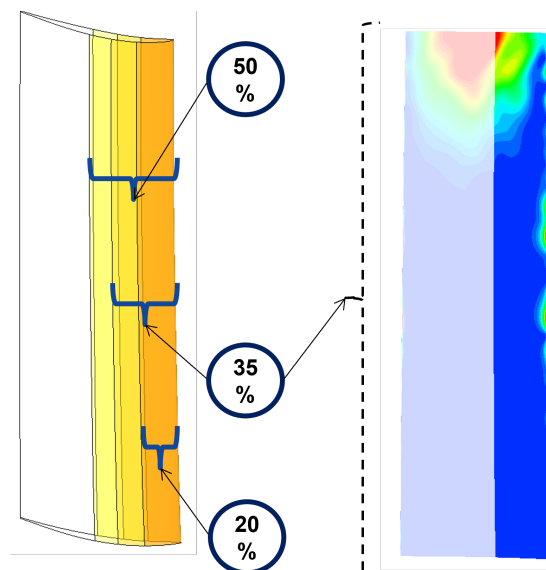


Figure VI.20: Illustration of the areas considered for the limited integration in FWH far-field propagation code.

Figure VI.20 depicts the different areas considered for the FWH analogy, with an integration of the pressure sources limited around the LE.

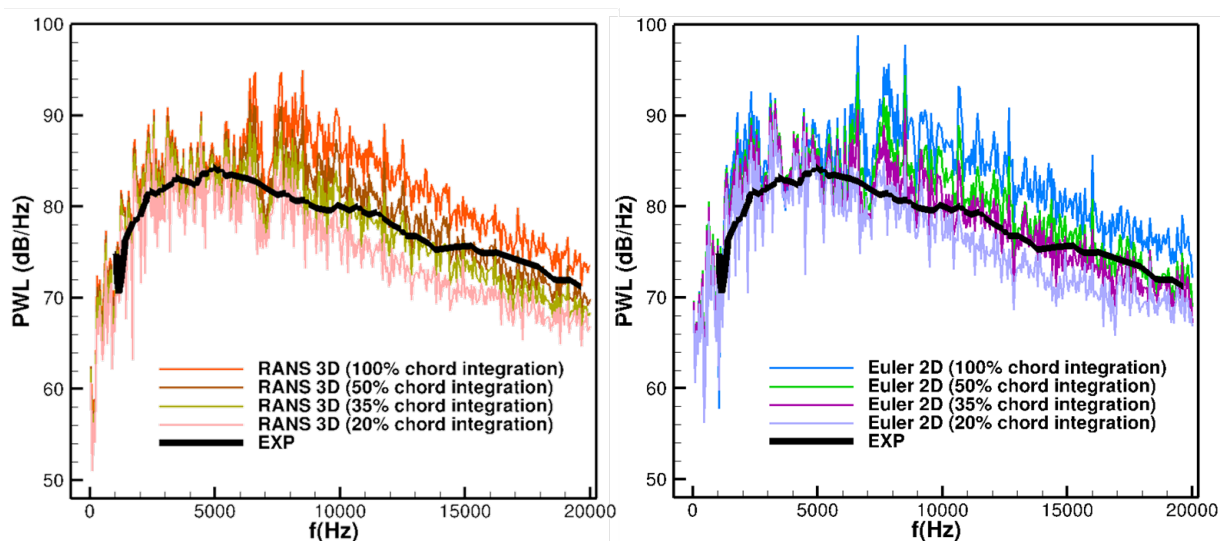


Figure VI.21: Downstream PWL spectra with limited surface integration in FWH post-processing.

The same trend is observed in Fig. VI.21 for RANS and Euler based CAA. The more the integrated area is limited, the more the medium and high frequency contributions are reduced. With a 35% limitation, a very close result to the experimental data is retrieved. As pointed before, peaks are stronger with the Eulerian simulation. It might be due to the fact that the simulation domain has been deformed, which could increase resonance phenomena, similarly to the phenomenon observed in the InnoSTAT rectilinear cascade configuration. To confirm this acoustic resonance assumption, a test case is proposed. Instead of injecting synthetic turbulence, three dipolar and harmonic sources are considered in the simulation domain close to the LE and

the hub at a frequency of 16 kHz. Since the synthetic turbulence is constant from vane-to-vane along the azimuthal direction, the dipoles are set with zero phase shifts.

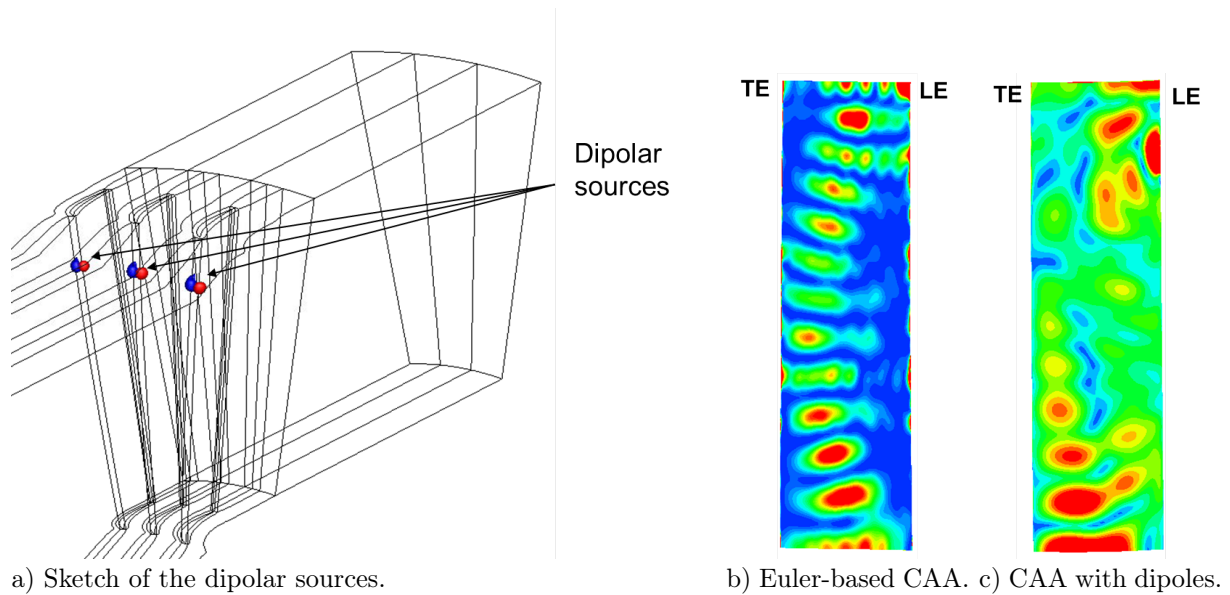


Figure VI.22: Comparison of dipolar sources with synthetic turbulence on p^2 distribution over vane skin. Frequency of interest is 16 kHz (f_7), as indicated in Fig. VI.17.

Interestingly, although this dipolar source representation is simplistic, a similar pattern is recovered in terms of pressure distribution along the span in Fig. VI.22. This observation accentuates the idea that the pressure sources observed at mid-chord are highly associated with an acoustic phenomenon. The use of a 2D (k_x, k_r) synthetic turbulence model (instead of a 3D (k_x, k_θ, k_r) turbulence) might be questionable at this stage, as these resonance effects would probably be less pronounced if k_θ wave number component was considered. Moreover, it has been observed during simulations on the InnoSTAT rectilinear cascade in Part V that the acoustic correlation between adjacent vanes has a huge influence on the acoustics. Yet, up to now, only the central vane has been considered for the acoustic post-processing on the NASA SDT configurations. The influence of the number of vanes taken into account for acoustics far-field prediction is now discussed.

VI.1.3 Impact of the number of vanes taken into account on the far-field acoustics

First, a CAA simulation on a double sized domain is considered (6 vanes instead of 3). The Eulerian mean flow field is retained here.

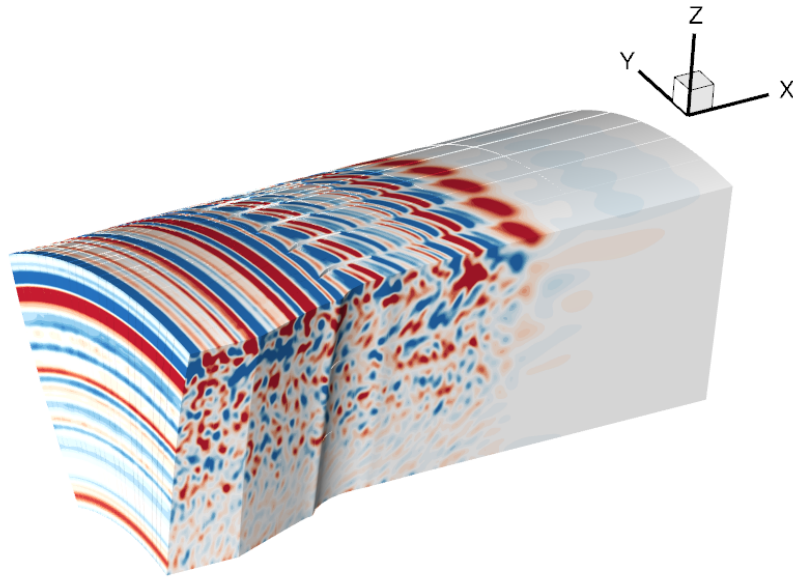
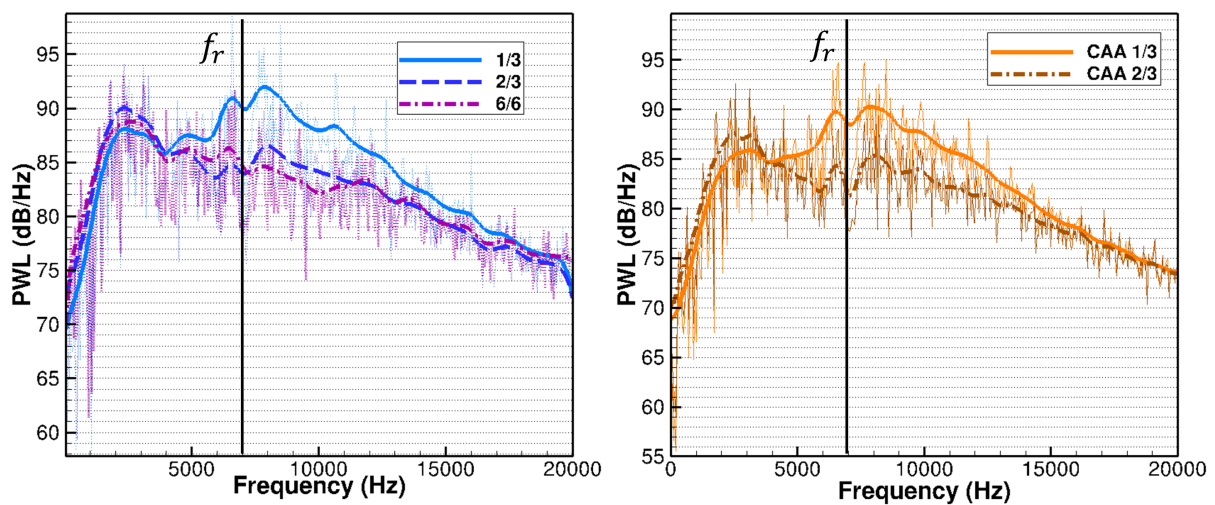


Figure VI.23: u'_y contour map between ± 10 m/s.

Figure VI.23 illustrates the fluctuating velocity field with the 6-vanes computation. The visualization of fluctuating velocity appears to be cleaner in comparison with Fig. VI.8. Indeed, for the 6-vanes computations, a temporal ramp has been added on the synthetic turbulence sources injected at the entrance plane of the CAA domain. The temporal ramp removes the "spurious mean value trails" visible in Fig. VI.8. This simple process allows to generate more physical snapshots in terms of isotropic turbulence structures, even if it has been verified that the previous transient structures had no impact on the accuracy of the CAA solution. In the following, different number of vanes are considered for the far-field propagation: 1/3, 2/3, 6/6 for the Euler based CAA and 1/3, 2/3 for RANS based CAA.



a) CAA with Eulerian mean flow.

b) CAA with RANS mean flow.

Figure VI.24: Downstream PWL spectra for different combinations of vanes taken into account during the acoustic post-processing.

Figure VI.24 demonstrates that taking into account multi-vane channels (at least 2/3) in the FWH calculation has huge impact. The difference in levels is maximum around the first resonance frequency $f_r = c_0/(2s) = c_0/(2r_{\text{mid}}2\pi/54) \approx 7$ kHz, with r_{mid} the radius at mid-span. Overestimation of noise levels around the latter frequency was already observed during simulations on the InnoSTAT rectilinear cascade in Chapter V.2. Finally, taking 6/6 vanes reduces slightly further the resonance bump.

VI.1.4 Cross-comparisons with other numerical solutions

The acoustic spectra, obtained with CAA sAbrinA are compared to experimental data along with numerical data from alternative numerical approaches. First, a wall modeled NS-LES (WMLES) with TurboAVBP solver [20, 150], which includes 2 rotor blades and 5 stator vanes, along with the nacelle is considered. They have indeed modified the number of vanes from 54 to 55 to achieve a $2\pi/11$ angular periodicity in both stator and rotor domains. Far-field acoustics have been obtained considering a FWH analogy based on the Goldstein's formulation. Second, a LBM solution provided by PowerFLOW solver is proposed in [52]. A 360° computation was performed including all the nacelle geometry with rotor and stator stages. As for far-field acoustics, a porous FWH approach has been considered, which avoids modeling ducted propagation at the radiation's step. Third, in [176], a 2D CAA solution computed by PIANO LEE solver on a 5 vanes configuration and impacted by a 2D RPM synthetic turbulence (see Chapter III.2) is compared to experiments. A 55-vanes computation with cyclostationarity is also presented in the paper. Taking into account all vanes provides a smoother solution in the low frequency region. A fully 3D synthetic turbulence has been also proposed in [109], but on another turbofan configuration.

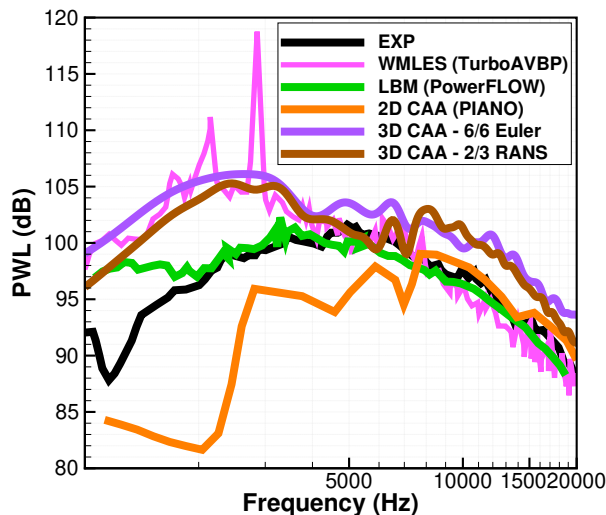


Figure VI.25: Downstream PWL spectra obtained from several numerical simulations and compared to experimental data.

All results are concatenated in Fig. VI.25, where an overestimation of the CAA (simulations with sAbrinA) is still observable in high-frequencies in comparison with experimental data. However, the CAA solution is now much closer in comparison with previous studies [154]. The CAA result

might have been slightly improved if a RANS based computation with 6 vanes had been considered, due to slightly lower levels in Fig. VI.17. A 3D Eulerian mean flow field computation with a realistic duct could also represent an improvement, it is expected to reduce peak's amplitude observed in Fig. VI.17. In the low-frequency range, a huge overestimation of the noise radiation is observed as for the WLES (the peak around 3 kHz is associated to the first BPF). Surprisingly, the 2D CAA with PIANO under-predicts levels below 10 kHz. Authors noticed in [176] that a 360° results in smaller oscillations in the low frequency region of the spectrum. Only the LBM matches very well the experimental data from 2 kHz to 20 kHz. It can be noted that apart the LBM solution, other approaches consider a Goldstein's analogy with in-duct mode propagation.

Possible improvements

In order to reduce the bump in low frequencies, increasing the number of vanes might represent a step forward. This configuration with an increased number of vanes should be ideally associated with a 3D turbulence (k_x, k_θ, k_r) . First attempts using a 3D synthetic turbulence on turbofan configurations have been investigated by Cader in [47]. Figure VI.26 illustrates the resulting velocity field. However, generating 3D turbulence in annular geometries remains challenging (cf. Chapter III.4). Considering a turbulence varying along the cascade direction $(k_x, k_\theta, k_r = 0)$, as on the InnoSTAT rectilinear cascade configuration $(k_x, k_y, k_z = 0)$, might represent a more convenient solution. In fact, as for the rectilinear cascade configurations, an almost identical solution is obtained in comparison to a fully 3D turbulence. Perspectives in terms of extending synthetic turbulence methodology to (k_x, k_θ, k_r) structures (for turbofan cases) is addressed in Chapter III.4.

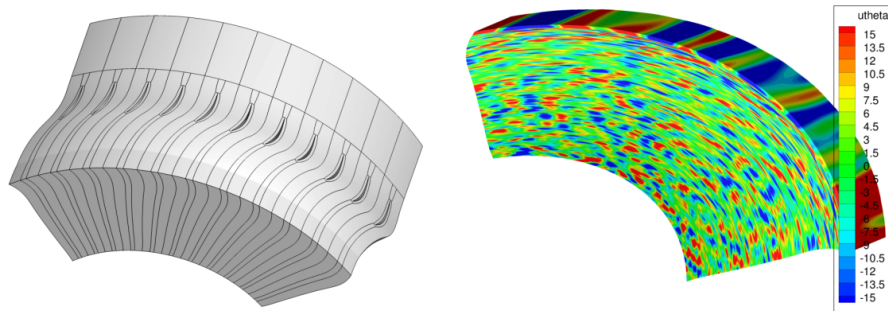


Figure VI.26: 11-vane CAA mesh (left) and synthesized velocity turbulent field (right), extracted from [47].

VI.2 ECL-B3 PHARE-2: preliminary serrated design and evaluation

VI.2.1 Backgrounds from ONERA studies on similar turbofan models

Following experiment on the rectilinear cascade analyzed in Part V, the second InnoSTAT test campaign will take place in 2023 at the Centrale Lyon PHARE-2 facility on the ECL-B3 test rig. This turbofan mock-up has been briefly presented in Section II.3.3. New designs inspired by results from the rectilinear cascade will be compared to the baseline stator and to a serrated geometry proposed by ONERA along with Safran in the framework of a European project ENOVAL [4].

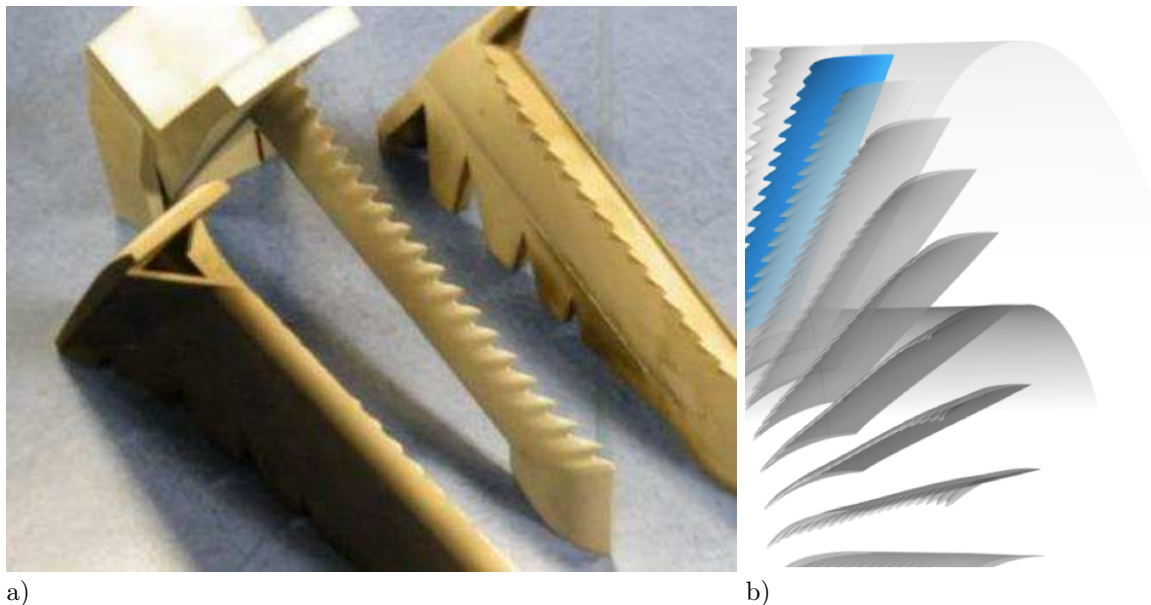


Figure VI.27: Prototype of OGV serrations proposed by ONERA and Safran Aircraft Engines during ENOVAL (a). 3D view of the serrated OGV02W19H4 (b).

This geometry illustrated in Fig. VI.27 has been defined considering an averaged turbulence length scale. It has been manufactured by Safran during ENOVAL and it will be used as a reference for the low-noise concept during InnoSTAT. This design has been defined to account for a spanwise averaged value of the turbulence length scale L_l . The initial design OGV02W19H8

had been defined with 19 serrations and $h_s = \lambda_s = 2 \times L_l = 8$ mm. But RANS calculation had shown excessive aerodynamic penalties which has resulted in the final design OGV02W19H4 with h_s twice smaller. Moreover, OGV02W19H4 illustrated in Fig. VI.27 also includes a reduction of the serrations amplitude near the shroud for mechanical constraints. A CAA simulation with sAbrinA and (k_x, k_r) turbulence (as for NASA SDT simulation in this thesis) has been performed to evaluate the noise reduction [154]. A rather small 2 to 4 dB noise reduction was obtained. But it should be noted that the CAA was done considering a higher regime at 82 Nn instead of 55 Nn (priority for Safran). These rather small reductions can be explained by the non-optimal criteria finally adopted (h_s reduced by a factor 2). Moreover, this radially uniform serrated design did not account for local variations of the turbulence length scale which certainly limits the noise reduction efficiency.

Although the rotor geometry for InnoSTAT is unknown, the stator should be the same than during the ENOVAL project. Thus, all the flow values are given below for the turbofan F07C-OG02 configuration proposed by Safran. The regime of interest is the APP OP, which corresponds approximately to 55% of the nominal speed. Mean flow velocities in Fig. VI.28 have been provided by a RANS calculation. It should be noted that for this configuration velocities remains roughly unchanged from the mixing plane up to the stator LE. The absolute velocity U , has been obtained considering a zero radial velocity. Indeed, the empirical and analytical model have been derived assuming a mean flow aligned with the airfoil's chord.

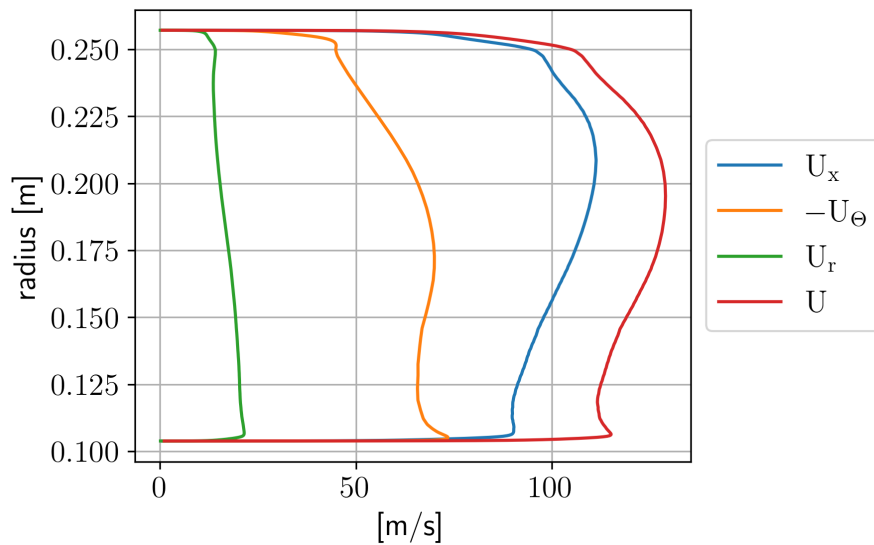


Figure VI.28: Mean flow velocities at the APP OP. Values extracted from a RANS mixing plane calculation.

Additional RANS calculations with the rotor alone have been used to estimate the turbulent inflow properties at the stator LE. The radial profiles of TI and L_l are plotted in Fig. VI.29. It should be noted that the L_t profile is obtained by using the Ganz-based approach (see [110, 144, 145] for more details).

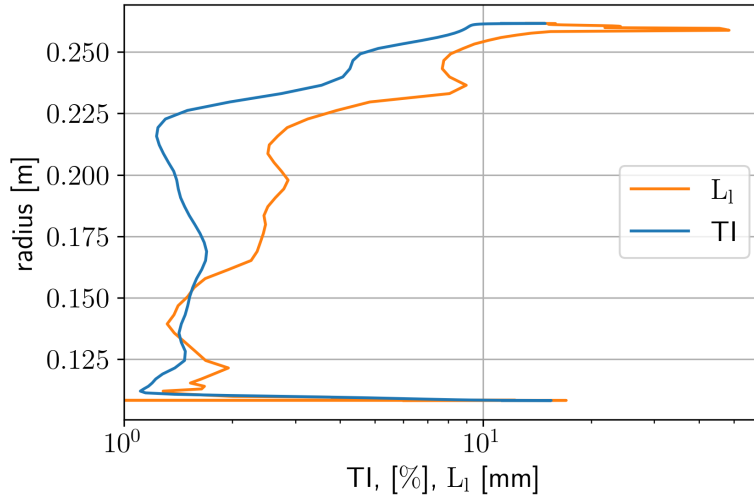


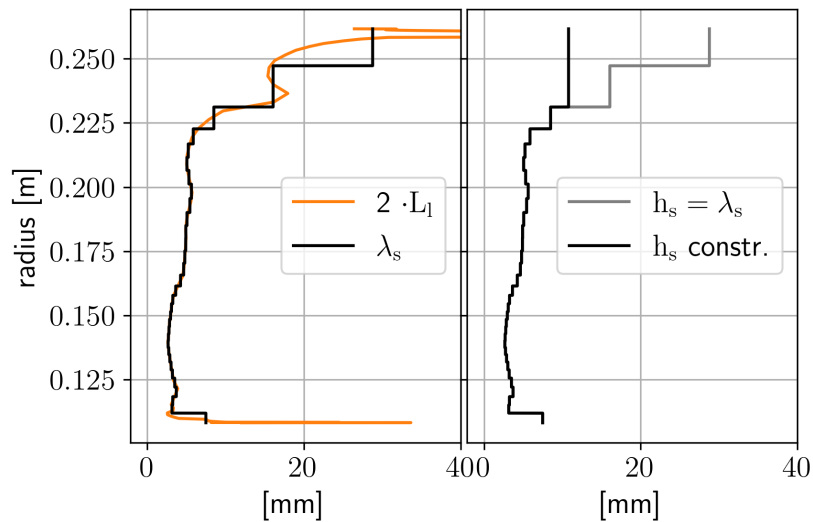
Figure VI.29: Turbulence properties at the stator LE location from a RANS calculation.

VI.2.2 Serrated-OGV design using turbulence inflow characteristics from RANS

After the ENOVAL project, ONERA has introduced a new design methodology focused on spanwise varying serrations [144] in the framework of another European project TurboNoiseBB [13]. Some information can also be found in Appendix G. Indeed, contrary to the rectilinear cascade configuration, the properties of the turbulence field are varying along the span as plotted in Fig. VI.29. This variation needs to be taken into account to enhance the local noise reduction from serrations. The following steps are performed in order to choose the serrations amplitude h_s and wavelength λ_s . The criteria from Part IV are again considered, *i.e.*, $\lambda_s = 2L_l$ and $h_s = \lambda_s$.

- Starting from the shroud, half of a wavelength is defined, *i.e.* of a width $\lambda_s/2$. The idea is to avoid having serration root near the shroud which could generate corner flows and degrade aerodynamics. To determine λ_s an iterative procedure is performed in order to achieve $\frac{1}{\lambda_s/2} \int_{\lambda_s/2} 2L_l(r)dr = \lambda_s$.
- The same iterative procedure is achieved to determine serration's wavelength toward the shroud. But this time a full serration is considered: $\frac{1}{\lambda_s} \int_{\lambda_s} 2L_l(r)dr = \lambda_s$.
- For the serration at the hub the value of λ_s is tweaked in order to get exactly half a serration as for the shroud.
- The serration amplitude is chosen accordingly to $h_s = \max(\lambda_s, 0.2 \cdot c)$. Indeed, similarly to [144], the amplitude of the serration is limited with respect to the chord, here 20% of the reference chord length.

The process presented above is depicted in Fig. VI.30.

Figure VI.30: Set-up of the evolutive serration parameters h_s and λ_s .

As proposed in Part V, for reduce aerodynamic penalties, the minimal chord of the serrated design is kept unchanged. The 2D pattern of the low-noise vane is illustrated in Fig. VI.31.

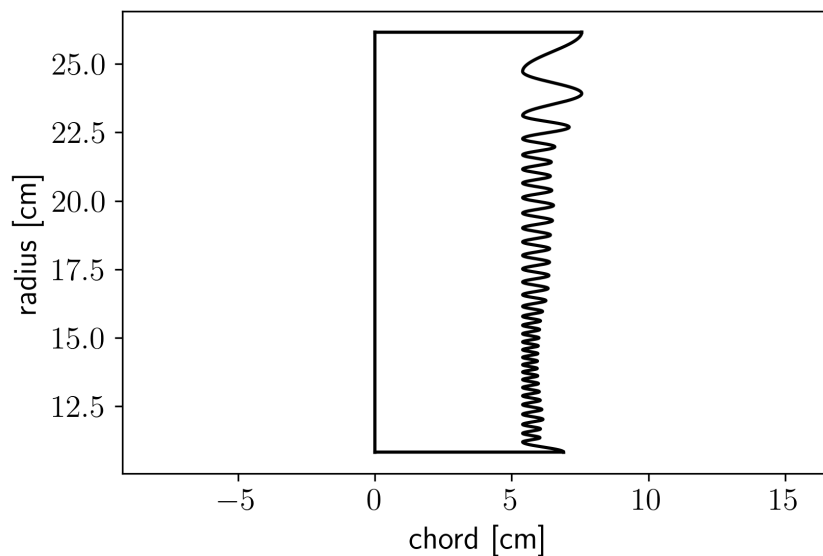


Figure VI.31: 2D shape of the serrated vane.

One should remark that no threshold value was considered for minimum serration wavelength. This could be easily imposed in order to avoid any structural issue. It can be also noted that continuously varying serrations (not presented here) might be considered instead of the strip calculation. However, this geometry definition is not suited for noise reduction assessment by the WH analytical solution.

Then, the ersatzZ morphing code is used to apply the 2D pattern to the 3D geometry of the baseline vane. The same morphing laws than introduced in Part IV for the rectilinear cascade are used but, with an increased mean chord as for the serrated geometry d_2 defined in Part V.

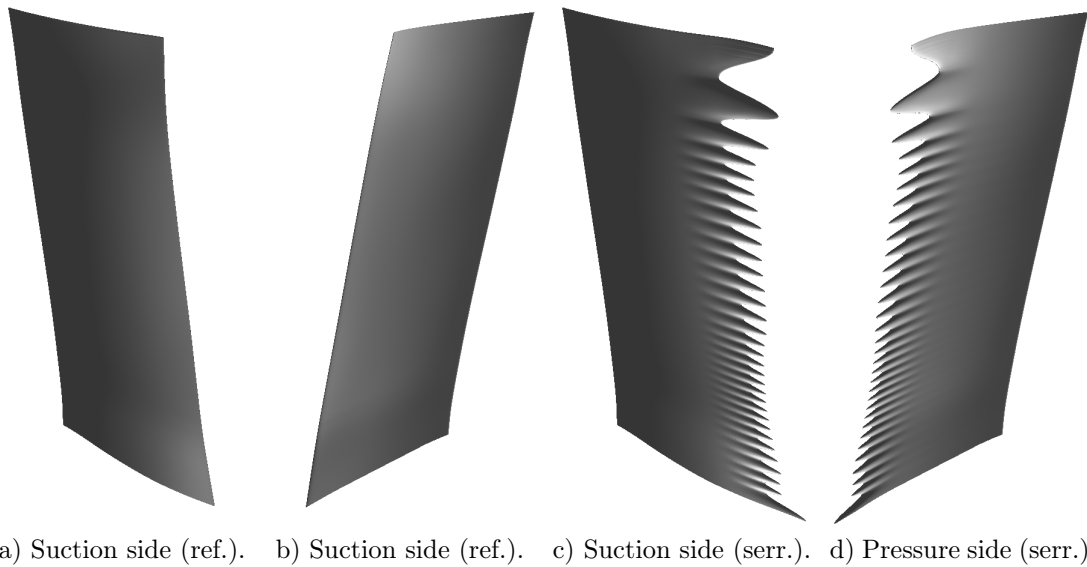


Figure VI.32: Comparison off the baseline (reference) vane geometry with the low-noise design provided by ersatzZ.

The baseline and low noise design are compared in Fig. VI.32, along with the full stator stage with the low-noise vanes in Fig. VI.33.

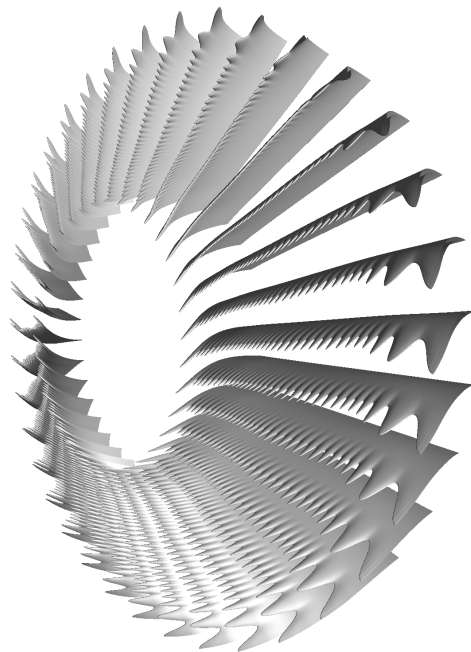


Figure VI.33: 3D view of the stator with serrated vanes.

VI.2.3 Analytical assessment of the noise reduction

An analytical assessment is proposed to estimate the noise reduction by means of the WH technique implemented and extended in Part IV. As already achieved in Appendix G and in [144], a strip calculation is performed. To this end, the mean flow value U , TI, and L_l are

averaged on each strip corresponding to a serration, as shown in Fig. VI.34 and Fig. VI.35.

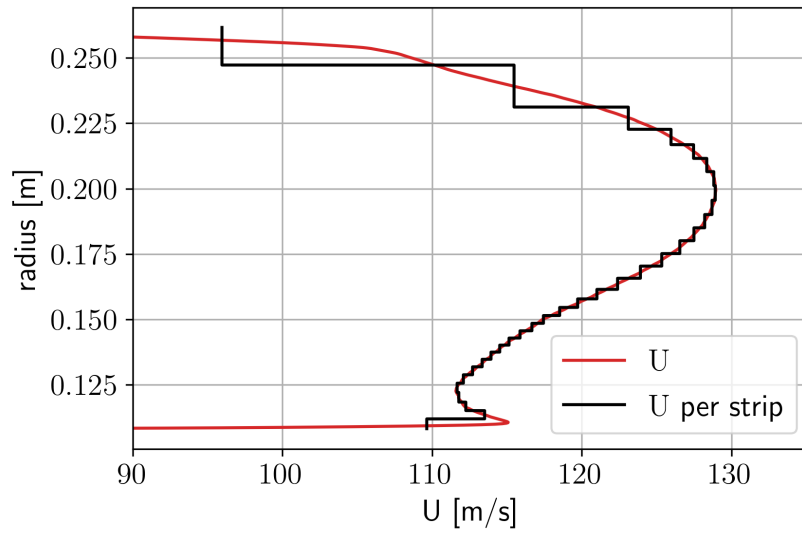


Figure VI.34: Discretization per strip of the absolute velocity U .

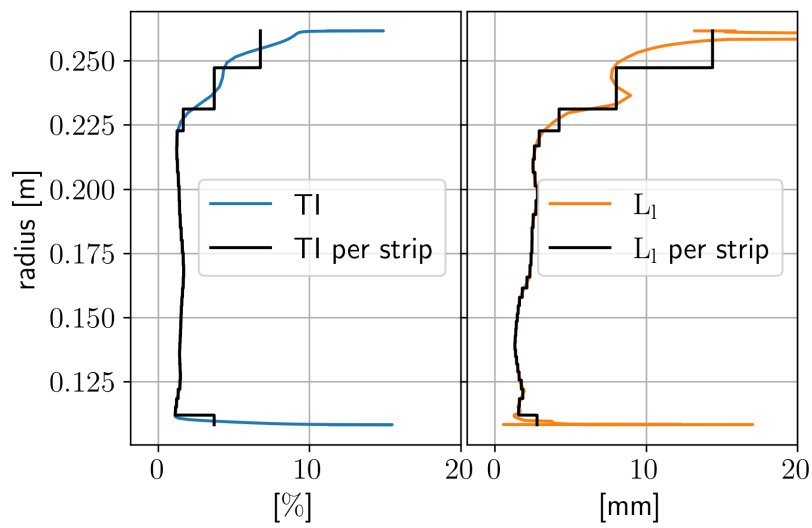


Figure VI.35: Discretization of the turbulence properties per strip.

The noise reduction obtained using the WH technique in the frequency domain is plotted in Fig. VI.36.

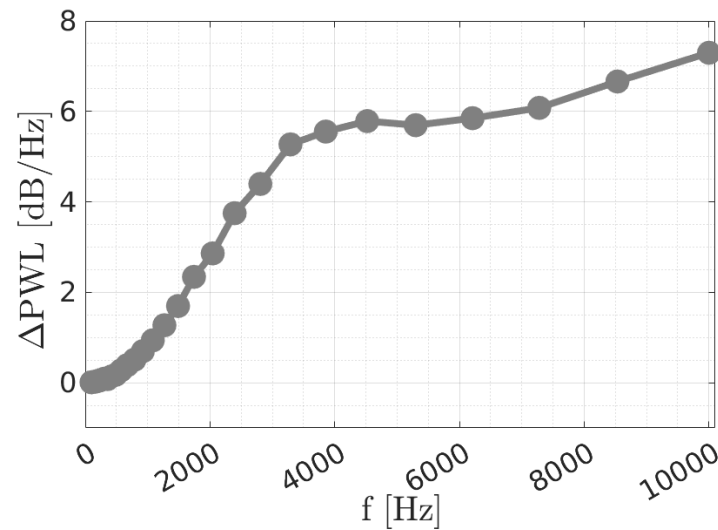


Figure VI.36: Noise reduction provided by the WH technique.

A 6 dB noise reduction is expected in the mid-frequency range. However, it is a theoretical value assuming a flat plate impinged by a HIT. This is why, among other, the work presented above is only preliminary.

VI.2.4 Future work

Therefore, prior to the InnoSTAT test campaign and serrated stator manufacturing planned in 2023, the preliminary serrated design, following the main steps proposed above, will be completed taking into account the pre-test data from the ECL-B3 test rig. CAD geometries and engine operating regimes will be provided by Safran. Noise reductions at the three acoustic certification points will be analytically estimated. In addition, aerodynamic penalties will be checked through RANS calculations at the approach regime and aerodynamic design point. Some optimization of the 3D vane shape might be proposed to reduce even further the aerodynamic penalties. Finally, the baseline stator and the definitive serrated geometry proposed by ONERA will be simulated using LBM simulations (with the compressible version of the ProLB solver) on the test ECL-B3 test bench.

This page intentionally left blank.

Conclusions and Perspectives

Looking at future quiet aeroengines, this thesis has been aiming at developing innovative low-noise stator concepts for the rotor-stator interaction noise reduction with dedicated prediction methods. This study also allowed to apply and extend different prediction methods, from low to high fidelity, to more realistic data sets. These methods include: an analytical solution for flat plates with leading edge serrations (low-fidelity), a CFD/CAA-LEE approach with 3D synthetic turbulence (intermediate fidelity), and LBM calculations (high-fidelity). They have been applied on the baseline geometry and two ONERA's serrated designs for the InnoSTAT experimental test campaign on a rectilinear cascade. Comparing all those methods on a single bench also enabled a better understanding of the limitations of the different models and their associated assumptions. Furthermore, it has been demonstrated that a wavy leading edge treatment can significantly reduce the broadband noise, up to 5 dB in the installed configuration, while limiting the aerodynamic penalties. Finally, extension of the noise prediction approaches and the serration design methodology to more realistic annular configurations have been discussed.

With respect to the analytical assessment of leading edge patterns for noise reduction, a state of the art solution proposed in [30] and based on the Wiener-Hopf technique has been extended to take into account finite span geometries and successfully implemented in a MATLAB code. In parallel, this extension has allowed a strip calculation of spanwise varying leading edge serrations impinged by a spanwise varying unsteady inflow (investigated in Chapter VI and Appendix G). A good agreement has been observed between the analytical solution and the CAA-LEE calculations on the rectilinear cascade configuration. However, the analytical model has its limitations. It tends to over-predict the noise reduction at low frequencies [131] in particular for very acute geometries as investigated in Appendix F. Indeed, it lacks the modeling of the secondary vortex mechanisms pointed out in [56, 50], which can play a major role as for the leading edge noise reduction especially for slitted geometries [50]. Regarding the CAA-LEE, a first contribution has consisted in substituting the genuine RANS mean flow by an Eulerian one using an open source 2D Euler code. This strategy avoids the need to filter the RANS variables to satisfy the non-viscous assumptions of the CAA calculations. In addition to the possible setting of a fully Eulerian mean flow, the generation of a synthetic turbulence coming from Fourier modes decomposition has been successfully extended to fully three-dimensional fields with 3 wavenumbers and 3 velocity components (suitable for a Cartesian coordinate system) and numerically interfaced with the CAA solver sAbrinA. However, to achieve this result, a dedicated windowing has to be introduced to cancel the spanwise velocity fluctuations at the hard-wall boundaries in order to ensure the divergence-free property. Moreover, although the extension to 3D turbulence has been demonstrated in Cartesian coordinates with a homogeneous inflow, the transposition to cylindrical coordinate systems is not trivial. Indeed, as discussed in Part III, it requires to relax the wavenumber discretization constraint along one of the directions in space. In parallel to the theoretical developments for 3D synthetic turbulence, all the generation routines have been optimized in order to lower the associated CPU cost and keep it at a low level compared to the CAA calculation itself. In addition to the synthetic turbulence generation methodology, a parametric study on full span CAA simulations has been performed to highlight how the turbulence structure influences the leading edge noise predictions. Hence, the turbulence variation along the cascade direction is fundamental for assessing accurately the cascade effect and blade to blade interac-

tions, whereas the spanwise variation of the turbulence is more crucial for assessing the acoustic performances of the serrations. Finally, regarding the acoustic generation and propagation, a parametric study on the number of vanes taken into account within the simulation domain and for the Ffowcs Williams-Hawkings post-processing has demonstrated that this number has to be carefully chosen to properly capture the cascade effects and blade to blade interactions. At last, a challenging high fidelity approach based on the LBM (using the code ProLB) has been applied on the cascade configuration by simulating the entire experimental set-up (including turbulence grid, wind tunnel walls, and microphone antenna). The 2 billion points LBM solution has been favorably compared to a reference RANS calculation along with experimental data in terms of pressure coefficient at the vane skin. LBM has also demonstrated its ability to accurately reproduce the turbulence generated by the grid (with suitable correction for iso-grid comparison with experiment). This allows to get rid of the definition of a prescribed synthetic turbulence like in the hybrid CAA approach. Moreover, LBM may model more complex phenomena such as non-uniform viscous mean flow and secondary vortices generated at the peaks and roots of the serrations. Concerning the acoustics, LBM matches experimental far-field acoustics both in terms of absolute noise levels and noise reductions. Direct noise calculations are the only way to assess the actual sound radiation patterns involving inherent installation effects, whereas indirect solutions achieved from a Ffowcs Williams-Hawkings integral (solid surface formulation) are shown to be much less accurate. However, Ffowcs Williams-Hawkings extrapolation can be satisfying for relative noise reduction assessment although a little over-prediction in high frequencies appears. Finally, regarding the design of 3D serrated geometries, a noticeable improvement proposed during this thesis lies in the new morphing laws in Parts IV and V, to provide a 3D vane geometry accordingly to a 2D leading edge pattern. This innovative deformation methodology has significantly reduced the aerodynamic penalties, closely approaching the values for the reference profile. In addition, the design has been able to achieve a promising sound power level reduction around 4 to 6 dB in a relevant frequency range (the frequency of maximum efficiency increasing with the speed flow).

A preliminary extension to turbofan configurations has been presented in Part VI. In a first step, a 6-channel 3D CAA simulation, with a 2D Eulerian mean flow per slice, has been performed on the NASA SDT case showing again the importance of the cascade effect and blade to blade interactions. Then, in preparation for the InnoSTAT test campaign on the PHARE ECL-B3 turbofan configuration, a spanwise varying serrated design has been proposed and the achievable noise reduction has been assessed analytically.

In terms of perspectives, the main task would consist in following the work started in Part VI. Outside of the development, prediction, and validation of aerodynamic and acoustic behavior of serrated designs, the present CAA methodology applied for the rotor-stator interaction assessment could be studied further. Indeed, only a 2D turbulence with a spanwise variation has been applied on the reference NASA SDT case in Part VI. It would be appealing to study the impact of a turbulent field varying along the annular cascade direction (adding angular wave number contribution) involving quasi 360 degrees simulations, which could match better the experimental results in particular at low frequencies. Furthermore, it could be interesting to set up a 3D Eulerian mean flow instead of the 2D calculation per slice.

In preparation for the InnoSTAT test campaign on the PHARE ECL-B3 test bench, a serrated design proposed by ONERA will be manufactured. Beyond the validation through compressible LBM simulations and experiments in 2023 of the new design methodology on realistic Fan-OGV stage configurations, the turbulent field properties may need a further investigation. Indeed, although there is little variation on the turbulence intensity prediction between numerical approaches, there is still a huge uncertainty about the turbulence length scale estimation [90, 111], whether from RANS or LES calculations. However, a small deviation on the actual turbulence length scale should not noticeably impact on the noise reduction. For instance in [138] (page 78), a maximal loss of around -0.5 dB was observed when twice smaller or twice larger turbulent length scale were considered. In terms of noise reduction efficiency at high frequencies, it could also be interesting to investigate the noise induced by laminar-turbulent transition as discussed in Lewis [120] (see pages 140-141) and to verify whether or not it limits the noise reduction allowed by the serrations. Apart from the broadband noise component, it is crucial to have a look at the tonal noise reduction achievable by the serrated designs. Besides the noise reduction, a critical point to reach a higher TRL and to implement a serrated OGV on a demonstrator is to check that the aerodynamic penalties are acceptable on a turbofan rig. It was partly studied in previous studies (ENOVAL [154], TurboNoiseBB [144]) using RANS calculations, but it will have to be performed again before the tests. To this purpose, genuine optimization methods could be used or more recent adjoint method could be implemented [48].

Finally, serrated designs could be applied on other configurations than UHBR turbofans, such as future Unducted Single Fan (USF) configurations studied in the framework of CFM Rise [3], for which the rotor-stator interaction mechanism is expected again to be a major contributor to the engine noise.

Appendices

A Calculation of 1D spectra from velocity Fourier transform

The set average of the product of the Fourier transform of the velocity and its complex conjugate is considered. Equation is expanded.

$$\begin{aligned} \langle \widetilde{\mathbf{u}}_i^*(\mathbf{X}, f) \widetilde{\mathbf{u}}_j(\mathbf{X}, f') \rangle &= \left\langle \int_{-\infty}^{+\infty} \mathbf{u}'_i(\mathbf{X}, t) e^{i2\pi f t} dt \int_{-\infty}^{+\infty} \mathbf{u}'_i(\mathbf{X}, t') e^{-i2\pi f' t'} dt' \right\rangle \\ \Leftrightarrow \langle \widetilde{\mathbf{u}}_i^*(\mathbf{X}, f) \widetilde{\mathbf{u}}_j(\mathbf{X}, f') \rangle &= \left\langle \int_{-\infty}^{+\infty} \int_{-\infty}^{+\infty} \mathbf{u}'_i(\mathbf{X}, t) \mathbf{u}'_i(\mathbf{X}, t') e^{i2\pi(f t - f' t')} dt dt' \right\rangle \\ \Leftrightarrow \langle \widetilde{\mathbf{u}}_i^*(\mathbf{X}, f) \widetilde{\mathbf{u}}_j(\mathbf{X}, f') \rangle &= \int_{-\infty}^{+\infty} \int_{-\infty}^{+\infty} \langle \mathbf{u}'_i(\mathbf{X}, t) \mathbf{u}'_i(\mathbf{X}, t') \rangle e^{i2\pi(f t - f' t')} dt dt' \end{aligned}$$

A change of variable, $t' = t + \tau$, is applied.

$$\langle \widetilde{\mathbf{u}}_i^*(\mathbf{X}, f) \widetilde{\mathbf{u}}_j(\mathbf{X}, f') \rangle = \int_{-\infty}^{+\infty} \int_{-\infty}^{+\infty} \langle \mathbf{u}'_i(\mathbf{X}, t) \mathbf{u}'_i(\mathbf{X}, t + \tau) \rangle e^{i2\pi(f - f')t} e^{-i2\pi f' \tau} dt d\tau$$

The velocity correlation tensor can be recognized (see Eq. III.11).

$$\begin{aligned} \langle \widetilde{\mathbf{u}}_i^*(\mathbf{X}, f) \widetilde{\mathbf{u}}_j(\mathbf{X}, f') \rangle &= \int_{-\infty}^{+\infty} \int_{-\infty}^{+\infty} R_{ij}(\mathbf{X}, \tau) e^{i2\pi(f - f')t} e^{-i2\pi f' \tau} dt d\tau \\ \Leftrightarrow \langle \widetilde{\mathbf{u}}_i^*(\mathbf{X}, f) \widetilde{\mathbf{u}}_j(\mathbf{X}, f') \rangle &= \int_{-\infty}^{+\infty} R_{ij}(\mathbf{X}, \tau) \int_{-\infty}^{+\infty} e^{i2\pi(f - f')t} dt e^{-i2\pi f' \tau} d\tau \end{aligned}$$

The mathematical identity, $\delta(f - f') = \int_{-\infty}^{+\infty} e^{i2\pi(f - f')t} dt$ is used.

$$\langle \widetilde{\mathbf{u}}_i^*(\mathbf{X}, f) \widetilde{\mathbf{u}}_j(\mathbf{X}, f') \rangle = \int_{-\infty}^{+\infty} R_{ij}(\mathbf{X}, \tau) \delta(f - f') e^{-i2\pi f' \tau} d\tau$$

Let us consider that $f = f'$.

$$\begin{aligned} \langle \widetilde{\mathbf{u}}_i^*(\mathbf{X}, f) \widetilde{\mathbf{u}}_j(\mathbf{X}, f) \rangle &= \delta(0) \int_{-\infty}^{+\infty} R_{ij}(\mathbf{X}, \tau) e^{-i2\pi f' \tau} d\tau \\ \Leftrightarrow \langle \widetilde{\mathbf{u}}_i^*(\mathbf{X}, f) \widetilde{\mathbf{u}}_j(\mathbf{X}, f) \rangle &= \delta(0) \int_{-\infty}^{+\infty} \langle \mathbf{u}'_i(\mathbf{X}, t) \mathbf{u}'_i(\mathbf{X}, t + \tau) \rangle e^{-i2\pi f' \tau} d\tau \end{aligned}$$

The change of variable $\tau = \frac{l_\xi}{U}$ is performed under the frozen turbulence assumption (see Eq. (III.9)).

$$\langle \widetilde{\mathbf{u}}_i^*(\mathbf{X}, f) \widetilde{\mathbf{u}}_j'(\mathbf{X}, f) \rangle = \delta(0) \int_{-\infty}^{+\infty} \langle \mathbf{u}'_i(\mathbf{X}, t) \mathbf{u}'_i(\mathbf{X} + \mathbf{l}_\xi, t) \rangle e^{-i2\pi f' \frac{l_\xi}{U}} d\frac{l_\xi}{U}$$

Once again, the velocity correlation tensor can be recognized (see Eq. III.11).

$$\langle \widetilde{\mathbf{u}}_i^*(\mathbf{X}, f) \widetilde{\mathbf{u}}_j'(\mathbf{X}, f) \rangle = \delta(0) \frac{1}{U} \int_{-\infty}^{+\infty} R_{ij}(\mathbf{l}_\xi, t) e^{-ik_\xi l_\xi} dl_\xi$$

The inverse Fourier transform of R_{ij} is taken (see Eq. (III.13)).

$$\langle \widetilde{\mathbf{u}}_i^*(\mathbf{X}, f) \widetilde{\mathbf{u}}_j'(\mathbf{X}, f) \rangle = \delta(0) \frac{1}{U} \int_{-\infty}^{+\infty} \int_{-\infty}^{+\infty} \int_{-\infty}^{+\infty} \int_{-\infty}^{+\infty} \phi_{ij}(\mathbf{k}) e^{ik_\xi l_\xi} dk_z dk_\eta dk_\xi e^{-ik_\xi l_\xi} dl_\xi$$

The 1D spectrum notation from Section III.1.3 is used.

$$\langle \widetilde{\mathbf{u}}_i^*(\mathbf{X}, f) \widetilde{\mathbf{u}}_j'(\mathbf{X}, f) \rangle = \delta(0) \frac{1}{U} \int_{-\infty}^{+\infty} \int_{-\infty}^{+\infty} \phi_{ij}^{1D}(k_\xi) e^{ik_\xi l_\xi} dk_\xi e^{-ik_\xi l_\xi} dl_\xi$$

The frozen assumption (see Eq. (III.20)), provides: $k_\xi = \frac{2\pi f}{U}$.

$$\langle \widetilde{\mathbf{u}}_i^*(\mathbf{X}, f) \widetilde{\mathbf{u}}_j'(\mathbf{X}, f) \rangle = \delta(0) \frac{2\pi}{U} \phi_{ij}^{1D} \left(k_\xi = \frac{2\pi f}{U} \right)$$

Finally, the relation between the velocity Fourier transform and the correlation spectrum is obtained.

$$\langle \widetilde{\mathbf{u}}_i^*(\mathbf{X}, f) \widetilde{\mathbf{u}}_j'(\mathbf{X}, f) \rangle = \delta(0) \frac{2\pi}{U} \phi_{ij}^{1D} \left(k_\xi = \frac{2\pi f}{U} \right) \quad (\text{VI.1})$$

B An algorithm to determine the direction of the velocity for 3D turbulence structures

Let us consider the wavenumber $\mathbf{k} = (k_{\xi,l}, k_{\eta,lm}, k_{z,n})^T$ in the coordinate system (ξ, η, z) . The goal is to build an orthonormal basis $(\mathbf{k}_a, \mathbf{k}_b, \mathbf{k}_c)$ from \mathbf{k} in order to determine σ_{lmn} such as $\mathbf{k} \cdot \sigma_{lmn} = 0$. The main steps of the procedures are mentioned below with α_{lmn} a random phase term sorted for each mode (l, m, n) .

1. $\mathbf{k}_c = \frac{\mathbf{k}}{\|\mathbf{k}\|}$

2. Supposing that $k_{\xi} > 0$

$$\left\{ \begin{array}{l} \mathbf{k}_a = \left(-\frac{k_{\eta}^2 + k_z^2}{k_{\xi}}, k_{\eta}, k_z \right)_{(\xi, \eta, z)}^T, \text{ if } |k_{\eta}| + |k_z| \neq 0 \\ \mathbf{k}_a = (0, k_{\eta}, 0)_{(\xi, \eta, z)}^T, \text{ if } |k_{\eta}| + |k_z| = 0 \end{array} \right.$$

3. $\mathbf{k}_a = \frac{\mathbf{k}_a}{\|\mathbf{k}_a\|}$ and $\mathbf{k}_b = \frac{\mathbf{k}_b}{\|\mathbf{k}_b\|}$

4. $\mathbf{k}_b = \mathbf{k}_c \wedge \mathbf{k}_a$

5. $\sigma_{lmn} = \cos(\alpha_{lmn})\mathbf{k}_a + \sin(\alpha_{lmn})\mathbf{k}_b$, with $\alpha_{lmn} \in [0, 2\pi]$

C Link between formulations based on the turbulence energy spectrum and the velocity autocorrelation spectra

For the sake of simplicity, let us assume that $\beta_c = 0$. In order to achieve the comparison between the formulations, an amplitude of a given mode $u'_i = 2\sqrt{E(k)\Delta k} \sigma_i = 2\sqrt{E(k)/(2\pi k^2)\Delta k_x\Delta k_y\Delta k_z} \sigma_i$ is considered. The directivity of the velocity is given by the vector $\boldsymbol{\sigma}$ which satisfies Eq. (VI.2), following Appendix. B.

$$\boldsymbol{\sigma} = \cos(\alpha) \frac{k}{k^2 \sqrt{k_y^2 + k_z^2}} \begin{pmatrix} -(k_y^2 + k_z^2) \\ k_x k_y \\ k_x k_z \end{pmatrix} + \sin(\alpha) \frac{1}{k^2 \sqrt{k_y^2 + k_z^2}} \begin{pmatrix} 0 \\ -k_z k^2 \\ k_y k^2 \end{pmatrix} \quad (\text{VI.2})$$

The next step is to consider the mean value (denoted by the subscript *mean*) of the squared norm of the vector $\boldsymbol{\sigma}$ from a statistical point of view, considering an infinite number of α randomly generated.

$$\begin{aligned} \sigma_x^2 &= \cos^2(\alpha) \frac{1}{k^2} (k_y^2 + k_z^2) & \Rightarrow \sigma_{x,mean}^2 &= \frac{1}{2} \frac{1}{k^2} (k_y^2 + k_z^2) = \frac{1}{2} \left(1 - \frac{k_x^2}{k^2}\right) \\ \sigma_y^2 &= \frac{1}{k^4 (k_y^2 + k_z^2)} \left(\cos(\alpha) k_x k_y k - \sin(\alpha) k_z k^2\right)^2 & \Rightarrow \sigma_{y,mean}^2 &= \frac{1}{2} \frac{1}{k^2} (k_x^2 + k_z^2) = \frac{1}{2} \left(1 - \frac{k_y^2}{k^2}\right) \\ \sigma_z^2 &= \frac{1}{k^4 (k_y^2 + k_z^2)} \left(\cos(\alpha) k_x k_z k + \sin(\alpha) k_y k^2\right)^2 & \Rightarrow \sigma_{z,mean}^2 &= \frac{1}{2} \frac{1}{k^2} (k_x^2 + k_y^2) = \frac{1}{2} \left(1 - \frac{k_z^2}{k^2}\right) \end{aligned}$$

The expression of averaged (mean) velocities, with respect to α , can now be expanded.

$$\begin{aligned} u'_{x,mean}{}^2 &= 4 \frac{E(k)}{4\pi k^2} \left(1 - \frac{k_x^2}{k^2}\right) \Delta k_x \Delta k_y \Delta k_z \\ u'_{y,mean}{}^2 &= 4 \frac{E(k)}{4\pi k^2} \left(1 - \frac{k_y^2}{k^2}\right) \Delta k_x \Delta k_y \Delta k_z \\ u'_{z,mean}{}^2 &= 4 \frac{E(k)}{4\pi k^2} \left(1 - \frac{k_z^2}{k^2}\right) \Delta k_x \Delta k_y \Delta k_z \end{aligned}$$

If one considers the squared amplitude of the average statistical velocities ($u'_{i,mean} = 2\sqrt{\varphi_{ii}\Delta k_x\Delta k_y\Delta k_z}$),

the formulations which would have been obtained using autocorrelation spectra $\varphi_{ii} = E(k)/(4\pi k^2)(1 - k_i^2/k^2)$ are recovered. To conclude, it has been demonstrated that if an infinite number of modes is generated, the two formulations (relying on the energy spectrum or the autocorrelation velocity spectra) tend towards the same limit.

D Determining conditions under which a divergence-free formulation can be achieved

The choice has been made to alter the u'_z component, with the aim of achieving a divergence free formulation.

$$\frac{\partial u'_z}{\partial z} = -f_w(z)A \sin(\mathbf{k} \cdot \mathbf{X} - \omega t + \psi) k_z \sigma_z + f'_w(z)A \cos(\mathbf{k} \cdot \mathbf{X} - \omega t + \psi) \sigma_z - g'_w(z)A \sigma_z \quad (\text{VI.3})$$

From Eqs. (III.51) and (VI.3), one can obtain that $g'_w(z) = f'_w(z) \cos(\mathbf{k} \cdot \mathbf{X} - \omega t + \psi)$. More precisely, $g_w(z)$ is a piecewise function likewise $f_w(z)$, defined as follows,

$$\left\{ \begin{array}{ll} \forall z \in [z_{min}, z_{min} + L_w], & g'_w(z) = \frac{\pi}{2L_w} \sin\left(\pi \frac{z - z_{min}}{L_w}\right) \cos(\mathbf{k} \cdot \mathbf{X} - \omega t + \psi) \\ \forall z \in [z_{min} + L_w, z_{max} - L_w], & g'_w(z) = 0 \\ \forall z \in [z_{max} - L_w, z_{max}], & g'_w(z) = \frac{\pi}{2L_w} \sin\left(\pi \frac{z - z_{max}}{L_w}\right) \cos(\mathbf{k} \cdot \mathbf{X} - \omega t + \psi) \end{array} \right. \quad (\text{VI.4})$$

The idea of the following paragraphs is to demonstrate the conditions under which the previous system of equations (Eq. (VI.4)) can be satisfied taking into account that both functions f_w and g_w are C^1 and cancel in z_{min} and z_{max} . Let us consider that $k_z \neq \pm\pi/L_w$ (the case $k_z = \pm\pi/L_w$ which is not detailed here and leads to the equality $\sin(k_x x + k_y y + \pi/L_w z_{min} - \omega t + \psi) = 0$, which cannot be ensured for every set of variables).

$$\left\{ \begin{array}{ll} \forall z \in [z_{min}, z_{min} + L_w], & g_w(z) = \frac{-\pi^2}{2\pi^2 - 2k^2 L_w^2} \cos(\mathbf{k} \cdot \mathbf{X} - \omega t + \psi) \cos\left(\pi \frac{z - z_{min}}{L_w}\right) \\ & - \frac{kT\pi}{2\pi^2 - 2k^2 L_w^2} \sin(\mathbf{k} \cdot \mathbf{X} - \omega t + \psi) \sin\left(\pi \frac{z - z_{min}}{L_w}\right) + C_a \\ \forall z \in [z_{min} + L_w, z_{max} - L_w], & g_w(z) = C_b \\ \forall z \in [z_{max} - L_w, z_{max}], & g_w(z) = \frac{-\pi^2}{2\pi^2 - 2k^2 L_w^2} \cos(\mathbf{k} \cdot \mathbf{X} - \omega t + \psi) \cos\left(\pi \frac{z - z_{max}}{L_w}\right) \\ & - \frac{kL_w\pi}{2\pi^2 - 2k^2 L_w^2} \sin(\mathbf{k} \cdot \mathbf{X} - \omega t + \psi) \sin\left(\pi \frac{z - z_{max}}{L_w}\right) + C_c \end{array} \right. \quad (\text{VI.5})$$

The integrated form of Eq. (VI.4) is given by Eq. (VI.5), where three constants C_a , C_b , and C_c need to be determined. The functions f_w and g_w have to be damped near the boundaries, for example at z_{min} , $g_w(z_{min}) = 0$. Thus, the constant C_a satisfies,

$$C_a = \frac{\pi^2}{2\pi^2 - 2k^2 L_w^2} \cos(k_x x + k_y y + k_z z_{min} - \omega t + \psi) \quad (\text{VI.6})$$

The continuity has to be ensured in $z = z_{min} + L_w$, leading to $C_b = g_w(z_{min} + L_w)$.

$$C_b = \frac{\pi^2}{2\pi^2 - 2k^2 L_w^2} \cos(k_x x + k_y y + k_z(z_{min} + L_w) - \omega t + \psi) + \frac{\pi^2}{2\pi^2 - 2k^2 L_w^2} \cos(k_x x + k_y y + k_z z_{min} - \omega t + \psi) \quad (\text{VI.7})$$

Thus, the constant C_b can be expressed by Eq. (VI.7).

$$C_c = \frac{\pi^2}{2\pi^2 - 2k^2 L_w^2} \cos(k_x x + k_y y + k_z z_{max} - \omega t + \psi) \quad (\text{VI.8})$$

Likewise at $z = z_{max}$, $g_w(z_{max}) = 0$ which leads to Eq. (VI.8).

$$C_b = \frac{\pi^2}{2\pi^2 - 2k^2 L_w^2} \cos(k_x x + k_y y + k_z(z_{max} - L_w) - \omega t + \psi) + \frac{\pi^2}{2\pi^2 - 2k^2 L_w^2} \cos(k_x x + k_y y + k_z z_{max} - \omega t + \psi) \quad (\text{VI.9})$$

Thereafter, $C_b = g_w(z_{max} - L_w)$ and C_b has also to satisfy Eq. (VI.9).

$$\begin{aligned} & \cos\left(k_x x + k_y y + k_z z_{min} + \frac{k_z L_w}{2} - \omega t + \psi\right) \cos\left(\frac{k_z L_w}{2}\right) \\ &= \cos\left(k_x x + k_y y + k_z z_{min} + k_z L_w - \frac{k_z L_w}{2} - \omega t + \psi\right) \cos\left(\frac{k_z L_w}{2}\right) \end{aligned} \quad (\text{VI.10})$$

The constraint that $C_b = g_w(z_{min} + L_w) = g_w(z_{max} - L_w)$ imposes that Eq. (VI.10) has to be verified.

E Flow chart representing the synthetic turbulence generation

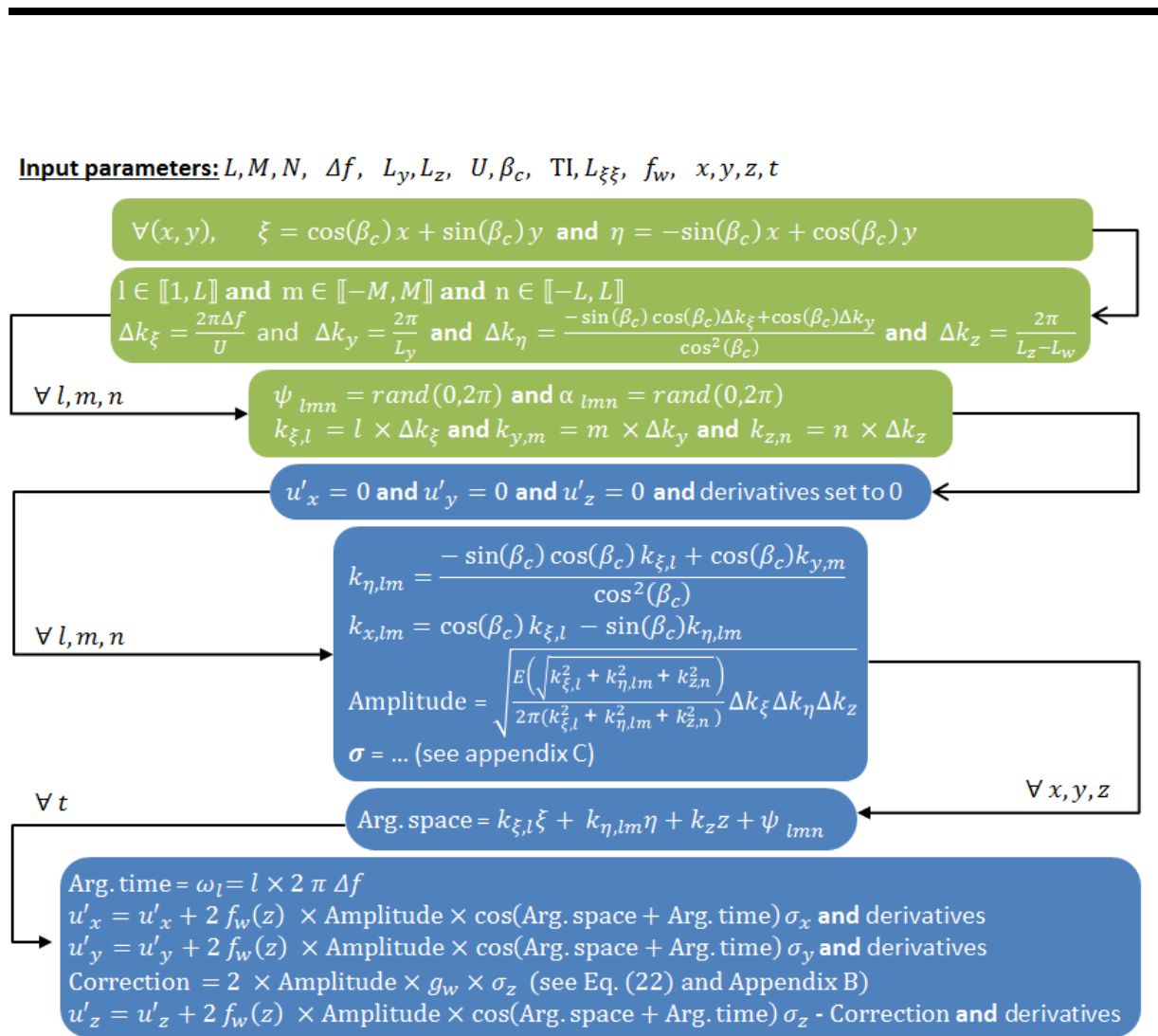


Figure VI.37: Flow chart representing the synthetic turbulence generation.

F Validation of the WH formulation on experimental data from LE parametric studies at ISVR

Accuracy and limitations of the WH model, presented in Section II.1.2.2, are investigated through available experimental results carried out at ISVR (Institute of Sound and Vibration Research) by C. Paruchuri [138]. In the following, $M = 0.18$, $L_l = 2L_t = 7.5$ mm, $TI = 2.5$ %, $c = 15$ cm, $L_z = 25$ cm. Moreover, the turbulence comes from a planar Liepmann turbulence spectrum and it is supposed to be frozen, isotropic and homogeneous, see Part III. First, the acoustic response depending on the serration's amplitude is investigated, whereas the serration's wavelength λ_s equals 15 mm.

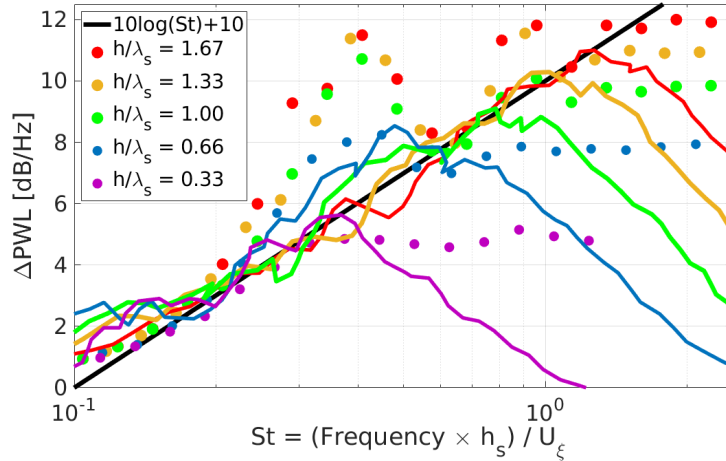


Figure VI.38: Noise reduction for various serration amplitudes

In Fig. VI.38, the analytical solutions (dots) reproduce adequately the noise reduction due to the variation of the serration's amplitude (experiments in colored lines). However, for high h/λ_s ratios, the theoretical solution exhibits oscillations, which may be due to the fact that the "energy" term E_n , please refer to [28], becomes small. An analogy can be drawn with [29], where the WH-technique is applied to TE noise predictions. If these oscillations are not considered, the experimental data is satisfactorily predicted. It has to be noted that the green curve is close to the ONERA design from Part IV for which $\lambda_s = 2L_l = 4L_t$ and $h_s = \lambda_s$. Moreover, C. Paruchuri provides in his study [138] an evolution law for the peak reduction, that relates the

PWL reduction (in dB) of a given serrated geometry to a specific Strouhal number $St = \frac{fh_s}{U_\xi}$:

$$\Delta PWL = 10 \log(St) + 10, \text{ in dB}$$

The empirical log-law is plotted in Fig. VI.38, showing a very good agreement with solution up to the peak reduction. Beyond the peak, the WH solution exhibits a "plateau" whereas the experiment shows a decrease of the PWL reduction due to the contribution of TE noise not accounted for in the WH model.

Secondly, the variation of the radiated noise is analyzed depending on the serration's wavelength, whereas the serration's amplitude h_s equals 25 mm. The same oscillations appear in Fig. VI.39 for very sharp edges. If these oscillations are discarded, the evolution of the maximal noise reduction with respect to the serration amplitude is properly estimated, except for extreme values: $h_s/\lambda_s \approx 5$.

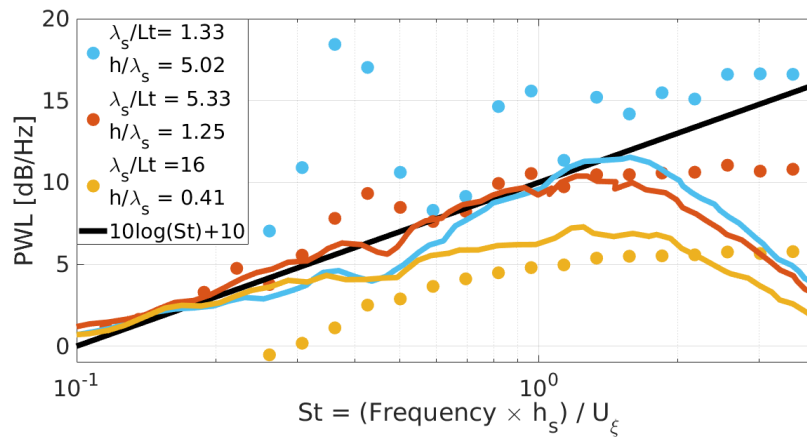


Figure VI.39: Noise reduction for various serration wavelengths.

Here again, the experimental decrease of the reduction at high frequencies is not predicted, which may be due to the missing trailing edge contribution in the analytical model. The red curve is close to the ONERA design from Part IV for which $\lambda_s = 2L_t = 4L_t$ and $h_s = \lambda_s$.

G Application to a low-noise OGV in the framework of TurboNoiseBB

In the framework of the European project TurboNoiseBB, ONERA has designed serrated OGV's assessed by RANS, CAA and analytical calculations [144]. For detailed explanations about the design methodology, please refer to [144]. The WH model is applied to both the baseline and low-noise OGVs. The OGVs are assumed to radiate noise to the far-field as isolated flat plates, i.e., airfoil thickness, duct propagation and cascade effects are neglected here.



Figure VI.40: 2D low-noise OGV 2D designs: "GanzUniform" (left), "GanzUniformOpt" (middle) and "GanzRadialOpt" (right).

Firstly, uniform inflow conditions are imposed by setting radially averaged turbulence statistics (case of Fig. VI.40, left). This is convenient for the WH formulation that assumes a periodic LE along the span, such as the "GanzUniform" OGV design in Fig. VI.40. This OGV design takes into account two significant geometrical modifications discussed in [144]: (1) limitation of serration amplitude and (2) local suppression of LE serrations near the hub. Radially averaged turbulence statistics are used in the WH analytical model for the baseline case ($h_s = 0$).

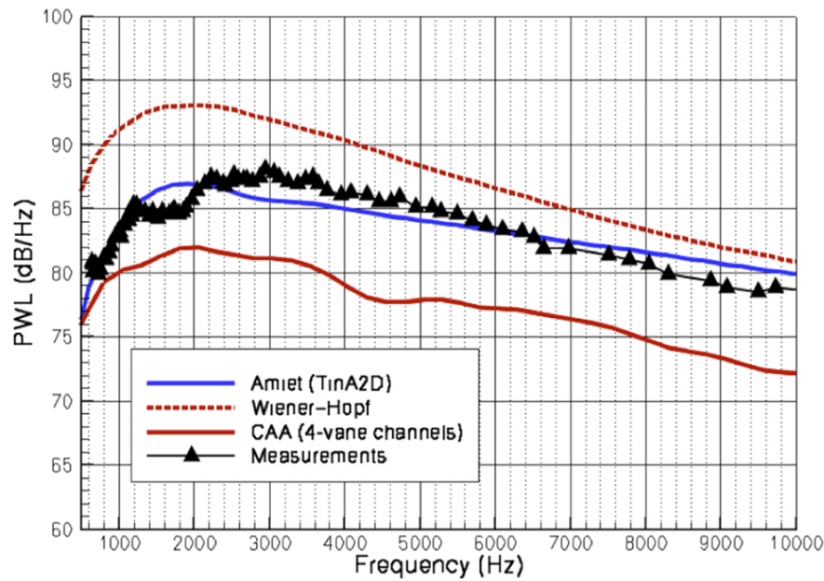


Figure VI.41: PWL spectra at APP OP for the baseline OGV using different methods (CAA, WH, Amiet-based) and compared to measurements.

The baseline case is compared to numerical, experimental, and analytical predictions using Amiet's model at approach OP in Fig. VI.41. The PWL from the WH analytical model has been computed from the contribution of 44 single-vanes ($+10 \log(44)$ dB), which corresponds to the vane count of the OGV stage in the experimental set-up. This implies that LE noise radiates to the free-field in contrast with the PWL spectrum from the extended Amiet's model in the TinA2D code, which accounts for duct propagation from an annular cascade [153]. Although the PWL spectrum is over-predicted by the WH method at low and mid-range frequencies, the spectral shape is well-predicted, and the levels tend to converge to the Amiet-based solution at high frequency. This is mainly due to the free-field radiation assumption in the WH formulation, which is known to be a high frequency approximation. Overall, this result is considered to be sufficiently accurate to assess the aeroacoustic response of isolated airfoils with LE serrations. Then, the "GanzUniform Opt" OGV design is used to assess the acoustic performances at three different fan speeds that correspond to the acoustic certification OPs, using radially averaged profiles of TI and TLS from RANS simulations provided by DLR (see figure 5 in [144]) and mean flow values from table I in [144].

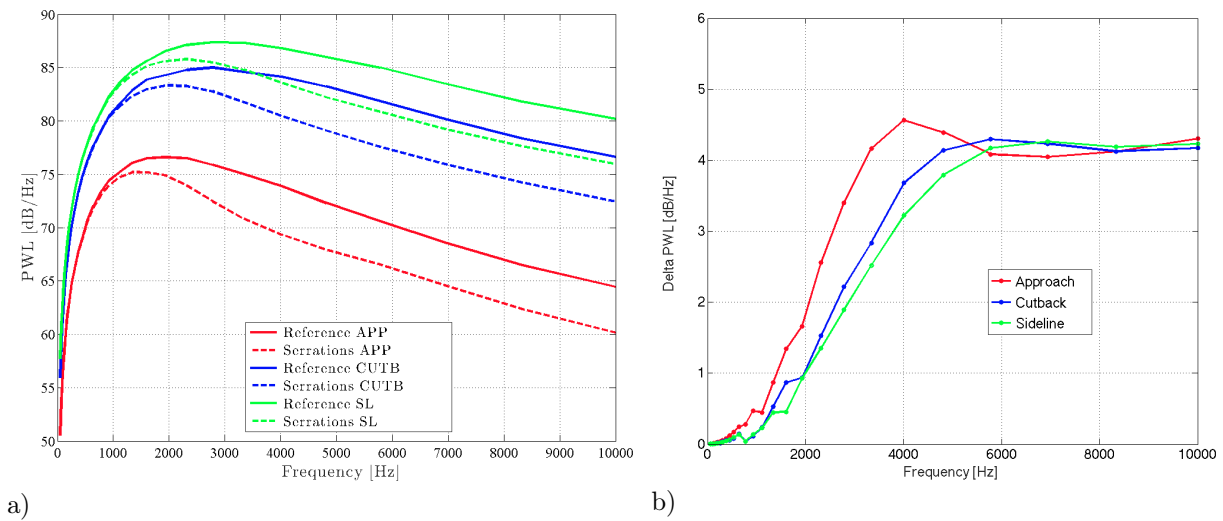


Figure VI.42: PWL (a) and Δ PWL (b) spectra from WH calculations (1 vane) on reference and low-noise OGV designs at the 3 OPs.

The WH calculations are performed for a single vane, and the resulting PWL and Δ PWL spectra are shown in Fig. VI.42a and Fig. VI.42b, respectively. Significant PWL reductions can be observed at all OPs, although the design was optimized for the APP OP. This is consistent with the results shown in the Δ PWL, where the maximum noise reduction is obtained at APP OP. It can be also observed that the frequency associated to the maximum PWL reduction increases with the mean flow speed (from APP to SDL). This trend is in good agreement with the basic design rules and initial results discussed in [144], in which the maximum PWL reductions varies between 4 and 6 dB.

Finally, it is proposed here to split the actual "GanzRadialOpt" OGV in spanwise strips to account for the spanwise varying LE (see Fig. VI.40 on the right). To this end, 9 strips are defined along the span, where the last strip corresponds to the straight LE region near the hub, and the inflow characteristics are radially averaged over each strip. The periodicity condition in the WH model is still valid for each strip, as the serration pattern is roughly preserved in the spanwise direction. Using these assumptions, the WH-based predictions (for a single vane) are presented in Fig. VI.43. It can be seen that the PWL spectrum provided by the free-field Amiet's solution [18] for the baseline case (using the strip technique for the characteristics of the incoming flow) has been included in Fig. VI.43 (on the left). A good agreement can be observed between WH and Amiet solutions, which is consistent with the findings for the FLOCON test-case results in Section IV.1.2. The shape of WH-based PWL spectra for the baseline and serrated LE vanes are quite similar to those shown in Fig. VI.42a (APP OP), but the strip technique leads to higher levels in the PWL spectrum. The analytical Δ PWL spectrum is plotted in Fig. VI.43 (on the right) and compared to the most accurate CAA prediction (figure 22 in [144]). The WH prediction obtained from the strip technique is rather close to the one shown in Fig. VI.42b (with "GanzUniformOpt" design and radially averaged profiles), but a slightly higher PWL reduction reaching 5 dB at approximately 3.5 kHz can be observed. Although the WH analytical model predicts larger noise reductions than CAA simulations, the trends are relatively similar up to 7

kHz. The acoustic benefit predicted by the analytical model might be slightly over-estimated due to the flat plate and uniform mean flow assumptions [135, 55]. Then, it seems reasonable to conclude that the expected PWL reduction from the most promising low-noise OGV is within these two limits. The WH method provides an OAPWL reduction of 3.5 dB (2.3 dB from CAA) and a PWL reduction of at least 4 dB (2 dB from CAA) can be achieved in the considered frequency range.

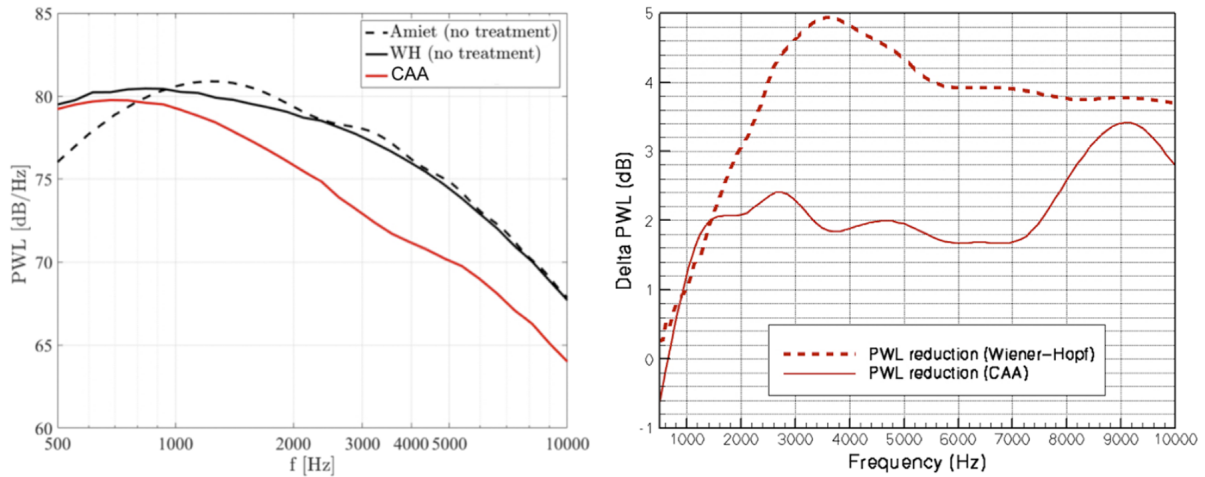


Figure VI.43: PWL predictions (single vane calculation) from WH model for baseline and "GanzRadialOpt" OGVs and free-field Amiet model for the baseline case (left), and Δ PWL prediction from the WH model compared to the CAA results (right).

H Manufacturing

COMOTI has performed several tests in order to ensure the printing quality and durability. They consisted in roughness measurement, which is defined by two quantities: the arithmetical mean deviation of the measured profile and average value maximum height of profile. Measurements were performed at several locations, shown in Fig. VI.44. Obtained roughness values were smaller than $0.5 \mu\text{m}$



Figure VI.44: Locations of the roughness measurements (black dots).

Moreover, 3D optical measurements were achieved, using GOM Atos system OGV, with samples placed on a rotary table depicted in Fig. VI.45. Pictures were taken for a 3D body reconstruction. Resulting 3D scans showed a general tolerance of $\pm 0,25 \text{ mm}$. The deviation to the reference CAD geometry is illustrated in Fig. VI.46.

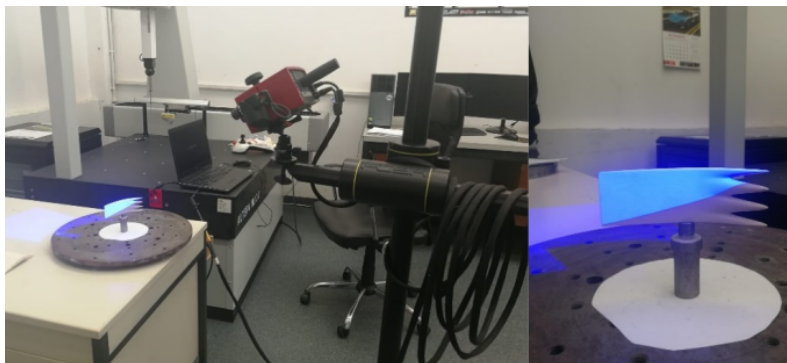


Figure VI.45: 3D optical measurements using GOM Atos system.

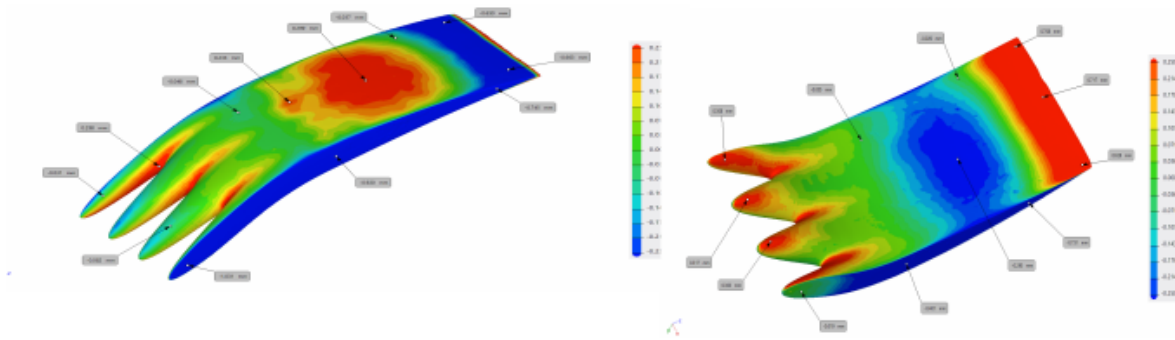


Figure VI.46: 3D body reconstruction from optical measurement. Colormap showing the deviation to the reference CAD model. 3D Scan isometric view of the upper side (left) and 3D Scan isometric view of the lower side (right).

Finally, the post-manufacturing testing at COMOTI, has been complemented by a static bending test (not detailed here).

The author would like to thank COMOTI for the manufacturing of ONERA's serrated designs and also for sharing the data and pictures taken during this process.

This page intentionally left blank.

Bibliography

- [1] *On the Fast Prediction of Open Rotor Tonal Interaction Noise*, volume 2B: Turbomachinery of *Turbo Expo: Power for Land, Sea, and Air*, 06 2015. doi: 10.1115/GT2015-42579. URL <https://doi.org/10.1115/GT2015-42579>. V02BT41A006.
- [2] *Assessment of Profile Transformation for Turbomachinery Large Eddy Simulations - From Academic to Industrial Applications*, volume 2C: Turbomachinery — Design Methods and CFD Modeling for Turbomachinery; Ducts, Noise, and Component Interactions of *Turbo Expo: Power for Land, Sea, and Air*, 06 2021. doi: 10.1115/GT2021-59293. URL <https://doi.org/10.1115/GT2021-59293>. V02CT34A020.
- [3] 2022. URL https://www.cfmaeroengines.com/wp-content/uploads/2021/07/CFM_RISE_Whitepaper_Media.pdf.
- [4] 2022. URL <https://cordis.europa.eu/project/id/604999>.
- [5] 2022. URL https://commons.wikimedia.org/wiki/File:Gas_turbine_efficiency.png.
- [6] 2022. URL <https://cordis.europa.eu/project/id/213411/reporting>.
- [7] 2022. URL <https://www.innostat-cs2.eu/>.
- [8] 2022. URL <https://ntrs.nasa.gov/api/citations/20050214860/downloads/20050214860.pdf>.
- [9] 2022. URL <https://www.icao.int/Meetings/Green/Documents/day%20pdf/session%20/2-Dickson.pdf>.
- [10] 2022. URL http://lmfa.ec-lyon.fr/IMG/pdf/projet_phare-2_2014-02-27_com.pdf?1093/ae778dca2cd8aa640f92b80e3f316d520835bb76.
- [11] Numerical simulation of aerodynamic noise with dlr’s aeroacoustic code piano, 2022. URL https://elib.dlr.de/118928/1/Piano_handbook_5.2_open.pdf. PIANO manual for version 5.2 – January 11, 2008.
- [12] 2022. URL <http://www.prolb-cfd.com/>.
- [13] 2022. URL <https://ec.europa.eu/inea/en/horizon-2020/projects/h2020-transport/aviation/turbonoisebb>.
- [14] F. G. Aguilera. *Aerodynamic and aeroacoustic modelling of engine fan broadband noise*. PhD thesis, University of Southampton, March 2017. URL <https://eprints.soton.ac.uk/412640/>.
- [15] F. G. Aguilera, J. R. Gill, D. Angland, and X. Zhang. *Wavy Leading Edge Airfoils Interacting with Anisotropic Turbulence*. 2017. doi: 10.2514/6.2017-3370. URL <https://arc.aiaa.org/doi/abs/10.2514/6.2017-3370>.
- [16] J. Al-Am, V. Clair, A. Giaouque, J. Boudet, and F. Gea-Aguilera. Direct noise predictions of fan broadband noise using LES and analytical models. In *28th AIAA/CEAS Aeroacoustics 2022 Conference*, number AIAA 2022-2882, Southampton, United Kingdom, June 2022. American Institute of Aeronautics and Astronautics. doi: 10.2514/6.2022-2882. URL <https://hal.archives-ouvertes.fr/hal-03697923>.
- [17] Y. Al-Okbi, T. P. Chong, and O. Stalnov. Leading edge blowing to mimic and enhance the serration effects for aerofoil. *Applied Sciences*, 11(6), 2021. ISSN 2076-3417. URL <https://www.mdpi.com/2076-3417/11/6/2593>.
- [18] R. Amiet. Acoustic radiation from an airfoil in a turbulent stream. *Journal of Sound and Vibration*, 41(4):407–420, 1975. ISSN 0022-460X. doi: [https://doi.org/10.1016/S0022-460X\(75\)80105-2](https://doi.org/10.1016/S0022-460X(75)80105-2). URL <https://www.sciencedirect.com/science/article/pii/S0022460X75801052>.

-
- [19] R. K. Amiet. High frequency thin-airfoil theory for subsonic flow. *AIAA Journal*, 14(8):1076–1082, Aug. 1976. doi: 10.2514/3.7187.
- [20] C. P. Arroyo, T. Leonard, M. Sanjosé, S. Moreau, and F. Duchaine. Large Eddy Simulation of a Scale-model Turbofan for Fan Noise Source Diagnostic. In *17th International Symposium on Transport Phenomena and Dynamics of Rotating Machinery (ISROMAC2017)*, Maui, United States, Dec. 2017. URL <https://hal.archives-ouvertes.fr/hal-02419816>.
- [21] T. Astoul. *Towards improved lattice Boltzmann aeroacoustic simulations with non-uniform grids: application to landing gears noise prediction*. PhD thesis, Aix-Marseille Université, 2021.
- [22] T. Astoul, G. Wissocq, J.-F. Boussuge, A. Sengissen, and P. Sagaut. Analysis and reduction of spurious noise generated at grid refinement interfaces with the lattice Boltzmann method. *Journal of Computational Physics*, 418:109645, 2020. ISSN 0021-9991. doi: <https://doi.org/10.1016/j.jcp.2020.109645>. URL <https://www.sciencedirect.com/science/article/pii/S0021999120304198>.
- [23] T. Astoul, G. Wissocq, J.-F. Boussuge, A. Sengissen, and P. Sagaut. Lattice Boltzmann method for computational aeroacoustics on non-uniform meshes: A direct grid coupling approach. *Journal of Computational Physics*, 447:110667, Dec. 2021. doi: 10.1016/j.jcp.2021.110667. URL <https://doi.org/10.1016/j.jcp.2021.110667>.
- [24] H. Atassi and M. Logue. *Effect of Turbulence Structure on Broadband Fan Noise*. 2008. doi: 10.2514/6.2008-2842. URL <https://arc.aiaa.org/doi/abs/10.2514/6.2008-2842>.
- [25] H. Atassi and M. Logue. Modeling tonal and broadband interaction noise. *Procedia Engineering*, 6:214–223, 2010. ISSN 1877-7058. doi: <https://doi.org/10.1016/j.proeng.2010.09.023>. URL <https://www.sciencedirect.com/science/article/pii/S1877705810005692>. IUTAM Symposium on Computational Aero-Acoustics for Aircraft Noise Prediction.
- [26] H. Atassi and I. Vinogradov. *Modelling Broadband Fan Noise and Comparison with Experiments*. 2007. doi: 10.2514/6.2007-3691. URL <https://arc.aiaa.org/doi/abs/10.2514/6.2007-3691>.
- [27] H. M. Atassi, A. A. Ali, O. V. Atassi, and I. V. Vinogradov. Scattering of incident disturbances by an annular cascade in a swirling flow. *Journal of Fluid Mechanics*, 499:111–138, 2004. doi: 10.1017/S0022112003007031.
- [28] L. Ayton and C. Paruchuri. An analytical and experimental investigation of aerofoil–turbulence interaction noise for plates with spanwise-varying leading edges. *Journal of Fluid Mechanics*, 865:137–168, 2019. doi: 10.1017/jfm.2019.78.
- [29] L. J. Ayton. Analytic solution for aerodynamic noise generated by plates with spanwise-varying trailing edges. *Journal of Fluid Mechanics*, 849:448–466, 2018. doi: 10.1017/jfm.2018.431.
- [30] L. J. Ayton and J. W. Kim. An analytic solution for the noise generated by gust–aerofoil interaction for plates with serrated leading edges. *Journal of Fluid Mechanics*, 853:515–536, 2018. doi: 10.1017/jfm.2018.583.
- [31] P. J. Baddoo and L. J. Ayton. An analytic solution for gust–cascade interaction noise including effects of realistic aerofoil geometry. *Journal of Fluid Mechanics*, 886:A1, 2020. doi: 10.1017/jfm.2019.1016.
- [32] C. Bailly and D. Juvé. *A stochastic approach to compute subsonic noise using linearized Euler’s equations*. 1999. doi: 10.2514/6.1999-1872. URL <https://arc.aiaa.org/doi/abs/10.2514/6.1999-1872>.
- [33] C. Bailly, P. Lafon, and S. Candel. Computation of noise generation and propagation for free and confined turbulent flows. In *Aeroacoustics Conference*, State College, France, 1996. American Institute of Aeronautics and Astronautics. doi: 10.2514/6.1996-1732. URL <https://hal.archives-ouvertes.fr/hal-02431563>.
- [34] G. Bampanis. *Airfoil turbulence-impingement noise reduction by porous cells or wavy leading-edge design*. Theses, Université de Lyon, Jan. 2021. URL <https://tel.archives-ouvertes.fr/tel-03578386>.
- [35] G. Bampanis and M. Roger. *On the Turbulence-Impingement Noise of a NACA-12 Airfoil with Porous Inclusions*. 2020. doi: 10.2514/6.2020-2577. URL <https://arc.aiaa.org/doi/abs/10.2514/6.2020-2577>.
- [36] G. Bampanis, M. Roger, D. Ragni, F. Avallone, and C. Teruna. Airfoil-turbulence interaction noise source identification and its reduction by means of leading edge serrations. In *25th AIAA/CEAS Aeroacoustics Conference*, 2019. doi: 10.2514/6.2019-2741. URL <https://arc.aiaa.org/doi/abs/10.2514/6.2019-2741>.
-

-
- [37] G. Bampanis, M. Roger, and S. Moreau. On a three-dimensional investigation of airfoil turbulence-impingement noise and its reduction by leading-edge tubercles. *Journal of Sound and Vibration*, 520:116635, Mar. 2022. doi: 10.1016/j.jsv.2021.116635. URL <https://hal.archives-ouvertes.fr/hal-03775045>.
- [38] W. Bechara, C. Bailly, P. Lafon, and S. Candel. Stochastic approach to noise modeling for free turbulent flows. *AIAA Journal*, 32(3):455–463, Mar. 1994. doi: 10.2514/3.12008. URL <https://hal.archives-ouvertes.fr/hal-02388323>.
- [39] T. M. Biedermann, T. P. Chong, F. Kameier, and C. O. Paschereit. Statistical–empirical modeling of airfoil noise subjected to leading-edge serrations. *AIAA Journal*, 55(9):3128–3142, 2017. doi: 10.2514/1.J055633. URL <https://doi.org/10.2514/1.J055633>.
- [40] T. M. Biedermann, P. Czeckay, T. F. Geyer, F. Kameier, and C. O. Paschereit. Effect of inflow conditions on the noise reduction through leading edge serrations. *AIAA Journal*, 57(9):4104–4109, 2019. doi: 10.2514/1.J057831. URL <https://doi.org/10.2514/1.J057831>.
- [41] V. P. Blandeau, P. F. Joseph, G. Jenkins, and C. J. Powles. Comparison of sound power radiation from isolated airfoils and cascades in a turbulent flow. *The Journal of the Acoustical Society of America*, 129(6):3521–3530, 2011. doi: 10.1121/1.3569706.
- [42] J. Blazek. *Computational Fluid Dynamics 3rd Edition. Principles and Applications*. Butterworth-Heinemann, Germany, 2015.
- [43] C. Bogey and C. Bailly. Three-dimensional non-reflective boundary conditions for acoustic simulations: far field formulation and validation test cases. *Acta Acustica united with Acustica*, 88:463 – 471, 2002. URL <https://hal.archives-ouvertes.fr/hal-02342291>.
- [44] V. Bonneau. *Prévision du bruit d’interaction tonal et à large bande d’une soufflante de nouvelle génération en régime subsonique*. PhD thesis, Ecole Nationale Supérieure des Ingénieurs de Poitiers, 2015.
- [45] S. Bouley, B. François, M. Roger, H. Posson, and S. Moreau. On a two-dimensional mode-matching technique for sound generation and transmission in axial-flow outlet guide vanes. *Journal of Sound and Vibration*, 403:190–213, 2017. ISSN 0022-460X. doi: <https://doi.org/10.1016/j.jsv.2017.04.031>. URL <https://www.sciencedirect.com/science/article/pii/S0022460X17303590>.
- [46] L. Bowen, A. Celik, M. Azarpeyvand, and C. R. da Silva. *Porous geometry effects on the generation of turbulence interaction noise*. 2021. doi: 10.2514/6.2021-2193. URL <https://arc.aiaa.org/doi/abs/10.2514/6.2021-2193>.
- [47] A. Cader, C. Polacsek, T. L. Garrec, R. Barrier, F. Benjamin, and M. Jacob. Numerical prediction of rotor-stator interaction noise using 3d caa with synthetic turbulence injection. In *Proc. of the AIAA/CEAS Aeroacoustics Conference*, Atlanta, United States, 2018.
- [48] L. Cambier, S. Heib, and S. Plot. The Onera elsA CFD software: input from research and feedback from industry. *Mechanics & Industry*, 14(3):159–174, 2013. doi: 10.1051/meca/2013056. URL <https://hal.archives-ouvertes.fr/hal-01293795>.
- [49] M. Cannard. *Slitted leading-edge profiles for the reduction of broadband interaction noise*. PhD thesis, University of Southampton, March 2020. URL <https://eprints.soton.ac.uk/447834/>.
- [50] M. Cannard, P. Joseph, J. Turner, J. Kim, and C. Paruchuri. Physical mechanisms and performance of slitted leading-edge profiles for the reduction of broadband aerofoil interaction noise. *Journal of Sound and Vibration*, 473:1–17, May 2020. URL <https://eprints.soton.ac.uk/438617/>.
- [51] A. Careta, F. Sagués, and J. Sancho. Stochastic generation of homogeneous isotropic turbulence with well-defined-spectra. *Physical review. E, Statistical physics, plasmas, fluids, and related interdisciplinary topics*, 48:2279–2287, 10 1993. doi: 10.1103/PhysRevE.48.2279.
- [52] D. Casalino, A. Hazir, and A. Mann. Turbofan broadband noise prediction using the lattice boltzmann method. *AIAA Journal*, 56(2):609–628, 2018. doi: 10.2514/1.J055674.
- [53] D. Casalino, F. Avallone, I. Gonzalez-Martino, and D. Ragni. Aeroacoustic study of a wavy stator leading edge in a realistic fan/ogv stage. *Journal of Sound and Vibration*, 442:138–154, 2019. ISSN 0022-460X. doi: <https://doi.org/10.1016/j.jsv.2018.10.057>. URL <https://www.sciencedirect.com/science/article/pii/S0022460X18307375>.
- [54] D. Cerizza, D. Casalino, and I. Gonzalez-Martino. *An Extension of the Acoustics Evaluation of the NASA SDT turbofan with Lattice-Boltzmann methods*. 2022. doi: 10.2514/6.2022-2886. URL <https://arc.aiaa.org/doi/abs/10.2514/6.2022-2886>.
-

-
- [55] P. Chaitanya, P. Joseph, S. Narayanan, C. Vanderwel, J. Turner, J. W. Kim, and B. Ganapathisubramani. Performance and mechanism of sinusoidal leading edge serrations for the reduction of turbulence-aerofoil interaction noise. *Journal of Fluid Mechanics*, 818:435–464, 2017. doi: 10.1017/jfm.2017.141.
- [56] P. Chaitanya, P. Joseph, and L. J. Ayton. Leading-edge profiles for the reduction of airfoil interaction noise. *AIAA Journal*, 58(3):1118–1129, 2020. doi: 10.2514/1.J058456. URL <https://doi.org/10.2514/1.J058456>.
- [57] W. Chen, W. Qiao, F. Tong, L. Wang, and X. Wang. Numerical investigation of wavy leading edges on rod-airfoil interaction noise. *AIAA Journal*, 56(7):2553–2567, 2018. doi: 10.2514/1.J055825. URL <https://doi.org/10.2514/1.J055825>.
- [58] C. Cheong, P. Joseph, and S. Lee. High frequency formulation for the acoustic power spectrum due to cascade-turbulence interaction. *The Journal of the Acoustical Society of America*, 119(1):108–122, 2006. doi: 10.1121/1.2139626. URL <https://doi.org/10.1121/1.2139626>.
- [59] Christophe Diette. Numerical benchmarking of lbm simulations applied to turbulence-cascade configurations, 2022. 33 Congress of the International Council of the Aeronautical Sciences ICAS 2022 – Stockholm, Sweden.
- [60] Christophe Diette. Open fan engine architecture for next generation smr, 2022. 33 Congress of the International Council of the Aeronautical Sciences ICAS 2022 – Stockholm, Sweden.
- [61] V. Clair. *Calcul numérique de la réponse acoustique d'un aubage soumis à un sillage turbulent*. Theses, Université Claude Bernard - Lyon I, Nov. 2013. URL <https://tel.archives-ouvertes.fr/tel-01009856>.
- [62] V. Clair, C. Polacsek, G. Reboul, and T. Le Garrec. Numerical simulation of turbulence interaction noise applied to a serrated airfoil. In S. F. d'Acoustique, editor, *Acoustics 2012*, Nantes, France, Apr. 2012. URL <https://hal.archives-ouvertes.fr/hal-00810644>.
- [63] V. Clair, C. Polacsek, T. L. Garrec, G. Reboul, M. Gruber, and P. Joseph. Experimental and numerical investigation of turbulence-airfoil noise reduction using wavy edges. *AIAA Journal*, 51:2695–2713, 11 2013. doi: 10.2514/1.J052394.
- [64] I. Cozza, A. Iob, and R. Arina. Broadband trailing-edge noise prediction with a stochastic source model. *Computers & Fluids*, 57:98–109, 2012. ISSN 0045-7930. doi: <https://doi.org/10.1016/j.compfluid.2011.12.011>. URL <https://www.sciencedirect.com/science/article/pii/S0045793011003835>.
- [65] N. Curle and M. J. Lighthill. The influence of solid boundaries upon aerodynamic sound. *Proceedings of the Royal Society of London. Series A. Mathematical and Physical Sciences*, 231(1187):505–514, 1955. doi: 10.1098/rspa.1955.0191. URL <https://royalsocietypublishing.org/doi/abs/10.1098/rspa.1955.0191>.
- [66] M. Daroukh. *Effects of distortion on modern turbofan tonal noise*. PhD thesis, Institut National Polytechnique de Toulouse, 2017.
- [67] M. Daroukh, T. Le Garrec, and C. Polacsek. Low-speed turbofan aerodynamic and acoustic prediction with an isothermal lattice boltzmann method. *AIAA Journal*, 60(2):1152–1170, 2022. doi: 10.2514/1.J060752. URL <https://doi.org/10.2514/1.J060752>.
- [68] S. Deck. Recent improvements in the Zonal Detached Eddy Simulation (ZDES) formulation. *Theoretical and Computational Fluid Dynamics*, 26(6):523–550, Dec. 2012. doi: 10.1007/s00162-011-0240-z.
- [69] M. Dieste and G. Gabard. Random particle methods applied to broadband fan interaction noise. *Journal of Computational Physics*, 231(24):8133–8151, 2012. ISSN 0021-9991. doi: <https://doi.org/10.1016/j.jcp.2012.07.044>. URL <https://www.sciencedirect.com/science/article/pii/S0021999112004299>.
- [70] E. Envía. *Influence of vane sweep on rotor-stator interaction noise*. PhD thesis, The University of Arizona, 1988. URL <http://hdl.handle.net/10150/184609>.
- [71] E. Envía and M. Nallasamy. Design selection and analysis of a swept and leaned stator concept. *Journal of Sound and Vibration*, 228(4):793–836, 1999. ISSN 0022-460X. doi: <https://doi.org/10.1006/jsvi.1999.2441>. URL <https://www.sciencedirect.com/science/article/pii/S0022460X99924410>.
-

-
- [72] R. Ewert. Broadband slat noise prediction based on CAA and stochastic sound sources from a fast random particle-mesh (rpm) method. *Computers & Fluids*, 37:369–387, 05 2008. doi: 10.1016/j.compfluid.2007.02.003.
- [73] Y. Feng, P. Boivin, J. Jacob, and P. Sagaut. Hybrid recursive regularized thermal lattice boltzmann model for high subsonic compressible flows. *Journal of Computational Physics*, 394:82–99, 2019. ISSN 0021-9991. doi: <https://doi.org/10.1016/j.jcp.2019.05.031>. URL <https://www.sciencedirect.com/science/article/pii/S0021999119303626>.
- [74] J. E. Ffowcs Williams, D. L. Hawkings, and M. J. Lighthill. Sound generation by turbulence and surfaces in arbitrary motion. *Philosophical Transactions of the Royal Society of London. Series A, Mathematical and Physical Sciences*, 264(1151):321–342, 1969. doi: 10.1098/rsta.1969.0031. URL <https://royalsocietypublishing.org/doi/abs/10.1098/rsta.1969.0031>.
- [75] A. Finez, M. Jacob, M. Roger, and E. Jondeau. *Broadband Noise Reduction Of Linear Cascades With Trailing Edge Serrations*. 2011. doi: 10.2514/6.2011-2874. URL <https://arc.aiaa.org/doi/abs/10.2514/6.2011-2874>.
- [76] M. Fiore, M. Daroukh, and M. Montagnac. Loss assessment of a counter rotating open rotor using URANS/LES with phase-lagged assumption. *Computers and Fluids*, 228:105025, 2021. doi: 10.1016/j.compfluid.2021.105025. URL <https://hal.archives-ouvertes.fr/hal-03325185>.
- [77] B. François, C. Polacsek, and R. Barrier. Zonal Detached Eddy Simulation of the Fan-Outlet Guide Vanes Stage of a Turbofan Engine: Part I—Methodology, Numerical Setup, and Aerodynamic Analysis. *Journal of Turbomachinery*, 144(11), 07 2022. ISSN 0889-504X. doi: 10.1115/1.4054528.111004.
- [78] G. Elias. Rapport technique : Analyse au second ordre des fonctions aléatoires pour la caractérisation des écoulements turbulents. <http://fs.fish.govt.nz/Page.aspx?pk=7&sc=SUR>, 2002. Département Simulation Numérique des écoulements et Aéroacoustique - ONERA.
- [79] F. Gea-Aguilera, X. Zhang, X. Chen, and J. Gill. Synthetic turbulence methods for leading edge noise predictions. In *21st AIAA/CEAS Aeroacoustics Conference*, 06 2015. doi: 10.2514/6.2015-2670.
- [80] F. Gea-Aguilera, J. Gill, and X. Zhang. Synthetic turbulence methods for computational aeroacoustic simulations of leading edge noise. *Computers & Fluids*, 157:240–252, 2017. ISSN 0045-7930. doi: <https://doi.org/10.1016/j.compfluid.2017.08.039>. URL <https://www.sciencedirect.com/science/article/pii/S0045793017303274>.
- [81] F. Gea-Aguilera, J. Gill, and X. Zhang. On the effects of fan wake modelling and vane design on cascade noise. *Journal of Sound and Vibration*, 459:114859, 2019. ISSN 0022-460X. doi: <https://doi.org/10.1016/j.jsv.2019.114859>. URL <https://www.sciencedirect.com/science/article/pii/S0022460X19304134>.
- [82] W. K. George, P. D. Beuther, and J. L. Lumley. Processing of random signals. In B. W. Hansen, editor, *Proceedings of the Dynamic Flow Conference 1978 on Dynamic Measurements in Unsteady Flows*, pages 757–800, Dordrecht, 1978. Springer Netherlands. ISBN 978-94-009-9565-9.
- [83] T. F. Geyer. *Measurement of the turbulence interaction noise generated by flat plates with perforated leading edges*. 2020. doi: 10.2514/6.2020-2576. URL <https://arc.aiaa.org/doi/abs/10.2514/6.2020-2576>.
- [84] J. Gill, X. Zhang, and P. Joseph. Single velocity-component modeling of leading edge turbulence interaction noise. *The Journal of the Acoustical Society of America*, 137:3209, 06 2015. doi: 10.1121/1.4921547.
- [85] S. Glegg and W. Devenport. Chapter 9 - turbulent flows. In *Aeroacoustics of Low Mach Number Flows*, pages 185–220. Academic Press, 2017. ISBN 978-0-12-809651-2. doi: <https://doi.org/10.1016/B978-0-12-809651-2.00009-6>. URL <https://www.sciencedirect.com/science/article/pii/B9780128096512000096>.
- [86] S. A. L. Glegg. The Response of a Swept Blade Row to a Three-Dimensional Gust. *Journal of Sound Vibration*, 227(1):29–64, Oct. 1999. doi: 10.1006/jsvi.1999.2327.
- [87] M. E. Goldstein. Unsteady vortical and entropic distortions of potential flows round arbitrary obstacles. *Journal of Fluid Mechanics*, 89(3):433–468, 1978. doi: 10.1017/S0022112078002682.
- [88] V. Golubev, R. Mankbadi, and J. Scott. *Numerical Inviscid Analysis of Nonlinear Airfoil Response to Impinging High-Intensity High-Frequency Gust*. 2004. doi: 10.2514/6.2004-3002. URL <https://arc.aiaa.org/doi/abs/10.2514/6.2004-3002>.
-

- [89] I. Gonzalez-Martino and D. Casalino. *Fan Tonal and Broadband Noise Simulations at Transonic Operating Conditions Using Lattice-Boltzmann Methods*. 2018. doi: 10.2514/6.2018-3919. URL <https://arc.aiaa.org/doi/abs/10.2514/6.2018-3919>.
- [90] S. Grace, I. Gonzalez-Martino, and D. Casalino. Analysis of fan-stage gap-flow data to inform simulation of fan broadband noise. *Philosophical Transactions of the Royal Society A: Mathematical, Physical and Engineering Sciences*, 377(2159):20190080, 2019. doi: 10.1098/rsta.2019.0080. URL <https://royalsocietypublishing.org/doi/abs/10.1098/rsta.2019.0080>.
- [91] S. Guo, Y. Feng, J. Jacob, F. Renard, and P. Sagaut. An efficient lattice boltzmann method for compressible aerodynamics on d3q19 lattice. *Journal of Computational Physics*, 418:109570, 2020. ISSN 0021-9991. doi: <https://doi.org/10.1016/j.jcp.2020.109570>. URL <https://www.sciencedirect.com/science/article/pii/S0021999120303442>.
- [92] S. Gu erin, C. Kissner, P. Seeler, R. Bl azquez, P. Carrasco Lara na, H. de Laborderie, D. Lewis, P. Chaitanya, C. Polacsek, and J. Thisse. ACAT1 benchmark of rans-informed analytical methods for fan broadband noise prediction: Part ii - influence of the acoustic models. *Acoustics*, 2(3): 617–649, 2020. ISSN 2624-599X. URL <https://www.mdpi.com/2624-599X/2/3/33>.
- [93] T. Hainaut, G. Gabard, and V. Clair. Caa study of airfoil broadband interaction noise using stochastic turbulent vorticity sources. In *21st AIAA/CEAS Aeroacoustics Conference*, Dallas, United States, 2015. American Institute of Aeronautics and Astronautics. doi: 10.2514/6.2015-2222. URL <https://hal.archives-ouvertes.fr/hal-02085980>.
- [94] A. Hales, L. J. Ayton, R. Kisler, A. Mahgoub, C. Jiang, R. Dixon, C. de Silva, D. Moreau, and C. J. Doolan. *Reduction of Leading-Edge Noise by Tailored Turbulence Anisotropy*. 2022. doi: 10.2514/6.2022-3046. URL <https://arc.aiaa.org/doi/abs/10.2514/6.2022-3046>.
- [95] D. Hanson. Theory for broadband noise of rotor and stator cascades with inhomogeneous inflow turbulence including effects of lean and sweep. *NASA Technical Reports*, 06 2001.
- [96] A. S. Hersh, P. T. Soderman, and R. E. Hayden. Investigation of acoustic effects of leading-edge serrations on airfoils. *Journal of Aircraft*, 11(4):197–202, 1974. doi: 10.2514/3.59219. URL <https://doi.org/10.2514/3.59219>.
- [97] R. Hixon, R. Nallasamy, and S. Sawyer. Parallelization strategy for an explicit computational aeroacoustics code. In *8th AIAA/CEAS Aeroacoustics Conference & Exhibit*, 06 2002. ISBN 978-1-62410-119-9. doi: 10.2514/6.2002-2583.
- [98] R. Hixon, A. Sescu, R. Nallasamy, and S. Sawyer. Prediction of noise from realistic rotor-wake/stator- row interaction using computational aeroacoustics. In *15th AIAA/CEAS Aeroacoustics Conference (30th AIAA Aeroacoustics Conference)*, 05 2009. doi: 10.2514/6.2009-3339.
- [99] R. Hixon, A. Sescu, and S. Sawyer. Vortical gust boundary condition for realistic rotor wake/stator interaction noise prediction using computational aeroacoustics. *Journal of Sound and Vibration*, 330(16):3801–3817, 2011. ISSN 0022-460X. doi: <https://doi.org/10.1016/j.jsv.2011.03.011>. URL <https://www.sciencedirect.com/science/article/pii/S0022460X1100191X>. Computational Aero-Acoustics (CAA) for aircraft noise prediction - Part A.
- [100] T. Horstmann. *M ethodes num eriques hybrides bas ees sur une approche Boltzmann sur r eseau en vue de l'application aux maillages non-uniformes*. PhD thesis, Ecole Centrale de Lyon, 2018. URL <http://www.theses.fr/2018LYSEC027>. 2018LYSEC027.
- [101] M. S. Howe. Noise produced by a sawtooth trailing edge. *The Journal of the Acoustical Society of America*, 90(1):482–487, 1991. doi: 10.1121/1.401273. URL <https://doi.org/10.1121/1.401273>.
- [102] S. Huang, Q. Li, and J. Wu. A general inflow turbulence generator for large eddy simulation. *Journal of Wind Engineering and Industrial Aerodynamics*, 98(10):600–617, 2010. ISSN 0167-6105. doi: <https://doi.org/10.1016/j.jweia.2010.06.002>. URL <https://www.sciencedirect.com/science/article/pii/S0167610510000644>.
- [103] L. S. Hultgren and R. O. Arechiga. Full-scale turbofan engine noise-source separation using a four-signal method. In *NASA Technical Reports*, 2016.
- [104] J. Jacob, O. Malaspinas, and P. Sagaut. A new hybrid recursive regularised Bhatnagar–Gross–Krook collision model for lattice Boltzmann method-based large eddy simulation. *Journal of Turbulence*, pages 1 – 26, Nov. 2018. doi: 10.1080/14685248.2018.1540879. URL <https://hal.archives-ouvertes.fr/hal-02114308>.

-
- [105] N. Jarrin, R. Prosser, J.-C. Uribe, S. Benhamadouche, and D. Laurence. Reconstruction of turbulent fluctuations for hybrid rans/les simulations using a synthetic-eddy method. *International Journal of Heat and Fluid Flow*, 30(3):435–442, 2009. ISSN 0142-727X. doi: <https://doi.org/10.1016/j.ijheatfluidflow.2009.02.016>. URL <https://www.sciencedirect.com/science/article/pii/S0142727X09000538>. The Seventh International Symposium on Engineering Turbulence Modelling and Measurements, ETMM7.
- [106] A. Juknevičius and T. Chong. On the leading edge noise and aerodynamics of thin aerofoil subjected to the straight and curved serrations. *Journal of Sound and Vibration*, 425:324–343, 07 2018. doi: [10.1016/j.jsv.2018.02.038](https://doi.org/10.1016/j.jsv.2018.02.038).
- [107] J.-H. Kim, K.-S. Choi, G. Lacagnina, P. Chaitanya, P. Joseph, S. M. Hasheminejad, T. Pei Chong, M. F. Shahab, M. Omidyeganeh, and A. Pinelli. Aerodynamic and aeroacoustic optimization of leading-edge undulation of a naca 65(12)-10 airfoil. *AIAA Journal*, 60(4):2342–2353, 2022. doi: [10.2514/1.J060716](https://doi.org/10.2514/1.J060716). URL <https://doi.org/10.2514/1.J060716>.
- [108] J. W. Kim and S. Haeri. An advanced synthetic eddy method for the computation of aerofoil-turbulence interaction noise. *J. Comput. Phys.*, 287:1–17, 2015.
- [109] C. Kissner and S. Guérin. Comparison of predicted fan broadband noise using a two- versus a three-dimensional synthetic turbulence method. *Journal of Sound and Vibration*, 508:116221, 2021. ISSN 0022-460X. doi: <https://doi.org/10.1016/j.jsv.2021.116221>. URL <https://www.sciencedirect.com/science/article/pii/S0022460X21002935>.
- [110] C. Kissner, S. Guérin, P. Seeler, M. Billson, P. Chaitanya, P. Carrasco Laraña, H. de Laborderie, B. François, K. Lefarth, D. Lewis, G. Montero Villar, and T. Nodé-Langlois. ACAT1 benchmark of rans-informed analytical methods for fan broadband noise prediction—part i—influence of the rans simulation. *Acoustics*, 2(3):539–578, 2020. ISSN 2624-599X. URL <https://www.mdpi.com/2624-599X/2/3/29>.
- [111] C. Kissner, S. Guérin, P. Seeler, M. Billson, P. Chaitanya, P. Carrasco Laraña, H. de Laborderie, B. François, K. Lefarth, D. Lewis, G. Montero Villar, and T. Nodé-Langlois. ACAT1 benchmark of rans-informed analytical methods for fan broadband noise prediction—part i—influence of the rans simulation. *Acoustics*, 2(3):539–578, 2020. ISSN 2624-599X. URL <https://www.mdpi.com/2624-599X/2/3/29>.
- [112] C. A. Kissner and S. Guérin. *Fan Broadband Noise Prediction for the ACAT1 Fan Using a Three-Dimensional Random Particle Mesh Method*. 2020. doi: [10.2514/6.2020-2520](https://doi.org/10.2514/6.2020-2520). URL <https://arc.aiaa.org/doi/abs/10.2514/6.2020-2520>.
- [113] C. A. Kissner and S. Guérin. Influence of wake and background turbulence on predicted fan broadband noise. *AIAA Journal*, 58(2):659–672, 2020. doi: [10.2514/1.J058148](https://doi.org/10.2514/1.J058148). URL <https://doi.org/10.2514/1.J058148>.
- [114] R. H. Kraichnan. Diffusion by a random velocity field. *The Physics of Fluids*, 13(1):22–31, 1970. doi: [10.1063/1.1692799](https://doi.org/10.1063/1.1692799). URL <https://aip.scitation.org/doi/abs/10.1063/1.1692799>.
- [115] G. Lacagnina, P. Chaitanya, J.-H. Kim, T. Berk, P. Joseph, K.-S. Choi, B. Ganapathisubramani, S. M. Hasheminejad, T. P. Chong, O. Stalnov, M. F. Shahab, M. Omidyeganeh, and A. Pinelli. Leading edge serrations for the reduction of aerofoil self-noise at low angle of attack, pre-stall and post-stall conditions. *International Journal of Aeroacoustics*, 20(1-2):130–156, 2021. doi: [10.1177/1475472X20978379](https://doi.org/10.1177/1475472X20978379). URL <https://doi.org/10.1177/1475472X20978379>.
- [116] A. Lafitte. *Prédiction de l'aéroacoustique de jets subsoniques confinés à l'aide d'une méthode stochastique de génération de la turbulence*. Theses, Ecole Centrale de Lyon, Nov. 2012. URL <https://tel.archives-ouvertes.fr/tel-00805414>.
- [117] M. Lebrun. *Vers une prédiction globale du bruit des soufflantes à partir de l'analogie acoustique et des outils de mécanique des fluides numérique*. PhD thesis, Ecole Centrale de Lyon, 2002.
- [118] E. Lévêque, F. Toschi, L. Shao, and J.-P. Bertoglio. Shear-improved Smagorinsky model for large-eddy simulation of wall-bounded turbulent flows. *Journal of Fluid Mechanics*, 570:491–502, 2007. doi: [10.1017/S0022112006003429](https://doi.org/10.1017/S0022112006003429). URL <https://hal.archives-ouvertes.fr/hal-00272169>.
- [119] E. Leveque, H. Touil, S. Malik, D. Ricot, and A. Sengissen. Wall-modeled large-eddy simulation of the flow past a rod-airfoil tandem by the lattice boltzmann method. *International Journal of Numerical Methods for Heat and Fluid Flow*, 28:00–00, 04 2018. doi: [10.1108/HFF-06-2017-0258](https://doi.org/10.1108/HFF-06-2017-0258).
- [120] D. Lewis. *From analytical to fully numerical predictions of the broadband noise radiated by a full fan-OGV stage*. PhD thesis, Ecole Centrale de Lyon, 2020.
-

-
- [121] D. Lewis, S. Moreau, and M. C. Jacob. *Broadband Noise Predictions on the ACAT1 Fan Stage Using Large Eddy Simulations and Analytical Models*. 2020. doi: 10.2514/6.2020-2519. URL <https://arc.aiaa.org/doi/abs/10.2514/6.2020-2519>.
- [122] D. Lewis, J. de Laborderie, M. Sanjosé, S. Moreau, M. C. Jacob, and V. Masson. Parametric study on state-of-the-art analytical models for fan broadband interaction noise predictions. *Journal of Sound and Vibration*, 514:116423, 2021. ISSN 0022-460X. doi: <https://doi.org/10.1016/j.jsv.2021.116423>. URL <https://www.sciencedirect.com/science/article/pii/S0022460X21004673>.
- [123] H. W. Liepmann, J. Laufer, and K. Liepmann. On the spectrum of isotropic turbulence. In *Technical note 2473*. National Advisory Committee for Aeronautics, 1951.
- [124] M. J. Lighthill. On Sound Generated Aerodynamically. I. General Theory. *Proceedings of the Royal Society of London Series A*, 211(1107):564–587, Mar. 1952. doi: 10.1098/rspa.1952.0060.
- [125] X. Liu, P. Chaitanya, and P. Joseph. Proper orthogonal decomposition method for the prediction of fan broadband interaction noise. *AIAA Journal*, 60(9):5336–5356, 2022. doi: 10.2514/1.J061176. URL <https://doi.org/10.2514/1.J061176>.
- [126] B. Lyu and L. Ayton. Rapid noise prediction models for serrated leading and trailing edges. *Journal of Sound and Vibration*, 469:115136, 12 2019. doi: 10.1016/j.jsv.2019.115136.
- [127] B. Lyu, L. J. Ayton, and P. Chaitanya. On the acoustic optimality of leading-edge serration profiles. *Journal of Sound and Vibration*, 462:114923, 2019. ISSN 0022-460X. doi: <https://doi.org/10.1016/j.jsv.2019.114923>. URL <https://www.sciencedirect.com/science/article/pii/S0022460X19304857>.
- [128] V. Masson, H. Posson, M. Sanjose, T. Léonard, S. Moreau, and M. Roger. *Fan-OGV interaction broadband noise prediction in a rigid annular duct with swirling and sheared mean flow*. 2016. doi: 10.2514/6.2016-2944. URL <https://arc.aiaa.org/doi/abs/10.2514/6.2016-2944>.
- [129] L. Mazella, C. C. Paruchuri, G. Lacagnina, Y. Mao, and P. Joseph. *Experimental investigation of the noise control performance of leading edge serrations in a rectilinear cascade*. 2019. doi: 10.2514/6.2019-2472. URL <https://arc.aiaa.org/doi/abs/10.2514/6.2019-2472>.
- [130] S. Moreau. Turbomachinery noise predictions: Present and future. *Acoustics*, 1(1):92–116, 2019. ISSN 2624-599X. doi: 10.3390/acoustics1010008. URL <https://www.mdpi.com/2624-599X/1/1/8>.
- [131] S. Moreau, G. Bampanis, and M. Roger. *Analytical and experimental investigation of leading-edge noise reduction on a flat plate with serrations*. 2020. doi: 10.2514/6.2020-2542. URL <https://arc.aiaa.org/doi/abs/10.2514/6.2020-2542>.
- [132] G. Mouret, N. Gourdain, and L. Castillon. Adaptation of Phase-Lagged Boundary Conditions to Large Eddy Simulation in Turbomachinery Configurations. *Journal of Turbomachinery*, 138(4), 12 2015. ISSN 0889-504X. doi: 10.1115/1.4032044. URL <https://doi.org/10.1115/1.4032044>. 041003.
- [133] D. Mueller, H.-J. Schulz, G. Zitouni, and W. Baumann. *Europe's Largest Aero Acoustic Test Facility for Aero Engine Fans - The Development and Operation of the AneCom AeroTest Anechoic Chamber*. 2005. doi: 10.2514/6.2005-3050. URL <https://arc.aiaa.org/doi/abs/10.2514/6.2005-3050>.
- [134] M. Namba and J. Schulten. Third computational aeroacoustics (CAA) workshop on benchmark problems: Category 4 – fan stator with harmonic excitation by rotor wake. NASA Technical Memorandum 2000-209790, pp. 73-85, NASA, 2000.
- [135] S. Narayanan, P. Chaitanya, S. Haeri, P. Joseph, J. W. Kim, and C. Polacsek. Airfoil noise reductions through leading edge serrations. *Physics of Fluids*, 27(2):025109, 2015. doi: 10.1063/1.4907798. URL <https://doi.org/10.1063/1.4907798>.
- [136] Niedoba, P., Jicha, M., and Cermak, L. On stochastic inlet boundary condition for unsteady simulations. *EPJ Web of Conferences*, 67:02082, 2014. doi: 10.1051/epjconf/20146702082. URL <https://doi.org/10.1051/epjconf/20146702082>.
- [137] P. Sagaut. Master's program course "modélisation des écoulement en interaction nse02". <http://fs.fish.govt.nz/Page.aspx?pk=7&sc=SUR>, 2012. Institut Jean Le Rond d'Alembert - Université Peirre et Marie Curie - pp. 35-38.
- [138] C. Paruchuri. *Aerofoil geometry effects on turbulence interaction noise*. PhD thesis, University of Southampton, April 2017. URL <https://eprints.soton.ac.uk/415884/>.
-

-
- [139] R. Paterson and R. Amiet. *Acoustic radiation and surface pressure characteristics of an airfoil due to incident turbulence*. 1976. doi: 10.2514/6.1976-571. URL <https://arc.aiaa.org/doi/abs/10.2514/6.1976-571>.
- [140] A. Pereira, E. Salze, J. Regnard, F. Gea-Aguilera, and M. Gruber. *New modular fan rig for advanced aeroacoustic tests - Modal decomposition on a 20" UHBR fan stage*. 2019. doi: 10.2514/6.2019-2604. URL <https://arc.aiaa.org/doi/abs/10.2514/6.2019-2604>.
- [141] G. Podboy, M. Krupar, S. Helland, and C. Hughes. *Steady and unsteady flow field measurements within a NASA 22 inch fan model*. 2002. doi: 10.2514/6.2002-1033. URL <https://arc.aiaa.org/doi/abs/10.2514/6.2002-1033>.
- [142] C. Polacsek, G. Reboul, V. Clair, T. Le Garrec, G. Dufour, and H. Deniau. Turbulence-airfoil interaction noise reduction using wavy leading edge: an experimental and numerical study. In *18th International Congress on Sound & Vibration*, Rio de Janeiro, Brazil, 2011. URL <https://hal.archives-ouvertes.fr/hal-02086038>.
- [143] C. Polacsek, V. Clair, T. Garrec, G. Reboul, and M. Jacob. Numerical predictions of turbulence/cascade-interaction noise using computational aeroacoustics with a stochastic model. *AIAA Journal*, 53:1–16, 10 2015. doi: 10.2514/1.J053896.
- [144] C. Polacsek, A. Cader, M. Buszyk, R. Barrier, F. Gea-Aguilera, and H. Posson. Aeroacoustic design and broadband noise predictions of a fan stage with serrated outlet guide vanes. *Physics of fluids*, 32(10):107107, 2020.
- [145] C. Polacsek, M. Daroukh, B. François, and R. Barrier. Zonal Detached Eddy Simulation of the Fan-Outlet Guide Vanes Stage of a Turbofan Engine: Part II—Broadband Noise Predictions. *Journal of Turbomachinery*, 144(11), 07 2022. ISSN 0889-504X. doi: 10.1115/1.4054764. URL <https://doi.org/10.1115/1.4054764>. 111005.
- [146] R. Poletto, T. Craft, and A. Revell. A new divergence free synthetic eddy method for the reproduction of inlet flow conditions for les. *Flow, Turbulence and Combustion*, 91:1–21, 10 2013. doi: 10.1007/s10494-013-9488-2.
- [147] S. B. Pope. *Turbulent Flows*. Cambridge University Press, 2000. doi: 10.1017/CBO9780511840531.
- [148] H. Posson, M. Roger, and S. Moreau. On a uniformly valid analytical rectilinear cascade response function. *Journal of Fluid Mechanics*, 663:22–52, 2010. doi: 10.1017/S0022112010003368. URL <https://hal.archives-ouvertes.fr/hal-00566055>.
- [149] H. Posson, S. Moreau, and M. Roger. Broadband noise prediction of fan outlet guide vane using a cascade response function. *Journal of Sound and Vibration*, 330(25):6153–6183, 2011. ISSN 0022-460X. doi: <https://doi.org/10.1016/j.jsv.2011.07.040>. URL <https://www.sciencedirect.com/science/article/pii/S0022460X11006213>.
- [150] C. Pérez Arroyo, T. Leonard, M. Sanjosé, S. Moreau, and F. Duchaine. Large eddy simulation of a scale-model turbofan for fan noise source diagnostic. *Journal of Sound and Vibration*, 445: 64–76, 2019. ISSN 0022-460X. doi: <https://doi.org/10.1016/j.jsv.2019.01.005>. URL <https://www.sciencedirect.com/science/article/pii/S0022460X19300112>.
- [151] R. Pérez-Torró and J. W. Kim. A large-eddy simulation on a deep-stalled aerofoil with a wavy leading edge. *Journal of Fluid Mechanics*, 813:23–52, 2017. doi: 10.1017/jfm.2016.841.
- [152] G. Reboul. *Modélisation du bruit à large bande de soufflantes de turboréacteurs*. Theses, Ecole Centrale de Lyon, Nov. 2010. URL <https://tel.archives-ouvertes.fr/tel-00562647>.
- [153] G. Reboul, C. Polacsek, S. Lewy, and S. Heib. Aeroacoustic computation of ducted-fan broadband noise using les data. *The Journal of the Acoustical Society of America*, 123:3539, 06 2008. doi: 10.1121/1.2934519.
- [154] G. Reboul, A. Cader, C. Polacsek, T. L. Garrec, R. Barrier, and N. B. Nasr. *CAA Prediction of Rotor-Stator Interaction Using Synthetic Turbulence: Application to a Low-Noise Serrated OGV*. 2017. doi: 10.2514/6.2017-3714. URL <https://arc.aiaa.org/doi/abs/10.2514/6.2017-3714>.
- [155] S. Redonnet and J. Caltagirone. *Simulation de la propagation acoustique en présence d'écoulements quelconques et de structures solides par résolution numérique des équations d'Euler*. PhD thesis, Université de Bordeaux, 2001. URL <https://books.google.fr/books?id=1BPgzQEACAAJ>.
- [156] S. Redonnet, E. Manoha, and P. Sagaut. *Numerical simulation of propagation of small perturbations interacting with flows and solid bodies*. 2001. doi: 10.2514/6.2001-2223. URL <https://arc.aiaa.org/doi/abs/10.2514/6.2001-2223>.
-

-
- [157] T. Rigall, B. Cotté, and P. Lafon. Low-noise synthetic turbulence tailored to lateral periodic boundary conditions. *Fluids*, 6(6), 2021.
- [158] M. Roger, C. Schram, and L. D. Santana. *Reduction of Airfoil Turbulence-Impingement Noise by Means of Leading-Edge Serrations and/or Porous Material*. 2013. doi: 10.2514/6.2013-2108. URL <https://arc.aiaa.org/doi/abs/10.2514/6.2013-2108>.
- [159] E. Salze, A. Pereira, P. Souchotte, J. Regnard, F. Gea-Aguilera, and M. Gruber. *New modular fan rig for advanced aeroacoustic tests - Acoustic characterization of the facility*. 2019. doi: 10.2514/6.2019-2603. URL <https://arc.aiaa.org/doi/abs/10.2514/6.2019-2603>.
- [160] A. Sescu and R. Hixon. Toward low-noise synthetic turbulent inflow conditions for aeroacoustic calculations. *International Journal for Numerical Methods in Fluids*, 73(12):1001–1010, 2013. doi: <https://doi.org/10.1002/flid.3833>. URL <https://onlinelibrary.wiley.com/doi/abs/10.1002/flid.3833>.
- [161] A. Sescu, R. Hixon, and S. Sawyer. Validation of a caa code using a benchmark wake-stator interaction problem. In *15th AIAA/CEAS Aeroacoustics Conference (30th AIAA Aeroacoustics Conference)*, 05 2009. doi: 10.2514/6.2009-3340.
- [162] X. Shan, X.-F. Yuan, and H. Chen. Kinetic theory representation of hydrodynamics: a way beyond the navier-stokes equation. *Journal of Fluid Mechanics*, 550:413–441, 2006. doi: 10.1017/S0022112005008153.
- [163] Z. Shen and X. Zhang. *Random-eddy-superposition technique for leading edge noise predictions*. 2018. doi: 10.2514/6.2018-3597. URL <https://arc.aiaa.org/doi/abs/10.2514/6.2018-3597>.
- [164] Z. Shen and X. Zhang. Direct anisotropic filter method of generating synthetic turbulence applied to turbulence-airfoil interaction noise prediction. *Journal of Sound and Vibration*, 458: 544–564, 2019. ISSN 0022-460X. doi: <https://doi.org/10.1016/j.jsv.2019.07.003>. URL <https://www.sciencedirect.com/science/article/pii/S0022460X1930389X>.
- [165] M. Siefert and R. Ewert. *Sweeping Sound Generation in Jets Realized with a Random Particle-Mesh Method*. 2009. doi: 10.2514/6.2009-3369. URL <https://arc.aiaa.org/doi/abs/10.2514/6.2009-3369>.
- [166] P. Spalart, S. Deck, M. Shur, K. Squires, M. Strelets, and A. Travin. A new version of detached-eddy simulation, resistant to ambiguous grid densities. *Theoretical and Computational Fluid Dynamics*, 20:181–195, 07 2006. doi: 10.1007/s00162-006-0015-0.
- [167] C. K. W. Tam and Z. Dong. Radiation and outflow boundary conditions for direct computation of acoustic and flow disturbances in a nonuniform mean flow. *Journal of Computational Acoustics*, 04(02):175–201, 1996. doi: 10.1142/S0218396X96000040. URL <https://doi.org/10.1142/S0218396X96000040>.
- [168] C. Teruna, F. Avallone, D. Casalino, and D. Ragni. Numerical investigation of leading edge noise reduction on a rod-airfoil configuration using porous materials and serrations. *Journal of Sound and Vibration*, 494:115880, 2021. ISSN 0022-460X. doi: <https://doi.org/10.1016/j.jsv.2020.115880>. URL <https://www.sciencedirect.com/science/article/pii/S0022460X20307173>.
- [169] C. Teruna, L. F. Rego, D. Casalino, D. Ragni, and F. Avallone. *Full-Scale Application of Porous Leading-Edge Treatments in a Fan Stage for Mitigating Rotor-Stator Interaction Noise*. 2022. doi: 10.2514/6.2022-2963. URL <https://arc.aiaa.org/doi/abs/10.2514/6.2022-2963>.
- [170] F. Tong, W. Qiao, W. Chen, H. Cheng, R. WEI, and X. WANG. Numerical analysis of broadband noise reduction with wavy leading edge. *Chinese Journal of Aeronautics*, 31(7): 1489–1505, 2018. ISSN 1000-9361. doi: <https://doi.org/10.1016/j.cja.2018.03.020>. URL <https://www.sciencedirect.com/science/article/pii/S1000936118301328>.
- [171] F. Tong, W. Qiao, K. Xu, L. Wang, W. Chen, and X. Wang. On the study of wavy leading-edge vanes to achieve low fan interaction noise. *Journal of Sound and Vibration*, 419:200–226, 2018. ISSN 0022-460X. doi: <https://doi.org/10.1016/j.jsv.2018.01.017>. URL <https://www.sciencedirect.com/science/article/pii/S0022460X18300257>.
- [172] H. Touil, S. Malik, E. Lévêque, D. Ricot, and A. Sengissen. Wall-modeled large-eddy simulation of the flow past a rod-airfoil tandem by the Lattice Boltzmann method. *International Journal of Numerical Methods for Heat and Fluid Flow*, 28(5):1096–1116, 2018. doi: 10.1108/HFF-06-2017-0258. URL <https://hal.archives-ouvertes.fr/hal-02084828>.
-

-
- [173] J. M. Turner and J. W. Kim. On the universal trends in the noise reduction due to wavy leading edges in aerofoil–vortex interaction. *Journal of Fluid Mechanics*, 871:186–211, 2019. doi: 10.1017/jfm.2019.314.
- [174] Y. Wang, K. Zhao, X.-Y. Lu, Y.-B. Song, and G. J. Bennett. Bio-inspired aerodynamic noise control: A bibliographic review. *Applied Sciences*, 9(11), 2019. ISSN 2076-3417. doi: 10.3390/app9112224. URL <https://www.mdpi.com/2076-3417/9/11/2224>.
- [175] A. Wohlbrandt, N. Hu, S. Guérin, and R. Ewert. Analytical reconstruction of isotropic turbulence spectra based on the gaussian transform. *Computers & Fluids*, 132:46–50, jun 2016. doi: 10.1016/j.compfluid.2016.03.023. URL <https://doi.org/10.1016%2Fj.compfluid.2016.03.023>.
- [176] A. Wohlbrandt, C. Kissner, and S. Guérin. Impact of cyclostationarity on fan broadband noise prediction. *Journal of Sound and Vibration*, 420:142–164, 2018. ISSN 0022-460X. doi: <https://doi.org/10.1016/j.jsv.2018.01.039>. URL <https://www.sciencedirect.com/science/article/pii/S0022460X18300476>.
- [177] R. Woodward, C. Hughes, R. Jeracki, and C. Miller. *Fan Noise Source Diagnostic Test – Far-field Acoustic Results*. 2002. doi: 10.2514/6.2002-2427. URL <https://arc.aiaa.org/doi/abs/10.2514/6.2002-2427>.
- [178] R. Yu and X.-S. Bai. A fully divergence-free method for generation of inhomogeneous and anisotropic turbulence with large spatial variation. *Journal of Computational Physics*, 256:234–253, 2014. ISSN 0021-9991. doi: <https://doi.org/10.1016/j.jcp.2013.08.055>. URL <https://www.sciencedirect.com/science/article/pii/S0021999113005998>.
- [179] S. Zhong, X. Zhang, B. Peng, and X. Huang. An analytical correction to amiet’s solution of airfoil leading-edge noise in non-uniform mean flows. *Journal of Fluid Mechanics*, 882, 01 2020. doi: 10.1017/jfm.2019.839.